

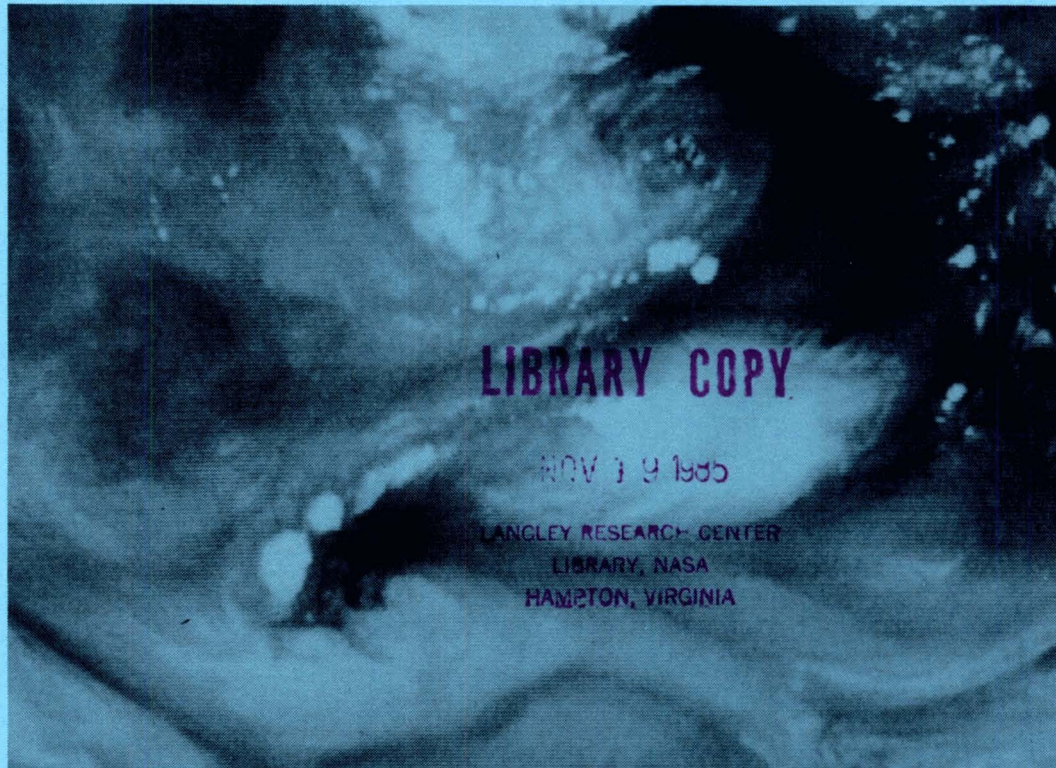
**NASA
Reference
Publication
1151**

October 1985

FOR REFERENCE

NOT TO BE TAKEN FROM THIS ROOM

**VAS Demonstration:
(VISSR Atmospheric Sounder)
Description and Final Report**



**NASA
Reference
Publication
1151**

1985

**VAS Demonstration:
(VISSR Atmospheric Sounder)
Description and Final Report**

Edited by
**H. E. Montgomery
and L. W. Uccellini**

*Goddard Space Flight Center
Greenbelt, Maryland*



National Aeronautics
and Space Administration

**Scientific and Technical
Information Branch**

FOREWORD

As this document shows, we have concluded a successful demonstration of the VISSR Atmospheric Sounder (VAS). The technical advantages of VAS are easy to enumerate: improved signal-to-noise ratio through multiple sampling, higher horizontal resolution, and smaller and constant nadir viewing angle. All contribute to better instrument performance, but by far the greatest value of VAS over polar orbiters is its capability for continuous observation. Weather is air in motion, and VAS allows us to observe atmospheric changes as they occur. Although all sounders (VAS included) do not have the absolute accuracy we desire, this document shows the great value of high relative accuracy.

The achievements documented here would not have occurred were it not for the superb team work of the participants. Individuals in the laboratories of the university, government, and industry all pulled together to make the effort a success. This was a NASA experiment on a NOAA operational spacecraft. Mixing research and operations does have its problems, but has some advantages as well. One soon learns where the important performance requirements lie.

What about the future? These results are the foundation for future satellites. The VAS experience suggests that extension into the microwave region, and increased spectral resolution in the infrared region, are essential so that we can obtain soundings through persistent clouds and with improved vertical resolution. Geostationary microwave instruments and high spectral resolution infrared interferometers are feasible and would be highly useful. The administrative mechanisms of interagency cooperation must be put into motion as soon as possible to accomplish this. We must not lose the momentum that the VAS Demonstration has given to the geostationary weather observing program.

Professor Verner E. Suomi
Director
Space Science and Engineering Center
University of Wisconsin-Madison

CONTENTS

	<i>Page</i>
Foreword.	iii
Acknowledgments.	xv
Acronyms and Abbreviations.	xvii
Executive Summary.	xxi
1. INTRODUCTION	1
1.1 History	1
1.2 Objectives	1
2. VAS INSTRUMENT DESCRIPTION	3
2.1 Background	3
2.2 The VAS Instrument	3
2.2.1 VISSR Mode	6
2.2.2 Dwell-Sounding Mode	6
2.2.3 Multispectral Imaging Mode.	7
2.3 Ground Operation	7
2.3.1 Demonstration Dedicated	7
2.3.2 Interrupt Mode	7
2.3.3 Transparent VAS Mode	7
3. DATA ACQUISITION AND COMMAND NETWORK	9
3.1 NOAA CDA Station.	9
3.2 GSFC Data Acquisition and Processing System	11
3.2.1 Data Flow	11
3.2.2 Research Software.	13
3.2.2.1 Temperature/Moisture Sounding Software	13
3.2.2.2 Meteorological Assessment Software	13
3.3 UW Data Acquisition and Processing System.	13
3.3.1 Reception and Preprocessing	13
3.3.2 McIDAS Applications.	14

CONTENTS (Continued)

	<i>Page</i>
3.3.2.1 Meteorological Data Acquisition	14
3.3.2.2 McIDAS III Computer	14
3.3.2.3 McIDAS Video Terminals	14
3.3.2.4 Computer Operating System	16
3.3.2.5 McIDAS Control Program	16
3.3.2.6 McIDAS Application Programs	16
4. VAS INSTRUMENT PERFORMANCE APPRAISAL	17
4.1 Introduction	17
4.2 Specifications For the VAS Instrument	18
4.3 Radiometric Noise and the Spin Budget	22
4.4 Detector-to-Detector Registration	23
4.5 Comparison of Geosynchronous and Polar Sounders	26
4.6 Comparison of VAS with Radiosondes	27
4.7 Truncation Errors	28
4.8 Zero-Point Calibration Errors	28
4.9 Droop Along a VAS Scanline	28
4.10 Spin-to-Spin Reproducibility	30
4.11 "Scattered Light" and Resampling Errors	31
4.12 Ground System Operations	32
4.13 Summary and Discussion	33
5. VALIDATION AND STATISTICAL ANALYSIS OF VAS SOUNDINGS	35
5.1 Statistical Validation of VAS Retrievals at GSFC	35
5.1.1 The VAS Retrieval Method	35
5.1.2 Measuring the Accuracy of VAS Soundings	36
5.1.3 Data Preparation	36
5.1.4 Absolute Errors	38
5.1.5 Relative Errors	38
5.1.6 Summary of Validation and Statistical Analysis of GSFC Retrievals	39
5.2 UW NESDIS (CIMSS) Results	43
5.2.1 Profile Characteristics	43
5.2.2 Statistical Validations	45
5.2.2.1 Comparisons with Radiosondes	45
5.2.2.2 Comparisons with Dropsondes	46
5.2.2.3 Comparisons of Gradient Winds with Aircraft Observations	46
5.3 AVE/VAS Ground Truth Experiment	50
5.3.1 MSFC Special Network Statistical Evaluations	54
5.3.1.1 Data Set Preparation	54
5.3.1.2 Statistical Analysis of Gridded Data	57

CONTENTS (Continued)

	<i>Page</i>
5.3.1.3 Vertical Structure of VAS Retrievals	68
5.3.1.4 Horizontal Structure of VAS Retrievals	68
5.3.1.5 Discussion and Conclusions	71
5.3.2 GSFC Verification of VAS Regression Soundings of 6 March 1982	77
5.3.2.1 "VAS Plus Surface" Regression Soundings	77
5.3.2.2 Statistics of Retrieval Errors	77
5.3.2.2.1 Minimum Screening	77
5.3.2.2.2 Stringent Co-location	78
5.3.2.2.3 Effect of Cloud Contamination	79
5.3.2.3 Field Analysis and Comparisons	79
5.3.2.4 Discussion and Summary	80
5.3.3 UW NESDIS (CIMSS) Special Network VAS Evaluation	83
5.3.3.1 Ageostrophic Winds	83
5.3.3.2 Time Coupling of Geopotential Analyses	89
5.3.3.3 Differential Properties Algorithm	89
6. METEOROLOGICAL ASSESSMENT OF VAS IN MONITORING THE PRE-CONVECTIVE ENVIRONMENT FOR SEVERE LOCAL STORMS.	95
6.1 GSFC Assessment	95
6.1.1 Phase 1 of GSFC Research Effort: Pre-launch VAS Simulation Study	95
6.1.2 Phase 2 of GSFC Research Effort: Assessment of VAS Imagery.	96
6.1.3 Phase 3 of GSFC Research Effort: Assessment of VAS Retrievals for Pre-Storm Environments	106
6.1.4 Summary of GSFC Research Effort	111
6.2 UW Assessment.	114
6.2.1 Nowcasting Applications to Severe Weather Forecasting	114
6.2.2 Objective Estimation of Severe Weather Probability	121
6.2.3 Application to NMC Limited Area Numerical Forecasts	121
6.2.4 Tropical Storm Trajectory Forecasting	125
6.2.5 Sea Surface Temperature (SST) Determination	127
6.2.6 Specifying Heights and Velocities of Cloud Motions.	129
7. VAS DATA AVAILABILITY	133
7.1 Introduction.	133
7.2 Data Description.	133

CONTENTS (Continued)

	<i>Page</i>
7.3 UW/NOAA VAS Data Archive	141
7.3.1 Data Availability	141
7.3.2 How to Order UW/NOAA Data	141
7.4 GSFC VAC Data Archive	157
7.4.1 Data Availability	157
7.4.2 How to Order GSFC Data	157
References	161
 Appendix—Publications and Reports Supported by the VAS Demonstration	
Book and Journal Articles	164
Reviews of the VAS Demonstration	165
Presentations at Conferences and Workshops	165
Technical Reports from NASA/GSFC	167
Technical Reports from SBRC	167
Technical Reports from NOAA/UW/SSEC	168
Technical Reports from Westinghouse Corp.	168
Technical Reports from CSC	168
Technical Reports from MSFC/TAMU	169

ILLUSTRATIONS

<i>Figure</i>		<i>Page</i>
2-1	VAS Spacecraft Spin-Scan Geometry and Image Data Format Arrangement	4
2-2	Filter Wheel Spectral Band/Filter Position	6
3-1	VAS Demonstration Data Acquisition and Command Network	10
3-2	VAS Demonstration Data Acquisition and Command Network for Transparent VAS Mode	10
3-3	VAS S/DB Functional Elements	11
3-4	GSFC Data Acquisition and Processing System	12
3-5	University of Wisconsin Ground System.	13
3-6	McIDAS III	15
3-7	McIDAS Terminal Configuration	15
4-1	Standard VAS Weighting Functions	21
4-2	Focal Plane Geometry	25
4-3	Repeated scans of the Earth's limb at 11 μm	32
5-1	Errors in VAS Profile Retrievals for July 13, 1981	40
5-2	Residual Errors in VAS Parameter Retrievals, with and Without Ancillary Surface Data on July 13, 1981	40
5-3	Time Series of 920 mb Dewpoint Fields, Retrieved from VAS Data of July 13, 1981 with and Without Ancillary Surface Data	41
5-4	Comparison of VAS and AVE-VAS Special Network Radiosonde Temperature and Dewpoint Observations at 2300 GMT 6 March	44
5-5	The 7 March 1982 (0000 GMT) AVE-VAS Special Network Radiosonde Locations and Analyses of the Geopotential Height Calculated from VAS Soundings	45
5-6	Retrieval of Atmospheric Temperature and Dewpoint (Solid Curves) at Grand Cayman	46
5-7a	Cumulative Frequency of Wind Vector Magnitude Differences for Three Separate ACARS Comparisons.	50
5-7b	Cumulative Frequency of Wind Vector Directional Differences for Three Separate ACARS Comparisons.	50
5-8	Locations of Regional-Scale and Meso- β -Scale Rawinsonde Sites.	51

ILLUSTRATIONS (Continued)

<i>Figure</i>		<i>Page</i>
5-9	Locations of Special Network Meso- β -Scale Rawinsonde Network.	52
5-10	National Weather Service Thickness (SFC to 500 mb) and Surface Analysis for 1200 GMT, 6 March 1982.	55
5-11	National Weather Service 300-mb Analysis for 1200 GMT, 6 March 1982.	55
5-12	GOES Visible Image for 1800 GMT, 6 March 1982	56
5-13	VAS 6.7 μ m Water Vapor Channel for 1730 GMT, 6 March 1982.	56
5-14	Mean Difference (Radiosonde-Satellite) Between Rawinsonde and Satellite Gridded Temperature Fields as a Function of Pressure	57
5-15	As in Figure 5-14 Except for Dewpoint Temperature	64
5-16	As in Figure 5-14 Except for a Single Layer Value of Precipitable Water from the Surface Through 350 mb	64
5-17	As in Figure 5-14 Except for Geopotential Height Values	64
5-18	As in Figure 5-14 Except for Thickness Calculated.	64
5-19	Vertical Profiles of Temperature and Dewpoint Temperature Over the Grid Region	65
5-20	Gridded Field Analysis of 500 mb Temperature for Radiosonde and Satellite Data	69
5-21	Same as Figure 5-20 Except for Dewpoint Temperature at 700 mb	72
5-22	Same as in Figure 5-20 Except for Precipitable Water	74
5-23	As in Figure 5-14 Except for the Magnitude of the Temperature Gradient in $^{\circ}$ C/100km	76
5-24	VAS/AVE Profiles at HEN	78
5-25	VAS/AVE Fields of 500 mb Temperature	81
5-26	VAS/AVE Fields of 850 mb Dewpoint	82
5-27	Schematic Representation of the Wind Components Calculated in This Study.	84
5-28	500 mb Geopotential Analyses Obtained From the Special Network Radiosondes	85
5-29	500 mb Geopotential Analyses Derived From the VAS Temperature and Moisture Profiles and Conventional Surface Observations.	86
5-30	Scatter Diagram of the Rawinsonde Speed Observations Compared to Values Derived from the Geopotential Analyses of the Radiosondes Using a Gradient Wind Approximation	87

ILLUSTRATIONS (Continued)

<i>Figure</i>		<i>Page</i>
5-31	Same as Figure 5-30 Except for Wind Direction.	90
5-32	Top: 300 mb Wind Speeds for the Special Network Rawinsonde Bottom: Wind Barbs Representing the Satellite-Derived Gradient Winds and the Special Network Rawinsondes	91
6-1	Upper Air, Surface, and Radar Maps for July 13, 1981	97
6-2	Three-hourly VAS Visible Images for July 13, 1981.	98
6-3	Three Hourly Sequence of VAS Split Window Images for July 13	98
6-4	Radiosonde Soundings for Salem, Illinois.	99
6-5	Sequence of 6.7 μm Moisture Images for July 13, 1981	100
6-6	Upper Air, Surface, and Radar Maps for July 20, 1981	101
6-7	VAS Visible Images for July 20, 1981	102
6-8	Split Window-low Level Water Vapor Images for July 20, 1981	103
6-9	6.7 μm Middle Level Dryness.	103
6-10	Two-hourly Vertical Moisture Gradients Over Kansas and Oklahoma on 20 July 1981	105
6-11	Time Sequence of 850 mb Temperature and Dewpoint Analyses with RAOB Comparisons at 0000Z for 13 July 1981	108
6-12	Vertical Cross Section of θ_e From South Dakota Through Southern Illinois	110
6-13	VAS Derived Precipitable Water for 20 July 1981	112
6-14	VAS Derived Lifted Index for 20 July 1981	113
6-15	Full Disk Images Obtained on 20 July 1981	115
6-16	Analyses of VAS Total Precipitable Water and VAS 300 mb Gradient Wind Isotachs Over 6.7 μm Water Vapor Image for 26 April 1982, 1555 GMT.	116
6-17a	Analysis of VAS Total-totals Index Over Infrared Image for 26 April 1982, 1555 GMT	117
6-17b	Same as Figure 6-17a except for 1925 GMT	118
6-17c	Same as Figure 6-17a Except for 2025 GMT.	119
6-18	Analyses of VAS 300 mb Gradient Wind Isotachs from 1800 GMT and Change of Precipitable Water With NSSFC Watch Box No. 283 Over Visible Imagery at 1800 GMT 20 July 1981	120

ILLUSTRATIONS (Continued)

<i>Figure</i>		<i>Page</i>
6-19	Graphical Regression Flow Chart	122
6-20	Forecasts of Severe Weather Probability Using VAS Soundings.	123
6-21	SAT-Minus-NOSAT LFM Height Analysis Differences	124
6-22	Final Combined Wind Set Consisting of VAS and TIROS Gradient Winds, Water Vapor Motion Winds, and Cloud Drift Winds for Hurricane Debby.	125
6-23	Composite 850-200 mb Wind Analysis for Hurricane Debby	126
6-24	Count to Reflectance Conversion for GOES-5.	128
6-25	Scatter Diagram of 2 Channel VAS/Buoy SST Matches.	129
6-26	Monthly Mean for March 1982 VAS SST Fields	130
6-27	Bispectral and CO ₂ Absorption Cloud Top Pressures (mb) Plotted Versus the Position Along the Cirrus Anvil	131
7-1	Calendar of VAS Data Acquisition	134

TABLES

<i>Table</i>		<i>Page</i>
2-1	VAS Infrared Spectral Bands	3
2-2	VAS Operating Modes	5
4-1	Design Features of the VAS Channels	18
4-2	Estimated Sensitivity of the VAS Channels.	19
4-3	Specifications for the VAS Channels	22
4-4	Radiance Noise Observed in the VAS Channels	23
4-5	Signal-to-Noise for T* = 320K	24
4-6	VAS Spin Budgets Required for Sounding	24
4-7	Measured Values of Detector Offsets.	25
4-8	Comparisons of VAS and HIRS Characteristics	26
4-9	Brightness Differences Between VAS and HIRS.	27
4-10	VAS Radiances (Brightness Temperatures) Compared to Radiances (Brightness Temperature) Determined from LFM Analysis of Radiosonde Data	28
4-11	Radiance (erg/etc.) Errors Due to Truncation	29
4-12	VAS Zero-Point Errors for Outer Space	29
4-13	Radiance Droop Along a VAS Scanline	30
4-14	Relative Spin-to-Spin Reproducibility of a Scanline	31
5-1	Data Sources for the VAS Preconvective Case Studies.	37
5-2	Subsets of Collocated VAS/Surface/Radiosonde Data.	37
5-3	Statistical Errors in VAS Profile Retrievals Using Independent Data on July 13, 1981	38
5-4	Statistical Errors in VAS Profile Retrievals Using Independent Data from July 13 and 20, 1981	39
5-5	Statistical Comparison of the Coherence of VAS Retrieval 920 mb Dewpoint Fields on July 13, 1981, With and Without Surface Data	42
5-6	Statistical Coherence of VAS + SFC Fields of 920 mb Dewpoint	42
5-7	Summary of Comparisons Between VAS and Radiosonde Data for Bermuda, San Juan, and West Palm Beach	47

TABLES (Continued)

<i>Table</i>	<i>Page</i>
5-8 Summary of Comparisons Between VAS and ODW for 14/15 and 15/16 September 1982	48
5-9 Comparison of ACARS and VAS Winds	49
5-10 Processor Data Load (PDL) Description	53
5-11 VAS Data Acquisition Summary for Special Ground Truth Network Experiment	53
5-12 Mean and Root-Mean-Square (RMS) Difference (Radiosonde-Satellite)	58
5-13 Mean and Root-Mean-Square (RMS) Difference (Radiosonde-Satellite)	61
5-14 Residual Differences Between VAS and AVE Profiles on 6 March 1982 with Minimal Data Rejection Requirements	79
5-15 Residual Differences Between VAS and AVE Profiles on 6 March 1982 with (a) Close Surface Locations and (b) Cloud-Free Requirements	80
5-16 Wind Speeds Derived from Geopotential Analysis of the VAS and Radiosonde Data Compared with Winds Measured by the Rawinsonde Soundings	88
5-17 Wind Direction Derived from Geopotential Analysis of the VAS and Radiosonde Data Compared to Winds Measured by the Rawinsonde	89
6-1 Comparisons of MFE (nm) for Selected Cases During Hurricane Debby	127
7-1 VAS Dedicated Normal Operation (NO) and Severe Storm Day (SSD) Schedule	135
7-2 VAS Dedicated Cooperative Convective Precipitation Experiment (CCOPE) Schedule	136
7-3 VAS Interrupt Special Network (SN) Schedule	137
7-4 VAS Interrupt Hurricane Day (HD) Schedule	138
7-5 Transparent VAS 16-Hour Routine Operation (RO(16)) Schedule	139
7-6 Transparent VAS Hurricane Research Day Schedule B (HRDB)	140
7-7 Catalogue of VAS Data Gathered at the University of Wisconsin	142
7-8 Modes of Operation and Types of Support	155
7-9 VAS Data Availability at GSFC	158

ACKNOWLEDGMENTS

Thanks to all of the talented people who contributed to the overwhelming success of the VAS Demonstration Project. A partial list of these people follows. We apologize to any one whose name was inadvertently missed.

COMPUTER SCIENCE CORPORATION

Dr. Marcus Allen
Dr. Noren Butra
Mr. Samuel R. Carter
Mr. Forest D. Eastham
Ms. Lindsey L. Grace
Mr. Ira Graffman
Mr. Wally P. Gross
Ms. Joy R. Karahisar
Mr. Michael Koslowski
Mr. William J. Koster
Mr. Michael A. Kostka
Dr. Tay-How Lee
Mr. Anthony J. Mostek
Dr. Thomas Mottershead
Dr. Myron S. Nack
Dr. Richard L. Pitter
Ms. Cynthia A. Raab
Mr. Wayne Robinson
Ms. Linda A. Rollin
Ms. Nancy E. Sarstedt
Mr. Henry M. Sielski
Mr. Mel Wahlberg
Mr. Robert S. Wnuk
Dr. Frank Y. Yap

GENERAL SOFTWARE CORPORATION

Mr. Jeffrey C. Chen
Mr. Dennis Keyser

REPUBLIC MANAGEMENT SYSTEMS

Mr. Michael Hutchinson
Mr. Brian Squibb
Mr. John Stokes

RESEARCH AND DATA SYSTEMS

Mr. Gary Chatters
Mr. David Larko
Mr. Michael Valardo

SANTA BARBARA RESEARCH CENTER

Mr. Frank Malinowski

WESTINGHOUSE ELECTRIC CORPORATION

Mr. Harold D. Ausfresser
Mr. Thomas E. Adensam
Mr. Rob H. Haughton
Mr. Lowell Harmon
Mr. Stanley Kay
Mr. Robert W. Pahr, III
Ms. Francie C. Scilipoti
Mr. Dick Willis

TEXAS A&M

Dr. James Scoggins

UNIVERSITY OF WISCONSIN

Ms. Elsa Althen
Dr. Richard Daly
Mr. Ralph Dedecker
Mr. David N. Erickson
Mr. William Hibbard
Mr. David Jones
Dr. Paul Menzel
Dr. Fred Mosher
Mr. Robert Norton
Mr. Peter Raphael
Mr. Joseph Reuden
Dr. Henry Revercomb
Mr. Anthony Schreiner
Dr. Larry Sromovsky
Mr. Ron Steiner
Ms. Janean Steussey
Mr. Tod Stewart
Mr. Eric W. Suomi
Dr. Verner Suomi
Mr. Robert Uram
Mr. Christopher Velden
Mrs. Delores Wade
Mr. Gary Wade
Mr. J. T. Young

NESDIS

Mr. Geary Callan
Mr. Gary K. Davis
Dr. Christopher M. Hayden
Mr. Leroy Herman
Mr. Ben Howell
Mr. Fred Nagle
Mr. James H. Norton
Mr. Henry L. Schmidt
Mr. David Small
Dr. William L. Smith
Mr. Harold M. Woolf

NASA HEADQUARTERS

Mr. Ray Arnold
Dr. James Dodge
Mr. Michael Garbacz
Mr. James Greaves
Mr. Jules Lehman
Dr. Shelby Tilford

MSFC

Dr. Gary Jedlovek
Dr. Robert Turner
Dr. Gregory Wilson

GSFC

Dr. Albert Arking
Mr. William C. Bryant
Dr. Dennis Chesters
Mr. Charles Cosner
Mr. James F. Cunningham
Mr. John T. Dalton
Ms. Mary L. desJardins
Mr. Daniel L. Endres
Mr. J. Patrick Gary
Ms. Dorothy P. Helfer
Mr. David R. Howell
Ms. Rita K. Jamros
Mr. Joseph R. Johns
Mr. Richard S. Nankervis
Dr. Ralph A. Petersen
Mr. Richard J. Pinamonti
Mr. Larry Rouzer
Mr. William C. Shenk
Ms. Kelly L. Wilson
Mr. Joseph Woytek

ACRONYMS AND ABBREVIATIONS

ACARS	Aircraft and Communications Addressing and Reporting System
A/D	Analog to Digital
AOIPS	Atmospheric and Oceanographic Image Processing System
APS	Applications Processors
ASDAR	Aircraft to Satellite Delay Relay
ATS	Applications Technology Satellite
AVE	Atmospheric Variability Experiment
AVHRR	Advanced Very High Resolution Radiometer on TIROS/NOAA Satellites
bpi	Bits per inch
C	Degrees Centigrade
CC	Correlation Coefficient
CCOPE	Cooperative Convective Precipitation Experiment
CCP	Communications Control Processor
CCT	Computer Compatible Tape
CDA	Command and Data Acquisition Facility at Wallops Island, Virginia
CIMSS	Cooperative Institute for Meteorological Satellite Studies of NESDIS
CLIPER	Climatology and Persistence
cm	Centimeters
CO	Checkout of VAS
Corr	Correlation
Covar	Covariance
CPU	Central Processing Unit
CRT	Cathode Ray Tube
D/A	Digital to Analog
D	VAS Demonstration Dedicated Mode
DEC	Digital Equipment Corporation
DI	Dwell Imaging
DIR	Dwell Imaging Regional
DOC	Department of Commerce
DS	Dwell Sounding
DSA	Dwell Soundings Averaged
Dsfc	Dewpoint at surface
DSR	Dwell Sounding Regional
DSU	Dwell Soundings Unaveraged
EMR	Electro Mechanical Research Company
ergs/etc	Ergs/sec-cm ² -steradian-cm ⁻¹
E-W	East-West
FAA	Federal Aviation Administration
FOV	Field of View
ft	Feet
g	Accelerator due to gravity
gm	Gram
GEMPAK	General Meteorological Package
GHz	Gigahertz
GLAS	Goddard Laboratory for Atmospheric Sciences
GMT	Greenwich Mean Time

GOES	Geostationary Operational Environmental Satellite
GSFC	Goddard Space Flight Center
GVHRR	Geosynchronous Very High Resolution Radiometer
h	Hurricane or tropical disturbance coverage with VAS
HD	Hurricane Day
HDDT	High Density Digital Tape
HDTR	High Density Tape Recorder
HgCdTe	Mercury Cadmium Telluride Alloy
HIRS	High Resolution Infrared Sounder on TIROS/NOAA Satellite
hr	Hour
HRDA	Transparent VAS Hurricane Research Day Schedule A
HRDB	Transparent VAS Hurricane Research Day Schedule B
HURRAN	Hurricane Analog model
I	VAS Interrupt Mode
IAT	Interactive Applications Terminal
IBM	International Business Machines
IGFOV	Instantaneous Geometrical Field of View
InSb	Indium Antimonide Alloy
I/O	Input/Output
IR	Infrared
K	Degrees Kelvin
KB	Kilobytes
Kbps	Kilobits per second
km	Kilometer
LBR	Laser Beam Recorder
LFM	Limited Area Fine Mesh
LI	Lifted Index
m	Meters
mb	Millibar
Mb	Megabits
MB	Megabytes
Mbps	Megabits per second
McIDAS	Man/Computer Interactive Data Access System
MFE	Mean Forecast Errors
MFM	Moveable Fine Mesh Model
MHz	Megahertz
min	Minute
mm	Millimeters
mr	Milliradian
ms ⁻¹	Meters per second
MSFC	Marshall Space Flight Center
MSI	Multispectral Imaging
na	Not available
NA	Not applicable
NASA	National Aeronautics and Space Administration
ND	Normal Day Coverage
NEDT	Noise Equivalent Delta Temperature
NEDR	Noise Equivalent Delta Radiance
NESDIS	National Environmental Satellite Data and Information Service of NOAA
NHC	National Hurricane Center
NSSFC	National Severe Storms Forecast Center
NSSL	National Severe Storms Laboratory

NWS	National Weather Service
nm	Nautical mile
NMC	National Meteorological Center
NO	Normal Operation
NOAA	National Oceanic and Atmospheric Administration of DOC
NOVA	NOAA Operational VAS Assessment
NOVAS	Analysis with no VAS data
NRZS	Non-Return to Zero Signal
N-S	North-South
O&A	Orbit and Attitude
ODW	Omega Dropwindsonde
OS/MVS	Operating System/Multiple Virtual Storage for an IBM computer
OS/VS1	Operating System/Virtual System 1 for an IBM computer
PCM	Pulse Code Modulation
PDL	Processor Data Load
PDP	DEC Programmable Data Processor
PMT	Photomultiplier Tube
PSK	Phase Shift Key
PW	Precipitable Water
RAOB	Radiosonde Observation
RDI	Rapid Dwell Imaging
RGB	Red/Green/Blue
RISOP	Rapid Interval Storm Operation Plan
RMS	Root Mean Square
RO(16)	Transparent VAS Routine Operation 16 hours per day
RO(MSI)	Routine Operational - Regular NOAA schedule with MSI substituted for VISSR (no dwell sounding)
RPM	Revolutions per Minute
R/W	Read/Write
s	Second
S	Data gathering for science
SANBAR	Sander's Barotropic Model
SB	Total Spin Budget for all the spectral bands
SBC	Single Board Computer
SBRC	Santa Barbara Research Center
S/C	Spacecraft
S/DB	Synchronizer/Data Buffer
SDD	Satellite Data Services Division
SFOV	Sounding Field of View
SFC	Surface
SMS	Synchronous Meteorological Satellite
SN	Special Network
S/N	Signal to Noise Ratio
SOC	Satellite Operational Control Center, Suitland, MD (NOAA)
Soline Condx	Sola Line Conditioner by the Sola Company
SS	Severe Storm support for Kansas City
SSD	Severe Storm Day
SSEC	Space Science and Engineering Center
SST	Sea Surface Temperature
stdv	Standard deviation
T	Transparent VAS Operations (20 minutes MSI, 10 minute DS, every half hour)
T*	Brightness temperature

T&C	Telemetry and Command
TIROS	Television Infrared Observation Satellite
TMSI	Transparent MSI activities
Tsfc	Surface Temperature
TVAS(X)	Transparent VAS schedule for X hours
TVM	Transparent VAS Mode
UW	University of Wisconsin
VAP	VAS Assessment Processor
VAS	VISSR Atmospheric Sounder on GOES Satellites
VASTRA	VAS Trajectory model
VAX	DEC's Virtual Address Extension Computer
VISSR	Visible Infrared Spin-Scan Radiometer on GOES Satellites
VP	VAS Processor
VPP	VAS Preprocessor
VR	Transparent 15 minute MSI for RISOP support
WINDCO	A McIDAS computer program for cloud motion vector determination
ΔF	Scale factor used in the S/DB for calibration
$\Delta\nu$	Spectral bandwidth in cm^{-1}
θ_E	Equivalent potential temperature
λ	Wavelength in μm
μm	Micrometer
μs	Microseconds
σ	Random noise spatially averaged over an SFOV
ν	Wave number in cm^{-1}

EXECUTIVE SUMMARY

This document gives a summary of the Visible infrared spin-scan radiometer (VISSR) Atmospheric Sounder (VAS) Demonstration from its inception in November 1974 to its conclusion in October 1983. Specifically, the report describes important instrument and ground-based systems, instrument performance analyses, the meteorological evaluation of the initial VAS data sets, and the availability of VAS data for other researchers.

The VAS Demonstration had four overall objectives:

- The development of research-oriented and prototype/operational VAS data processing systems at Goddard Space Flight Center (GSFC) and University of Wisconsin (UW), respectively
- The evaluation of the performance of VAS instruments on GOES-4, 5, and 6
- The validation of temperature and moisture soundings derived from VAS and conventional ancillary data
- The assessment of the utility of VAS-derived information in analyzing severe weather situations

To meet these objectives, a VAS Demonstration Data Acquisition and Command Network was developed. This VAS network consists of a VAS instrument on the Geostationary Operational Environmental Satellite (GOES) spacecraft and three ground facilities: the Command and Data Acquisition (CDA) station at Wallops Island, Virginia, the Goddard Space Flight Center Data Acquisition and Processing System, and the University of Wisconsin Data Acquisition and Processing System. A brief description of each is given in the following sections, and a detailed description appears in the main report.

INSTRUMENT DESCRIPTION

The VAS instrument is a radiometer with three operating modes: the operational VISSR mode, the multi-spectral imaging (MSI) mode, and the dwell-sounding (DS) mode. The VISSR mode is routinely used by

NOAA/NESDIS for its operational products, which include a 0.9-km visible picture and an 11-micrometer infrared (IR) picture of 6.9-km resolution. The two other modes are VAS unique. The MSI mode can provide the operational VISSR capability plus two additional IR bands, which are selectable from a list of 12. The DS mode is used primarily for sounding, to obtain the temperature and moisture profiles.

In order to readily exercise the capabilities of the VAS and yet allow NESDIS to fulfill its operational commitments, a transparent VAS mode (TVM) configuration was implemented. This mode allowed the VAS Demonstration to obtain both MSI and DS data routinely, while NESDIS concurrently supplied operational VISSR data to its users.

SYSTEM DESCRIPTIONS

Wallops CDA Station System

The satellite transmits data to the Command and Data Acquisition Station at 28 Mbps. These data are received by a 13-meter dish and brought into a computer (the synchronizer/data buffer), where they are reformatted and quality checked, and merged with telemetry, operations schedules, and navigation parameters. These data are then retransmitted to the spacecraft at 1.75 Mbps. This facility also commands the GOES and transmits processor data loads (PDL's) to the VAS.

Goddard Space Flight Center System

The VAS data are received by an 8-meter dish at the GOES Test Laboratory (GTL) and microwaved to the preprocessor. The visible images can be recorded on a laser film recorder. The preprocessor passes data to the processor by a shared dual ported disk. It also provides PDL's, their execution schedule, and navigation parameters to the CDA using ground communications. The processor performs parameter extraction, synthesis, and meteorological research. The processor also provides extracted parameters to an application processor for further meteorological analysis.

University of Wisconsin System

The VAS data are received by an 8-meter dish on the roof of the Space Science and Engineering Center at the University of Wisconsin in Madison. The video cassette archive system records all geostationary satellite data (VAS and VISSR). The data are brought into the Data Base Manager (DBM), where they are reformatted, quality checked, and passed on to the applications processor on the scientist's request. The DBM also receives and archives VISSR, Tiros-N, and other ancillary data. The scientist performs parameter extraction, synthesis, and meteorological research on the applications processor through interactive user terminals. The processed data are then archived in the DBM. The archived data and other stored data are available to outside users such as NOAA/Kansas City and GSFC. In addition, the DBM provides PDL's, their execution schedules, and VAS calibration parameters to the CDA station at Wallops.

INSTRUMENT PERFORMANCE

The VAS instrument has been flown on GOES-4, -5, and -6, which were launched on September 9, 1980, May 22, 1981, and April 28, 1983, respectively.

The postlaunch performance of the VAS radiometer meets its prelaunch design specifications. Single-sample noise is lower than expected, especially for the small longwave and large shortwave detectors. Detector-to-detector offsets are correctable to within the resolution limits of the instrument. Truncation, zero-point, and droop errors are insignificant. Absolute calibration errors, estimated from High Resolution Infrared Sounder (HIRS) and from radiation transfer calculations, indicate moderate but stable biases. Relative calibration errors from scan line to scan line meet sounding requirements temporally (50 to 70 spins at 100 RPM) and spatially (30 by 30 km²) averaged sounding fields-of-view. "Scattered light" and resampling errors slightly reduce contrast and channel-to-channel registration for very high resolution work.

Although the distant geosynchronous station of the VAS instrument makes accurate radiometry difficult, the frequent and relatively stable measurements, which VAS provides at fixed angle and resolution, permit meso-scale measurements that were previously unavailable.

INSTRUMENT VALIDATION

In order to validate the relative and absolute radiometric accuracy of the VAS instruments, comparisons were

made between other satellite data (Tiros-N/NOAA), radiosonde data from the operational network and from a special network experiment. The satellite comparisons were made with the HIRS instrument, which is a high resolution infrared sounder on the NOAA series of operational polar orbiters.

Several case studies were made using VAS data and conventional radiosonde data. All of the various types of algorithms used for extracting temperatures and moisture profiles from VAS data require the use of conventional data. It was found that VAS-derived soundings (VAS plus conventional data) were within 1° to 2°C absolute of radiosonde. The relative accuracy within mesoscale fields of low-level VAS soundings is impressive. Reproducible horizontal gradients are on the order of 200 km, and temporal correlations are in excess of 90 percent over 3-hour intervals throughout the day. It appears that VAS soundings produced in the "case study" mode provide the accuracy required for an analysis of a preconvective environment. It was also found that conventional surface reports act as valuable "channels" of mesoscale information about the boundary layer, resolving ambiguities and improving the space/time continuity of VAS soundings in the lower troposphere. VAS and conventional data retrievals are more accurate than VAS-only or SFC-only retrievals below 700 mb. As expected, the differences are larger for moisture because the small-scale features of the moisture distribution produce discrepancies (due to space and time differences between the satellite and radiosonde observations) and because the VAS lower vertical resolution moisture profiles cannot capture highly structured vertical features as well as the radiosonde.

A special radiosonde network was set up in Texas to "ground truth" the VAS. This experiment provided contemporaneous and collocated radiosonde and VAS data at high temporal and spatial resolution. Although comparisons between the VAS and special network experiments are still being finalized at various research centers, initial results appear to be in line with validation studies based on the operational radiosonde network.

METEOROLOGICAL ASSESSMENT

The assessment of VAS data in meteorological application can be divided into the image and sounding evaluation. VAS images were successfully used in delineating mesoscale distribution of lower and middle tropospheric

moisture fields. A “split window” technique was derived to produce images of low-level water vapor. Upper to middle-tropospheric water vapor can be effectively monitored by the 6.7- μm water vapor channel. The technique of overlaying the 6.7-micron upper tropospheric VAS moisture channel with the VAS split-window low-level moisture field has proven useful in delineating regions in which dry air overlies moist air. This indicates a potential for convective instability (dry air over moist air) within which intense convection rapidly develops. The image analyses show a strong tendency for thunderstorm development along the edge of mid-level dry bands, often at a scale not resolvable using conventional radiosonde data. The temporal evolution of the moisture fields, clearly evident with “looping” time sequences of VAS images, also provides a measure of the differential moisture advection, which acts to destabilize the atmosphere, making it more conducive for the development of severe convective storms.

Soundings derived from VAS radiances, incorporating information from conventional radiosonde and surface data were applied to numerous severe storm cases in both case study and forecast modes. The evaluation shows that VAS soundings add useful quantitative information with mesoscale resolution that cannot be resolved with the operational network alone. The sounding information can be used to measure convective instability in a pre-storm environment. While these results

are promising, certain problems were also encountered. Perhaps the biggest problem is the impact of clouds, not only on the quality of the soundings, but also on the spatial and temporal continuity of the VAS sounding fields as well. Nevertheless, the VAS has great potential for filling the temporal and spatial data gaps that currently exist within the conventional data base, providing a means to better study and predict severe local storms.

SUMMARY

The VAS Demonstration has exceeded all expectations. All of the functional objectives and requirements were fully met. Specifically,

- Systems at GSFC and UW were successfully utilized.
- VAS-4, VAS-5, and VAS-6 met individual specifications for single-sample noise, detector-to-detector offsets, and calibration.
- Temperature and moisture soundings demonstrated temperature within 2°C absolute and 1°C relative, and moisture within 25 percent.
- VAS images and soundings can be used to effectively fill spatial and temporal gaps in the conventional, operational, and polar orbiter data base.

INTRODUCTION

H. Montgomery

D. Endres

Goddard Space Flight Center

National Aeronautics and Space Administration

Greenbelt, Maryland

1.1 HISTORY

Meteorological satellite data have been available since 1960. These measurements were first made from near-Earth orbit, and since 1966, from both near-Earth and geosynchronous orbits. The first geosynchronous altitude observations were made using a camera on the spinning Applications Technology Satellite-1 (ATS-1) that recorded images of the Earth at approximately half-hour intervals. Wind velocities were estimated from cloud motions. Studies were made of cloud growth and decay associated with small-scale weather systems. Subsequently, a similar camera was launched on ATS-3. In 1974, two advanced radiometers were put into geosynchronous orbit. Each radiometer employed a high-resolution visible channel and an 11-micrometer infrared channel. These instruments provided the ability to determine cloud motion at night and to estimate cloud and terrestrial surface temperature. One instrument, the Geosynchronous Very High Resolution Radiometer (GVHRR), flown on the three-axis stabilized ATS-6 satellite, acquired meteorological data for a 2-month period in 1974. The other instrument, the Visible and Infrared Spin Scan Radiometer (VISSR), was flown on the spinning Synchronous Meteorological Satellites (SMS-1 and -2) and the Geostationary Operational Environmental Satellites (GOES-1, GOES-2, and GOES-3). The SMS/GOES spacecraft provided day and night coverage with temporal and spatial resolutions useful for severe storm research. The VAS (a second-order acronym for VISSR Atmospheric Sounder) evolved from a concept for sounding from geosynchronous orbit, which was originally proposed by Professor V. E. Suomi of the University of Wisconsin (UW) in 1969. This concept was formalized in April 1972 by UW in the form of a preliminary instrument specification. Later in 1972, the National Oceanic and Atmospheric Administration (NOAA) requested that the National Aeronautics and

Space Administration (NASA) proceed with the development of a VAS instrument. This led to a VAS instrument conceptual design study by Santa Barbara Research Center (SBRC) in June 1973 and to the formation of a VAS Working Group consisting of representatives from NASA, NOAA, and UW in July 1973. As a result of this working group, a mutually acceptable conceptual design for the VAS evolved and was documented by SBRC in February 1974. About the same time, both NASA and NOAA saw the need to bridge the gap between space hardware and the user community. This led to a commitment by NASA in November 1974 to a program that would demonstrate the VAS capabilities for meteorological research. This program was called the VAS Demonstration. In March 1975, NASA and NOAA agreed that the VAS instruments would be flown in lieu of VISSR instruments on GOES-D, -E, and -F, that were launched on September 9, 1980, May 22, 1981, and April 28, 1983, respectively. Due to the efforts of the VAS Demonstration Team, both the UW and Goddard Space Flight Center (GSFC) ground stations were ready to receive and assess the first VAS data that were transmitted from GOES-4. The experience gained from GOES-4, as well as that from GOES-5 and GOES-6, has repeatedly demonstrated the necessity of having two independent ground receiving stations. Only with two independent systems is it possible to detect and correct errors that would otherwise remain undetected.

1.2 OBJECTIVES

The VAS Demonstration effort was funded by NASA for evaluating the performance of the VAS instruments and for demonstrating the capabilities of a VAS prototype system to provide useful geosynchronous satellite data for supporting weather forecasts and atmospheric

INTRODUCTION

research. The specific objectives of the Demonstration were:

- The development of research-oriented and prototype/operational VAS data processing systems at GSFC and UW, respectively
- The evaluation of the performance of the VAS instruments on GOES-4, GOES-5, and GOES-6
- The validation of temperature and moisture soundings derived from VAS and conventional ancillary data

- The assessment of the utility of VAS-derived information in analyzing severe weather situations

GSFC was the NASA field center that was given the primary responsibility of conducting the VAS Demonstration. Members of the VAS Demonstration Team include scientists from UW's Space Science and Engineering Center (SSEC), NOAA's National Environmental Satellite Data and Information Service (NESDIS) Development Laboratory in Wisconsin, and NASA's Marshall Space Flight Center (MSFC).

The remainder of this document will specifically address how the VAS Demonstration Team has met each of the foregoing objectives.

VAS INSTRUMENT DESCRIPTION

H. Montgomery
D. Endres
*Goddard Space Flight Center
National Aeronautics and Space Administration
Greenbelt, Maryland*

This section provides a description of the VAS operating modes. For a complete description of the VAS instrument, refer to the VAS-DGOES Data Book (Malinowski and Ruiz, 1980). Since the VAS is a modified VISSR, it is appropriate to describe the VISSR first, and then the VAS in terms of changes to the VISSR.

2.1 BACKGROUND

The VISSR was used by NOAA on SMS-1 and SMS-2 and on GOES-1, GOES-2, and GOES-3. It provided day and night cloud coverage with its visible and infrared (IR) detectors. The eight visible (0.55 to 0.75 μm)

photomultiplier tubes (PMT's) had a spatial resolution of 0.9 km. These data were quantized to 6 bits. The two IR (11 μm) HgCdTe detectors had a spatial resolution of 8 km. These data were quantized to 8 bits. The two IR detectors were located along the same scan line, and provided redundant data. Functional capabilities enabled the calibration of IR data once per image.

2.2 THE VAS INSTRUMENT

The added capabilities of VAS, relative to VISSR, provide the additional atmospheric measurements that enable extensive research in atmospheric science from

Table 2-1
VAS Infrared Spectral Bands

Spectral Band	Atmos. Press. (mb)	ν (cm^{-1})	λ (μm)	$\Delta\nu$ (cm^{-1})	Nominal Single-Sample S/N for 320 K Scene Temperature		Remarks	
					6.9-km IGFOV	13.8-km IGFOV	Band	Detector Type
1	70	678.7	14.73	10	NA	37.4	CO ₂	HgCdTe
2	125	690.6	14.48	16	NA	92.3	CO ₂	HgCdTe
3	200	701.6	14.25	16	50.4	100.8	CO ₂	HgCdTe
4	500	713.6	14.01	20	65.3	130.6	CO ₂	HgCdTe
5	920	750	13.33	20	64.1	128.3	CO ₂	HgCdTe
6	850	2210	4.525	45	NA	108.9	N ₂ O	InSb
7	Surf.	790	12.66	20	60.7	121.4	H ₂ O	HgCdTe
8	Surf.	895	11.17	140	607.1*	953.5	Window	HgCdTe
9	600	1377.2	7.261	40	24.2	48.5	H ₂ O	HgCdTe
10	400	1487	6.725	150	73.7	147.4	H ₂ O	HgCdTe
11	300	2250	4.444	40	NA	83.7	N ₂ O	InSb
12	Surf.	2535	3.945	140	NA	111.1	Window	InSb

*For 340 K scene temperature.

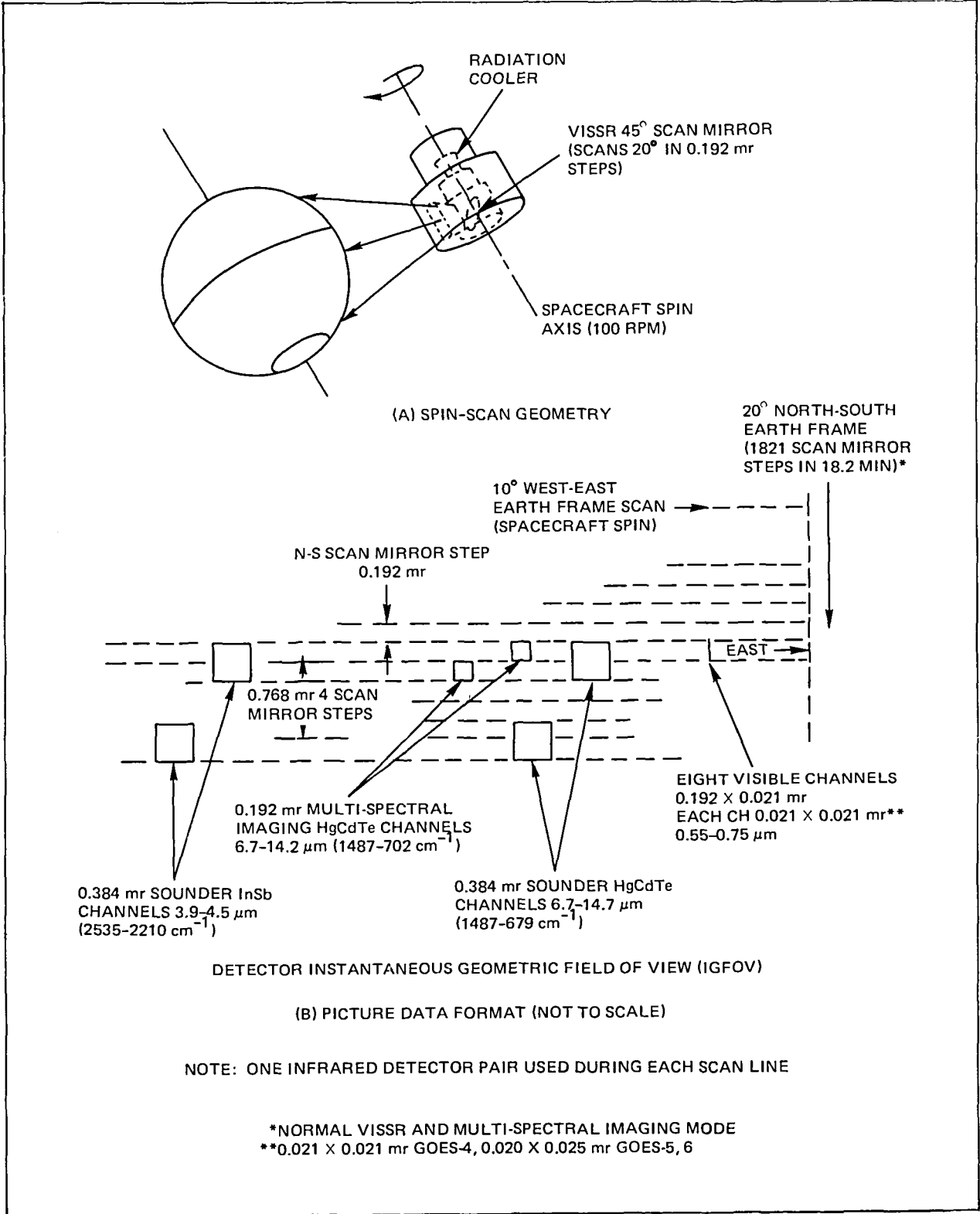


Figure 2-1. VAS/Spacecraft Spin-Scan Geometry and Image Data Format Arrangement

**Table 2-2
VAS Operating Modes**

Instrument Mode	Function	Spins Per Step	Visible			Infrared			Data			North-South Coverage Rate (km/min)		
			Res. (km)	Res. (km)	No. of Bands	Rate (Mbps)	No. of Bits		GOES-4	GOES-5	GOES-6			
							VIS	IR						
VISSR	NOAA operational	1	0.9	6.9	1	28 ⁽¹⁾	6	8	690	690	690			
Multispectral imaging	Imaging	1	0.9	(2)	(2)	28 ⁽¹⁾	6	10/8 ⁽³⁾	690	690	690			
Dwell sounding	Sounding	>1	0.9	13.8	12	28 ⁽¹⁾	6	10	21.2 ⁽⁴⁾	64.2 ⁽⁴⁾	61.3 ⁽⁴⁾			

- (1) Backup wideband mode of 14 Mbps may be selected. This provides reduced visible resolution.
- (2) This is programmable. The capability exists to select four spectral bands at 13.8-km resolution or band 8 (11 μm) at 6.9-km resolution, plus two additional bands at 13.8-km resolution.
- (3) All MSI IR data are 10-bit except when collected in the transparent mode. (See paragraph 2.3.3.)
- (4) These north-south coverage rates are based on nominal spin budgets. In general, the coverage rate can be calculated by:

$$\frac{2760}{4 + (2) \text{ (spin budget)}} \text{ km/min for GOES-4}$$

and

$$\frac{5520}{8 + 2 \text{ (spin budget)}} \text{ km/min for GOES-5 and 6}$$

the geostationary vantage point. Instrument flexibility, including spectral band selection, spatial resolution, signal-to-noise (S/N) ratio, and geographic location, are incorporated into various instrument modes to provide measurements which best meet the needs of the research scientist. Table 2-1 lists the infrared spectral bands, and detector information for the VAS instrument. Whereas the VISSR had only one IR spectral band, the VAS has 12. The VISSR IR band corresponds to band 8 of the VAS. The IR spatial resolution is selectable for the VAS.

All 12 bands are available at a resolution of 13.8 km, and seven of them are also available at a resolution of 6.9 km. Although the visible detector configuration of the VAS is identical to the VISSR, the IR detector configuration has changed in two important ways. The first change is that the two 8-km resolution detectors have been replaced by two 6.9-km resolution detectors that are no longer located along the same scanline, but are offset by one scanline. Although the instantaneous geometrical fields of view (IGFOV) of these VAS infrared detectors are smaller than those of the VISSR, the same

minimum noise equivalent delta temperature (NEDT) requirement (1.2 K at 200 K scene temperature) was met. The second change is the addition of four 13.8-km resolution detectors (two HgCdTe plus two InSb). Figure 2-1 shows the detector configuration and the spin-scan geometry. As shown in this figure, during each satellite spin, all eight visible detectors and one pair of IR detectors (either the two small HgCdTe detectors, the two large HgCdTe detectors, or the two large InSb detectors) view the Earth on west-east lines. As with the VISSR, a maximum north-south frame (full Earth disk) results from a total of 1821, 0.192 mr steps of a scan mirror. Another significant difference is that the VISSR IR data were encoded to 8 bits. For the VAS, this is selectable at either 8 or 10 bits. Further dissimilarities are that the electronic calibration staircase of the VISSR is replaced by a linear ramp in the VAS, and the internal thermal calibration signal is available in each scanline of the frame in the thermal channels, rather than once per image. The three distinct VAS instrument modes that accomplish both the operational and research mission are described in the following para-

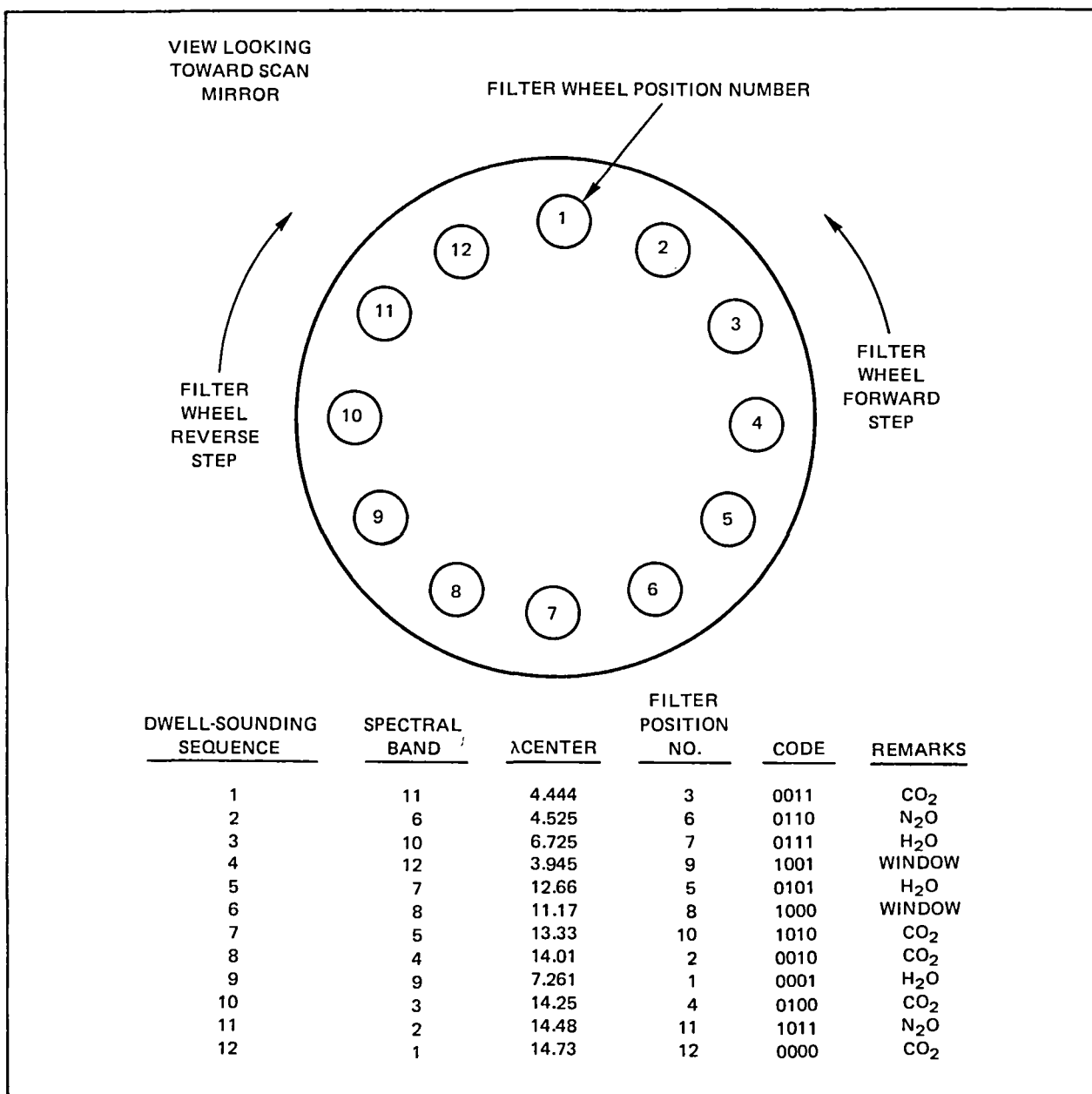


Figure 2-2. Filter Wheel Spectral Band/Filter Position

graphs. Table 2-2 summarizes the instrument modes of operations and functions used in the time frame of the VAS Demonstration.

2.2.1 VISSR Mode

The VAS, when operated in the VISSR mode, provides data which are compatible with all original NESDIS VISSR data users. This mode provides both visible, and

IR data. The IR (11 μm) data are 6.9-km resolution and encoded to 8 bits.

2.2.2 Dwell-Sounding Mode

The dwell-sounding mode (DS) for the VAS Demonstration provides both visible and IR data. Up to 12 IR spectral filters in a filter wheel covering the range from 678.7 cm^{-1} (14.73 μm) to 2535 cm^{-1} (3.94 μm) can

be positioned into the optical train while the scanner is dwelling on a single scanline. The filter wheel can be programmed so that each spectral band (filter) can dwell on a single scanline for from 0 to 255 spacecraft spins. Figure 2-2 shows the dwell-sounding sequence for the 12 spectral bands, as well as the filter position numbers associated with them. Either the 6.9- or 13.8-km resolution detectors can be selected for the seven filter positions that operate in the spectral region from 701.6 cm^{-1} ($14.25 \text{ }\mu\text{m}$) to 1487 cm^{-1} ($6.725 \text{ }\mu\text{m}$). For the remaining five spectral bands, only the 13.8-km resolution detectors are used. Selectable frame size, position, and step direction are also programmable by ground command. In this mode, 10-bit infrared data are provided.

In some of the spectral bands, temporal (dwell) averaging of repeatedly scanned lines is required to enhance the S/N ratio. For GOES-4, 63 satellite spins along each scanline were required to obtain the desired sounding data for all 12 VAS infrared channels. This number of spins per line was adequate to obtain soundings having a 30- by 30-km resolution. For GOES-5 and GOES-6 the spin budgets are 39 and 41, respectively. The spin budget for GOES-4 was greater than that for GOES-5 and GOES-6 due to a failure in its upper large HgCdTe detector. The parameters associated with the spectral filters, detector size, dwell spins, and scan direction are selected by ground control, broadcast to GOES, and preset in the VAS electronics memory. Programming is accomplished using a dedicated command line in which a bit stream of 184 bits sets the processor memory to the desired program. The bit stream requires approximately 11 seconds for transmission and loading into the spacecraft.

2.2.3 Multispectral Imaging Mode

The multispectral imaging (MSI) mode can provide 0.9-km resolution visible data, 6.9-km resolution band 8 data, plus data in any two selected spectral bands having a spatial resolution of 13.8 km. Except in the transparent mode (paragraph 2.3.3), all IR data were encoded to 10 bits. This mode of operation takes advantage of the small HgCdTe detector offset in the N-S plane. Using the data from these detectors simultaneously, produces a complete infrared map when they are operated every other scanline. Therefore, the larger detectors can be used during half of the imaging/scanning sequence to obtain additional spectral information. Unlimited N-S frame size and position within the maximum N-S field-of-view (FOV) scan direction can be

selected. Parameters are programmed by ground commands as in the dwell-sounding mode.

2.3 GROUND OPERATION

During the demonstration, the data were acquired with three different ground network configurations: (1) demonstration dedicated mode (D), (2) interrupt mode (I), and (3) transparent VAS mode (TVM). The following paragraphs describe these configurations.

2.3.1 Demonstration Dedicated

In this configuration, the scientist at GSFC or UW could select the instrument operating mode that he desired. After this, he also selected the filters, the detector size, the picture center, and the north/south limits of the picture. These commands were then transmitted to the VAS Wallops synchronizer/data buffer (S/DB) by ground line, reformatted into the 184-bit VAS command, and transmitted to the spacecraft. When the data associated with this command were received at GSFC or UW, the scientist could select from this picture frame the exact east-west and north-south limits he wished to investigate. This mode was not only scientist/data interactive, but it was scientist/instrument interactive also.

2.3.2 Interrupt Mode

In the interrupt mode configuration, NESDIS canceled its regularly scheduled operational VISSR data at pre-scheduled times. During these times, VAS data were acquired in lieu of the operational VISSR data. The instrument configuration was commanded by NESDIS in a prearranged manner. During these times, the scientist/data interactive nature was preserved in the sense that the scientist could select portions of the transmitted data for further study. However, the scientist/instrument interactive nature was not available because the instrument configuration commands were submitted in advance.

2.3.3 Transparent VAS Mode

In the transparent mode, the normal half-hourly VISSR operation is replaced by the TVM for about 16 hours per day. During each half-hour in this mode, the VAS is operated in the MSI mode for 15 minutes and in the dwell-sounding (DS) mode for 10 minutes. The remaining 5 minutes in the half-hour are used for reconfiguration. This mode allows the NESDIS operational users to

obtain the regular VISSR data (extracted as a subset of the MSI data) for 1500 lines out of the normal 1821 lines while VAS ground stations (e.g., UW and GSFC) simultaneously acquires MSI data in addition to the subsequent 10 minutes of DS data. In this mode, all

commands are prescheduled and issued by NESDIS. This requires the simultaneous downlink of two data streams (VISSR and VAS) and the use of a second GOES, used only as a repeater. Section 3.1 describes the operational configuration for this procedure.

DATA ACQUISITION AND COMMAND NETWORK

H. Montgomery
D. Endres
D. Howell
*Goddard Space Flight Center
National Aeronautics and Space Administration
Greenbelt, Maryland*

P. Raphael
*Space Science and Engineering Center
University of Wisconsin
Madison, Wisconsin*

The elements of the VAS Demonstration and Command Network, shown in Figure 3-1, consist of the following:

- GOES/VAS Instrument
- NOAA Command and Data Acquisition (CDA) Station
- GSFC Data Acquisition and Processing System
- UW Data Acquisition and Processing System

The VAS, carried on board the GOES-4, GOES-5, and GOES-6 satellites, is a radiometer with eight visible channel detectors and six thermal detectors that detect infrared radiation in 12 spectral bands. A filter wheel in front of the detector is used to achieve the spectral selection. The spatial resolution is 0.9 km in the visible and 7 to 14 km in the infrared, depending on the detector used. Full Earth-disk coverage is accomplished by spinning in the west-to-east direction at 100 RPM and by stepping a scan mirror from north to south. Additional VAS instrument characteristics are provided in the previous section.

3.1 NOAA CDA STATION

The satellite transmits data to the NOAA CDA station at 28 Mbps. These data are brought into a computer, called the S/DB, where they are reformatted, calibrated, quality checked, and merged with telemetry, operations schedules, and navigation parameters. The data are then retransmitted to the spacecraft at 1.75 Mbps. The CDA

station commands the GOES and transmits processor data loads (PDL's) to the VAS. The PDL is a command that is sent to the spacecraft for configuring the VAS instrument. This command selects operational VISSR, MSI, or DS modes and defines the north-to-south extent of the image, spectral bands, number of spins per band (when in the DS mode), and detector size.

Figure 3-1 presents the CDA station configuration used for the Demonstration Dedicated and Interrupt modes described in paragraphs 2.3.1 and 2.3.2, respectively. Figure 3-2 shows the configuration needed to operate in the TVM mode described in paragraph 2.3.3.

The VAS S/DB performs several functions. These functions, shown schematically in Figure 3-3, are as follows:

- a. Receiving VAS Data :
 - Demod/Demux supplies S/DB with VAS digital data in operating modes at 14 and 28 Mbps.
 - Real-time data unit provides Sun pulse.
 - PCM telemetry reception to monitor VAS instrument temperatures, etc.
- b. Satellite Commanding :
 - Command Encoder initiates conventional octal commands and special PDL's.

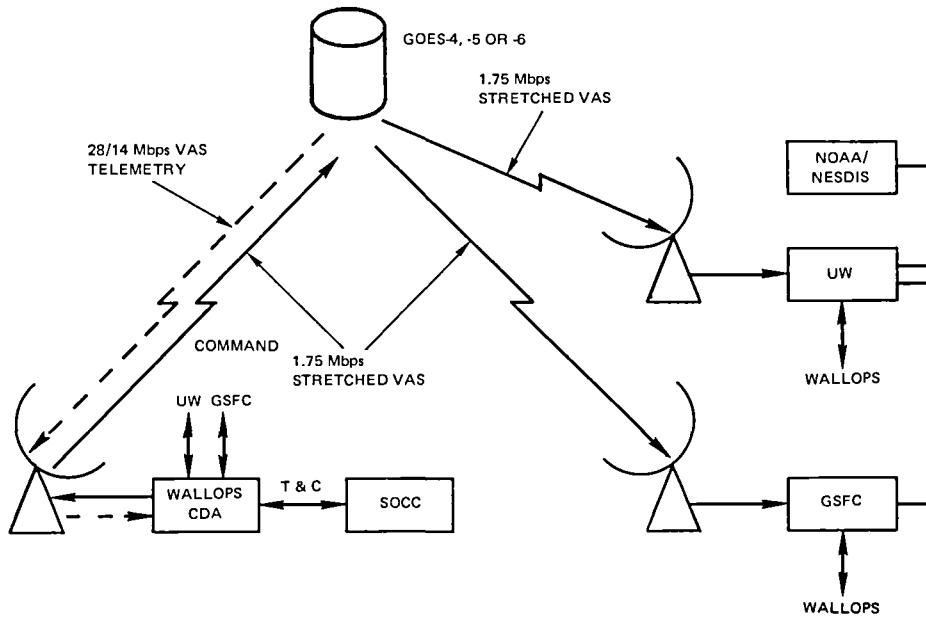


Figure 3-1. VAS Demonstration Data Acquisition and Command Network

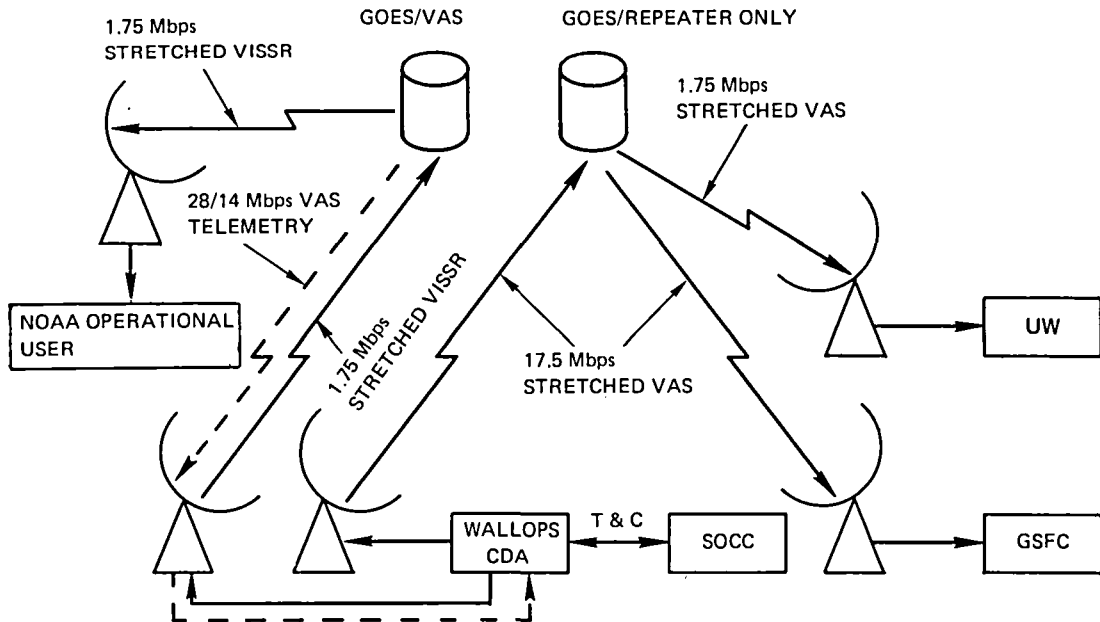


Figure 3-2. VAS Demonstration Data Acquisition and Command Network for Transparent VAS Mode

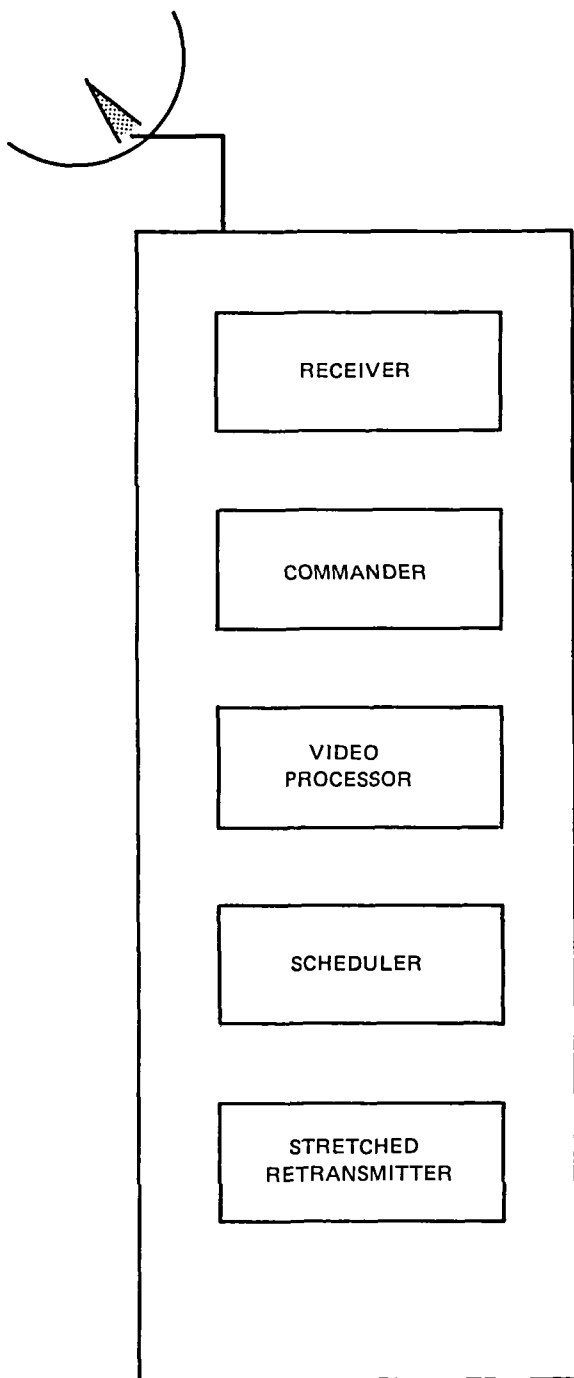


Figure 3-3. VAS S/DB Functional Elements

- Frequency and Timing System
 - Tracking Sun pulse and phase-lock loop
 - Providing Sun/Earth (beta) angle delay
 - Generating equal angle clock
 - Delaying retransmission to GOES

- Programming Onboard Processor—Verifying commands
- c. Video Processing:
 - On-line alteration of data
 - Equal angle interpolation and resampling of equal time data
 - Calibration of radiances
 - Correction for detector geometry
 - Navigation
 - Quality control
 - Bit error rate measurement
 - Horizon detection
- d. Scheduling and Housekeeping:
 - Schedule PDL's
 - Verify PDL's
 - Submit to interrogation by Satellite Operational Control Center, UW, or GSFC
- e. Stretched VAS Retransmission—Broadcast stretched data to designated GOES transponder.

3.2 GSFC DATA ACQUISITION AND PROCESSING SYSTEM

The GSFC Data Acquisition and Processing System (Figure 3-4) consists of several subsystems, including:

- VAS receiving station
- VISSR receiving station
- VAS preprocessor (VPP)
- VAS processor (VP)
- VAS Assessment processor (VAP)
- Atmospheric and Oceanic Image Processing System (AOIPS)

3.2.1 Data Flow

The stretched VAS data at 1.75 Mbps are received by the 7.3-m (24-ft) dish at the VAS receiving station. These

data are demodulated, reconstructed by the bit synchronizer, and fed into the frame synchronizer that interfaces with the VPP. The VPP (a PDP 11/70 with a 176-Mb disk) performs a variety of preprocessing tasks before transferring the data to a dual-ported disk for subsequent processing by the VP. The VPP reformats, quality checks, archives on high density digital tapes (HDDT's), and temporally averages (in the DS mode) the VAS data.

The VP user selects data from the dual-ported disk for processing. These data are merged with the conventional data from the 604 line, which allows temperature and moisture extraction to be performed on the sounding processor. These parameters are accessed by either the AOIPS or the VAP for further meteorological research.

3.2.2 Research Software

3.2.2.1 Temperature/Moisture Sounding Software

The capability exists for the production of temperature and moisture profiles from VAS and conventional 604-line data. Man-interactive processing of VAS multi-channel data is used to ensure the quality of satellite radiances and to avoid cloud-contaminated retrievals. Images of the VAS channels can be quickly displayed in radiance or brightness temperature units. Multispectral image products are used to provide quantitative fields of meteorological parameters at VAS resolution. VAS soundings can be immediately compared to ground truth (if available) or previous soundings.

3.2.2.2 Meteorological Assessment Software

The meteorological assessment is performed using the General Meteorological Package (GEMPAK). This package is a collection of programs for processing data that are either regularly spaced (e.g., interpolated to a grid, output by a model) or irregularly spaced (e.g., 604-line data, satellite temperature soundings). GEMPAK has the capability to list data, quality control data, grid irregularly spaced data, display data on image analysis terminals, overlay other data (e.g., station data or contour data) on satellite images, perform diagnostics (e.g., calculate temperature advection, velocity divergence), and perform vertical cross-section analyses of conventional or VAS data.

3.3 UW DATA ACQUISITION AND PROCESSING SYSTEM

3.3.1 Reception and Preprocessing

The stretched VAS signal from the CDA station is captured by the antenna systems that are mounted on the

roof of the 15-story Meteorology and Space Science and Engineering Center building located in Madison, Wisconsin. These antenna systems are designed to receive the GOES 1.6871-GHz satellite data signals, which are processed by the UW ground systems (Figure 3-5).

The received 1.6871-GHz signal is down-converted to 67.1-MHz and is amplified to a usable level for the phase shift key (PSK) demodulator. The EMR 729 PSK demodulator package outputs the meteorological data in the form of a nonreturn to zero signal (NRZS). These data are in turn fed to line drivers which take them to the 6th floor for bit- and frame-synchronization. At this point, the signal is ready to be archived continuously at full resolution (Suomi, 1982) for both visible and

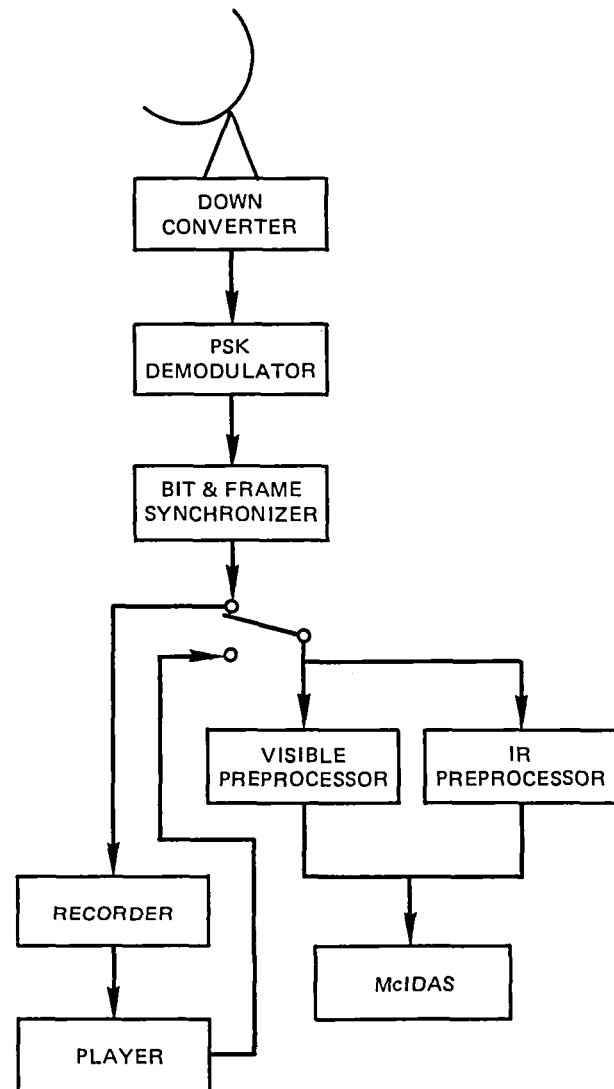


Figure 3-5. University of Wisconsin Ground System

infrared, and/or to be ingested into the Man/computer Interactive Data Access System (McIDAS) main computer (Suomi *et al.*, 1983).

Next, the data are preprocessed to be amenable to scientific interpretation in the form of image display or conversion into quantitative meteorological temperature, moisture, or wind values. The visible image preprocessor enables data reduction of the visible data by pixel averaging along a scanline. The visible data are averaged over 1, 2, 3, 4, 6, and 8 pixel (instantaneous field-of-view) values as predetermined by the user.

The infrared (IR) preprocessor performs averaging and updating on serial bit streams provided by GOES. The IR preprocessor is concerned with the first two sectors of data—irradiance 1 and irradiance 2. Each IR sector has information corresponding to the intensity of infrared radiance. For each scanline, the preprocessor checks to see when a new scanline number appears. When a new geographical scanline begins, a sequence of operations is initiated. For scan swaths having the same line number and spectral channel number as the previous swath, the IR preprocessor performs vector averaging on the two swaths of data. Each word is averaged with the corresponding word in the other swath. When the unit detects a different scanline and/or spectral channel number, it transfers the average data to the McIDAS, where it is stored on disk in a sounding file for scientific application.

3.3.2 McIDAS Applications

McIDAS allows remote and local access to a wide range of data from satellites and conventional observations, time-lapse displays of imagery data, overlaid graphics, and current and past meteorological data. The available software permits analysis of a wide range of digital images, as well as temperature and moisture sounding data obtained from GOES and the polar orbiting satellites. McIDAS can generate multicolor composites of conventional and satellite weather data, radar, and forecasts in a wide variety of two- and three-dimensional displays, as well as time lapse movies of these analyses.

The distinctive feature of McIDAS is its ability to ingest meteorological satellite and conventional data in real time and make it readily available to both local and remote users. McIDAS is best described in terms of the six distinct components that follow.

3.3.2.1 Meteorological Data Acquisition

McIDAS ingests VISSR visible and infrared images, as well as the VAS multispectral imagery and sounding data provided in real time, through direct acquisition using three antennas. Meteorological data from North America, Service C radiosonde observations, weather radar pictures, pilot reports, National Meteorological Center (NMC) forecast products, etc. are also ingested by dedicated and dial-up communications lines. The McIDAS central processing unit (CPU) communicates with other computers using dedicated communications lines.

3.3.2.2 McIDAS III Computer

The current hardware configuration is shown schematically in Figure 3-6. The previous generation of McIDAS was built around a Harris/6 minicomputer. McIDAS III is built around a medium-scale computer (IBM 4341 Group II). The current memory capacity of the McIDAS III is 8 Mb (2 real and 6 virtual Mb) of addressable memory. Peripheral data storage is provided by five IBM 3350 disk units, each of which is capable of storing 640 Mbytes.

3.3.2.3 McIDAS Video Terminals

Figure 3-7 shows the terminal configuration schematically. This terminal consists of an image display cathode ray tube (CRT), an alpha numeric CRT, a keyboard, and two cursor control joysticks.

A typical McIDAS terminal can store a number of image and graphic frames for rapid access. All available frames and graphic overlays can be displayed in a movie loop at variable rates up to 15 frames per second.

A wide variety of types and sizes of cursors are generated by the local microprocessor. These cursors can be positioned anywhere on the monitor display by using keyboard control or a pair of coarse and vernier joysticks.

A displayed image can be enhanced locally by changing from the default display mode, in which the displayed brightness is proportional to the digital data numbers.

Data tablets are used to simplify the entering of commands. These data tablets can be programmed so that a specific location selected by a pointer performs a specific function. The data tablet is proving to be an efficient means of manipulating the complex data in an operational environment.

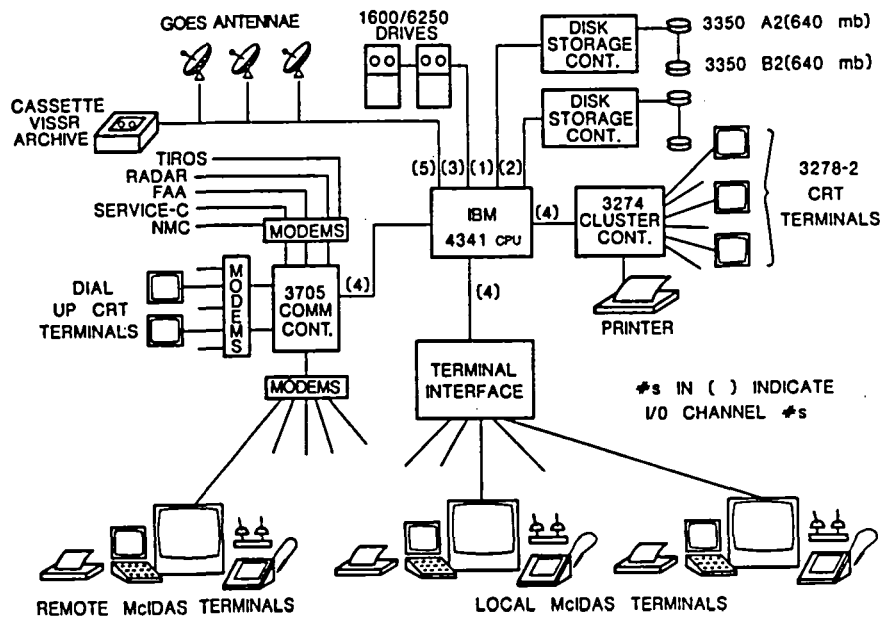


Figure 3-6. McIDAS III

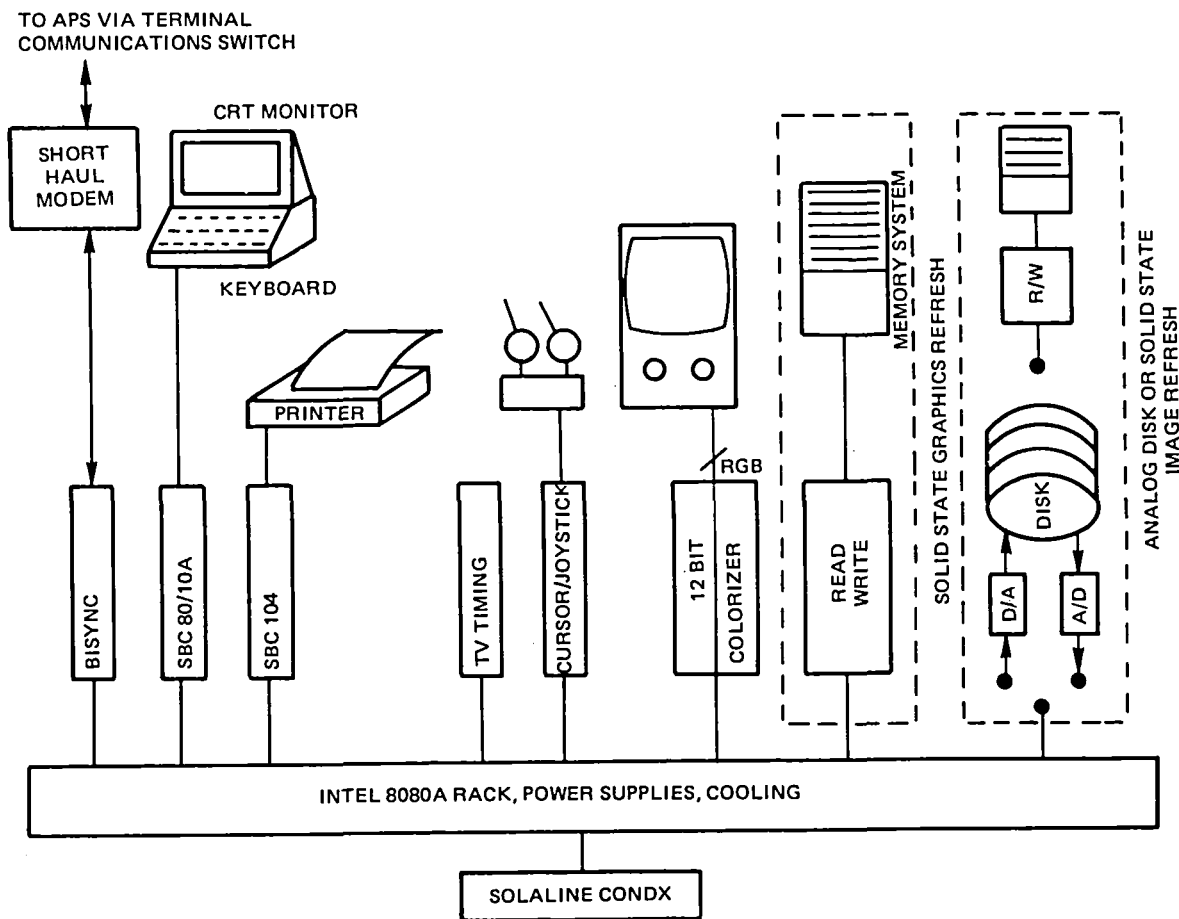


Figure 3-7. McIDAS Terminal Configuration

3.3.2.4 Computer Operating System

The IBM 4341 CPU is run under Operating System/Virtual System 1 (OS/VS1), which is batch-oriented. The interactive program editing, computing, and video processing support is provided by the Editor and the McIDAS Control Program.

3.3.2.5 McIDAS Control Program

The McIDAS Control Program appears as an applications program to the computer operating system, and as the operating system to the McIDAS applications programs. It executes in a single partition of OS/VS1, or in a address space in OS/MVS.

The two ways in which commands can be entered to the executive are:

- Single-letter key-ins for fixed and user-defined functions
- Explicit commands that can accept an argument list

Repeated tasks or proceeding steps can often be chained in a single macro command.

3.3.2.6 McIDAS Applications Programs

Over 300,000 lines of source code (Fortran, 1977 standard) are currently operative on McIDAS III. A few example applications are:

- Image Data-Oriented Applications Programs
 - Digital processing of image data
 - Cloud and water vapor motion (i.e., wind vector) determination
 - Image navigation
 - Statistical image analysis
 - Stereo image display
- Non-image Data Analysis
 - Satellite sounding retrieval
 - Data interpolation
 - Graphical analysis
 - Statistical analysis of user data
 - “Nowcasting” or display of current conventional and satellite weather data
 - Simple advective forecasting of short-term mesoscale weather phenomena
 - Forecasting with a sophisticated limited-area mesoscale primitive equation numerical prediction model

VAS INSTRUMENT PERFORMANCE APPRAISAL

D. Chesters

*Goddard Laboratory for Atmospheric Sciences
Goddard Space Flight Center
National Aeronautics and Space Administration
Greenbelt, Maryland*

W. P. Menzel

*Cooperative Institute for Meteorological Satellite Studies
National Environmental Satellite Data Information Service
National Oceanic and Atmospheric Administration
U.S. Department of Commerce*

H. E. Montgomery

*Goddard Space Flight Center
National Aeronautics and Space Administration
Greenbelt, Maryland*

W. D. Robinson

*General Software Corporation
Landover, Maryland*

4.1 INTRODUCTION

The VAS Demonstration was designed to modify and improve the VISSR instrument on the operational GOES satellites. The new instrument provides calibrated infrared radiances in several bandpasses that are sensitive to the temperature and water vapor distribution in the troposphere. Relatively accurate data are required for multispectral images of the structure and changes in the atmosphere. Very accurate radiances are required for retrievals of temperature and moisture profiles. Major efforts have been made to evaluate the performance of each VAS radiometer, before and after launch.

The previous VISSR instrument provided visible images of the Earth, along with infrared data in a single 11- μm window channel (Bristor, 1975). The VAS instrument has expanded the previous infrared capability by providing 12 channels of radiometric data between 4 and 15 μm . The channels were chosen to distinguish among the effects of tropospheric temperature, moisture, and cloud cover on the upwelling radiances. All 12 channels can be operated at 13.8-km horizontal resolution (instantaneous geometrical field-of-view (IGFOV) at nadir). The brighter longwave channels can be operated

using the small (6.9-km IGFOV) detectors that provide the operational VISSR 11- μm data. The radiometer has been upgraded to yield higher precision values (10 bits instead of 8) from redundant sensors (3 independent detector pair instead of 1 redundant pair). VAS radiances are carefully calibrated with outer space (3 K), and an internal target (approximately 300 K). This calibration is accomplished by a physical model with correction coefficients for the radiative contributions from the foreoptics components of the VAS telescope, where temperatures are continuously monitored by the GOES system. Radiometric noise can be reduced by "dwell averaging" several spins on the same line and channel. The "spin budget" refers to the number of spins allocated to the channels. Noise can also be reduced after data collection, by judicious averaging of the clear adjacent fields-of-view. Considerable effort has gone into prelaunch development of VAS radiometry (Montgomery and Endres, 1977; Malinowski and Ruiz, 1980; Menzel, 1980).

The first VAS instrument was launched on GOES-4, and was found to be a relatively stable, somewhat biased radiometer, capable of good multispectral imagery and

fair sounding accuracy (Menzel *et al.*, 1980; Smith *et al.*, 1980; Chesters *et al.*, 1980). The other instruments launched during the VAS Demonstration on GOES-5, and on GOES-6, have received similar evaluations (Menzel, 1981b, 1981c, 1983a, and 1983b; Chesters and Robinson, 1983). The ground system plays an important role in determining the quality of the VAS radiances. The data chain carries out many calibration and sampling operations before the user receives the data (Anon., 1978a, 1978b, 1979a, 1979c, 1979d, 1979e, and 1980). The VAS instrument on GOES-5 has provided most of the data for testing by users. These radiances are found to be useful for image sequences and sounding purposes (Greaves, 1983; Lee *et al.*, 1983; Smith, 1983; Menzel *et al.*, 1983b).

This radiometric performance appraisal is based upon these reports, along with previously unpublished material. Radiometric quality is compared to prelaunch specifications. Limitations are identified in the VAS instrument on board the geosynchronous spacecraft, and in the data processing system at the ground facility. As a result of the difficulty in assessing the radiometric errors of a remotely based infrared instrument without

external standards, many evaluations are made by comparing the relative variations within VAS radiances (between samples, lines, detectors, etc.) and by comparison to other satellite data. VAS performance is explicitly evaluated for radiometric noise factors and associated averaging requirements, registration among the detectors, truncation errors, zero-point errors, droop along a scanline, scan-to-scan reproducibility, "scattered light" and resampling errors, and ground system problems. Comparisons between the VAS geosynchronous, and high resolution infrared polar sounders, and between VAS radiances and radiosondes, were also evaluated. Finally, there is a summary of the radiometric quality and sounding limitations of the VAS instrument.

4.2 SPECIFICATIONS FOR THE VAS INSTRUMENT

Table 4-1 lists the general design features of the VAS channels (Montgomery and Endres, 1977). VAS channel 8 is the VISSR 11- μm window, operated with large detectors, providing a view of the surface that is significantly affected by molecular absorption from atmospheric water vapor, and carbon dioxide. Each of the VAS bandpasses was selected with temperature, water vapor, surface, and cloud detection in mind, based on

Table 4-1
Design Features of the VAS Channels

VAS Ch. No.	Spectral Filters			Purpose for Sounding	Main Absorbing Gas	Other Significant Effects
	Center		Width cm^{-1}			
	μm	cm^{-1}				
1	14.730	0678.7	10.0	temp	CO_2	O_3
2	14.480	0690.6	16.0	temp	CO_2	O_3
3*	14.250	0701.6	16.0	temp	CO_2	O_3
4*	14.010	0713.6	20.0	temp	CO_2	O_3
5*	13.330	0750.0	20.0	temp	CO_2	O_3
6	04.525	2210.0	45.0	temp+cloud	N_2O	Sun
7*	12.660	0790.0	20.0	moisture	H_2O	CO_2 +dust
8*	11.170	0895.0	140.0	surface	H_2O	CO_2 +dust
9*	07.261	1377.0	40.0	moisture	H_2O	CO_2
10*	06.725	1487.0	150.0	moisture	H_2O	—
11	04.444	2250.0	40.0	temp+cloud	$\text{N}_2\text{O}, \text{CO}_2$	Sun
12	03.945	2535.0	140.0	surface	H_2O	Sun+dust

*Available at 6.9 km as well as 13.8 km IGFOV

experience with the infrared sounders in polar orbit. The detailed spectral response (filter function) for each of the 12 VAS channels was measured prior to launch, and found to meet the center and width specifications, which are listed in Table 4-1 (Chesters and Robinson, 1983).

VAS calibration, noise, resolution, and registration requirements were thoroughly reviewed before the first VAS launch (Montgomery and Endres, 1977; Menzel, 1980). Other important VAS characteristics are:

- The large detectors project as 0.384-mr square IGFOV's (13.8-km horizontal resolution at nadir). The small detectors are approximately 0.192 mr square (6.9-km IGFOV's, slightly rectangular on GOES-5 and -6). East-west offsets between the detectors are corrected in software before VAS data are sent to the user.
- Successive infrared samples are autocorrelated by approximately 40 to 60 percent, due to 1/f noise and electronic filtering. Independent measurements are available after three to five samples.
- VAS resolution is diffraction limited. Only 80 percent of the radiance observed with a large detector is collected from within the IGFOV. Approximately 90 percent is collected within a circle of

radius 0.221 mr (15.9-km footprint at nadir). Ninety-nine percent is collected within a circle of radius 0.932 mr, which is a diameter equal to five large detector IGFOV's (70.0-km footprint at nadir). Geometrical projection further extends the footprint by 20 to 50 percent, at the latitudes of the United States.

- The scan mirror takes steps of 0.192 mr in the north-south direction, equal to the IGFOV for the small longwave detectors. A full-Earth frame consists of 1821 steps.
- The GOES nominal spin rate is 100 RPM. Infrared detectors are sampled every 8 μ s, as the footprint travels 0.084 mr. Therefore, the large detector IGFOV's are oversampled by a factor of 4.6, and the small detectors by a factor of 2.3.
- Earth-location requirements are ± 10.0 -km absolute, and ± 1.4 -km relative (± 10 percent of a large detector's IGFOV) accuracy.
- Each spin-scan produces a scanline from the "upper" and "lower" detector of a pair. Each infrared scanline consists of 3822 radiometric samples. Each sample is represented as a 10-bit positive integer. The 10-bit integers are converted into calibrated radiances by the data processing

Table 4-2
Estimated Sensitivity of the VAS Channels

VAS Ch. No.	Peak Responses (mb)	10%-90% Radiance Layer (mb)	Std. Sensitivity (K/ $^{\circ}$ C)			Std. T* (K)	Conversion dR/dT* (erg/etc./K)
			Temp	Dewpt	Surf		
1	70	4-120	1.00	.00	0.00	219	0.900
2	125	4-225	.99	.00	0.00	219	0.900
3	200	15-475	.91	-.02	0.00	223	1.000
4	500	40-900	.73	-.09	0.02	238	1.200
5	920	420-surf	.47	-.30	0.29	260	1.500
6	850	520-surf	.43	-.03	0.44	257	0.051
7	1000	720-surf	.33	-.37	0.63	270	1.600
8	surf	920-surf	.17	-.20	0.84	272	1.700
9	600	110-820	.82	-.70	0.02	254	0.430
10	400	240-620	.94	-.70	0.00	246	0.210
11	300	7-1000	.80	-.01	0.04	237	0.013
12	surf	surf-surf	.08	-.03	0.92	273	0.036

erg/etc. = erg(*sec cm² steradian cm⁻¹).

systems at the ground facilities. Bit-error rates during data transmission should be less than 1 in 10^6 . Bit errors in the transmitted infrared data are not correctable.

Table 4-2 lists the estimated sensitivity of the VAS channels for the U.S. Standard Atmosphere. The calculations were made by using the exact spectral filter functions, and line-by-line simulations of the upwelling radiances. The thickness of the central 80-percent radiance layer indicates the difficulty in assigning a radiance feature to the level of peak response. The channel sensitivities are estimated as the change in the calculated brightness temperature (T^*) for a one degree change in the temperature, or dewpoint, of the entire standard profile, or for a one degree change in surface (skin) temperature. The independent sensitivities of the brightness temperature to air temperature, dewpoint, or skin temperature indicates the difficulty with interpreting radiance variations within a single VAS channel. For instance, several channels have nearly equal or opposite sensitivity to temperature and dewpoint. These channels are insensitive indicators of dewpoint depression. Table 4-2 also lists conversion factors between radiance, and brightness temperature.

Figure 4-1 shows the weighting functions, $d\tau/d\ln P$, that were used for the construction of Table 4-2. The temperature sounding channels are plotted separately from the water vapor and window channels. The short-wave channels are indicated with dashed lines. The redundancy between the longwave and shortwave channels was designed for the detection of cloud contamination, by exploiting the differential sensitivity of the Planck function to cloud-top temperature. The sharp peaks of the upper air moisture channels in Figure 4-1 are due to the exponential distribution of water vapor in the U.S. Standard Atmosphere. In reality, the *vertical* structure of the water vapor weighting functions is not readily predictable or retrievable because they represent the radiance accumulation from the top few millimeters of the total water burden. On the other hand, VAS images in these channels provide high resolution information about the *horizontal* distribution of thick layers of water vapor. Figure 4-1 also shows that the lower troposphere (600 to 1000 mb) is not well resolved by any one of the VAS channels. The radiation from the lower troposphere is mixed with both surface and mid-tropospheric contributions in all the key VAS channels (5, 6, 7, 8, and 12). The shortwave infrared window (channel 12 at $3.9 \mu\text{m}$) is affected by reflected sunlight. No VAS water vapor channel has a peak response in the

lower troposphere, although the best low-level temperature sounding channel (5 at $13.3 \mu\text{m}$) is also sensitive to low-level water vapor. Simulated retrievals indicate that VAS soundings will suffer from ambiguities about the state of the lower atmosphere (Chesters *et al.*, 1982). Actual VAS soundings confirm these expectations, and demonstrate the value of conventional surface data as an aid to resolving the lower levels (Lee *et al.*, 1983). Table 4-3 lists the prelaunch sounding specifications for VAS performance (Montgomery and Endres, 1977). The sounding field-of-view (SFOV) requirements for absolute RMS errors are based on the principle that the input to a remote sensing algorithm must be more accurate than the output. For example, $\pm 0.2 \text{ K}$ input errors in brightness can produce $\pm 2.0^\circ\text{C}$ output errors in atmospheric temperature, after differences are taken among a dozen channels. The sounding error budget was drafted with the expectation of spatial averaging to 30 by 30 km^2 horizontal resolution at nadir (150 by 150 km^2 for VAS channel 1). The single-sample noise values are based upon the anticipated detector-amplifier noise, and filter bandwidths. The noise specifications apply to the large detectors. The single-sample noise was expected to be twice as large for the small detectors, so that horizontal averaging should produce the same signal-to-noise for the same spatial resolution. Nominal calibration requirements are $\pm 1.5 \text{ K}$ absolute, and $\pm 0.5 \text{ K}$ relative brightness temperature accuracy. Some of the faint channels (1, 9, and 11) have single-sample noise values which are much larger than the SFOV requirements. These bands are expected to require a large spin budget. While the shortwave channels appear to be relatively noisy, they can provide very large contrast over the Earth, as can be seen by comparing the mean and RMS deviation from the mean of the Earth's brightness listed in the last two columns of Table 4-3, for VAS channels 6, 11, and 12. The brightness difference between shortwave and longwave channels with similar weighting functions (Figure 4-1) is expected to aid in the detection of clouds. Although the VAS channels operate with detector pairs, producing an "upper" and "lower" scanline with each spin, the following post-launch performance tables list only a single value for each channel, in order to simplify the presentation. The upper large longwave detector on GOES-4 failed prior to launch, and the S/DB software for the small detectors was not debugged in time for their evaluation. On GOES-5, the noise in both detectors is very similar for all bands. The errors listed for GOES-6 are dominated by a noisy lower large longwave detector. These tables are constructed by selecting the *worst* of the values measured for the upper and lower detectors, on each

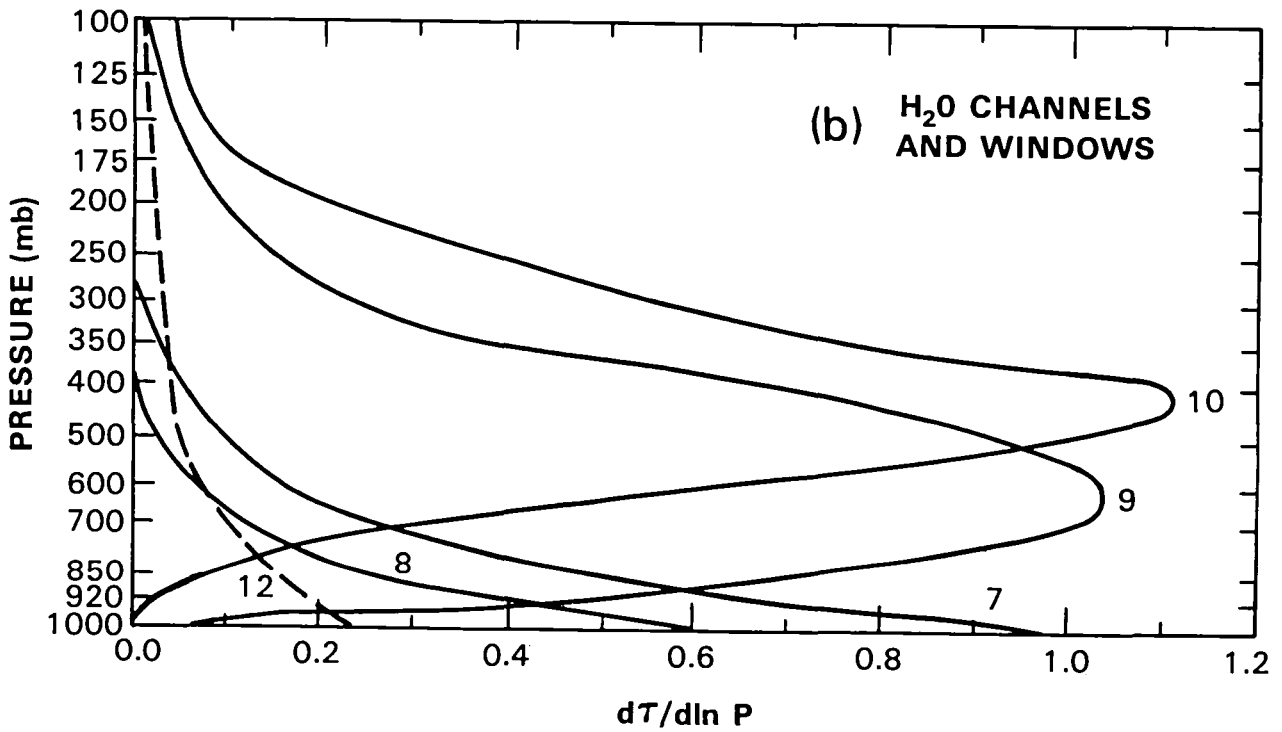
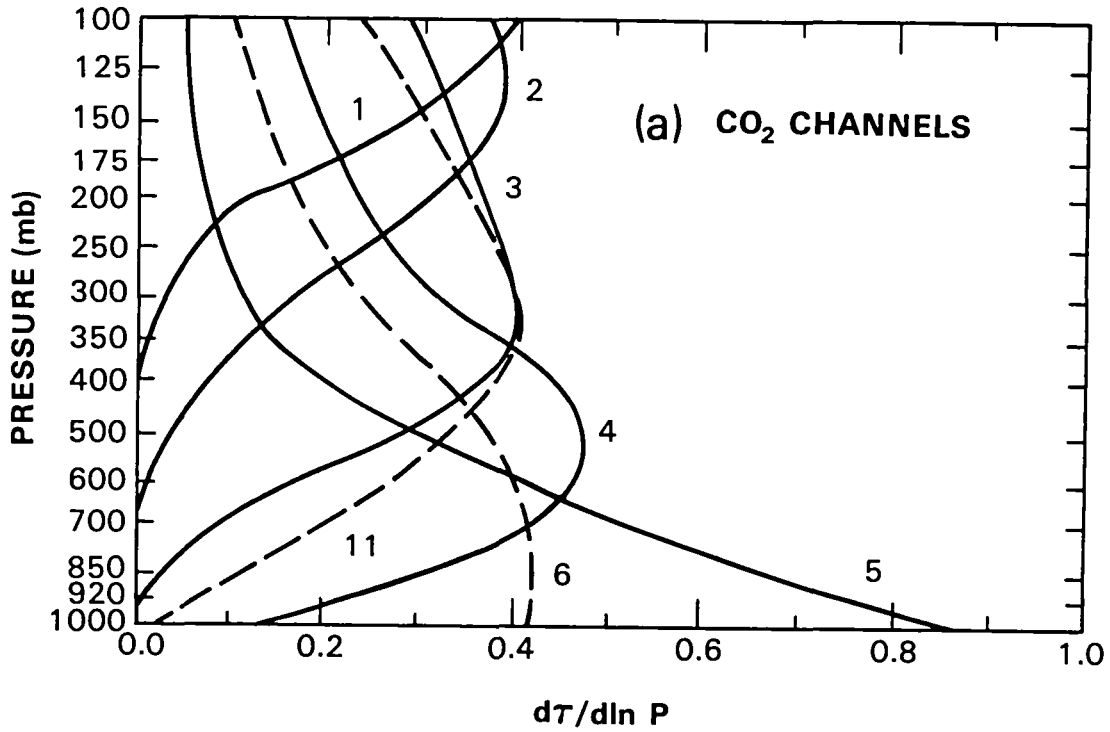


Figure 4-1. Standard VAS Weighting Functions

Table 4-3
Specifications for the VAS Channels

VAS Ch.	SFOV RMS	Sample Noise	Calibration Errors		Typical Scene	
			Absolute	Relative	Mean	±Dev.
Brightness temperature units (T*, Kelvin)						
1	0.3	5.3	1.5	0.5	216.0	10.0
2	0.3	2.2	1.5	0.5	218.0	09.0
3	0.3	1.8	1.5	0.5	226.0	07.0
4	0.2	1.2	1.5	0.5	245.0	09.0
5	0.2	1.0	1.5	0.5	274.0	15.0
6	0.1	1.6	1.5	0.5	274.0	17.0
7	0.2	1.0	1.5	0.5	289.0	19.0
8	0.2	0.1	1.5	0.5	295.0	21.0
9	0.4	3.4	1.5	0.5	257.0	10.0
10	0.5	1.6	1.5	0.5	242.0	07.0
11	0.3	6.7	1.5	0.5	244.0	11.0
12	0.1	0.8	1.5	0.5	296.0	22.0
Radiance units (R, erg/etc.)						
1	0.250	4.900	1.300	0.400	040.00	09.00
2	0.250	2.000	1.300	0.400	042.00	08.00
3	0.250	1.800	1.500	0.500	048.00	07.00
4	0.250	1.400	1.700	0.600	066.00	11.00
5	0.250	1.400	2.200	0.700	100.00	23.00
6	0.004	0.057	0.077	0.025	001.20	00.80
7	0.250	1.400	2.500	0.800	117.00	30.00
8	0.250	0.160	2.500	0.800	110.00	36.00
9	0.150	1.300	0.600	0.200	014.00	04.00
10	0.100	0.330	0.300	0.100	005.70	01.50
11	0.004	0.066	0.020	0.006	000.23	00.14
12	0.004	0.020	0.054	0.018	000.84	00.79

VAS instrument, in order to exercise the proper amount of caution in regards to the usefulness of the data.

4.3 RADIOMETRIC NOISE AND THE SPIN BUDGET

Table 4-4 compares the single-sample noise observed for the VAS channels, to the prelaunch specifications. The noise was measured by taking the standard deviation of 200 successive samples from outer space. The postlaunch noise measurements are better than the design specifications, especially in the case of the shortwave window (channel 12). GOES-4 carried the noisiest VAS instrument, GOES-5 carried the quietest, and GOES-6 carried a noisy large lower longwave detector, which dominates these statistics. The small detectors are less

than twice as noisy as the large, making them very useful for high resolution work.

Table 4-5 lists the postlaunch signal-to-noise values for a nominal scene at T* = 320 K, using the observed noise values from Table 4-4. This signal-to-noise format is used for engineering evaluations (Malinowski and Ruiz, 1980). For meteorological retrievals, the "signal" is the variability of the Earth's atmosphere (see the last column of Table 4-3).

Table 4-6 lists the spin budgets (SB) which would be necessary in order to reduce the random noise (σ) within a SFOV, to the sounding requirements for each

Table 4-4
Radiance Noise Observed in the VAS Channels

VAS Ch. No.	Specified Single-Sample Noise	Standard Deviation in Outer Space		
		GOES-4 18 Feb 81	GOES-5 4 Aug 81	GOES-6 24 May 83
Large detector noise (erg/etc.)				
1	4.9	4.4	2.8	2.8
2	2.0	2.6	1.5	1.8
3	1.8	1.5	1.1	1.4
4	1.4	1.4	0.9	1.2
5	1.4	1.2	0.8	0.7
6	0.057	0.031	0.023	0.021
7	1.4	0.9	0.8	0.9
8	0.16	0.2	0.2	0.3
9	1.3	1.2	0.6	0.7
10	0.33	0.3	0.2	0.2
11	0.066	0.030	0.027	0.023
12	0.020	0.008	0.007	0.009
Small detector noise (erg/etc.)				
3	3.6	na	2.5	2.4
4	2.8	na	1.9	2.1
5	2.8	na	1.5	1.6
7	2.8	na	1.4	1.5
8	0.032	0.4	0.3	0.3
9	2.6	na	1.3	1.2
10	0.67	na	0.3	0.3

VAS channel. These σ values were computed for the large detectors from single-sample random noise (NEDR) values, which were observed after the launch of each GOES satellite. For channel 1, the 150 by 150 km² SFOV is the spatial average of 50 successive samples along each scanline for 11 independent scanlines. For the remaining channels, the 30 by 30 km² SFOV is computed from six samples, and two scanlines. The number of spins required to achieve the sounding specifications in the second column of Table 4-6 is derived by assuming there will be a $N^{-1/2}$ reduction in noise from dwell averaging for N spins. GOES-5 and -6 have all detectors functioning, have lower noise levels than GOES-4, and are capable of sounding a given area in a much shorter time.

4.4 DETECTOR-TO-DETECTOR REGISTRATION

Figure 4-2 presents a projection of the focal plane containing the VAS infrared and visible detectors. Infrared detectors 1, 2, 3, and 4 are made of a HgCdTe alloy, for use with the longwave 6 to 15- μ m filters. Detectors 5 and 6 are made of an InSb alloy, for use with the short-wave 3 to 5- μ m filters. While the layout is not to scale, it shows that the relative north-south mirror step size is equal to the nominal IGFOV of a small detector. The small detectors are sampled 2.3 times per IGFOV, and the large detectors are sampled 4.6 times per IGFOV. Normally, VAS data is acquired with alternating 2 and 6 mirror steps in order to provide scanlines from the large upper and lower detectors which can be re-inter-

Table 4-5
Signal-to-Noise for T* = 320 K

VAS Ch. No.	Signal R(320 K) (erg/etc.)	R(320 K)/Noise		
		GOES-4 18 Feb 81	GOES-5 4 Aug 81	GOES-6 24 May 83
Large detector signal/noise				
1	185.	42.	66.	66.
2	184.	71.	123.	102.
3	183.	122.	166.	131.
4	182.	130.	202.	152.
5	178.	148.	223.	254.
6	6.25	202.	272.	298.
7	173.	192.	216.	192.
8	155.	775.	775.	517.
9	64.1	53.	107.	92.
10	49.0	163.	245.	245.
11	5.43	181.	201.	236.
12	2.13	266.	304.	237.
Small detector signal/noise				
3	183.	na	73.	76.
4	182.	na	96.	87.
5	178.	na	119.	111.
7	173.	na	124.	115.
8	155.	388.	517.	517.
9	64.1	na	49.	53.
10	49.0	na	163.	163.

Table 4-6
VAS Spin Budgets Required for Sounding

VAS Ch. No.	Specified SFOV Accuracy	Single-Sample Noise, SFOV Noise and Spin Budgets									
		GOES-4 11 Oct 80			GOES-5 9 June 81			GOES-6 18 May 83			
	RMS	NEDR	σ	SB	NEDR	σ	SB	NEDR	σ	SB	
1	0.25	4.130	0.250	1	2.780	0.220	1	3.960	0.240	1	
2	0.25	2.530	1.020	14	1.510	0.640	7	2.310	0.870	12	
3	0.25	1.760	0.750	9	1.240	0.520	5	1.680	0.670	8	
4	0.25	1.490	0.620	7	1.080	0.470	4	1.440	0.580	6	
5	0.25	1.130	0.460	4	0.870	0.370	3	0.950	0.370	3	
6	0.004	0.028	0.012	10	0.027	0.011	8	0.020	0.009	5	
7	0.25	1.070	0.430	3	0.740	0.300	2	0.940	0.350	2	
8	0.25	0.120	0.050	1	0.130	0.060	1	0.120	0.050	1	
9	0.15	1.230	0.510	12	0.690	0.290	4	0.810	0.310	5	
10	0.10	0.310	0.120	2	0.160	0.070	1	0.170	0.070	1	
11	0.004	0.026	0.011	8	0.027	0.011	9	0.022	0.009	6	
12	0.004	0.007	0.003	1	0.007	0.003	1	0.008	0.003	1	
Total spin budgets:				72					46	51	
The RMS, NEDR, and σ values have units of erg/etc.											

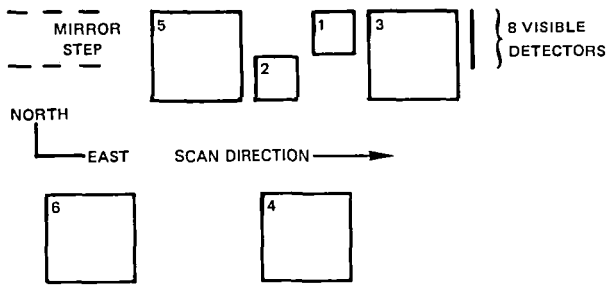


Figure 4-2. Focal Plane Geometry

the effective angular offsets between the detectors that are indicated in Figure 4-2. The prelaunch values are based upon a combination of measurements and ray tracing. The east-west values are utilized by the S/DB to register the images produced by each of the infrared detectors with respect to the visible image. The east-west and north-south offsets are documented in the stretched VAS data stream, so that the user may make final registration corrections. The postlaunch values were obtained by viewing landmarks with the visible and all 6 infrared detectors. The north-south differences between prelaunch and postlaunch registration are negligible. The east-west differences are comparable to the IGFOV of a large detector (0.384 mr), so that post-launch adjustments are necessary for optimum registration between lines from the different detectors. For GOES-4 and -6, the S/DB used the prelaunch offsets only. For GOES-5, the offsets used by the S/DB, were updated to the postlaunch values in Table 4-7 in January 1982.

leaved to form continuous north-south coverage without overlap. The focal plane offsets between these detectors must be removed in order to provide VAS data which is mutually aligned.

Table 4-7 lists the prelaunch and postlaunch values for

Table 4-7
Measured Values of Detector Offsets

Det. No.	GOES-4		GOES-5		GOES-6	
	E-W	N-S	E-W	N-S	E-W	N-S
Prelaunch measurements (mr)						
1	1.756	0.000	1.721	0.000	1.614	0.000
2	2.388	0.192	2.364	0.185	2.263	0.201
3	1.006	0.095	0.996	0.097	0.981	0.084
4	1.654	0.858	1.631	0.839	1.623	0.864
5	4.953	0.106	4.403	0.101	4.358	0.090
6	5.619	0.902	5.001	0.875	4.993	0.895
vis	0.000	0.023	0.000	-0.069	0.000	-0.047
Postlaunch measurements (mr)						
1	2.26	0.00	2.06	0.00	1.02	0.00
2	2.89	0.19	2.70	0.19	1.67	0.20
3	1.35	0.10	1.34	0.10	0.56	0.08
4	1.99	0.86	1.97	0.84	1.20	0.86
5	5.71	0.11	4.74	0.10	3.94	0.09
6	6.38	0.90	5.34	0.88	4.57	0.90
vis	0.00	0.17	0.00	0.16	0.00	0.00
E-W with respect to the visible PMT array (+west). N-S with respect to center of IR detector 1 (+south).						

Table 4-8
Comparison of VAS and HIRS Characteristics

Feature	VAS on GOES	HIRS on NOAA
Orbit	Geostationary	Polar
Altitude	30,000 km	800 km
Relative flux	1 unit	1400 units
Mirror radius	20 cm	7.5 cm
Sampling time	Programmable dwell (0 to 225) x 8 μ s	Single glance 700 μ s
IGFOV	13.8 or 6.9 km	21.8 km
Noise	± 0.5 K	± 0.1 K
Coverage	Programmable 15° latitude swath per 10 min	Suborbital 30° longitude swath per overpass
Frequency	Programmable e.g., 15 min intervals	Fixed every 12 hours
Calibration	Space/internal blackbody foreoptics corrections	Space/external blackbody
IR channels	12 TOTAL: 5 CO ₂ @ 13-15 μ m 2 CO ₂ , N ₂ O @ 4.4-4.5 μ m 3 H ₂ O @ 6.7,7.2,12.6 μ m 2 windows @ 11.2,3.9 μ m	19 TOTAL: 7 CO ₂ @ 13-15 μ m 5 CO ₂ , N ₂ O @ 4.2-4.5 μ m 3 H ₂ O @ 6.7,7.3,8.3 μ m 3 windows @ 11.1,4.0,3.7 μ m 1 O ₃ @ 9.7 μ m

4.5 COMPARISON OF GEOSYNCHRONOUS AND POLAR SOUNDERS

Table 4-8 presents a comparison between the main features of the VAS instrument on the GOES satellite (operating from a distant geosynchronous orbit), and the HIRS instrument on the NOAA satellites (operating from a low polar orbit). Radiometric calibration is more difficult for VAS without an external blackbody. The distant geosynchronous station receives much less flux from the Earth. The two instruments have coverage capabilities appropriate to their meteorological missions. VAS produces frequent views of the same area at fixed angle for mesoscale tropospheric analysis, while HIRS produces daily coverage of the entire Earth for global synoptic analysis. The VAS infrared bands are almost a subset of those on HIRS. VAS lacks the 15- μ m stratospheric bands, the 4.3- μ m bands, a split shortwave

window, and the thermal ozone band.

Table 4-9 presents a comparison between the brightness temperatures observed at the same locations by VAS and HIRS. The HIRS bands listed are those that are the most similar to the VAS bands. The transmittances of HIRS band 10 and VAS band 7 are similar, despite the difference in their wave numbers, ν (cm^{-1}). For the absolute calibration tests presented in Table 4-9, the brightness temperatures from all 19 HIRS bands are used in a multiple regression relation, to estimate the brightness of each VAS band. The regression coefficients were derived from synthetic radiances for all HIRS and VAS channels at 13 viewing angles from a statistical sample of 1200 NOAA/NESDIS radiosonde-rocketsonde climatological profiles. The observed VAS radiances are compared to the HIRS estimates of the VAS radiances for GOES-4 (1530 GMT on 19 January

Table 4-9
Brightness Differences Between VAS and HIRS

VAS		HIRS		$\langle T^* (\text{HIRS est.}) - T^* (\text{VAS obs.}) \rangle$					
				GOES-4 vs. NOAA-6		GOES-5 vs. NOAA-7		GOES-6 vs. NOAA-8	
Ch. No.	ν cm^{-1}	Ch. No.	ν cm^{-1}	Mean (K)	Dev. (\pm K)	Mean (K)	Dev. (\pm K)	Mean (K)	Dev. (\pm K)
1	679	2	679	0.94	1.38	0.78	0.80	-1.56	1.08
2	691	3	691	0.82	1.01	-0.43	0.47	-0.30	0.32
3	702	4	704	1.65	0.77	-0.20	0.21	0.14	0.51
4	714	5	716	1.28	0.40	-1.26	0.43	0.71	0.46
5	750	7	748	-1.03	0.45	-0.88	0.52	-2.80	0.49
6	2210	14	2212	-0.33	0.60	-2.52	0.55	-1.93	0.53
7	790	10	1217	-5.61	0.61	-2.97	1.07	-3.45	1.18
8	895	8	900	-3.61	0.92	0.76	0.99	-0.89	1.02
9	1377	11	1363	-1.21	1.29	-5.99	1.88	-2.73	0.99
10	1487	12	1484	0.12	0.99	-5.51	1.50	-0.78	0.99
11	2250	15	2240	0.95	1.39	na	na	na	na
12	2535	18	2511	-0.52	1.84	-2.89	1.07	-1.82	1.99

1981) with respect to NOAA-6 (1400 GMT on 19 January 1981), for 22 locations; for GOES-5 (1348 GMT on 10 November 1982) with respect to NOAA-7 (0936 GMT on 10 November 1982), for 23 locations; and for GOES-6 (1403 GMT on 15 December 1983) with respect to NOAA-8 (1331 GMT on 15 December 1983), for 28 locations. The mean and RMS deviation from the mean differences are listed in Table 4-9 for these two radiometer-to-radiometer comparisons. VAS band 11 data were not available from GOES-5 and GOES-6 for this case.

The agreement between these VAS and HIRS observations is surprisingly good for the CO₂ channels. The temperature calibrations of the respective instruments are accurate to only ± 1 K, which is approximately the agreement between the temperature sounding channels. The surface viewing bands 7, 8, and 12 are very sensitive to good navigation and time coincidence. The water vapor bands 9 and 10 are sensitive to the constancy of the water vapor concentration in each satellite's field-of-view. With 3-hr time separations, large differences are likely. Therefore, the results for these bands are inconclusive. In previous studies of GOES-4 (Menzel *et al.*, 1981; Chesters *et al.*, 1981), and from other data, the 15- μm bands (VAS channels 2, 3, and 4) were

found to exhibit a consistent negative bias reaching 2 to 3 K, with respect to both HIRS predictions and radiation transfer calculations at clear radiosonde sites. Consequently, sounding algorithms must be bias-resistant in order to derive soundings with the desired absolute accuracy from VAS radiances.

4.6 COMPARISON OF VAS WITH RADIOSONDES

The VAS radiances were also compared to radiative transfer calculations of VAS radiances using radiosonde data for several hundred cloud free fields-of-view. Table 4-10 shows the comparison. Data for the window bands are not presented because independent surface skin temperature analyses were not available. Data for the water vapor sensitive bands 9 and 10 are not presented because these determinations are less reliable than the carbon dioxide sensitive bands, since the vertical resolution of the VAS water vapor information is relatively poor. Also, band 11 data were not available for the GOES-5 and GOES-6 comparisons. As in the comparison with NOAA-6, the VAS radiances of GOES-4 (brightness temperatures) for bands 2-4 are consistently lower than the corresponding values from radiosonde analyses. The VAS calibration algorithm appears to be producing

Table 4-10
VAS Radiances (Brightness Temperatures)
Compared to Radiances (Brightness Temperatures)
Determined from LFM Analysis of Radiosonde Data

Band	$B^{-1}(R_{LFM}) - B^{-1}(R_V)$					
	GOES-4 Winter '81		GOES-5 November '83		GOES-6 January '84	
	Mean (°C)	Dev (°C)	Mean (°C)	Dev (°C)	Mean (°C)	Dev (°C)
1	1.3	4.6	2.0	0.6	1.1	0.6
2	3.2	3.1	1.4	0.6	1.7	0.4
3	2.8	1.6	0.6	0.6	0.4	0.5
4	1.7	1.4	-5	0.6	—	0.6
5	0.3	0.8	-8	0.8	-1.0	0.9
6	1.1	0.7	-2.2	0.6	-.5	0.7
7	—	—	—	—	—	—
8	—	—	—	—	—	—
9	—	—	—	—	—	—
10	—	—	—	—	—	—
11	2.1	2.5	—	—	—	—
12	—	—	—	—	—	—

values that are 2-3°C below the radiosonde values for these bands. The relative errors for GOES-5 and GOES-6 are typically less than 1°C for the CO₂ bands (this is well within the expected accuracy of the comparison). The relative errors for GOES-4 are somewhat larger (especially for the noisy bands 1 and 2).

4.7 TRUNCATION ERRORS

Table 4-11 lists the VAS radiance truncation errors. Truncation occurs when radiometric measurements are transmitted from GOES as 10-bit integers. Consequently, radiances are observed in distinctly quantized steps. The observed half-truncation values are compared to the single-sample noise and the SFOV requirements. Truncation errors have decreased during the 2 years between measurements due to improved data processing techniques. The biases from truncation errors are not significant for sounding.

4.8 ZERO-POINT CALIBRATION ERROR

Table 4-12 lists the observed zero-point radiances for outer space from all three VAS instruments. The average value of 200 samples near the east and west ends of a scanline were computed. The lower value is listed. There are no systematic trends in the sign of the zero-point errors. Their magnitudes are a fraction of the single-sample noise. The low end of the calibration curve is well determined.

4.9 DROOP ALONG A VAS SCANLINE

Table 4-13 lists the difference between the average radiance values of outer space to the west and east of the Earth. This procedure tests for possible "droop" in the electronic bias during a scan. Systematically, positive values indicate a decrease in the bias during the scan. The observed values for all three VAS instruments are

Table 4-11
Radiance (erg/etc.) Errors Due to Truncation

VAS Ch. No.	Specified Single-Sample Noise	Half-Truncation Errors			Specified SFOV Accuracy
		GOES-4 1981	GOES-5 1982	GOES-6 1983	
1	4.9	0.50	0.25	0.25	0.25
2	2.0	0.50	0.25	0.25	0.25
3	1.8	0.50	0.13	0.25	0.25
4	1.4	0.50	0.25	0.13	0.25
5	1.4	0.25	0.50	0.25	0.25
6	0.057	0.008	0.004	0.008	0.004
7	1.4	0.25	0.25	0.25	0.25
8	0.16	0.25	0.25	0.13	0.25
9	1.3	0.063	0.063	0.063	0.15
10	0.33	0.063	0.032	0.032	0.10
11	0.066	0.008	na	0.002	0.004
12	0.020	0.002	0.002	0.002	0.004

Table 4-12
VAS Zero-Point Errors for Outer Space

VAS Ch. No.	Specified Single-Sample Noise	<Outer Space>		
		GOES-4 18 Feb 81	GOES-5 4 Aug 81	GOES-6 24 May 83
Large detector zero-point (erg/etc.)				
1	4.9	+0.6	+0.8	-0.3
2	2.0	+0.7	+0.5	-0.5
3	1.8	-0.1	-0.5	+0.4
4	1.4	-0.0	-0.5	+0.6
5	1.4	-0.2	-0.6	+0.6
6	0.057	+0.006	+0.008	+0.002
7	1.4	-0.2	-0.4	+0.2
8	0.16	-0.3	+0.0	+0.0
9	1.3	+0.1	-0.1	+0.1
10	0.33	+0.1	-0.0	+0.1
11	0.066	+0.003	+0.009	+0.010
12	0.020	-0.002	+0.002	-0.001
Small detector zero-point (erg/etc.)				
3	3.6	na	+0.5	+1.0
4	2.8	na	+1.9	-1.4
5	2.8	na	-1.2	+0.7
7	2.8	na	-0.4	-0.5
8	0.32	-0.5	+0.9	-0.1
9	2.6	na	+0.3	+0.3
10	0.66	na	-0.2	+0.1

Table 4-13
Radiance Droop Along a VAS Scanline

VAS Ch. No.	Specified Single-Sample Noise	<West space> - <East space>		
		GOES-4 18 Feb 81	GOES-5 4 Aug 81	GOES-6 24 May 83
Large detector droop (erg/etc.)				
1	4.9	-0.5	-0.8	-0.9
2	2.0	+1.0	+0.7	+1.1
3	1.8	+1.1	+0.7	+0.8
4	1.4	+0.4	-0.6	+1.6
5	1.4	+0.2	-0.4	+1.3
6	0.057	-0.006	+0.022	+0.004
7	1.4	-0.4	+0.3	+0.6
8	0.16	-0.2	-0.1	+0.1
9	1.3	-0.1	-0.2	+0.5
10	0.33	+0.0	-0.0	-0.3
11	0.066	+0.000	+0.018	-0.018
12	0.020	-0.002	+0.002	-0.002
Small detector droop (erg/etc.)				
3	3.6	na	-0.9	-1.0
4	2.8	na	+1.1	+0.8
5	2.8	na	-0.8	+1.3
7	2.8	na	-1.3	+0.5
8	0.32	-0.5	-0.2	+0.0
9	2.6	na	+0.5	-0.5
10	0.66	na	+0.1	-0.0

much smaller than the single-sample noise and have random sign. The instrument maker has done an excellent job of keeping the droop below the level of detectability.

4.10 SPIN-TO-SPIN REPRODUCIBILITY

Table 4-14 lists the observed variability among VAS scanlines. The spin-to-spin variance was calculated from data that scanned the same line across the Earth nine times in each channel. The mean radiance for 1000 central samples was taken from each spin. The standard deviation among these nine well-determined mean values is listed. This number measures the relative calibration error among lines prior to dwell averaging. There are no design specifications for relative calibration stability from spin-to-spin. The "relative" accuracy specifications in Table 4-3 (i.e., ± 0.5 K in T^* for all VAS channels) are quoted without a specific test procedure. If we adopt

the variance in the mean brightness of a scanline as the test procedure, then Table 4-14 indicates that the relative calibration errors exceed the specification for the noisy narrowband channels (1, 2, 9, and 11). The observed spin-to-spin relative calibration errors are approximately one half of the observed single-sample noise. Temporal and spatial averaging is *necessary* to reduce the effect of the line-by-line calibration errors because these are average errors for the entire scanline. The relative calibration errors for such temporally and spatially averaged SFOV's meet the prelaunch requirements.

In sounding applications, VAS channels 1, 2, 9, and 11 are normally given little or no time in the spin budgets. No systematic study has been performed to determine the information content of these channels under conditions where the upper troposphere is meteorologically interesting. For instance, sudden stratospheric warming

Table 4-14
Relative Spin-to-Spin Reproducibility of a Scanline

VAS Ch. No.	Specified Relative Calibration	Variability among dwelled scanlines		
		GOES-4 18 Feb 81	GOES-5 4 Aug 81	GOES-6 24 May 83
Large detector deviation of the mean (erg/etc.)				
1	0.4	1.2	1.7	1.3
2	0.4	1.5	0.4	0.8
3	0.5	0.5	0.5	0.7
4	0.6	0.5	0.4	0.7
5	0.7	0.5	0.3	0.8
6	0.025	0.005	0.018	0.003
7	0.8	0.4	0.2	0.2
8	0.8	0.1	0.3	0.1
9	0.2	0.5	0.2	0.5
10	0.1	0.1	0.0	0.1
11	0.006	0.006	0.006	0.004
12	0.018	0.001	0.005	0.003
Small detector deviation of the mean (erg/etc.)				
3	0.5	na	2.8	0.6
4	0.6	na	0.9	0.5
5	0.7	na	0.5	0.4
7	0.8	na	0.6	0.5
8	0.8	na	0.1	0.1
9	0.2	na	0.6	0.3
10	0.1	na	0.2	0.1

and tropopause folding are potentially observable meso-scale phenomena which occur in the upper atmosphere, but scientific case studies have not yet been made. Likewise, shortwave channels have not been systematically tested for their intended function as cloud discriminators. On the other hand, the longwave sounding channels *have* been used successfully for cloud height and motion assignment (Menzel *et al.*, 1983a) and for cloud type classification (Szejwach, 1982).

In conclusion, the relative line-to-line calibration errors make it mandatory that spatial and temporal radiance averaging be employed to attain the specified sounding accuracy. Full-resolution FOV's (15 by 15 km² at nadir) have proven useful for imaging, and for those soundings that can be derived from a few of the brighter channels that probe the lower atmosphere. The small de-

tectors should prove useful for detecting cloud contaminated FOV's before spatial averaging.

4.11 "SCATTERED LIGHT" AND RESAMPLING ERRORS

Figure 4-3 plots the infrared samples from nine repeated radiance scans of the same line with the same filter and detectors for 100 samples containing the east limb of the Earth. These data are for the VAS 11- μ m channel on GOES-5, in August 1981. Figure 4-3 displays two radiometric errors which would hinder very high resolution (15 by 15 km² SFOV) sounding with VAS, "scattered light" and east-west misregistration.

"Scattered light" could be due to optical surface scattering, diffraction, electrical filter characteristics, or detector memory. Prelaunch measurements of the effec-

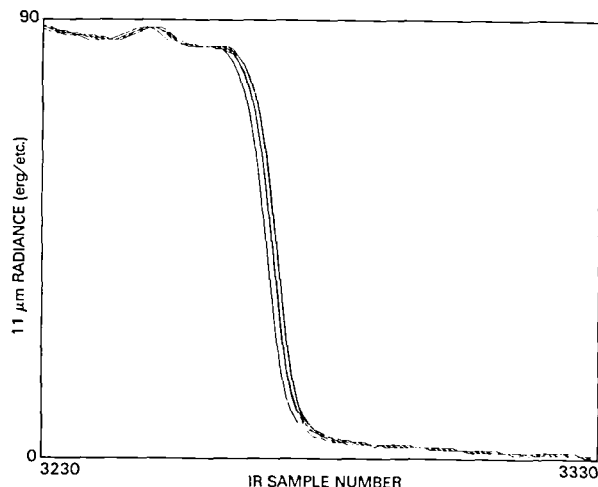


Figure 4-3. Repeated scans of the Earth's limb at 11 μm

tive field-of-view indicate that 99 percent of the light should be received from within a radius of approximately 15 samples. The higher levels observed in Figure 4-3 trailing the east limb appear to be due to an unexpectedly long time constant. In any case, Figure 4-3 implies that "scattered light" contributes a few percent smoothing to the contrast within a scene. Prelaunch studies indicate that for sounding applications in 30 by 30 km^2 SFOV's (where roughly 10 percent of the total energy originates from outside the indicated SFOV), the anticipated diffraction effects are not significant (Menzel, 1980).

The limb of the Earth in Figure 4-3 is distinctly resolved for each spin, but the east-west location varies by ± 1 sample. This error is not a fixed offset for the entire line, but occurs irregularly within each line, for lengths ranging from 10 to 50 samples. This jitter can reduce the accuracy of dwell averaging, and of very high resolution channel-to-channel comparisons, such as for the "split window" calculations of low-level moisture (Chesters *et al.*, 1983). The resampling in the S/DB hardware was improved in order to remove these slightly misregistered segments after September 1983.

4.12 GROUND SYSTEM OPERATIONS

Occasionally during the VAS Demonstration, the ground system had operational difficulties that affected the quality of the radiances, and otherwise prevented data transfer:

- Shortly after the launch of GOES-4, the S/DB computer developed data transfer problems,

which were traced to corroding leads on some of the chips. Subsequently, this problem was fixed.

- An entire scanline would be "dropped" in the VAS data chain due to data transmission errors, causing dwell averaging software to incorrectly mix channels together. These errors were detected after data reception had been completed, and images or data headers were examined. Problems such as these are now rare.
- Large east-west shifts of an entire scanline (by tens of samples) are sometimes observed in VAS images. These conditions are difficult to detect in dwell soundings because sounding data are temporally averaged and then used without visual assurance of every channel. These synchronization errors occur in short bursts (approximately once per day).
- Satellite-to-Earth coordinate transformations were initially in error by 50 to 100 km. After corrections were made to the navigation-determination software, VAS Earth-location errors met the requirements for absolute accuracy (± 10 km) when landmark corrections were processed on a daily basis.
- GOES' geosynchronous orbit causes the satellite to pass directly between the Sun and the Earth at noontime during equinox. VAS data reception is not practical near local noon during March, April, September, and October.

These problems were rare enough to provide the VAS Demonstration with enough experimental data to meet its objectives. Data reliability was very good during concentrated efforts, and exceeded 97 percent for the AVE/VAS Special Network Experiment (Greaves *et al.*, 1982). The VAS instruments are sound enough for operational use, but the ground system will require more resources in order to develop an equally reliable level of performance.

VAS data acquisition was not always permitted during the VAS Demonstration because VISSR mode operations precluded the VAS mode. NOAA has used GOES-5 as GOES-EAST and GOES-4 and -6 as GOES-WEST, especially during severe storms. The AVE/VAS experiment was in operation on weekends only, in order to minimize the impact upon the weekday VISSR schedule. During the VAS Demonstration, a Transparent (to the VISSR users) VAS Mode (TVM) was devised. The addi-

tional independent detectors on the VAS instrument can provide simultaneous VISSR (visible and $11\ \mu\text{m}$), and VAS (two additional infrared channels) data streams during the operational almost full disk imaging (first 15 minutes of each half hour). In the nonimaging intervals (10 minutes of each half hour), some VAS dwell sounding can also be accomplished. The remaining 5 minutes of each half hour is used for scan minor retrace. The TVM innovation alleviated the demand for daily VAS data for research and development.

4.13 SUMMARY AND DISCUSSION

The postlaunch performance of the VAS radiometer meets its prelaunch design specifications, particularly those related to image formation and noise reduction. GOES-5, currently operational as GOES-EAST, carried the best instrument. Single-sample noise is lower than expected, especially for the small longwave and large shortwave detectors. Detector-to-detector offsets are correctable to within the resolution limits of the instrument. Truncation, zero-point, and droop errors are insignificant. Absolute calibration errors, estimated from HIRS and from radiation transfer calculations, indicate moderate, but stable biases. Relative calibration errors from scanline to scanline are noticeable, but meet sounding requirements for temporally (50 to 70 spins

at 100 RPM) and spatially (30 by 30 km^2) averaged sounding fields-of-view. "Scattered light" and resampling errors slightly reduce contrast and channel-to-channel registration for very high resolution work. The complex ground system, which also influences the net radiometric quality of VAS data, was extensively tested and improved during the VAS Demonstration. The competing demands (NESDIS operational versus research) for both VISSR and VAS mode data were alleviated through the use of a Transparent VAS Mode (TVM), which simultaneously delivers both VISSR operational data and VAS research data.

The VAS instrument is a potentially useful radiometer for mesoscale sounding operations. Image quality is very good. Soundings derived from quality controlled data meet prelaunch requirements when calculated with noise-resistant and bias-resistant algorithms. The information from the mid-level and low-level channels is better than expected. Good results have even been obtained at 15- by 15- km^2 resolution. Useful work seems possible at 8- by 8- km^2 resolution. The information content of the faint, noisy upper air channels remains untested. While the distant geosynchronous station of the VAS instrument makes accurate radiometry difficult, the frequent and relatively stable measurements that VAS provides at fixed angle and resolution, permit mesoscale measurements which were previously unavailable.

VALIDATION AND STATISTICAL ANALYSIS OF VAS SOUNDINGS

The purpose of this section is to present the results of validation efforts, based on statistical evaluations of various parameters derived from VAS radiances. The section is divided into three parts: a report from GSFC on statistical comparisons based on radiosonde data from two summer cases; a report from UW-NESDIS Cooperative Institute for Meteorological Satellite Studies (CIMSS) on statistical comparisons based on radiosonde, dropsonde, and aircraft observations; and a three-part report from MSFC, GSFC, and CIMSS on a statistical comparison based on radiosonde data collected during a special network "ground-truth" experiment, funded by the Severe Storms Research Program at NASA Headquarters.

5.1 STATISTICAL VALIDATION OF VAS RETRIEVALS AT GSFC

D. Chesters

L. W. Uccellini

Goddard Laboratory for Atmospheric Sciences

Goddard Space Flight Center

National Aeronautics and Space Administration

Greenbelt, Maryland

During the VAS Demonstration, sounding studies at NASA/GSFC were concentrated on preconvective environments over the United States, where "ground truth" data are routinely available from the operational radiosonde network.

This statistical validation of the absolute and relative accuracy of soundings was performed using the radiances from GOES-5 during the postlaunch checkout on 13 July 1981 and 20 July 1981. Five frames of VAS dwell sounding data were taken over the United States at 1200, 1500, 1800, 2100, and 2300 Greenwich Mean Time (GMT) for each day with GOES-5 located at 85°W. These five frames provided a time-series of uniformly analyzed VAS soundings. The 1200 and 2300 GMT frames provided an opportunity for statistical comparisons with the operational radiosonde network. Objective verification is carried out in two ways. The absolute accuracy is measured by the mean and RMS profile

errors (VAS minus radiosonde) at clear air sites; and the relative accuracy is measured by the space-time correlations within the analyzed VAS fields. In addition, the relative impact on sounding accuracy by ancillary surface data or by satellite data is assessed by making comparisons of VAS retrievals with and without key "channels" of information.

5.1.1 The VAS Retrieval Method

There are fundamental problems in resolving any optically thin temperature and moisture structures in the lower troposphere with a satellite-based passive sounder, even with the radiometrically superior instruments and retrieval algorithms available from polar orbiters (Phillips *et al.*, 1979; Hillger and Vonder Haar, 1981; Schlatter, 1981). A VAS simulation study showed that VAS radiance data would have difficulty resolving gradients and extremes of temperature and moisture in the lower troposphere, and would be sensitive to radiometric errors, surface brightness variations, and unresolved clouds (Chesters *et al.*, 1982). Actual experience with the first VAS data indicated that any VAS sounding algorithm must be noise and bias-resistant (Menzel *et al.*, 1981; Chesters *et al.*, 1981).

Regression retrievals are being used for satellite soundings from the polar-orbiting instruments because the statistical approach is computationally simple, and error-resistant (Smith and Woolf, 1976). The notion of applying statistical retrievals that use the satellite radiances for interpolation between radiosonde sites predates the launch of VAS (Fritz, 1977), as does the notion of using conventional surface data to supplement the satellite retrievals in the lower troposphere (Hayden, 1980). The GSFC VAS retrievals are computed with a regression scheme that incorporates signal-to-noise preconditioning, and conventional surface data as ancillary information for the lower troposphere (Lee *et al.*, 1983). Quality control procedures include the person-in-the-loop approach for cloud screening using the 1 km visible imagery (Smith *et al.*, 1978).

Statistical training for the GSFC regression scheme is provided by clear-air radiosonde data, T(P), that are embedded within VAS radiance fields R(ν) over the

region of interest. Since there are significant correlations between surface data and the state of the lower troposphere (Stayert and Darkow, 1973), surface temperature and dewpoint reports Tsfc and Dsfc, are grouped with the radiances as statistical predictors of the radiosonde data. An estimate of the radiometric signal-to-noise $g^2 = \langle DR^2 \rangle / \langle \epsilon_R^2 \rangle$, and the observed variations in the predictors $DR(\nu) = R(\nu) - \langle R(\nu) \rangle$, are combined with the corresponding atmospheric variations $DT(P) = T(P) - \langle T(P) \rangle$, in order to calculate a regression matrix $M(P, \nu)$. The regression matrix from this training set is then used to calculate meteorological profiles $T'(P)$, from satellite radiances $R'(\nu)$, that have been observed at other points in space and time:

$$T'(P) = DT'(P) + \langle T(P) \rangle,$$

$$DT'(P) = \sum_{\nu} M(P, \nu) \circ DR'(\nu), \quad (1)$$

$$M(P, \nu) = \sum_{\nu'} \langle DT(P) DR(\nu') \rangle \circ [\langle DR(\nu') DR(\nu) \rangle (1 + g^{-2} \delta_{\nu'\nu})]^{-1}.$$

This preconditioned method is resistant to many of the problems which beset least-squares solutions when they are applied to a small sample of noisy training data (Marquardt and Snee, 1975). A signal-to-noise ratio of $g = 10/1$ is normally used for VAS soundings. Artificially small values of g can be applied to some predictors in order to determine the impact of suppressing individual VAS channels.

5.1.2 Measuring the Accuracy of VAS Soundings

Absolute errors are measured by comparing cloud-free VAS retrievals to the collocated radiosonde and surface values of temperature, dewpoint, thickness, precipitable water and equivalent potential temperature. Absolute accuracy is measured by the bias, standard deviation, RMS errors, and the "recovery rate" (r), of the standard deviation where:

$$\text{bias} = \langle T^f - T \rangle,$$

$$\text{RMS}^2 = \langle [T^f - T]^2 \rangle = \text{bias}^2 + \text{stdev}^2, \quad (2)$$

$$r = 1 - \text{stdev}^2 / \langle [T - \langle T \rangle]^2 \rangle.$$

RMS errors of less than $\pm 2^\circ\text{C}$ are required for useful soundings. A recovery rate of $r = 1$ indicates a perfect retrieval (except for a possible bias). A value of $r = 0$ indicates no improvement. Values of $r < 0$ indicate bad

retrievals (such as when the natural variance is too small to be detected or when there are too many cloud-contaminated fields-of-view). A ± 25 percent absolute error is the nominal target for VAS moisture retrievals.

Relative errors are assessed by the space and time continuity within the retrieved VAS fields. Spatial smoothness is measured with an RMS length scale k^{-1} computed from the variances in the horizontal gradients dT'/dx . Temporal continuity is measured with the correlation $C(t1, t2)$, between the variations from the mean $DT' = T' - \langle T' \rangle$, at corresponding locations within fields retrieved at times $t1$ and $t2$:

$$k^2 = \langle [dT'/dx - \langle dT'/dx \rangle]^2 \rangle / \langle [T' - \langle T' \rangle]^2 \rangle, \quad (3)$$

$$C(t1, t2) = \langle DT'(t1)DT'(t2) \rangle / [\langle DT'(t1)^2 \rangle \langle DT'(t2)^2 \rangle]^{1/2}.$$

The ensemble averages $\langle . . \rangle$ for measuring relative space-time coherence are taken horizontally over mesoscale fields of objectively analyzed VAS retrievals. Relatively large values for the RMS spatial gradients ($k^{-1} > 200$ km) indicate realistically smooth mesoscale retrievals, while small values ($k^{-1} < 100$ km) indicate ill conditioned retrievals, or unresolved clouds. Large values for the temporal correlation ($C > 90$ percent over 3 hr intervals) indicate a stable retrieval scheme. Low values ($C < 80$ percent) indicate large fluctuations which result from a detrimental impact of diurnal effects, or unresolved clouds.

5.1.3 Data Preparation

Table 5-1 lists the VAS, surface, and radiosonde data utilized for the two preconvective cases. On both days, there were similar masses of hot and humid air covering the eastern and central United States. Table 5-2 enumerates subsets of the 132 collocated clear-air sites which are used to carry out independent statistical training and testing. These two preconvective cases have been extensively analyzed (Lee *et al.*, 1983; Petersen *et al.*, 1982; Mostek *et al.*, 1984). Highlights from the data base preparation and coefficient calculations are as follows:

a. Temporal collocation is defined as ± 1 hr. Spatial collocation is defined as $\pm 0.5^\circ$ of latitude or longitude in order to avoid clouds. Coastlines present a problem for regression training, because the low-level environment

Table 5-1
Data Sources for the VAS Preconvective Case Studies

Date (July 1981)	13												14	20		21
Time (GMT)	12*	13	14	15*	16	17	18*	19	20	21*	22	23*	00	12*	23*	00
VAS	US	-	-	US	-	-	US	-	-	US	-	US	-	US	NC	-
SFC	565	-	-	546	-	577	-	-	-	574	-	-	562	564	556	-
RAOB	63	-	-	-	-	-	-	-	-	-	-	-	59	50	-	47

Times marked with an (*) are the nominal event labels. US denotes VAS dwell-sounding data covering the United States east of the Rockies, while the NC indicates a smaller coverage of the most northern and central United States. The number of SFC and RAOB reports are available within the 20°-55°N and 70°-110°W area.

Table 5-2
Subsets of Collocated VAS/Surface/Radiosonde Data

Date	Area	Subgroup	Dawn 1200 GMT	Dusk 2300 GMT	Day
13 July	Continental		41	40	81
		Training	28	28	56
		Testing	13	12	25
13 July	Regional		26	25	51
20 July	Regional		26	26	52

of the ocean is unlike that on land. Therefore, the "Regional" subset is drawn from the "Continental" selection with the coastal stations removed.

b. The lowest level reported from a radiosonde over the high plains is assigned to "1000 mb."

c. Often there are significant discrepancies between surface data and collocated radiosonde reports from the lowest level. This is an unexpected limitation to the usefulness of ancillary surface data as a statistical predictor of low-level soundings.

d. Composite parameters (e.g., thickness) are more accurately retrieved by direct regression from the VAS/surface predictors, rather than by computation from retrieved temperature and dewpoint profiles.

e. The dominant regression coefficients correctly imitate the radiative properties of the VAS channels. The surface temperature and dewpoint, dominate the VAS channels as predictors of the lowest levels.

f. Reflected sunlight in the 3.9- μ m window channel could be a serious source of error for VAS soundings. This channel has little impact upon the July 13 soundings, but was suppressed in the July 20 soundings, in order to improve midday coherence. This increased sensitivity may be due to the presence of unresolved cirrus clouds, which were more prevalent on July 20.

g. No VAS channel is particularly sensitive to water vapor between 500 and 800 mb.

5.1.4 Absolute Errors

Table 5-3 lists the absolute accuracy measurements of VAS-only, VAS + SFC, and SFC-only profile soundings for the independent Continental training and test sets on July 13. Temperature variations in the middle troposphere are too small ($< \pm 2^\circ\text{C}$) to be retrieved in any case. Temperature retrievals in the lower troposphere are fairly good, and meet prelaunch specifications ($< \pm 2^\circ\text{C}$) below 900 mb when surface data is included as a predictor. Dewpoint retrievals fail above 700 mb, where no VAS channel is moisture sensitive, and where radiosonde dewpoint values are not as numerous, and are too variable to be useful for validating VAS soundings. Ancillary surface data has a significant impact below 900 mb, especially on dewpoint retrievals. Bias errors in both temperature and moisture are small for retrievals that were trained and tested on the same environment.

Table 5-4 lists absolute accuracy measurements for the Regional subsets trained on July 20 and tested on July 13. Bias errors are a little larger between the different days, but the pattern of sounding errors is similar to the Continental results in Table 5-3. The similarity of these

results in two independent tests demonstrates the validity of the VAS + SFC sounding algorithm for midsummer preconvective conditions.

RMS error profile statistics are shown in Figure 5-1. Standard deviations in the radiosonde data indicate that most of the variance to be retrieved from midsummer preconvective environments occurs in the lowest layers of the troposphere, where the ancillary data provides the greatest impact.

Figure 5-2 shows bar graphs of the RMS errors in low-level temperature, dewpoint, equivalent potential temperature, and shows thickness and total precipitable water in two directly retrieved bulk parameters. These indicators of low-level stability are best retrieved by the VAS + SFC algorithms, with satellite and conventional data contributing useful, independent information about the lowest layers.

5.1.5 Relative Errors

Figure 5-3 shows a time series of five Midwestern meso-scale dewpoint fields, analyzed at 920 mb from VAS-

Table 5-3
Statistical Errors in VAS Profile Retrievals Using Independent Data on July 13, 1981

Press. Level (mb)	RAOB Ground Truth				(VAS-RAOB) Retrieved Accuracy and Recovery Rate								
	Train (N = 56)		Test (N = 25)		VAS Only			VAS + SFC			SFC Only		
	mean	stdv	mean	stdv	bias	stdv	r	bias	stdv	r	bias	stdv	r
Temperature (K)													
1000	300.1	± 5.1	300.3	± 5.1	.2	± 2.5	.8	.0	± 1.6	.9	.1	± 1.5	.9
920	297.2	3.7	297.4	3.6	.1	2.0	.7	.0	1.9	.7	-.2	2.0	.7
850	292.8	3.0	292.8	3.1	.3	2.2	.5	.3	1.9	.6	.0	2.4	.4
700	282.9	1.7	282.8	1.9	.3	1.4	.5	.3	1.4	.5	.1	1.7	.2
600	275.5	1.6	276.0	1.2	-.0	1.3	-.2	-.0	1.4	-.4	-.4	1.3	-.2
500	266.9	1.8	267.6	1.4	-.4	1.2	.3	-.3	1.3	.1	-.6	1.3	.1
Dewpoint (K)													
1000	293.5	± 4.0	293.1	± 3.9	.3	± 3.0	.4	.5	± 1.9	.8	.5	± 1.8	.8
920	290.3	3.4	290.0	2.7	.1	2.3	.3	.1	2.0	.5	.4	1.9	.5
850	286.5	3.1	286.7	2.4	-.7	2.1	.2	-.7	2.1	.2	-.2	2.1	.2
700	272.5	8.0	271.6	7.6	.4	6.4	.3	.4	7.1	.1	1.1	8.6	-.3

Table 5-4
Statistical Errors in VAS Profile Retrievals Using Independent Data from July 13 and 20, 1981

Press. Level (mb)	13 July Regional Data (N = 51)		13 July Retrieval Errors Using 20 July Matrices									20 July Regional Data (N = 52)	
			VAS Only			VAS + SFC			SFC Only				
	mean	stdv	bias	stdv	r	bias	stdv	r	bias	stdv	r	mean	stdv
Temperature (K)													
1000	300.2 ± 5.6		-0 ± 2.6	.8		-4 ± 1.4	.9		-5 ± 1.2	1.0		300.9 ± 6.2	
920	297.8	4.0	.4	1.7	.8	.5	1.9	.8	-.2	1.9	.8	298.7	5.2
850	293.2	3.4	.7	2.3	.5	.6	2.2	.6	.3	2.6	.4	294.3	4.3
700	283.1	1.8	.5	1.8	.0	.5	1.9	-.1	.3	1.6	.2	283.6	3.1
600	276.0	1.4	-.7	1.4	.0	-.7	1.4	.0	-.8	1.3	.1	275.3	2.5
500	267.5	1.5	-1.4	1.3	.2	-1.4	1.3	.2	-1.4	1.4	.1	266.0	2.6
Dewpoint (K)													
1000	292.6 ± 4.2		-1.0 ± 3.5	.3		-.3 ± 1.6	.9		-.1 ± 1.6	.9		291.7 ± 5.2	
920	289.9	3.6	-.6	2.9	.4	-.3	1.9	.7	.1	1.9	.7	289.3	4.2
850	286.5	3.1	-1.7	2.6	.3	-1.5	2.1	.5	-.7	2.2	.5	285.3	3.9
700	271.0	9.4	-1.0	9.4	.0	-.6	9.8	-.1	-1.1	9.2	-.0	270.1	7.2

only and VAS + SFC Regional retrievals on July 13. Soundings with either of the training sets, detect the principal moisture features: an east-west gradient, a dry slot across Missouri; and a moisture maximum in eastern Iowa, where thunderstorms later occurred. The VAS + SFC retrievals provide a superior match at the six radiosonde sites, available in the mesoscale field at 1200 and 2300 GMT. The VAS-only fields appear more chaotic, and less time continuous.

Table 5-5 lists measurements of the relative space and time continuity of the VAS mesoscale dewpoint soundings in Figure 5-3. The RMS length scale k^{-1} , is consistently larger for the VAS + SFC retrievals (173 km vs. 112 km). The frame-to-frame correlations $C(t, t + 3 \text{ hr})$, are significantly larger (91 percent vs. 75 percent). Most of the improvement in the continuity of these 920-mb dewpoint retrievals is traceable to the conventional surface dewpoint reports, as a predictor of the boundary layer. On the other hand, the correct location and orientation of mesoscale features are traceable to the VAS radiances, especially to the 11- and 12- μm "split

window" channels which are designed to sense the moisture content of the lower troposphere (Chesters *et al.*, 1983). Table 5-6 confirms the results in Table 5-5 for 920-mb dewpoint retrievals performed independently on mesoscale fields from the July 20 data sets. In both cases, VAS + SFC soundings display impressive relative accuracy in both space and time.

5.1.6 Summary of Validation and Statistical Analysis of GSFC Retrievals

The GSFC statistical retrieval algorithm utilizes VAS radiances in order to interpolate the space-time behavior of temperature and moisture fields between the 12-h conventional radiosonde observations. The algorithm is noise and bias-resistant, clouds are carefully avoided by interactive processing, and ancillary surface data are incorporated into the sounding process. Conventional surface reports act as valuable "channels" of mesoscale information about the boundary layer, resolving ambiguities and improving the space-time continuity of VAS soundings in the lower troposphere. VAS + SFC

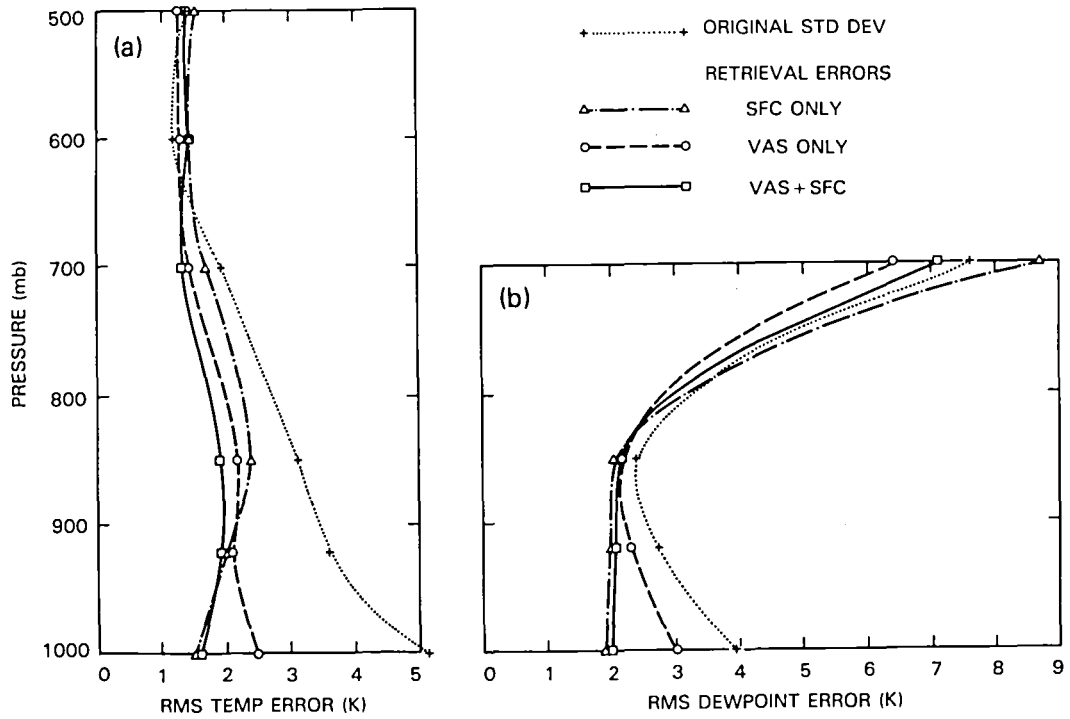


Figure 5-1. Errors in VAS Profile Retrievals for July 13, 1981

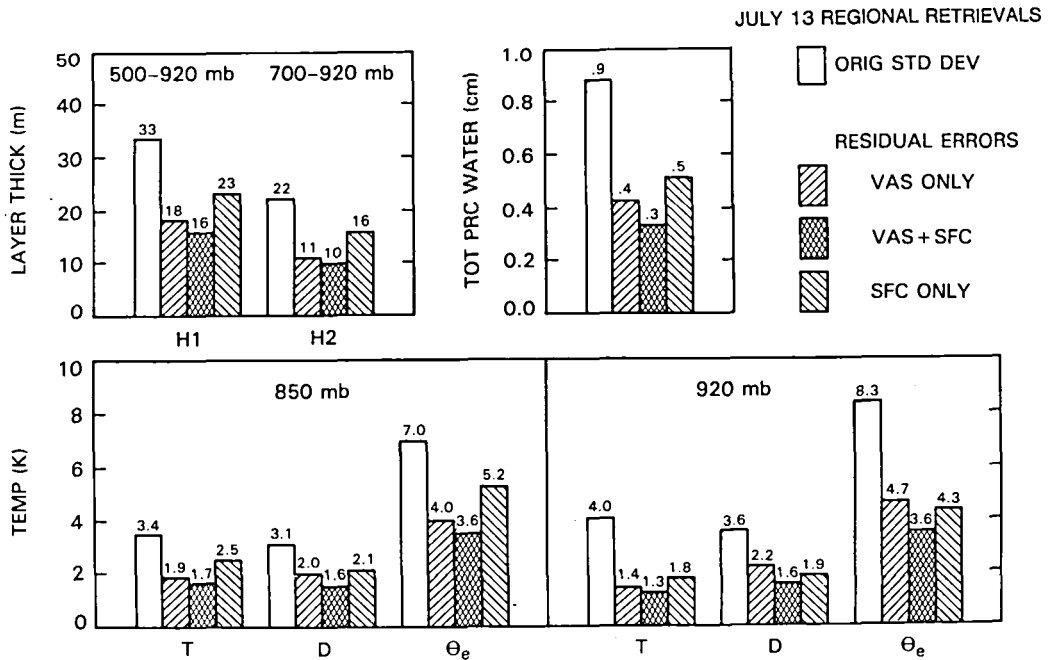


Figure 5-2. Residual errors in VAS Parameter Retrievals, with and without ancillary surface data on July 13, 1981

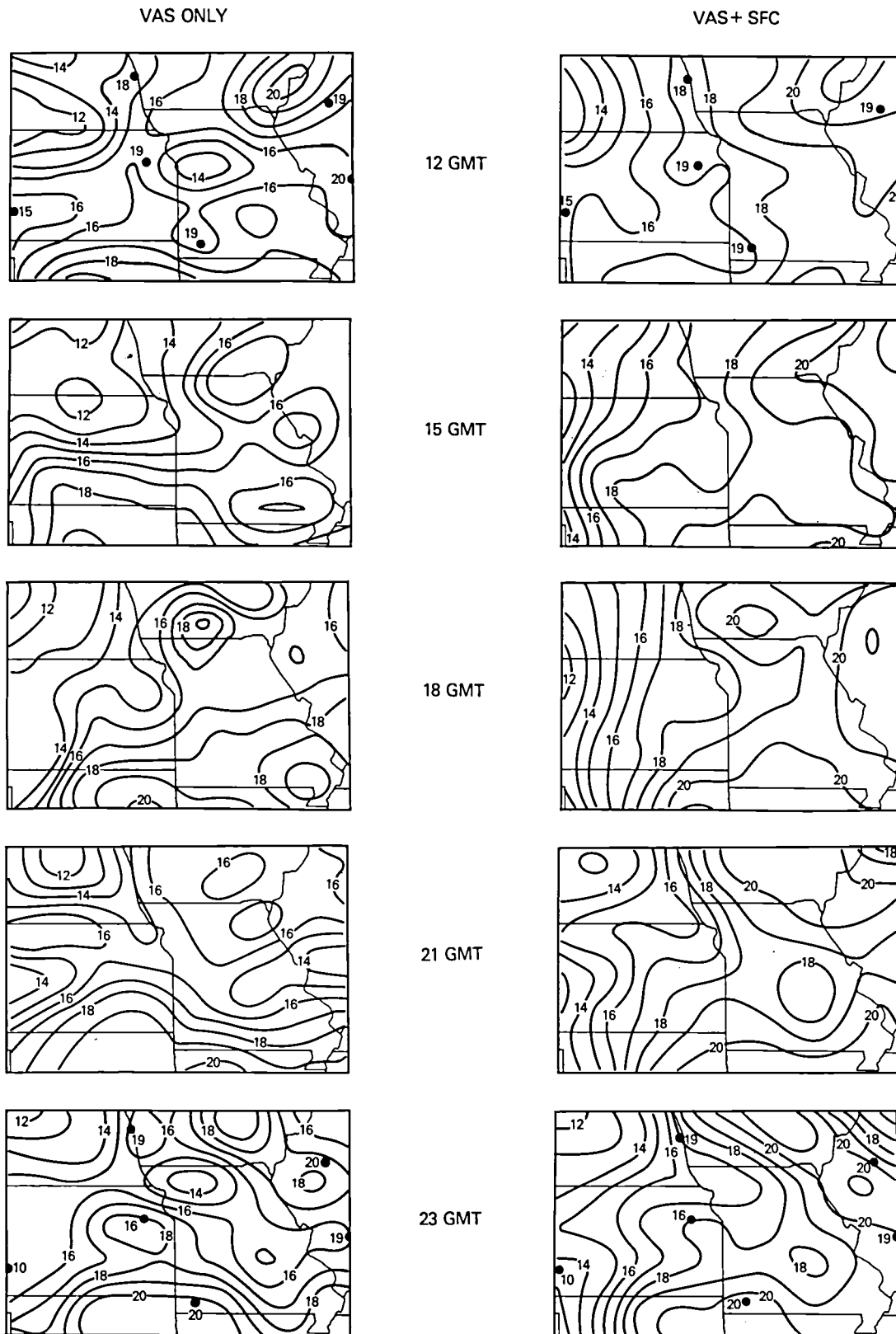


Figure 5-3. Time Series of 920 mb dewpoint fields, retrieved from VAS data on July 13, 1981 with and without ancillary surface data

Table 5-5
Statistical Comparison of the Coherence of VAS Retrieval 920 mb Dewpoint
Fields on July 13, 1981, With and Without Surface Data

Time GMT	Spatial Smoothness					Temporal Continuity		
	Case	Average Dewpoint (°C)	Stdv Dewpoint (°C)	Stdv Gradient (°C/km)	RMS Scale Length (km)	Case	Covar. (°C ²)	Corr. (%)
1200	VAS	16.0	1.76	0.018	99.4			
	VAS + SFC	17.6	1.83	0.010	182.7	VAS	2.7	76
1500	VAS	15.4	2.02	0.016	122.6	VAS + SFC	3.2	87
	VAS + SFC	17.8	2.04	0.011	181.4	VAS	3.3	77
1800	VAS	16.2	2.13	0.016	134.5	VAS + SFC	4.6	92
	VAS + SFC	18.1	2.45	0.012	200.0	VAS	2.7	68
2100	VAS	16.3	1.85	0.018	104.3	VAS + SFC	5.1	91
	VAS + SFC	17.8	2.29	0.014	163.0	VAS	3.0	81
2300	VAS	16.8	1.99	0.017	103.1	VAS + SFC	5.3	94
	VAS + SFC	17.7	2.44	0.017	142.5			

Table 5-6
Statistical Coherence of VAS + SFC Fields of 920 mb
Dewpoint, Independently Retrieved on July 20, 1981

Time GMT	Spatial Smoothness				Temporal Continuity	
	Area Avg. (°C)	Area Stdv (°C)	Gradient Stdv (°C/km)	RMS Scale Lg. (km)	Covar. (°C ²)	Corr. (%)
1200	16.5	1.56	0.0008	194.2	3.14	95
1500	16.6	2.13	0.0008	265.9	4.54	97
1800	16.2	2.20	0.010	230.3	4.81	97
2100	16.4	2.25	0.008	267.3	4.45	96
2300	16.7	2.06	0.0009	240.0		

retrievals are more accurate than either VAS-only or SFC-only retrievals below 700 mb. The lack of VAS sensitivity to water vapor in the middle troposphere limits moisture retrievals between 500 and 850 mb. The shortcomings of radiosonde dewpoint reports above 700 mb make statistical retrievals and verification unreliable above that altitude.

The paucity of clear-air radiosonde sites in the region of interest, and the lack of midday synoptic observations are the two major limitations in applying a regression technique to mesoscale case studies over the United States. Nevertheless, VAS statistical soundings meet prelaunch accuracy requirements for two midsummer preconvective case studies where there was enough clear-air collocated data from the synoptic radiosonde network to carry out independent training and testing. The combination of VAS and surface data provide measurements of low-level stability indicators (temperature, dewpoint, thickness, precipitable water and equivalent potential temperature) with mesoscale resolution (at least 100 km and 3 hr) and useful absolute accuracy ($\pm 2^\circ\text{C}$ temperature and dewpoint in the lower troposphere). The relative accuracy within mesoscale fields of low-level VAS + SFC soundings is impressive in that reproducible horizontal gradients are on the order of 200 km and temporal correlations are in excess of 90 percent over 3 hr intervals throughout the day. It appears that VAS soundings produced in the "case study" mode provide the accuracy required for an analysis of a preconvective environment.

5.2 UW-NESDIS (CIMSS) RESULTS

W. Smith

*Cooperative Institute for Meteorological
Satellite Studies*

*National Environmental Satellite Data
Information Service*

*National Oceanic and Atmospheric Administration
U.S. Department of Commerce*

At the Cooperative Institute for Meteorological Satellite Studies, a physical retrieval algorithm has been designed for operational applications of the VAS data (Smith, 1983). This method has been used since early 1981 in daily quasi-operational processing of VAS data for experimental usage by the National Weather Service. The algorithm is performed in two steps. In the first step, a guess profile is obtained from a numerical forecast model and/or climatological data, and is modified by an established iterative solution of the radiative transfer equa-

tion (Smith, 1970). In the second step, atmospheric structure perturbations of the iterative profile are calculated by a direct analytical solution. The resultant temperature and moisture profiles are a stable solution which satisfies the VAS radiance observations to within the experimental errors of measurement.

The vertical profiles are generated from either a 5 by 5 or a 10 by 10 array of VAS large detector (14 km) data, depending upon the intended application of the results. In example, for mesoscale severe storm forecast applications, the 75-km (5 by 5) resolution soundings are produced, whereas in analyzing the synoptic scale circulation, that steers tropical storms, the 150-km (10 by 10) resolution soundings are generated. A variety of meteorological forecast variables are produced from the soundings, including stability indices, geopotential heights, and gradient winds. The results of several validations studies performed at the CIMMS are provided in this section.

5.2.1 Profile Characteristics

Experience has shown that VAS retrievals successfully capture subsynoptic scale horizontal and temporal variations of vertically integrated temperature and moisture parameters that are used for convective storm forecasting. These include thermodynamic stability, total precipitable water, and thermal wind shear (Smith *et al.*, 1982). Aside from the inability to probe through clouds in the infrared, the major limitation of the VAS sounding is poor vertical resolution, particularly in the upper troposphere. This situation is evident in Figure 5-4 which compares VAS retrievals with coincident radiosonde observations obtained from the Atmospheric Variability Experiment (AVE)-VAS Special Network on 6 March 1982. These retrievals were made using a climatological first guess and 12-hour forecast first guess produced by NMC. The operational procedure is to use the NMC 12-h forecast to construct the initial profiles for the VAS retrievals at the beginning of the processing day (i.e., 1200 GMT), and to use the analyses of prior VAS soundings to construct the initial profiles for subsequent VAS retrievals. The comparisons are shown on a skew-T log-p diagram in order to dramatize the differences between the retrievals and the radiosonde. Since the "climatological profile" differs drastically from the VAS retrieval (Figure 5.4A), one can see by comparing Figures 5.4B and 5.4D that the moisture solutions and the temperature profile solutions below the 500-mb level are quite insensitive to the initial profile accuracy.

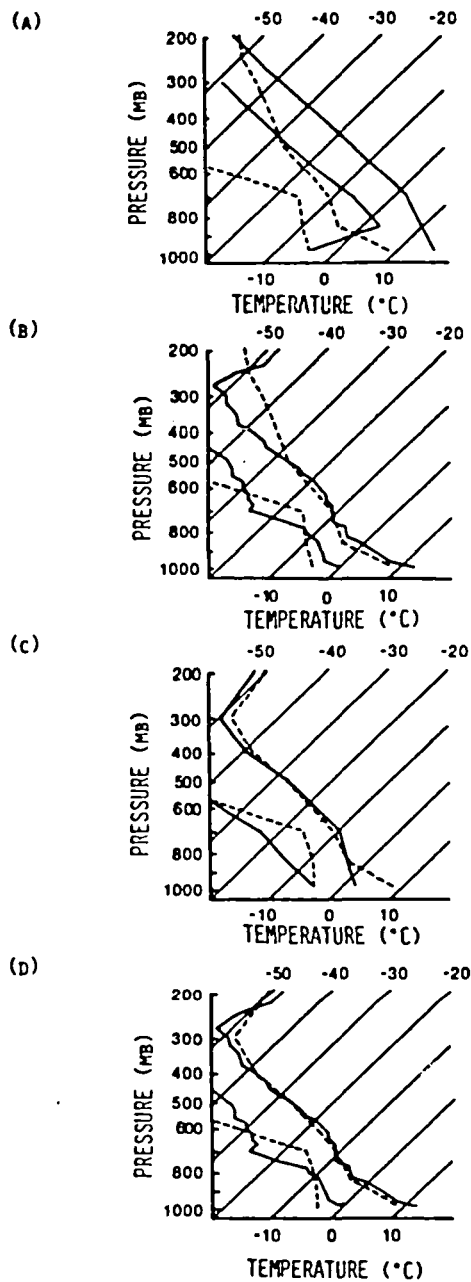


Figure 5-4. Comparison of VAS and AVE-VAS special network radiosonde temperature and dewpoint observations at 2300 GMT 6 March 1982 at Station 72101 (34.5°N, 98°W, in Figure 5.5). (A) and (C) show the VAS retrievals (dashed lines), and first-guess profiles (solid lines) using climatology and an NMC 12 h forecast [(A) and (C)], respectively. (B) and (D) display the VAS retrievals (dashed lines) and the radiosonde (solid lines) for the climatological and NMC forecast first guess situations, respectively.

Above the 500-mb level, the VAS retrieval accuracy becomes highly dependent upon the initial guess, indicating that the profile information content is limited at these upper levels. This result is due to the broad weighting functions at tropopause levels, and because the signal-to-noise ratio of the radiance measurement is low, due to low emitting temperatures.

On the other hand, Figure 5-5 provides a clear demonstration of the capability of the VAS retrievals to delineate small horizontal scale vertically integrated thermal features. These are portrayed by analyses of the geopotential height computed from VAS soundings, spaced at a distance of 30 km, over the special network area of Oklahoma and Texas, shown by the AVE-VAS radiosonde stations in Figure 5-5A. The VAS retrievals were obtained by using a 12-hour forecast first guess, and by using the climatological profile (Figure 5-4A). Although the agreement of the absolute values of the geopotentials with radiosonde observations is better in the case where the NMC first guess is used, both sets of retrievals capture the fine-scale horizontal pattern of geopotential at the three levels shown. The ability of the retrievals to capture the abrupt change of the geopotential pattern between the 500 and 300-mb levels (from a nearly north-south orientation of the contours to one of nearly east-west orientation) is particularly noteworthy. Horizontal gradient accuracies of better than 1°C for the VAS retrieved mean temperature of the layer between the surface and these atmospheric levels are indicated by these results. (Note, a 1°C variation in layer mean temperature corresponds to a geopotential height variation of 10, 20, and 35 m for the 700, 500, and 300-mb levels, respectively.)

Finally, Figure 5-6 presents an example VAS retrieval in the tropics, where the variability of atmospheric temperature and moisture processes show significant structural differences from the NMC forecast used as a first guess. A 50 percent relative humidity value is used to construct the initial guess for the moisture profile. Comparing the VAS profiles with a nearby radiosonde observation, the retrievals are significant improvements to the forecast, particularly for moisture and for temperature below the 500-mb level. The results from the routine application of VAS retrievals to geopotential height analyses for the NOAA Operational VAS Assessment (NOVA) program, indicate that a horizontal consistency is sufficient for defining the circulation at middle and upper-tropospheric levels (Veldon *et al.*, 1984).

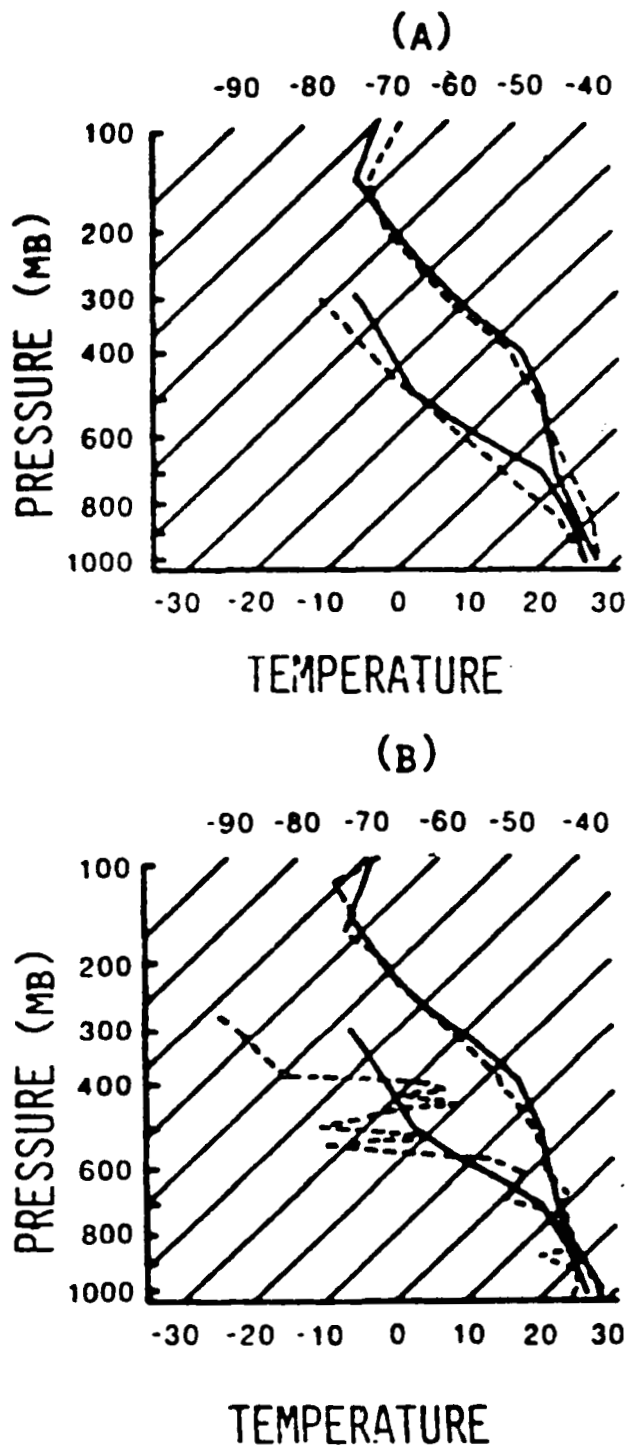


Figure 5-6. Retrieval of atmospheric temperature and dewpoint (solid curves) at Grand Cayman (19°N, 81°W) on 1 September 1982 (1200 GMT). In (A) the dashed curves depict the NMC 12 h forecast profile. In (B) the dashed profile is the Grand Cayman radiosonde observation.

expressed confidence in the temperature and thickness parameters. As expected, the differences are larger for moisture, because the small scale features of the moisture distribution produce discrepancies due to space and time differences between the satellite and radiosonde observations, and because the VAS lower vertical resolution moisture profiles cannot capture highly structured vertical features as well as the radiosonde. The VAS gradient winds averaged about 25 percent slower than radiosonde winds with a mean directional difference of about 30 degrees. Several factors may contribute to these differences, such as ageostrophic motions, and deficient height field gradients due to inadequate analyses across satellite data void areas (cloud regions). These results suggest that gradient winds computed in this manner generally are less useful than cloud motion winds in NHC tropical analyses (when both are available).

5.2.2.2 Comparisons with Dropsondes

A comprehensive meteorological data set, including VAS data, has been constructed from observations of Hurricane Debby from September 13-17, 1982. During this time, a dropsonde experiment was performed by the Atlantic Oceanographic and Meteorological Laboratory-Hurricane Research Division. This experiment provided an opportunity to compare VAS soundings produced in real-time, with Omega dropwindsonde (ODW) observations. Numerical comparisons, similar to the previously noted radiosonde comparisons, were made by NHC, and are shown in Table 5-8. A NOAA Research Facilities Center aircraft flew prescribed tracks throughout the environment of Hurricane Debby on two missions (September 14/15 and September 15/16, 1982). Comparisons were made wherever ODW and VAS soundings were sufficiently close in time and space. The results of the comparisons were quite similar to the radiosonde comparisons, with the temperatures and thicknesses again having the smallest differences. (No VAS gradient winds were generated in real time for September 14/15 so that the comparisons shown are for the September 15/16 case only.)

5.2.2.3 Comparisons of Gradient Winds with Aircraft Observations

Gradient winds represent motion that is parallel to the isobars or geopotential contours, on a constant pressure surface subject to a three way balance between the Coriolis force, the centrifugal force, and the horizontal

Table 5-7
Summary of Comparisons Between VAS and Radiosonde Data
for Bermuda, San Juan, and West Palm Beach
(15 September-18 November 1982)

Parameter	Mean (VAS-RAOB)	Standard Deviation	Range	Number of Cases
T850 mb	1.7°C	1.8°C	-2.6 to 6.8°C	51
T700	0.8	1.5	-2.5 to 5.2	51
T500	0.8	1.4	-1.8 to 5.3	51
T400	1.2	1.5	-1.6 to 4.8	45
T300	0.7	1.8	-2.9 to 7.0	44
T200	-0.1	1.8	-4.4 to 5.4	48
TD850	2.9°C	4.2°C	-10.3 to 13.7°C	51
TD700	7.7	8.0	-15.7 to 27.4	51
TD500	-0.4	8.8	-27.9 to 26.4	51
TD400	-1.3	8.1	-15.8 to 15.8	45
TD300	0.9	8.4	-14.7 to 16.6	44
TD200	-	-	- -	-
Z850	11 m	13 m	-22 to 60 m	51
Z700	18	19	-20 to 66	51
Z500	27	27	-23 to 100	51
Z400	29	28	-20 to 84	45
Z300	37	35	-27 to 109	44
Z200	43	53	-23 to 175	48
Z500-850	16 m	18 m	-13 to 71 m	51
Z400-850	20	21	-14 to 73	45
Z300-850	28	30	-16 to 96	44
Z500-700	9	11	-15 to 34	51
Z400-700	13	16	-13 to 58	45
Z200-400	9	29	-49 to 105	44
850	26°	18°	1 to 73°	30
wind 700	27	24	0 to 101	27
direc- 500	29	24	0 to 90	36
tion 400	30	28	2 to 134	32
300	36	27	2 to 123	38
200	30	21	1 to 85	42
850	-3 ms ⁻¹	4 ms ⁻¹	-23 to 4 ms ⁻¹	46
wind 700	-2	3	-18 to 4	46
speed 500	-1	4	-11 to 6	46
400	-1	5	-10 to 8	40
300	-1	6	-12 to 11	41
200	-5	9	-28 to 11	45

Table 5-8
Summary of Comparisons Between VAS and ODW for
14/15 and 15/16 September 1982

Parameter	Mean (VAS-ODW)	Standard Deviation	Range	Number of Cases
T850 mb	1.4°C	1.3°C	-1.4 to 4.9°C	42
T700	-0.3	1.2	-2.7 to 2.6	42
T500	-0.1	1.3	-2.4 to 2.3	35
T400	0.2	1.4	-3.1 to 3.3	24
TD850	1.6°C	3.2°C	-5.0 to 9.8°C	42
TD700	3.6	5.2	-8.9 to 14.9	42
TD500	-12.5	7.0	-36.4 to 6.0	35
TD400	-8.9	7.6	-25.3 to 7.5	24
Z850	-6 m	23 m	-68 to 26 m	42
Z700	0	22	-58 to 41	42
Z500	1	24	-56 to 44	35
Z400	2	27	-54 to 47	24
wind 850	39°	27°	3 to 97°	21
direc- 700	44	30	9 to 109	23
tion 500	24	26	0 to 95	22
400	20	14	2 to 48	13
wind 850	-3 ms ⁻¹	4 ms ⁻¹	-10 to 3 ms ⁻¹	23
speed 700	-3	3	-7 to 2	23
500	-3	4	-9 to 3	22
400	-4	5	-15 to 3	13
Z400-850	11 m	17 m	-16 to 45 m	24
Z500-850	6	14	-18 to 43	35
Z400-700	4	14	-16 to 34	24
location	29 nm	15 nm	6 to 54 nm	42
time	38 min	29 min	2 to 108 min	42

pressure gradient force. Although pure gradient flow can exist only under very special circumstances, it is often a good approximation of the true wind. In the computation of the gradient wind from VAS geopotential height analyses, the curvature of parcel trajectories must be determined. Strictly speaking, geopotential height analyses taken at two separate intervals (say separated by an hour or so), must be used to calculate the trajectory of an air parcel. It is standard practice to approximate the trajectory curvature by the curvature of the isobars (or geopotential contours), since the latter is easily measured at any time. The gradient wind

estimates verified in this section, are those obtained under the assumption that the parcel trajectories coincide with the streamlines of the gradient wind (i.e., geopotential contours). An improved wind estimating procedure is under development, that includes trajectory curvature and the isobaric component as can be determined from the time derivative of geopotential observed by VAS. In this section, statistical comparisons between the VAS "gradient" winds, and winds observed by the Aircraft Communications Addressing and Reporting System (ACARS) flown on commercial 747 aircraft are discussed. ACARS is similar to the

**Table 5-9
Comparison of ACARS and VAS Winds**

Date of Observation	Time (GMT)	Lat. (DDMM)	Lon. (DDMM)	ACARS Pressure (mb)	Direction (Deg. from N)	Speed (m/s)	Time (GMT)	Lat. (DDMM)	Lon. (DDMM)	VAS Pressure (mb)	Direction (Deg. from N)	Speed (m/s)	Distance between VAS and ACARS (km)		
10/13/82	1251	3613	8718	237	242	54	1300	3635	8721	250	254	46	39		
10/13/82	1259	3556	8814	237	240	54	1300	3553	8826	250	256	44	17		
10/13/82	1306	3540	8909	237	235	53	1300	3531	8911	250	256	40	15		
10/13/82	1308	3737	9229	195	235	38	1300	3721	9149	200	249	49	68		
10/13/82	1314	3522	9004	237	232	51	1300	3517	8943	250	256	43	36		
10/13/82	1315	3659	9315	195	235	43	1300	3725	9320	200	249	50	45		
10/13/82	1321	3504	9101	237	231	53	1300	3520	9114	250	253	46	34		
10/13/82	1323	3622	9358	195	233	42	1300	3541	9337	200	250	52	85		
10/13/82	1329	3445	9157	237	229	54	1300	3449	9156	250	252	50	5		
10/13/82	1330	3541	9438	195	238	41	1300	3545	9507	200	251	50	46		
10/13/82	1336	3427	9254	237	232	53	1300	3437	9316	250	251	53	36		
10/13/82	1338	3457	9511	195	240	45	1300	3455	9542	200	252	56	47		
10/13/82	1344	3408	9350	237	233	52	1300	3353	9346	250	254	53	29		
10/13/82	1345	3413	9543	263	238	53	1300	3404	9605	250	253	64	37		
10/13/82	1351	3349	9449	364	240	35	1300	3402	9437	400	256	46	29		
10/13/82	1359	3328	9551	433	243	36	1300	3259	9547	450	255	49	55		
10/14/82	1002	3908	7904	237	256	62	1200	3859	7845	250	267	51	33		
10/14/82	1004	3907	10646	195	074	29	1200	3937	10611	200	070	30	75		
10/14/82	1005	3143	10431	213	264	30	1200	3232	10421	200	275	32	94		
10/14/82	1009	3851	7959	237	255	63	1200	3832	7936	250	269	57	49		
10/14/82	1024	3822	8152	237	259	60	1200	3821	8144	250	262	48	9		
10/14/82	1028	3211	10028	214	264	31	1200	3222	10110	200	264	21	71		
10/14/82	1032	3806	8248	237	261	60	1200	3750	8254	250	267	45	31		
10/14/82	1039	3750	8345	237	261	59	1200	3730	8339	250	271	52	36		
10/14/82	1043	3225	9750	454	257	17	1200	3216	9806	500	256	10	29		
10/14/82	1047	3733	8441	237	258	59	1200	3643	8416	250	271	52	102		
10/14/82	1054	3716	8551	238	260	59	1200	3645	8542	250	271	52	59		
10/14/82	1102	3659	8633	237	257	55	1200	3729	8636	250	270	46	54		
10/14/82	1109	3640	8729	237	255	55	1200	3648	8706	250	270	47	46		
10/14/82	1117	3622	8825	237	257	51	1200	3648	8834	250	270	44	51		
10/14/82	1124	3602	8922	237	254	49	1200	3602	8856	250	267	46	33		
10/14/82	1132	3541	9019	237	255	46	1200	3518	9013	250	262	48	44		
10/14/82	1139	3520	9117	237	253	44	1200	3521	9140	250	255	42	36		
10/14/82	1147	3459	9213	237	250	42	1200	3437	9211	250	255	43	43		
10/14/82	1154	3437	9310	237	248	40	1200	3422	9330	250	248	31	41		
10/14/82	1202	3414	9407	237	248	38	1200	3344	9408	250	250	28	55		
10/14/82	1209	3352	9501	294	257	32	1200	3426	9500	300	255	26	65		
10/14/82	1217	3331	9549	437	266	25	1200	3347	9536	400	259	24	37		
10/14/82	1336	3952	7739	319	249	19	1200	3953	7713	300	268	42	38		
10/14/82	1344	3949	7801	242	251	18	1200	3948	7806	250	266	48	6		
							Average 45.00								Average 43.90
							Standard Deviation 12.68								Standard Deviation 10.88
(VAS-ACARS)	SPEED	Average Offset -1.10 m/s					Standard Deviation 10.11 m/s					RMS Error 10.04 m/s			
	DIRECTION	Average Offset 11.70°					Standard Deviation 6.64°					RMS Error 13.41°			

Aircraft to Satellite Delay Relay (ASDARS) program (Sparkman and Giraytys, 1981). The difference is that the ACARS data transfer is directly to the ground.

Several comparisons have been made between wind measurements obtained from ACARS data and those determined by the VAS gradient wind calculations. The aircraft reports used were close in time (within two hours), horizontal distance (within 111 kilometers), and vertical level (within 70 mb pressure), with respect to the satellite-derived winds.

The comparisons with VAS-derived gradient winds were accomplished on two separate days when the aircraft flew through clear air, at times when VAS sounding data were available. Table 5-9 shows these comparisons. The results show the VAS wind speeds to be offset by -1.10 m/s, and to have a root mean square deviation of 10.04 m/s. Wind directions are within 13 degrees. The VAS gradient wind calculation is based upon the assumption of steady state conditions in the atmosphere. Since a majority of ACARS observations are at relatively high altitudes (200 mb) with wind speeds approaching 50 m/s⁻¹, obviously there is a departure from the gradient wind assumption. However, the VAS/ACARS RMS difference (10.04 m/s⁻¹) is just slightly greater than the RAOB/ACARS RMS differences (Lord *et al.*, 1983), indicating that the VAS thermal winds at higher altitudes have accuracies comparable to other observation methods.

Figure 5-7 shows the cumulative frequency of vector magnitude and direction differences of VAS gradient,

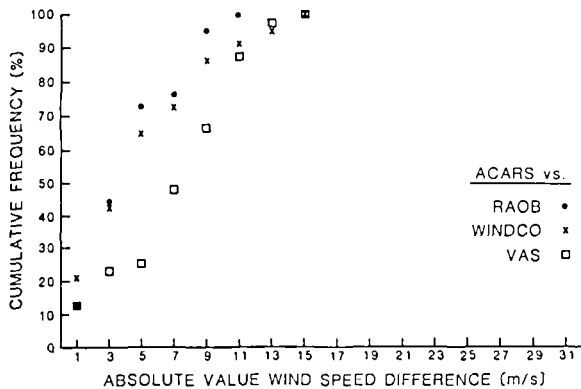


Figure 5-7a. Cumulative frequency of wind vector magnitude differences for three separate ACARS comparisons.

cloud motion (WINDCO), and rawinsonde winds with ACARS winds. The maximum differences between VAS and aircraft winds approach the maximum differences between cloud motion or rawinsonde and aircraft winds for more than 70 percent of the cases. However, there is a significant sample of cases where the VAS gradient winds appear inferior to cloud motion and radiosonde estimates on the basis of the ACARS comparisons. This is probably due to methods and assumptions used to compute the VAS-based gradient wind. Improvements in the wind calculation from VAS geopotential height analyses are expected with the inclusion of the parcel trajectory curvature and the isobaric component, evaluated from the VAS observed geopotential height tendency.

5.3 AVE/VAS GROUND TRUTH EXPERIMENT

J. Dodge
J. Greaves
NASA Headquarters
Washington, D.C.

H. Montgomery
Goddard Space Flight Center
National Aeronautics and Space Administration
Greenbelt, Maryland

One of the important aspects of the validation objectives was to conduct a "ground-truth" field experiment (AVE/VAS), to provide the data sets needed to validate the VAS measurements. The AVE/VAS experiment

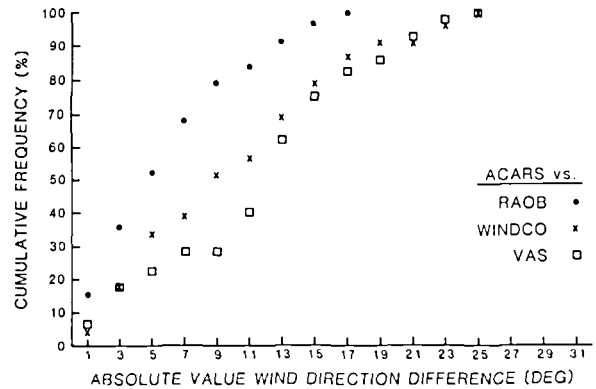


Figure 5-7b. Cumulative frequency of wind vector directional differences for three separate ACARS comparisons.

was a cooperative effort involving GSFC, MSFC, NOAA, Texas A&M University, and the University of Wisconsin, with funding provided by NASA's Severe Storms Research Program.

The Ground Truth Network consisted of a subsynoptic (or regional) area, centered over the U.S. Plains, where National Weather Service (NWS) rawinsonde stations were utilized. This network is shown in Figure 5-8. Nested within the central region of this network was a meso- β -scale network of special rawinsonde sites operated by NASA/MSFC, shown in Figure 5-9.

Rawinsonde balloon data were collected at all sites, every 3 hours (from 1200 GMT to 0600 GMT) for the following days: February 6 (shakedown day), March 6-7, March 27-28, April 24-25, and May 1-2, 1982. For the February shakedown day, rawinsondes were released at 1200, 1800, and 0000 GMT at the special rawinsonde stations only. The balloon releases occurred approximately 50 minutes before the observation time (i.e., the 1200 GMT release occurred between 1105 and

1115 GMT), allowing the rawinsonde to rise above 500 mb before the hour. Surface measurements at the special sites consisted of pressure, temperature, relative humidity, wind, sky conditions, and soil temperature measurements at a depth of 2 cm.

The VAS data were collected from GOES-5 at 75°W. All of the VAS data were obtained in the DS mode and precluded the operational VISSR images which would have come at those times. The basic PDL was the same for each time throughout the experiment, except for the frame centerline, and is shown in Table 5-10. This was adjusted periodically, to account for changes in the latitude of the subsatellite point, due to orbital inclination.

Table 5-11 provides a summary of all the VAS data acquired during the special ground truth period. A subjective evaluation of the quality of the data archived at both GSFC and UW is also provided, along with the latitude extent of each VAS data frame. The overall success rate was quite high. Out of the 39 possible data frames,

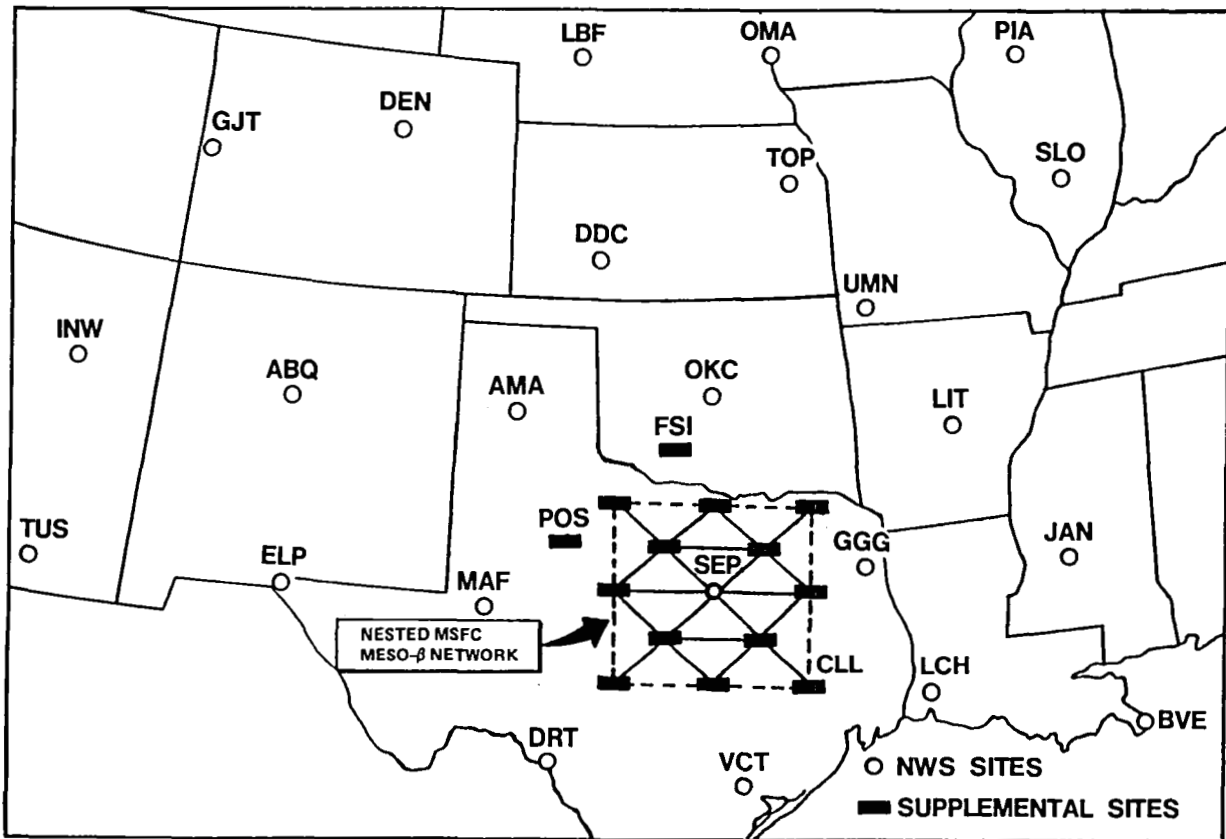


Figure 5-8. Locations of Regional-Scale and Meso- β -Scale Rawinsonde Sites

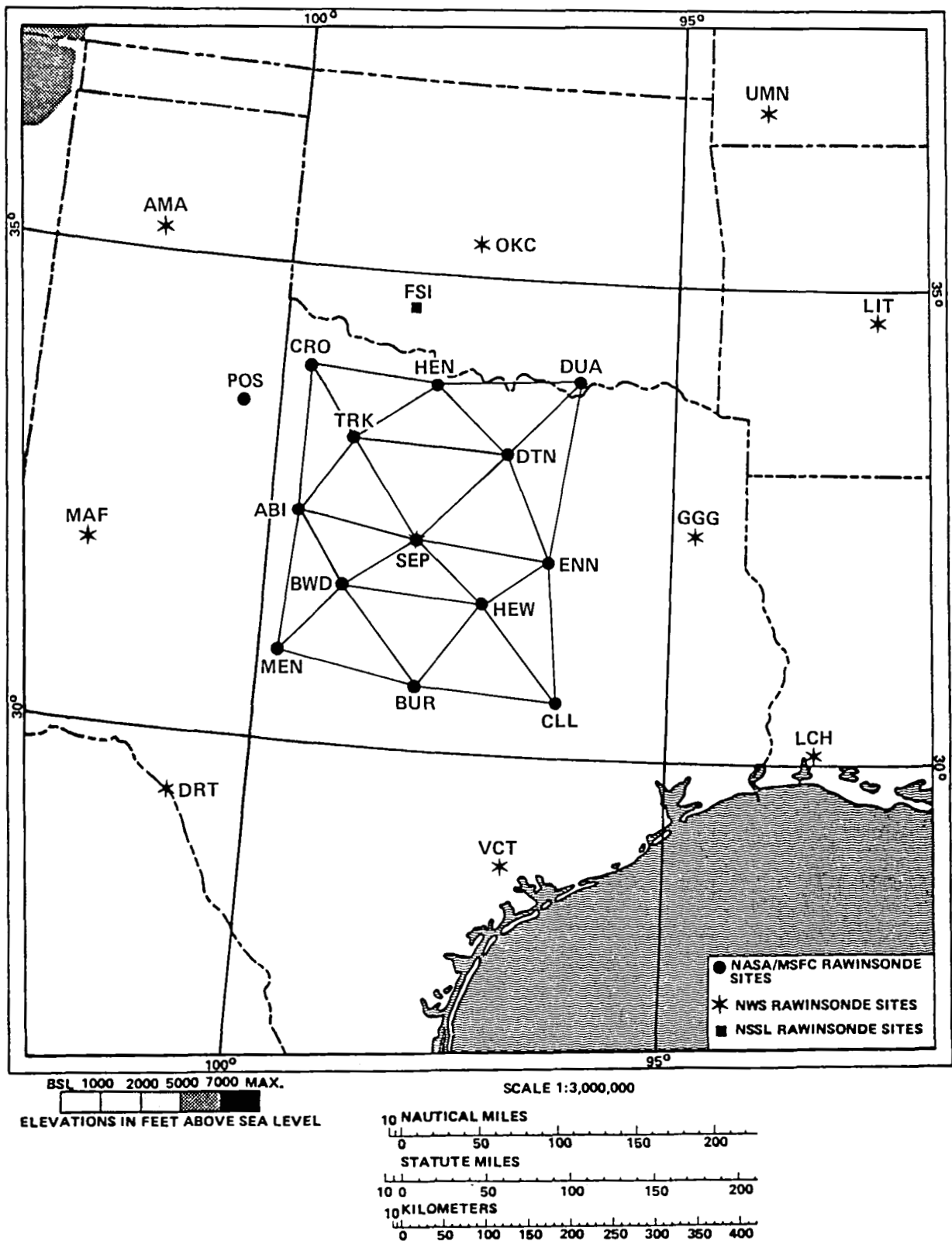


Figure 5-9. Location of Special Network Meso- β -Scale Rawinsonde Network

**Table 5-10
Processor Data Load (PDL) Description**

Mode: Dwell												
North-South extent: 224 mirror steps (approximately 18° of latitude centered at Stephenville, Tx.)												
Time to acquire sounding frame: 24.1 minutes												
Sounding detector size: Large (13.8 km)												
Spin Budget:												
Spectral Band	1	2	3	4	5	6	7	8	9	10	11	12
Spins	1	7	4	3	3	6	2	1	4	1	6	1

one (1100 GMT 27 March) was lost, due to a communications breakdown in scheduling the satellite. Although the GSFC and UW systems each failed to acquire 5 data frames, all 38 of the remaining data frames were acquired. One of these is considered to be of poor quality and is only marginally useful. Therefore, while the in-

dividual system success rates (fair or better) ranged from 82 to 87 percent, the combined system experienced a success rate of 97 percent, which points to the need for redundancy in ground-based systems, for important data gathering experiments.

**Table 5-11
VAS Data Acquisition Summary for Special Ground Truth Network Experiment**

Time (GMT)	February 6, 1982 (Shakedown)		March 6-7, 1982				March 27-28, 1982				April 24-25, 1982		May 1-2, 1982		
	Data Quality		Latitude Extent (°N)		Data Quality		Latitude Extent (°N)		Data Quality		Latitude Extent (°N)		Data Quality		Latitude Extent (°N)
	GSFC	UW	GSFC	UW	GSFC	UW	GSFC	UW	GSFC	UW	GSFC	UW	GSFC	UW	GSFC
1100	Good	Good	23-51	(1)	Good	28-47	(3)	(3)	—	Good	(1)	25-43	Good	Good	22-40
1430	Good	Good	23-51	(1)	Good	25-43	Good	Good	25-43	Good	Good	24-42	Good	Good	24-42
1730	Good	Good	26-51	Good	Good	24-42	(1)	Poor	23-41	Good	Good	24-41	Good	Good	25-44
2030	Good	Good	23-51	(1)	Good	23-41	Good	Good	23-40	Good	Good	23-41	Good	Good	27-47
2330	Good	Good	23-51	Fair	Good	23-40	Good	Good	24-42	Good	(1)	24-42	Good	Good	26-45
0230	(3)	(3)	—	Fair	Good	27-41	Good	(1)	24-42	Good	Poor	24-43	Good	Good	26-45
0530	(3)	(3)	—	(2)	(2)	—	(2)	(2)	—	(1)	Good	25-43	Good	Good	25-43
0830	(3)	(3)	—	Good	Good	25-43	Good	(1)	24-42	Good	Good	25-43	Good	Good	23-41
1100	(3)	(3)	—	Good	Good	24-43	Good	(1)	24-42	Good	Good	25-43	Good	Fair	25-40

NOTES: (1) Data not acquired
(2) Data not available (Satellite Eclipse)
(3) Data not scheduled

During the four days of observation, a large portion of the special network was covered by clouds (see Greaves *et al.*, 1982), making the derivation of VAS soundings a difficult, if not impossible task for each case. The weather conditions were relatively stable, in that the Texas region was usually cold and cloudy with steady light rains, or drizzle. The convection which occurred near the special network (e.g., April 24) was light to moderate. After reviewing the data, it was decided that the March 6 case provided the best opportunity for a validation of VAS soundings.

The surface map and thickness analysis in Figure 5-10 illustrates that the March 6 case was marked by a developing frontal wave in the southeast United States, with a significant thickness gradient across the special network in Texas. The strong thickness gradient is indicative of the thermal support for a significant jet streak system extending from northern Mexico toward the Great Lakes region, with the axis of maximum winds existing in Texas at 1200 GMT. This is shown in Figure 5-11. The cloud mass associated with the frontal system along the Southeast and Gulf Coasts is clearly illustrated in the visible satellite imagery at 1830 GMT, with a line of convection extending from central Louisiana to the Texas coast, as indicated in Figure 5-12. The 6.7- μ m water vapor channel from 1730 GMT, shown in Figure 5-13, depicts the clouds over the East and Southeast, along with a noticeably dry slot extending from northern Mexico toward Lake Michigan. This dry zone appeared to be associated with the jet system and baroclinic zone, shown in Figure 5-11, and propagated across the network during the 24-hour observing period. This case is well suited for comparing VAS soundings with the special network data set (given the clear conditions over Texas), and for determining the impact of VAS on capturing a significant baroclinic zone supporting an intense upper-level jet.

The comparison between the VAS and radiosonde soundings for the Special Network Experiment was conducted at MSFC, GSFC, and UW. The results from the three independent evaluations generally agree. The statistical analyses indicate that the VAS soundings are generally good above the 700 mb layer, but are poor below this level, due to the inability of the retrievals to adequately resolve the sharp inversion near the 800-mb level. The GSFC results also point to possible problems with the meso- β radiosonde data set, raising questions about the extent to which these data sets can be considered to be "ground truth."

5.3.1 MSFC Special Network Statistical Evaluation

G. Jedlovec*

G. Wilson

Atmospheric Sciences Division

Marshall Space Flight Center

National Aeronautics and Space Administration

Huntsville, Alabama

The MSFC validation effort consisted of comparing VAS retrievals produced by the physical retrieval technique (UW), with those produced by the regression retrieval technique (GSFC), and comparing these with the radiosonde data set.

5.3.1.1 Data Set Preparation

The following procedures were applied to the data sets before the statistical evaluation was performed. The ground truth radiosonde data were adjusted to a common hour of release, similar to that of Fankhauser (1969), applied by Fuelberg and Jedlovec (1982). The new valid times of radiosonde data become 1100, 1445, 1745, 2045, and 2345 GMT, corresponding to the time VAS was scanning the meso-network. This procedure provides for a consistent data set at all levels at the same time. The radiosonde data were interpolated to a uniform grid, with the balloon (radiosonde) position being recalculated at every level in the vertical. This procedure eliminated spatial discrepancies, since the same grid was also used for the satellite data.

The preprocessing of some of the satellite data was necessary before analysis. The parameter values obtained with the physical retrievals consisted of geopotential height, temperature, and dewpoint temperature values at the surface and mandatory reporting levels up to 100 mb. These values were linearly interpolated (with height) to 25-mb levels, corresponding to the ground truth data. Additional parameters (relative humidity and mixing ratio) were calculated from the 25-mb satellite data set as needed. The VAS soundings produced using a regression scheme required further preprocessing. Temperature and dewpoint values were provided at the mandatory levels. Surface data used in the regression technique were provided separately. In addition to interpolating to 25-mb pressure levels, and the calculation of relative humidity and mixing ratio, geopotential height values were also desired. To obtain these height values, the surface data were used to

*Universities Space Research Association Visiting Scientist.

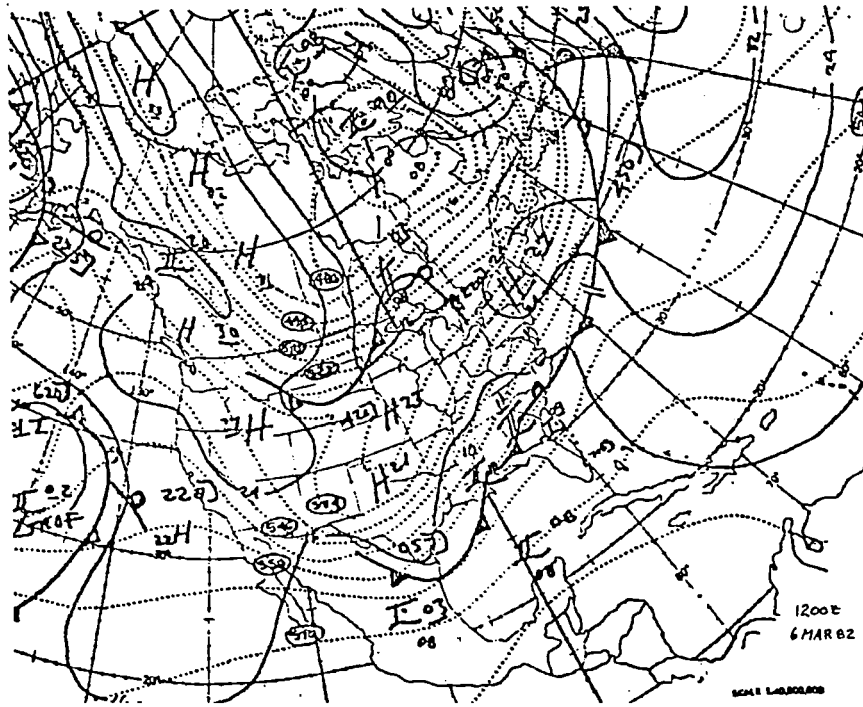


Figure 5-10. National Weather Service thickness (SFC to 500 mb) and surface analysis for 1200 GMT, 6 March 1982

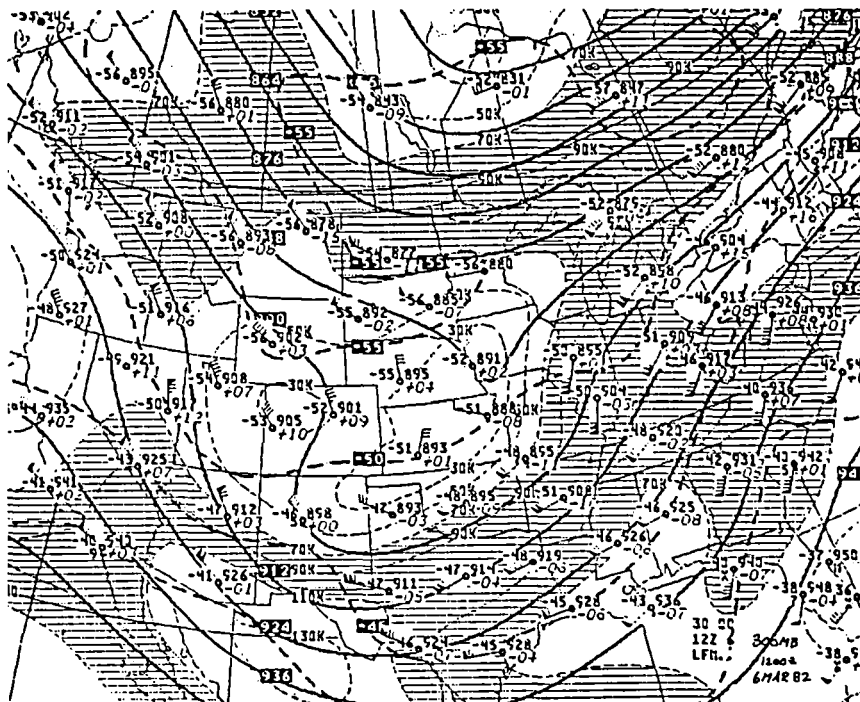


Figure 5-11. National Weather Service 300-mb analysis for 1200 GMT, 6 March 1982

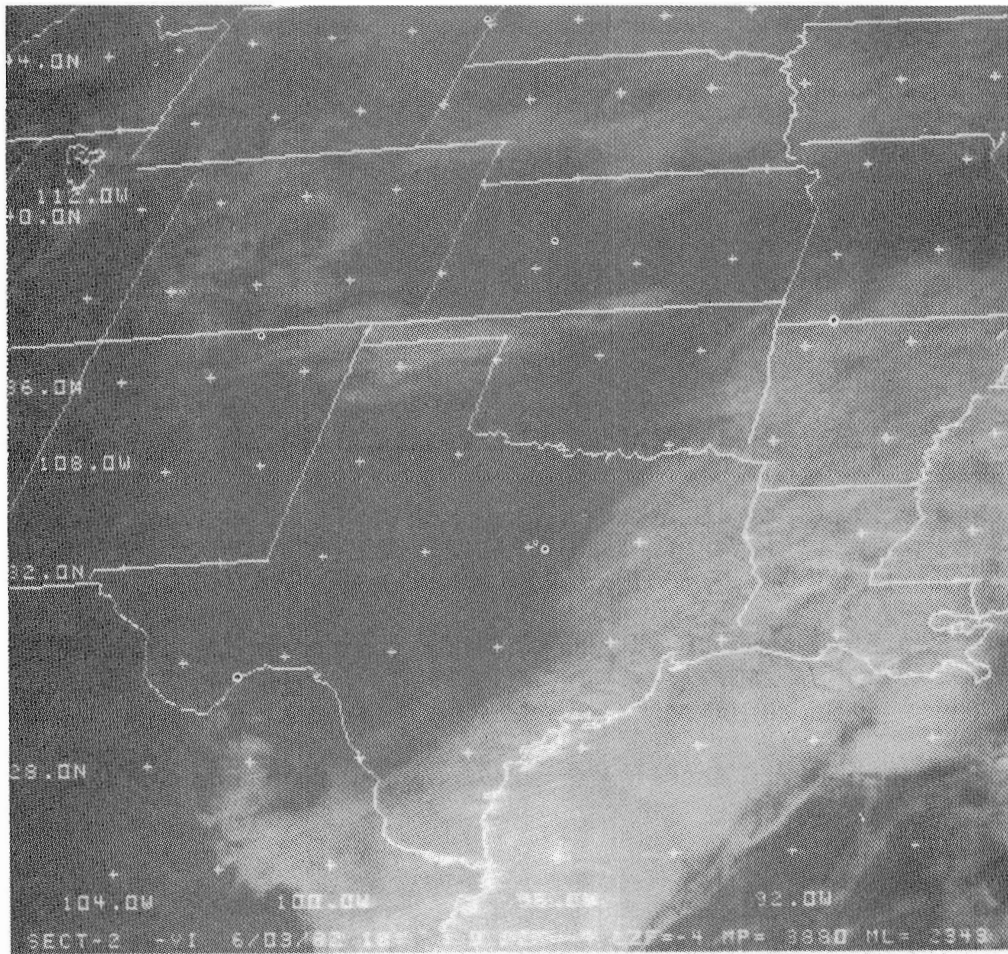


Figure 5-12. GOES visible image for 1800 GMT, 6 March 1982

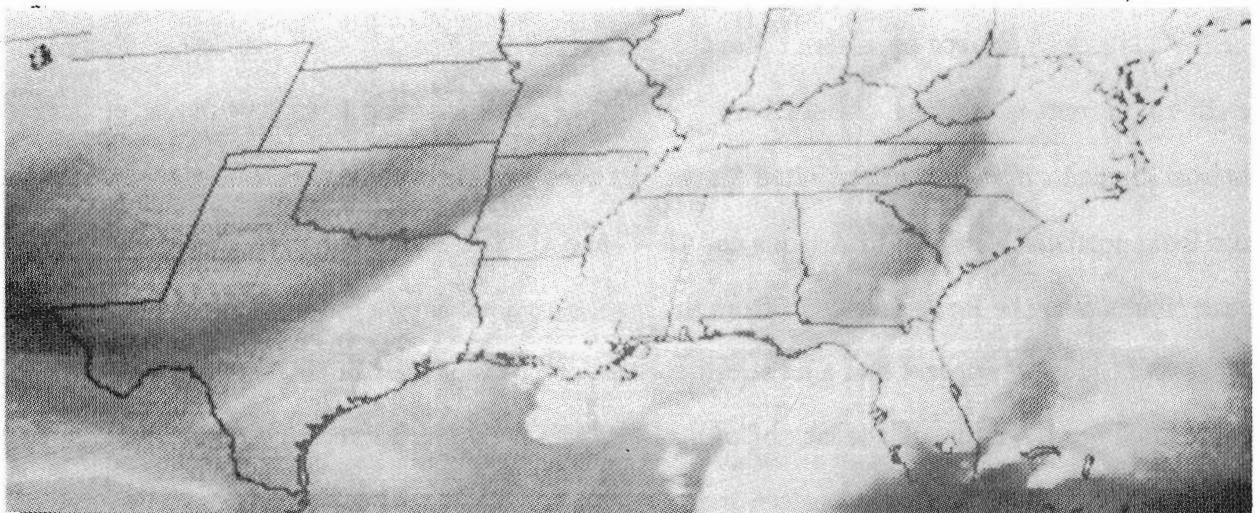


Figure 5-13. VAS 6.7 μm water vapor channel for 1730 GMT, 6 March 1982. Gray to black is moisture and clouds; light gray to white is dry signal down to approximately 700 mb level.

calculate a station pressure, which then was used along with temperature and moisture to compute geopotential height at 25-mb levels from the hypsometric equation. Having produced radiosonde and satellite sounding data sets with identical parameters at specified pressure levels, the data were put on a uniform grid centered over the mesoscale network, as indicated in Figure 5-8, using a Barnes (1964) analysis scheme. The scan radius and number of iterations that were used were 223 km and 4, respectively. Taking the previous steps in data handling, the following items should not be considered as explanations for radiosonde-satellite differences.

1. The radiosonde and satellite soundings have the *same valid times* at every level of the atmosphere.
2. *Spatial discrepancies* due to radiosonde drift have been eliminated in the gridding process.
3. The gridded fields of all parameters have the *same spatial, spectral response* despite different station spacings and locations.

In addition to the basic parameters to be considered in this study (temperature, height, dewpoint, and mixing ratio), derived values of relative humidity, thickness, mean layer temperature, mean layer relative humidity, and precipitable water were calculated from the gridded fields of radiosonde and satellite data.

5.3.1.2 Statistical Analysis of Gridded Data

Used as the objective criteria for evaluating the VAS soundings, mean and root-mean-square (RMS) differences between each set of satellite and radiosonde grids were calculated for various basic and derived parameters. Since the radiosonde represents an independent description of the mesoscale environment, and is considered the "ground truth" in this study, satellite estimates were subtracted from the ground truth values (RAO - SAT) in all calculations and comparisons. Mean and RMS differences for the physical and regression schemes are presented in Tables 5-12 and 5-13, for seven parameters at each of the five observation times. Each of the 18 pressure levels correspond to an analyzed grid level for both the radiosonde and satellite data. The mean differences for the first five parameters are graphically displayed as a function of pressure and time in Figures 5-14 thru 5-18. Figure 5-19 contains atmospheric profiles for the two satellite data sets and the radiosonde data computed from grid mean values as a

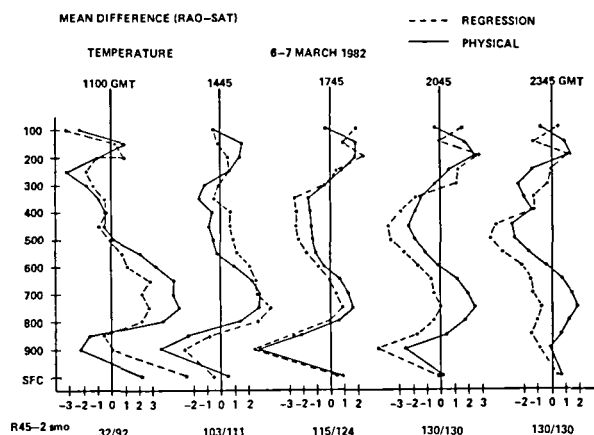


Figure 5-14. Mean difference (radiosonde-satellite) between rawinsonde and satellite gridded temperature fields as a function of pressure at 1100, 1445, 1745, 2045, and 2345 GMT. The physical retrieval difference profiles are solid lines (—) and the regression profiles are dashed lines (---). The units are °C. The number of grid points used at each time are displayed for the regression and physical retrievals, respectively.

function of time. Mean temperature differences between the radiosonde and satellite vary considerably as a function of pressure, time, and the retrieval scheme (Figure 5-14). Both satellite data sets show a warm bias ($T_R - T_S < 0$) in the lowest layer of the atmosphere extending up to about 850 mb. Maximum mean difference values reach 4.8°C and 5.1°C for the physical and regression schemes, at 900 mb (Table 5-12 and Table 5-13). Above this, a cold bias exists up to about 600 mb. These low-level biases are strongest for the first three time periods, and are of similar magnitude for each data set. This pattern changes somewhat for the last two time periods when the biases are smaller, and the regression retrievals indicate a warm bias from the surface up to about 300 mb. Large mean temperature differences also exist in the middle and upper troposphere. Maximum difference values occur between 400 and 500 mb, with a warm bias existing throughout a 300-mb layer at 1745, 2045, and 2345 GMT. Both of these bias regions appear to be related to large temperature inversions over the mesoscale grid region (Figure 5-19). A strong frontal inversion existed near the 900-mb level, in the grid mean profiles that weakened as surface heating warmed the lowest layers. This could indicate why the low-level satellite biases decreased in

Table 5-12
Mean and Root-Mean-Square (RMS) difference (radiosonde-satellite) for temperature (T),
dewpoint temperature (TD), precipitable water (PW), geopotential height (Z),
thickness and the magnitude of the vertical temperature and height
gradient (Grad T and Grad Z) as a function of pressure at (a) 1100 GMT,
(b) 1445 GMT, (c) 1745 GMT, (d) 2045 GMT, (e) 2345 GMT for
6 March 1982. The VAS retrieval technique is the "physical" technique.
Units are as indicated. Dashes (----) indicate values that were calculated
but not displayed. Asterisks (*) indicate values that were not computed.
Thicknesses are calculated in the 850 to 700 mb, 700 to 500 mb,
500 to 250 mb, 250 to 100 mb layers but are plotted at the layer midpoints.

(a) Time/Date: 1100 GMT 6 March 1982
 Number of grid points used: 92 "Physical"

		PARAMETERS						
		T (°C)	TD (°C)	PW (mm)	Z (m)	Thickness (m)	Grad T (°C/100km)	Grad Z (m/100km)
Pressure Levels	100	-2.3,2.4	----	----	-0.7,20.3	*	0.6,1.0	10.1,17.0
	150	1.0,1.3	----	----	13.5,29.6	*	0.1,0.7	11.2,25.1
	200	-0.9,1.5	----	----	10.1,28.7	-20.7,30.5	1.0,1.5	11.9,25.4
	250	-3.2,3.3	----	----	20.0,36.5	*	0.7,1.1	17.2,28.3
	300	-1.8,1.9	----	----	34.3,51.6	*	0.1,0.6	27.1,33.9
	350	-0.8,1.4	-3.8,4.2	----	43.3,56.9	*	0.4,0.9	26.8,32.1
	400	-0.3,1.7	-3.9,4.4	----	45.8,56.2	-29.0,32.2	1.0,1.3	24.4,27.8
	450	-0.5,1.9	-3.3,9.5	----	47.6,53.3	*	1.3,1.6	19.3,22.2
	500	0.2,1.8	0.4,10.2	----	49.1,53.3	*	1.6,1.8	12.1,16.1
	550	2.1,2.6	-5.0,10.3	----	46.6,50.2	*	1.3,1.7	8.4,12.3
	600	3.3,3.8	-4.0,11.3	----	39.9,42.7	29.4,33.1	1.4,1.8	4.7,8.5
	650	4.7,5.0	-5.2,12.9	----	29.9,31.8	*	1.0,1.4	2.0,6.6
	700	4.6,5.1	-6.1,13.0	----	19.7,20.7	*	1.4,1.8	0.2,4.7
	750	5.0,5.3	-7.2,11.2	----	9.7,10.3	*	1.3,1.6	0.7,3.5
	800	3.8,4.3	-3.0,7.3	----	1.2,3.9	20.6,23.1	1.6,1.9	2.4,4.7
	850	-1.4,2.5	0.8,3.5	----	-1.0,5.5	*	1.7,2.5	4.7,6.6
900	-2.2,2.6	0.7,2.0	----	6.8,9.0	*	0.3,0.9	6.2,7.7	
SFC	2.1,3.3	0.3,5.3	0.2,2.8	----	*	0.5,1.3	----	

Table 5-12 (Continued)

(b) Time/Date: 1445 GMT 6 March 1982

Number of grid points used: 111 "Physical"

		PARAMETERS						
		T (°C)	TD (°C)	PW (mm)	Z (m)	Thickness (m)	Grad T (°C/100km)	Grad Z (m/100km)
Pressure Levels	100	-0.5,0.9	----	----	19.0,31.8	*	0.1,0.7	9.0,27.1
	150	1.5,1.8	----	----	14.0,33.2	*	0.3,0.9	7.1,32.2
	200	1.3,1.9	----	----	-2.0,22.6	30.9,34.4	0.0,0.8	0.5,25.9
	250	0.7,1.3	----	----	-11.9,27.2	*	0.6,1.1	1.3,30.1
	300	-1.0,2.2	----	----	-5.2,24.8	*	0.0,0.9	10.1,29.8
	350	-1.5,1.7	2.1,4.8	----	4.7,23.9	*	0.0,0.9	14.2,27.2
	400	-0.7,2.2	-0.2,2.7	----	7.8,21.6	-25.1,33.7	1.0,2.2	10.0,24.1
	450	-0.9,2.5	-2.2,5.0	----	9.9,17.4	*	1.4,2.4	4.2,17.4
	500	-0.6,1.9	0.5,4.4	----	13.2,17.5	*	1.1,1.7	-0.3,12.5
	550	-0.3,1.2	0.0,4.2	----	15.4,18.7	*	0.8,1.2	-2.9,13.1
	600	1.0,1.3	-0.0,3.7	----	14.3,17.0	8.1,12.7	0.3,1.0	-4.7,11.2
	650	2.2,2.4	-1.3,5.0	----	10.6,13.6	*	0.4,0.9	-4.5,10.1
	700	2.7,2.9	-3.4,5.8	----	5.1,9.3	*	0.0,1.3	-2.7,8.6
	750	2.8,3.0	-4.6,6.1	----	-0.2,6.9	*	0.0,1.3	-0.6,6.1
	800	1.4,1.9	-2.8,4.5	----	-4.6,8.1	8.7,9.9	0.5,1.5	1.3,4.7
	850	-2.3,2.6	-1.3,2.2	----	-3.6,7.0	*	-0.4,0.9	3.1,5.1
900	-4.2,4.5	-1.7,2.1	----	6.6,8.2	*	-0.2,0.8	3.4,6.1	
SFC	0.5,0.9	1.6,1.9	-0.8,1.2	----	*	0.4,0.8	----	

(c) Time/Date: 1745 GMT 6 March 1982

Number of grid points used: 124 "Physical"

		PARAMETERS						
		T (°C)	TD (°C)	PW (mm)	Z (m)	Thickness (m)	Grad T (°C/100km)	Grad Z (m/100km)
Pressure Levels	100	-0.4,1.1	----	----	2.9,16.4	*	0.5,0.8	5.0,13.0
	150	1.7,1.8	----	----	0.2,17.6	*	0.0,0.5	1.7,12.1
	200	1.7,1.9	----	----	-16.5,24.1	25.6,28.9	0.3,0.7	0.5,15.4
	250	0.8,1.6	----	----	-22.7,28.0	*	0.9,1.1	4.5,17.9
	300	-0.3,1.8	----	----	-21.8,30.5	*	0.3,0.9	11.1,21.2
	350	-1.8,2.0	5.1,5.7	----	-15.5,28.8	*	-0.1,0.9	13.2,20.3
	400	-1.5,2.2	2.4,7.7	----	-10.7,23.7	-21.4,25.8	1.2,1.4	9.3,14.7
	450	-1.5,2.7	0.9,4.0	----	-5.7,16.2	*	1.8,2.0	0.9,10.1
	500	-1.3,2.3	1.3,3.3	----	-1.3,13.0	*	1.4,1.8	-4.2,9.0
	550	-1.0,1.7	-3.0,4.0	----	2.1,13.3	*	1.0,1.4	-6.7,9.5
	600	-0.5,1.4	-3.3,5.6	----	4.0,12.1	-3.2,11.6	0.2,0.7	-7.0,9.3
	650	0.6,1.5	-6.6,8.0	----	3.7,9.8	*	-0.1,0.7	-5.3,8.0
	700	1.2,1.8	-9.2,9.8	----	1.9,7.6	*	-0.0,0.5	-2.3,6.1
	750	1.6,1.9	-9.0,9.5	----	-0.6,7.2	*	0.1,0.8	0.6,5.6
	800	0.6,1.4	-6.7,7.3	----	-2.8,7.8	3.3,7.7	-0.1,0.6	3.4,6.0
	850	-2.1,2.6	-5.8,6.1	----	-1.4,7.1	*	-0.4,0.9	5.8,7.4
900	-4.8,5.0	-3.8,3.9	----	7.0,9.9	*	-0.1,0.6	6.7,8.2	
SFC	0.8,1.3	1.6,2.5	-2.9,3.1	----	*	1.1,1.3	----	

Table 5-12 (Continued)

(d) Time/Date: 2045 GMT 6 March 1982

Number of grid points used: 130 "Physical"

		PARAMETERS						
		T (°C)	TD (°C)	PW (mm)	Z (m)	Thickness (m)	Grad T (°C/100km)	Grad Z (m/100km)
Pressure Levels	100	-0.5,1.1	----	----	23.5,29.8	*	0.4,0.9	1.5,21.1
	150	1.7,1.9	----	----	15.3,24.5	*	0.3,0.7	-3.0,23.0
	200	2.3,2.5	----	----	-4.8,19.4	34.1,36.6	0.5,0.7	-6.3,24.2
	250	0.4,1.7	----	----	-10.6,17.3	*	1.2,1.4	-2.1,22.9
	300	-0.5,1.1	----	----	-11.9,19.1	*	0.2,1.0	-0.7,22.1
	350	-1.6,1.8	10.8,13.3	----	-3.6,13.6	*	-0.0,0.8	1.7,17.8
	400	-1.8,1.9	6.2,7.7	----	2.6,12.9	-27.5,29.4	0.4,1.0	0.1,13.9
	450	-2.3,2.8	4.3,6.4	----	10.5,15.5	*	1.2,1.6	-1.9,10.0
	500	-2.0,2.5	4.8,6.6	----	16.9,20.3	*	1.0,1.5	-4.5,9.6
	550	-1.0,1.6	1.0,3.3	----	21.5,24.3	*	0.6,1.0	-6.3,9.8
	600	-0.1,1.1	-2.5,3.7	----	22.8,25.1	-0.9,9.3	0.1,0.7	-6.1,9.1
	650	1.3,1.6	-4.6,5.1	----	21.3,23.3	*	-0.0,0.7	-4.5,7.7
	700	2.0,2.2	-7.4,7.9	----	17.9,19.8	*	-0.1,0.7	-2.0,5.3
	750	2.4,2.6	-6.8,7.0	----	13.9,16.4	*	0.1,0.8	0.9,4.5
	800	1.8,2.0	-3.9,4.3	----	10.1,13.4	9.8,11.0	0.1,0.7	3.5,5.3
	850	0.5,1.4	-2.2,3.0	----	8.0,11.7	*	-0.3,0.7	5.5,6.9
	900	-2.7,3.0	-0.7,1.6	----	10.3,12.3	*	0.7,0.9	3.6,6.3
SFC	0.2,1.1	1.7,2.2	-1.3,1.5	----	*	1.0,1.3	----	

(e) Time/Date: 2345 GMT 6 March 1982

Number of grid points used: 130 "Physical"

		PARAMETERS						
		T (°C)	TD (°C)	PW (mm)	Z (m)	Thickness (m)	Grad T (°C/100km)	Grad Z (m/100km)
Pressure Levels	100	-0.9,1.4	----	----	-17.0,31.7	*	0.3,0.8	12.1,28.1
	150	1.0,1.3	----	----	-21.2,28.6	*	0.3,0.6	3.4,26.9
	200	1.3,1.6	----	----	-33.2,36.9	19.6,30.3	0.8,1.0	0.7,25.1
	250	-1.3,1.9	----	----	-36.5,39.3	*	0.9,1.1	1.1,23.2
	300	-2.5,2.8	----	----	-21.3,25.8	*	0.7,1.5	3.5,20.1
	350	-2.2,2.3	7.8,8.6	----	-8.3,17.1	*	0.3,1.0	4.7,17.0
	400	-1.2,1.7	6.5,7.2	----	-3.0,14.6	-51.0,52.1	0.1,1.0	2.4,15.1
	450	-2.7,3.1	5.1,5.8	----	4.7,15.5	*	0.9,1.2	-1.2,12.8
	500	-2.5,3.0	6.0,6.9	----	14.5,18.7	*	0.9,1.2	-3.2,10.1
	550	-1.5,1.8	2.9,3.9	----	20.5,23.2	*	0.4,0.8	-4.6,9.6
	600	-0.2,0.9	1.1,2.7	----	22.5,24.7	-4.9,9.4	0.0,0.5	-4.0,8.4
	650	0.9,1.3	-1.2,2.7	----	21.9,23.5	*	-0.1,0.5	-2.7,6.6
	700	1.6,2.0	-3.1,4.0	----	19.4,20.5	*	-0.3,0.6	-1.0,4.9
	750	1.8,2.4	-3.3,4.1	----	16.2,16.9	*	0.2,0.7	0.5,3.8
	800	1.3,1.7	-0.7,2.0	----	13.3,14.1	7.7,10.4	0.0,0.6	2.2,3.9
	850	0.7,1.1	1.9,2.7	----	11.6,12.7	*	0.3,0.8	3.3,4.4
	900	-0.5,1.1	2.1,2.6	----	11.2,11.8	*	0.6,0.8	1.5,3.9
SFC	0.7,1.3	1.6,2.4	0.5,0.9	----	*	0.5,0.8	----	

Table 5-13
**Mean and Root-Mean-Square (RMS) differences (radiosonde-satellite) for temperature (T),
dewpoint temperature (TD), precipitable water (PW), geopotential height (Z),
thickness and the magnitude of the vertical temperature and height
gradient (Grad T and Grad Z) as in Table 5-12 except for the
"regression" retrieval algorithm**

(a) Time/Date: 1100 GMT 6 March 1982
Number of grid points used: 32 "Regression"

		PARAMETERS						
		T (°C)	TD (°C)	PW (mm)	Z (m)	Thickness (m)	Grad T (°C/100km)	Grad Z (m/100km)
Pressure Levels	100	-3.2,3.3	----	----	-1.0,24.9	*	1.3,1.5	-8.6,18.1
	150	0.3,0.5	----	----	20.0,32.0	*	0.3,0.5	-12.1,20.7
	200	1.0,1.6	----	----	12.3,28.7	-10.7,15.6	1.8,1.9	-8.3,21.1
	250	-1.7,2.1	----	----	9.7,28.9	*	0.9,1.3	-5.2,21.0
	300	-1.3,1.7	----	----	9.3,29.8	*	-0.6,0.8	21.1,26.6
	350	-0.5,0.7	7.5,7.7	----	15.7,32.2	*	0.3,0.8	22.2,26.9
	400	-0.4,1.4	6.4,6.7	----	18.1,31.8	-13.6,16.8	1.7,1.9	17.0,23.3
	450	-0.8,1.5	5.9,8.4	----	20.2,30.6	*	1.6,1.8	10.1,17.0
	500	-0.1,1.2	4.5,5.5	----	23.2,30.0	*	1.6,1.9	-1.6,12.1
	550	0.9,1.7	-7.1,11.7	----	20.7,27.4	*	1.7,2.1	-2.2,9.9
	600	1.2,1.9	-10.7,13.5	----	18.9,23.9	14.7,18.6	1.5,1.8	-6.2,11.3
	650	2.9,3.1	-13.6,15.5	----	14.1,18.8	*	0.6,0.8	-8.4,13.1
	700	2.2,2.5	-11.1,11.9	----	8.5,13.4	*	0.9,1.0	-9.2,13.2
	750	2.8,3.0	-4.6,5.7	----	3.4,10.0	*	1.1,1.5	-8.2,10.9
	800	2.3,2.7	4.9,5.4	----	-1.7,9.0	11.2,12.8	2.1,2.4	-4.4,7.5
	850	-0.6,1.0	1.2,2.5	----	-2.7,9.0	*	0.6,0.8	-1.6,5.1
	900	0.2,1.6	4.0,4.2	----	-3.5,7.4	*	0.4,0.9	0.2,4.0
SFC	5.5,6.0	1.1,6.9	0.8,1.3	----	*	3.0,3.2	----	

Table 5-13 (Continued)

(b) Time/Date: 1445 GMT 6 March 1982

Number of grid points used: 103 "Regression"

		PARAMETERS						
		T (°C)	TD (°C)	PW (mm)	Z (m)	Thickness (m)	Grad T (°C/100km)	Grad Z (m/100km)
Pressure Levels	100	-0.5,0.9	----	----	15.0,32.3	*	0.0,0.6	17.1,23.3
	150	-0.1,0.8	----	----	20.9,39.0	*	0.4,1.0	16.9,27.0
	200	0.4,0.8	----	----	16.3,36.8	6.1,20.2	0.3,0.6	13.0,26.0
	250	0.5,2.0	----	----	8.9,40.4	*	0.4,1.4	15.1,32.1
	300	-0.3,1.7	----	----	13.7,49.0	*	0.3,0.7	25.0,37.9
	350	-0.6,1.1	12.1,13.3	----	20.6,51.2	*	0.1,0.9	26.4,37.1
	400	0.7,2.4	4.0,5.4	----	18.6,43.8	-5.6,20.6	1.3,2.5	21.9,31.1
	450	0.6,2.9	-0.2,2.1	----	15.6,33.9	*	1.8,2.9	15.4,22.0
	500	0.9,2.5	-0.2,3.8	----	14.5,26.8	*	1.5,2.0	9.0,14.2
	550	1.1,2.3	1.1,4.1	----	12.3,21.0	*	1.5,1.8	5.0,9.5
	600	2.1,2.7	3.1,6.8	----	8.2,14.6	17.6,25.4	1.1,1.4	1.4,6.1
	650	2.6,3.0	3.0,7.5	----	2.8,8.7	*	1.1,1.4	-0.4,5.5
	700	2.6,2.9	2.2,5.4	----	-3.2,6.4	*	0.8,1.2	-0.5,4.6
	750	3.5,3.8	1.1,3.1	----	-9.4,10.3	*	0.7,1.0	-0.1,3.8
	800	2.7,3.2	2.1,2.6	----	-15.8,16.3	14.4,16.1	1.1,1.4	1.5,4.0
	850	-0.7,1.9	2.8,3.2	----	-17.5,18.2	*	0.1,0.9	3.6,5.0
	900	-2.6,3.1	2.0,2.6	----	-14.4,16.6	*	-0.1,0.8	4.7,5.8
SFC	-0.4,1.4	2.1,2.5	1.7,2.2	----	*	0.3,1.1	----	

(c) Time/Date: 1745 GMT 6 March 1982

Number of grid points used: 115 "Regression"

		PARAMETERS						
		T (°C)	TD (°C)	PW (mm)	Z (m)	Thickness (m)	Grad T (°C/100km)	Grad Z (m/100km)
Pressure Levels	100	1.8,2.0	----	----	-19.9,26.8	*	0.1,0.7	3.1,24.1
	150	0.9,1.2	----	----	-30.9,37.6	*	-0.0,0.6	-2.5,27.1
	200	2.3,2.4	----	----	-47.1,52.6	34.3,37.0	0.3,0.6	-5.3,31.3
	250	0.5,2.4	----	----	-54.3,58.4	*	-0.0,0.8	0.4,32.0
	300	-0.2,2.2	----	----	-54.3,58.7	*	-0.3,1.0	8.0,30.8
	350	-2.7,3.1	4.1,5.2	----	-46.7,52.8	*	-0.8,1.4	12.1,28.4
	400	-2.6,2.9	-1.9,5.4	----	-37.7,43.5	-33.0,37.0	1.0,1.4	10.0,21.1
	450	-2.6,3.3	-2.8,4.0	----	-28.9,32.5	*	1.6,2.1	3.1,15.3
	500	-2.4,2.9	-2.1,2.7	----	-21.2,24.1	*	1.2,1.7	-1.4,11.8
	550	-1.8,2.0	-2.9,3.5	----	-15.4,18.7	*	0.8,1.3	-3.6,11.1
	600	-0.8,1.2	-0.5,4.8	----	-12.1,15.1	-9.5,11.2	-0.2,0.8	-4.8,9.7
	650	-0.0,0.7	-1.5,4.7	----	-11.3,13.9	*	-0.2,0.7	-4.8,9.0
	700	0.3,0.7	-1.9,3.6	----	-11.7,13.7	*	-0.0,0.7	-4.3,8.4
	750	0.9,1.3	-1.6,3.0	----	-13.2,14.8	*	0.2,1.3	-4.3,8.5
	800	-0.0,1.0	0.7,2.0	----	-14.5,15.8	0.7,4.5	0.1,0.8	-3.8,8.6
	850	-2.5,2.9	1.1,1.7	----	-12.4,14.0	*	-0.1,0.8	-3.1,8.8
	900	-5.1,5.2	1.1,1.8	----	-5.4,8.9	*	-0.4,0.9	-3.1,8.2
SFC	0.4,1.5	1.6,2.4	0.4,0.8	----	*	0.4,1.2	----	

Table 5-13 (Continued)

(d) Time/Date: 2045 GMT 6 March 1982

Number of grid points used: 130 "Regression"

		PARAMETERS						
		T (°C)	TD (°C)	PW (mm)	Z (m)	Thickness (m)	Grad T (°C/100km)	Grad Z (m/100km)
Pressure Levels	100	1.5,1.6	----	----	-27.0,37.3	*	0.1,0.6	-2.3,27.1
	150	-0.2,0.7	----	----	-37.9,47.5	*	0.5,0.7	-8.0,34.3
	200	2.6,2.7	----	----	-52.2,60.1	34.3,37.7	0.1,0.8	-12.1,37.1
	250	1.1,2.9	----	----	-61.3,66.9	*	-0.3,1.0	-7.9,33.0
	300	1.0,1.9	----	----	-68.7,74.4	*	-0.1,1.4	-7.9,29.8
	350	-1.9,2.2	11.6,16.0	----	-63.9,69.6	*	-0.5,1.3	-5.5,25.1
	400	-2.9,3.1	1.3,5.7	----	-54.9,61.0	-30.2,34.3	0.0,1.2	-5.6,19.1
	450	-3.8,4.0	-1.4,2.7	----	-42.8,48.8	*	0.8,1.3	-6.2,16.3
	500	-3.8,4.1	-1.8,2.6	----	31.1,37.3	*	0.7,1.5	-7.9,15.0
	550	-2.7,3.0	-1.6,2.2	----	-22.1,28.2	*	0.4,1.3	-9.3,13.9
	600	-1.6,2.0	-1.4,2.4	----	-16.8,22.6	-18.3,21.0	-0.1,1.2	-9.6,13.1
	650	-0.8,1.3	-1.1,2.9	----	-14.1,19.3	*	-0.2,1.0	-9.1,12.4
	700	-0.4,1.0	-1.7,3.3	----	-12.8,17.4	*	-0.2,0.9	-8.3,10.5
	750	0.2,1.0	-1.9,2.6	----	-12.7,16.4	*	0.2,0.8	-6.9,9.9
	800	-0.5,1.6	0.2,1.2	----	-12.3,15.1	-2.3,6.7	0.3,0.8	-5.1,8.9
	850	-1.7,2.1	1.2,1.8	----	-10.5,12.4	*	-0.2,0.5	-2.1,7.6
	900	-4.6,4.7	0.6,1.3	----	-4.5,7.4	*	0.0,0.8	-2.6,6.8
SFC	-0.2,1.1	0.3,1.5	0.0,0.7	----	*	0.6,0.9	----	

(e) Time/Date: 2345 GMT 6 March 1982

Number of grid points used: 130 "Regression"

		PARAMETERS						
		T (°C)	TD (°C)	PW (mm)	Z (m)	Thickness (m)	Grad T (°C/100km)	Grad Z (m/100km)
Pressure Levels	100	0.5,0.8	----	----	-64.6,70.3	*	0.3,0.6	11.1,27.0
	150	-1.3,1.5	----	----	-63.5,67.6	*	0.4,0.7	1.3,26.1
	200	1.2,1.6	----	----	-66.3,70.0	8.6,22.8	0.2,1.0	-4.0,26.3
	250	-0.1,1.0	----	----	-73.2,76.4	*	0.1,0.8	-5.7,24.1
	300	-0.3,1.7	----	----	-67.3,71.2	*	1.1,1.8	-5.0,23.8
	350	-1.4,1.6	7.2,9.2	----	-61.6,66.1	*	0.2,1.0	-3.6,23.1
	400	-1.4,1.7	0.1,5.0	----	-57.3,61.8	-39.8,41.7	-0.0,1.0	-3.2,18.3
	450	-3.7,4.0	-1.2,3.6	----	-47.7,52.8	*	0.7,1.3	-3.9,16.9
	500	-4.3,4.8	-0.3,1.5	----	-33.4,37.3	*	0.6,1.4	-3.9,14.0
	550	-3.3,3.6	-0.5,1.6	----	-23.0,26.4	*	0.2,0.9	-4.2,11.9
	600	-2.0,2.2	0.3,1.8	----	-16.4,19.6	-24.2,26.5	-0.1,0.5	-3.1,11.1
	650	-1.4,1.6	-0.7,1.6	----	-12.3,15.2	*	-0.2,0.5	-1.9,8.9
	700	-1.2,1.4	-1.4,2.2	----	-9.2,11.9	*	-0.2,0.5	-0.6,7.8
	750	-0.7,1.2	-2.6,3.4	----	-7.4,10.4	*	0.2,0.8	0.6,7.1
	800	-1.0,1.4	-1.1,2.0	----	-5.8,9.3	-5.7,7.3	-0.1,0.7	2.2,6.9
	850	-1.4,1.9	0.8,1.8	----	-3.5,7.6	*	0.0,0.9	3.1,6.3
	900	-1.3,1.8	1.8,2.2	----	-0.9,5.3	*	0.5,0.9	1.9,4.7
SFC	0.5,1.3	0.4,1.8	0.4,0.8	----	*	0.5,0.8	----	

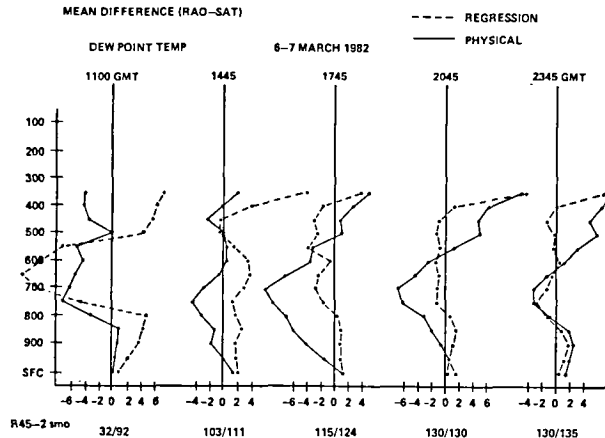


Figure 5-15. As in Figure 5-14 except for dewpoint temperature.

the later time periods. The increase in temperature bias in the middle troposphere at 1745 GMT, seems related to the inversion which developed when the tropopause lowered, creating a sudden change in lapse rate (Figure 5-19). The RMS differences between the radiosonde and satellite (Tables 5-12 and 5-13), show the largest values at pressure levels where large biases are indicated in mean difference temperature profiles. Values in these trouble areas approach and often exceed 3.0°C . In the well-behaved areas, RMS temperature difference values become as low as 1.0°C and consistently remain in the 1 to 2°C range.

Mean dewpoint temperature differences (Figure 5-15) indicate several major differences. First, there is a strong tendency for physical retrievals to overestimate low-level moisture and underestimate it aloft (although dewpoint may incorporate temperature biases as previously dis-

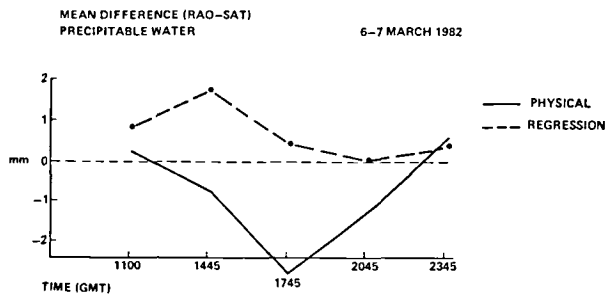


Figure 5-16. As in Figure 5-14 except for a single layer value of precipitable water from the surface through 350 mb.

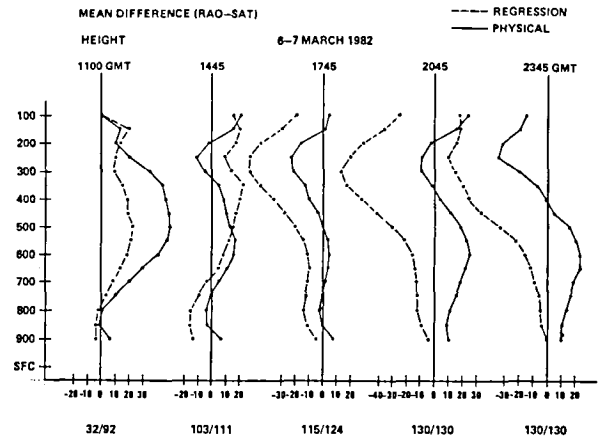


Figure 5-17. As in Figure 5-14 except for geopotential height values. Units are in meters.

cussed, the trends and magnitudes of the biases are different, allowing for the inference of moisture biases). Difference values reach a maximum near 700 mb and often exceed 5°C (Table 5-12). Upper-level underestimations of moisture above 500 mb are similar in magnitude to the low-level biases, especially at 2045 and 2345 GMT. The mean dewpoint temperature differences for the regression technique indicate a different picture (Table 5-13 and Figure 5-15). Difference values rarely exceeded 4°C , and are generally in the 2°C range, except in the first time period, when clouds permitted computations over only one-fourth of the grid. No consistent trend is evident, except for the tendency of the regression retrievals towards upper-level dryness, as revealed by the physical retrieval scheme. RMS dewpoint

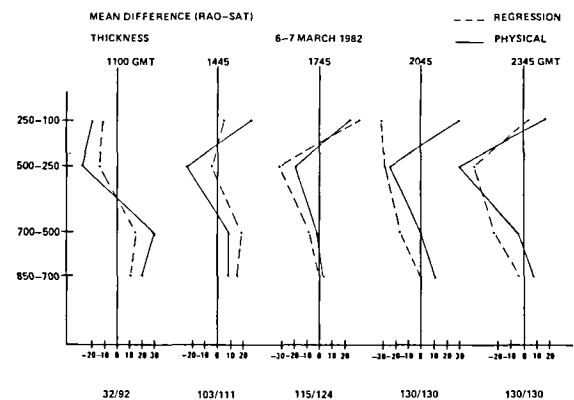


Figure 5-18. As in Figure 5-14 except for thickness calculated over the 850-700 mb, 700-500 mb, 500-250 mb, 250-100 mb layers. Units are in meters.

differences are considerably better for the regression retrievals than the physical ones, at all levels.

Typical values run in the range of 2 to 3°C in the lower levels and are slightly higher aloft. RMS dewpoint differences run about 50 percent higher than this at most levels. The grid mean dewpoint profiles in Figure 5-19 show these differences graphically. The regression retrievals maintain a vertical dewpoint profile in the grid mean which is consistent with ground truth data, although the physical retrievals do not realistically represent this quantity. Results of absolute moisture comparisons (mixing ratio) are not presented, but they indicate very similar findings to those of dewpoint.

Another means of evaluating the performance of VAS moisture retrievals is the investigation of precipitable

water in the column from the surface to 350 mb, since the contributions above this level should be negligible (Figure 5-16). It is obvious from this figure that the physical retrievals overestimate the moisture in the surface to 350-mb column, in the middle time periods. RMS differences (Tables 5-12 and 5-13) at 1745 GMT exceed 3.0 mm. Although traditionally this may not be extreme, it represents a 30 percent error, considering the fact that the mean satellite value over the grid region is 10.3 mm. The regression retrievals are quite well in determining atmospheric moisture content (except for the first two sounding times). RMS differences average to about 1.0 mm (not including the first time period).

In the evaluation of the geopotential height values, it must be remembered that the temperature biases (and,

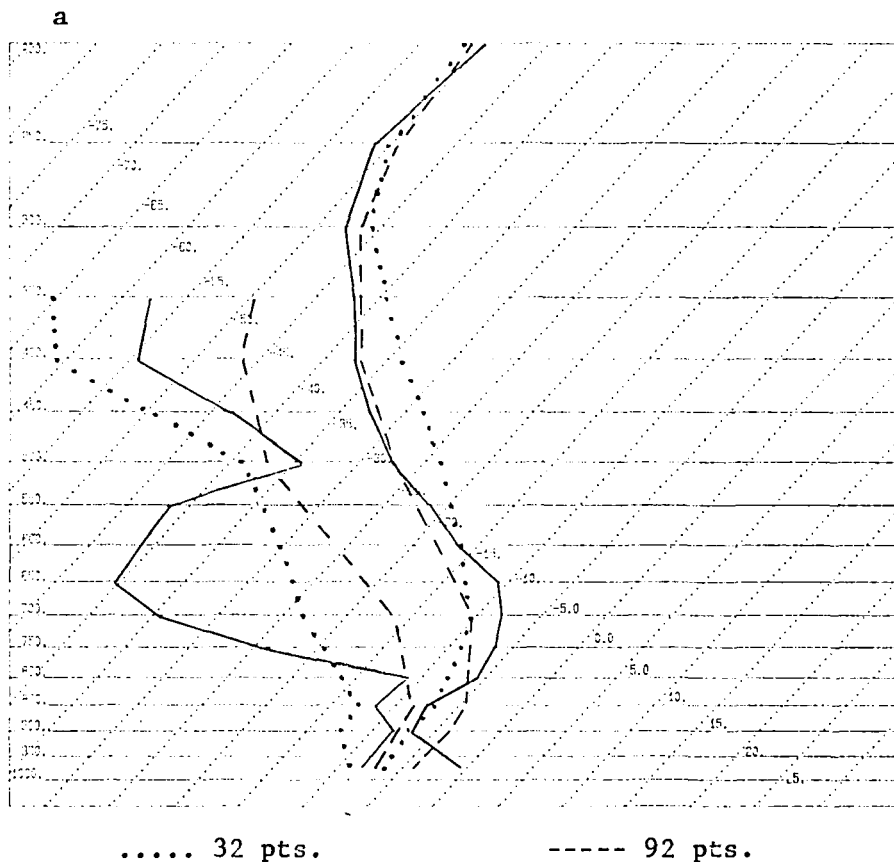


Figure 5-19. Vertical profiles of temperature and dewpoint temperature averaged over the grid region at 1100 GMT (a), 1445 GMT (b), 1745 GMT (c), 2045 GMT (d), 2345 GMT (e). The rawinsonde profiles are solid lines (—), the “physical” satellite retrievals are dashed lines (-----), and the “regression” retrievals are dotted lines (.....).

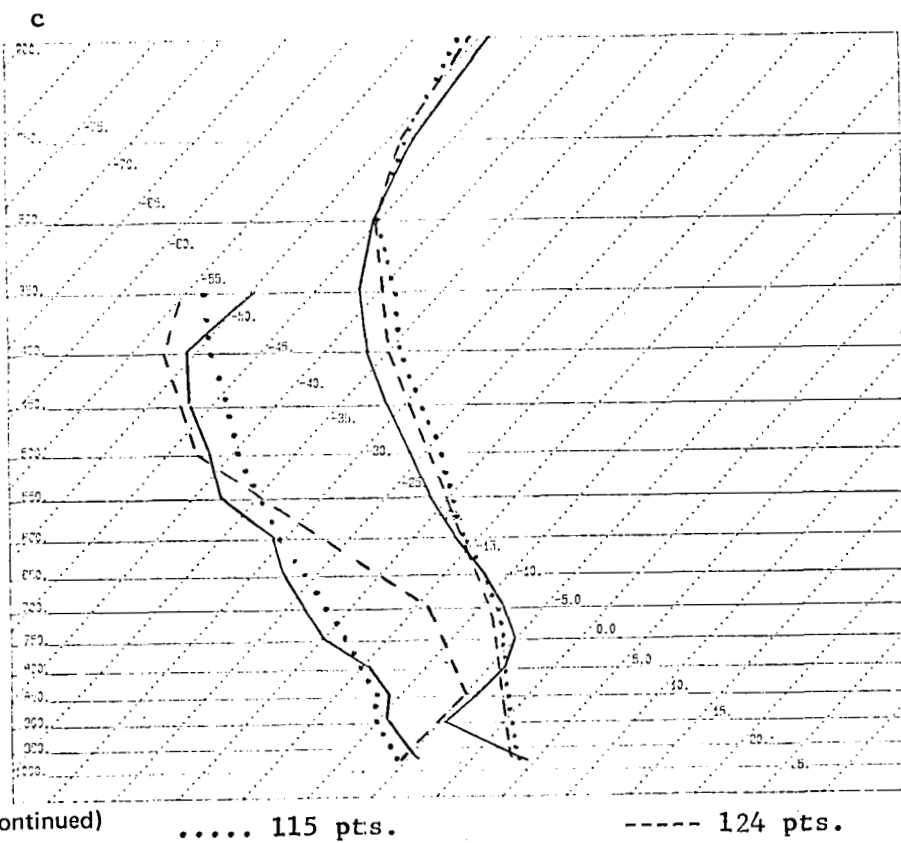
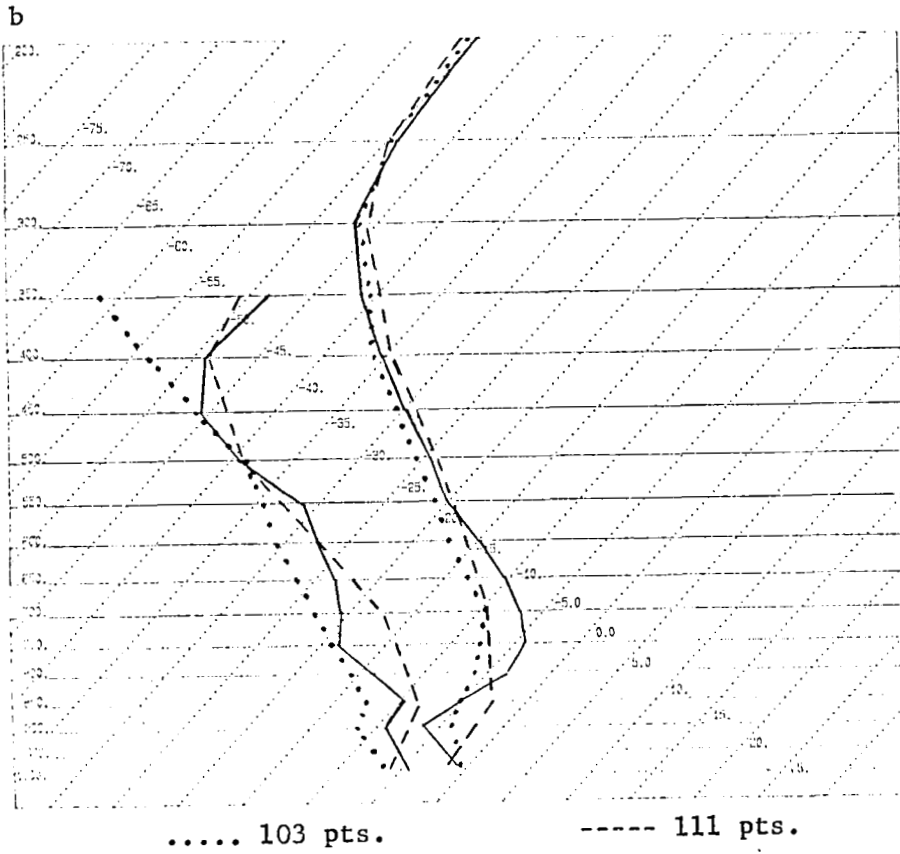


Figure 5-19. (Continued)

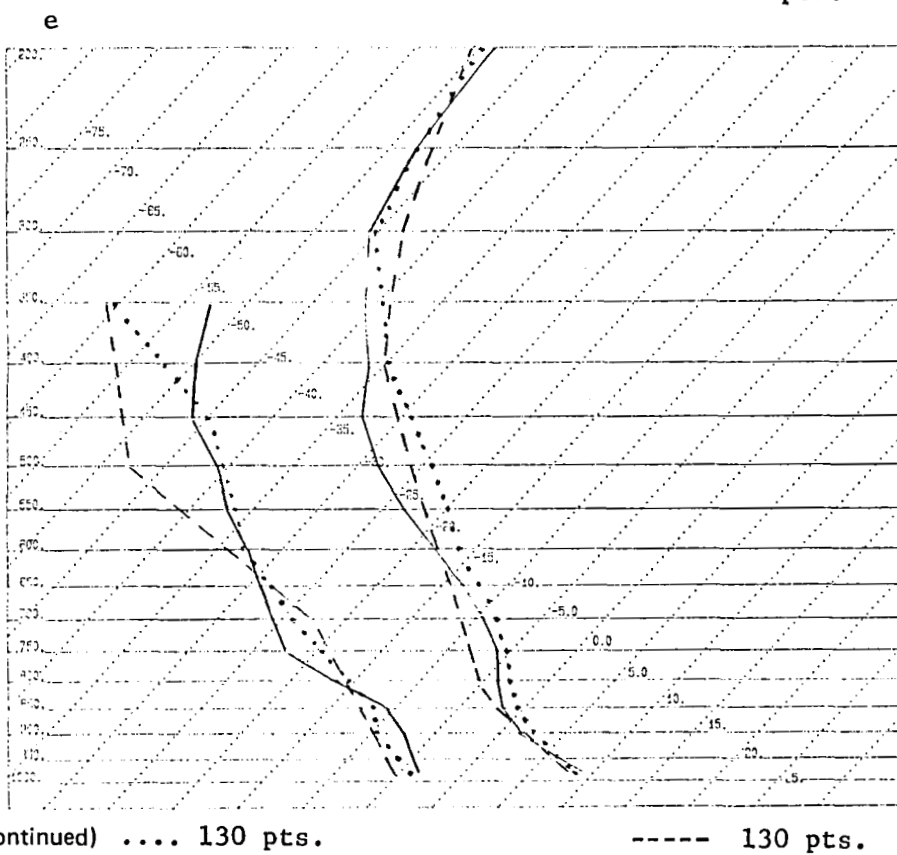
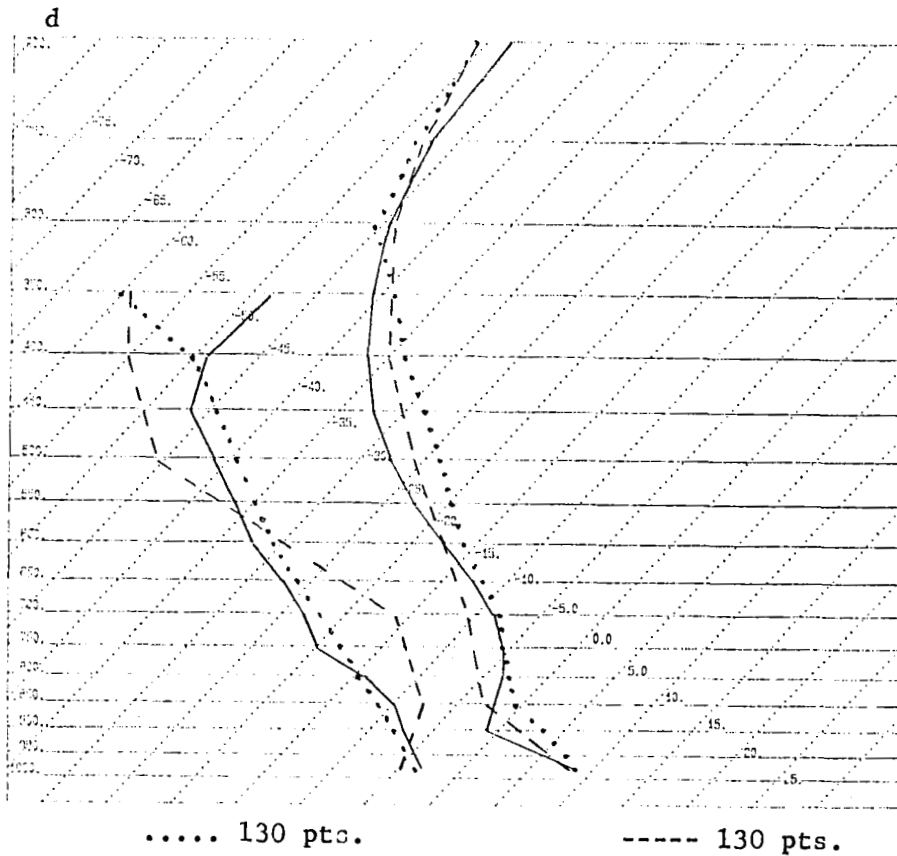


Figure 5-19. (Continued)

to a lesser degree, the moisture biases) will directly effect the height calculations. It should also be noted that alternating warm and cold satellite biases at adjacent pressure levels can have a compensating effect on the results. Therefore, the geopotential height, and the thickness will be evaluated for satellite retrievals. The mean and RMS differences for these parameters are presented in Tables 5-12 and 5-13. The mean differences for geopotential height and thickness, calculated over four arbitrary layers of the atmosphere, 850 to 700 mb, 700 to 500 mb, 500 to 250 mb, and 250 to 100 mb, are presented in Figure 5-17 and Figure 5-18. These parameters show the results of temperature biases at various levels. Warm temperature biases produce height and thickness values which are too large ($Z_R - Z_S < 0$), and in result, produce negative mean difference values. Low-level warm biases (Figure 5-14) produce small height biases in the lowest layer of the atmosphere. The cold bias centered around 700 mb, extends over many pressure levels, and has substantially more effect in producing reduced satellite-derived height values. As the temperature biases become smaller (by 1745 GMT at this level), the height and thickness biases become quite small for the physical, and the regression retrievals. These height biases change in the last two times as the temperature biases increase. Major height biases occur above 500 mb for both satellite sounding sets. Negative biases are considerably larger for the regression scheme. Maximum mean height difference values exceed 60 m over several layers at 2045 and 2345 GMT for the regression retrievals, but the corresponding physical difference values only exceed 30 m at 2345 GMT. This is mainly due to the integrated effect of the temperature biases from the middle layers (see Figure 5-14). Thickness values in the uppermost two layers indicate that similar biases exist for each retrieval method, except at 2045 GMT. Maximum mean difference thickness values occur in the 500 to 250-mb layer at all times with magnitudes around -30 m for each retrieval scheme, except at 2345 GMT, at which time the physical bias exceeds -50 m, and the regression bias approaches -40 m.

5.3.1.3 Vertical Structure of VAS Retrievals

In order to evaluate the performance of VAS soundings in describing the vertical structure of the atmosphere, grid mean values of temperature and dewpoint were plotted as a function of pressure (Figure 5-19). The radiosonde profiles (solid lines) indicate a strong low-level frontal inversion, that slowly becomes eroded by surface and boundary layer heating during the day. Dewpoint temperatures indicate a dry region above the

frontal inversion, with a slight increase in moisture above 450 mb. The satellite profiles (dashed lines) do not capture the complete vertical structure exhibited by the radiosonde data, and present more of a vertical mean profile of the atmosphere. This is due to the broad and overlapping weighting functions for each channel, and to the horizontal averaging performed in retrieval process to reduce the signal-to-noise ratio. As noted earlier, large biases exist at various levels and times, as well as large differences between each type of satellite retrieval. It should be noted that despite these biases, there is a tendency for both sets of VAS soundings to capture the inversions, and to mis-assign their pressure levels. This is best illustrated at 1445 GMT (Figure 5-19b), when the nose of the frontal inversion (temperature profile) appears to be centered at about 750 mb. The physical scheme (dashed line) puts the nose at 850 mb, and the regression scheme (dotted line) at 700 mb. Also, in the upper levels at 2045 GMT, an inflection point is reached at about 400 mb, although the satellite retrievals detect this at a much higher level. For the physical scheme, VAS temperature values were derived at standard levels only, and therefore could not be linearly interpolated to get an inflection point at a level between. The regression scheme retrieves a temperature and moisture value at 920 mb, providing the additional structure that seems well correlated to the ground truth radiosonde profile.

5.3.1.4 Horizontal Structure of VAS Retrievals

The statistical evaluation performed in 5.3.1.2 examined the grid point values of various satellites and rawinsonde parameters in relation to the mean, and deviations from the mean. In this section, rawinsonde and satellite grids will be shown that qualitatively indicate the horizontal resolution of VAS sounding data, and are followed by a quantitative discussion examining the gradient values of various parameters.

Figure 5-20 shows the horizontal temperature analysis at 500 mb over the mesoscale grid region for each data set at 1445, 1745, 2045, and 2345 GMT, for 6 March 1982. The ground truth radiosonde data exhibit a strong temperature gradient in the northwest to southeast direction. This gradient weakens with time, and a cold pocket develops over the center of the network by 2345 GMT. The VAS soundings capture these two features fairly well. The analysis of the physical retrievals indicate a somewhat weaker temperature gradient, aligned in the same direction. The physical retrievals show a weakening of the gradient with time, although they do not show a cold pocket at 2345 GMT. The regression retrievals

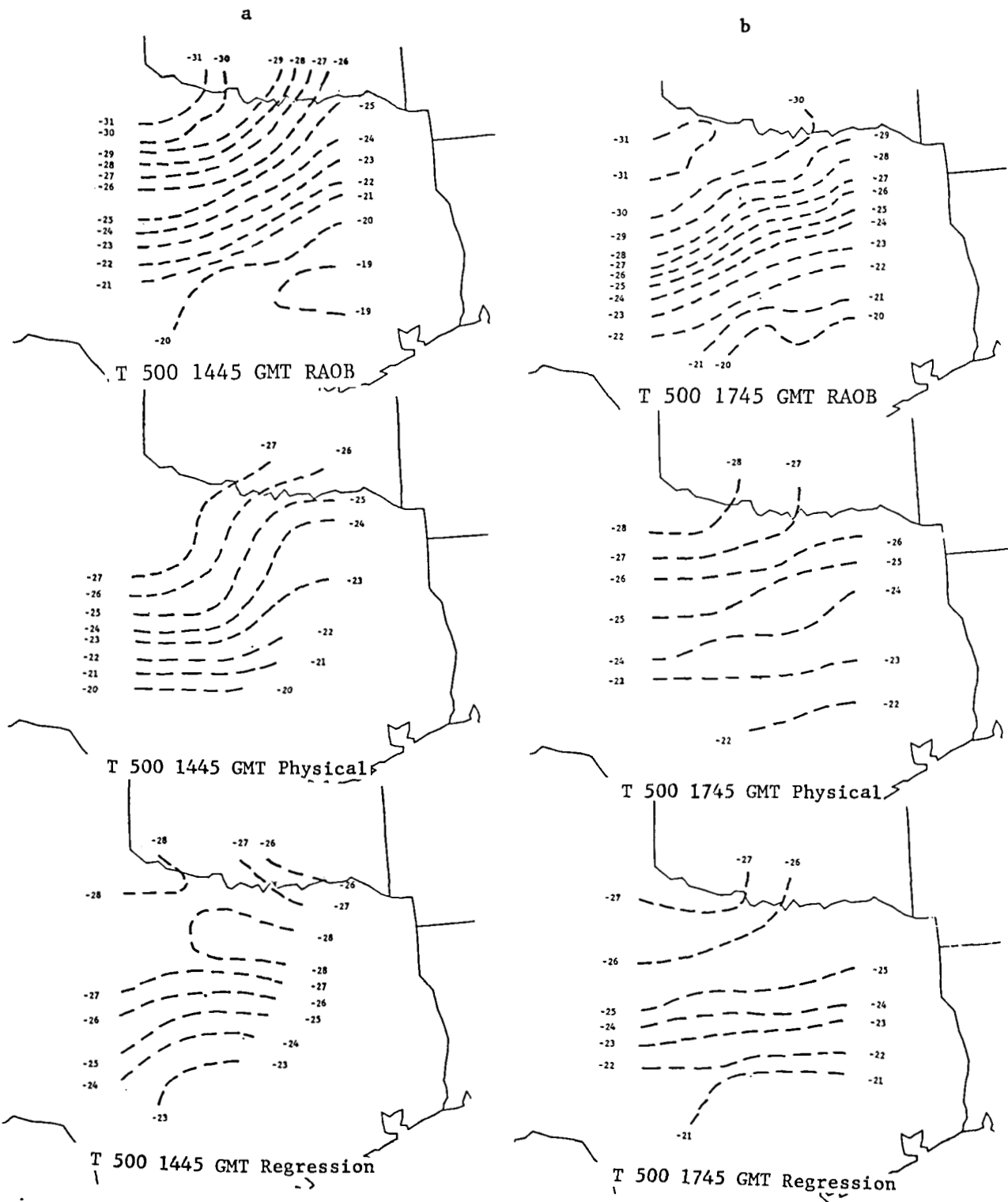


Figure 5-20. Gridded field analyses of 500 mb temperature for radiosonde and satellite data at a) 1445 GMT, b) 1745 GMT, c) 2045 GMT, and d) 2345 GMT. Units are in °C.

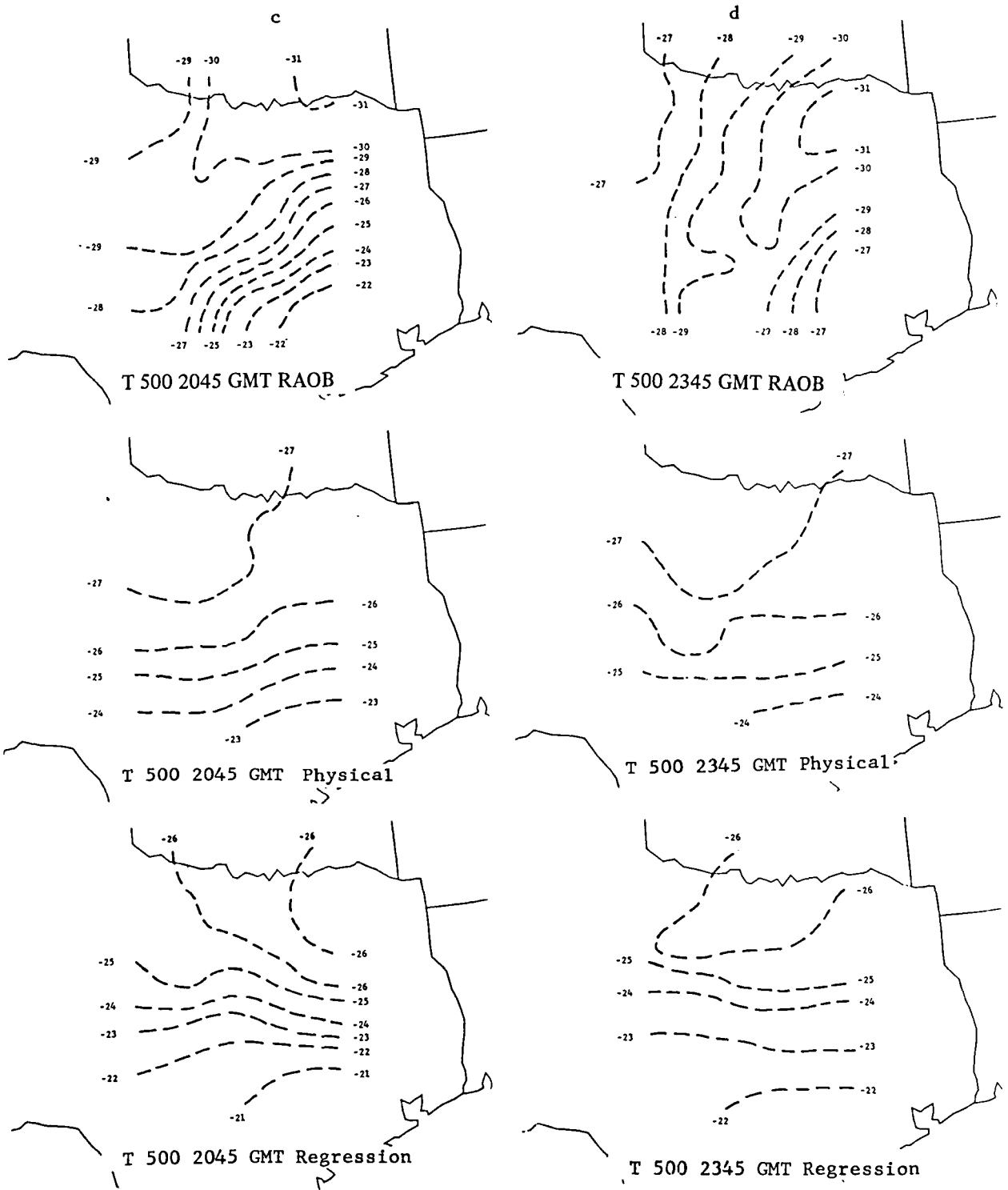


Figure 5-20. (Continued)

also represent the horizontal gradient fairly well (except for 1445 GMT), and seem to capture the cold pocket which developed over the network at the last two times. The strength of this cold pocket is not as strong as in the radiosonde data. The failure of the VAS soundings to capture the mesoscale cold region as it propagated through the network is largely responsible for the temperature biases noted earlier.

Figure 5-21 shows the 700-mb dewpoint temperature analysis over the mesoscale region. Large changes occur in the radiosonde analysis as colder and drier air moves into the region. A fairly strong gradient exists from cold dry air in the northwest portion of the network, to warmer and moister air in the southeast region. This gradient shifts to north-south alignment as it weakens by 2345 GMT. The physical retrievals analyzed over the region indicate a slightly reduced dewpoint gradient at 700 mb, with its axis in a north-south direction. The coldest and driest areas do not appear to be well represented. The regression retrievals do not represent the 700-mb dewpoint gradient as well as the physical retrievals, as the gradient is considerably weakened (appearing to represent a mean of the radiosonde dewpoint field). This is related to the lack of VAS moisture-related radiance information near the 700-mb level, as discussed by Lee *et al.* (1983).

Geopotential height analyses were also generated for the 300-mb level (not shown), for which large biases existed in both satellite sounding data sets. Despite these biases, both sets of soundings represent the 300-mb height field fairly well. The radiosonde analysis indicates a strong height gradient that shifts from a northwest-southeast alignment to a northeast-southwest one, as the upper-level trough moves through the region. The physical retrievals present a smoother geopotential height as compared to the radiosonde data, with a less defined trough pattern. The 300-mb height pattern, determined by the regression soundings, reveals more mesoscale variability than the physical retrievals, and nicely defines the upper-level trough as it becomes centered over the network at about 2345 GMT. It should be noted that despite the large biases evident in the fields, the patterns in the two VAS sounding height fields are similar to those of the radiosonde data. A quantitative presentation of this will be discussed shortly.

The final set of grids to be shown are that of precipitable water in a column integrated from the surface to 350 mb (Figure 5-22). The radiosonde grids indicate a strong moisture gradient similar to that of the dewpoint (dis-

cussed previously) that decreases with the impinging cold dry air. The physical grids indicate a similar trend and define the gradient pattern fairly well, despite the moisture bias at the middle times, as previously indicated. The regression retrievals present an overly smooth moisture field. The gradient pattern does not change with time as the drier air moves in, as indicated by radiosonde data.

5.3.1.4.1 Evaluation of Horizontal Gradients—In order to quantitatively evaluate the extent to which VAS soundings can be used to determine mesoscale gradients, the magnitude of the gradient of various parameters was evaluated at each grid point. Mean and RMS differences (Tables 5-12 and 5-13) were calculated as before. The results for the gradient of temperature are shown in Figure 5-23. The temperature gradient calculations indicate that largest gradient biases occur at the levels where temperature biases are greatest (Figure 5-14), which also are the levels where the mean radiosonde temperature gradient is large (not shown). A positive bias ($vT_R - vT_S > 0$) indicates a weaker satellite gradient when compared to the radiosonde grids. Most of the biases are positive for both satellite data sets (Figure 5-23). Negative satellite biases (satellite gradient is stronger than rawinsonde gradient) occur at various levels and times. These biases often occur when the satellite gradient is small. Largest mean difference values occur for both satellite data sets in the middle levels, and maintain values of about $1.5^\circ\text{C}/100\text{ km}$ at most times. Although this seems quite small, it represents 60 percent of the mean 500-mb gradient of $2.5^\circ\text{C}/100\text{ km}$ for the radiosonde data. Physical and regression differences are not always the same, and no recognizable trend is evident to explain them.

5.3.1.5 Discussion and Conclusions

The procedures used in this study have helped to reduce the known time and space discrepancies between the satellite sounding data sets, and the ground truth radiosonde data. Large differences between the two data types still exist, and are evident from the results. Also, differences exist in the two satellite sounding sets (presumably because of the retrieval procedures and not the input VAS radiance data). It is difficult to determine which retrieval scheme is better. The answer to this might depend on the application of the data. It is obvious that the physical scheme overestimates the low-level moisture, as demonstrated with various parameters. The vertical profile and statistical results for moisture from the regression scheme seem quite good,

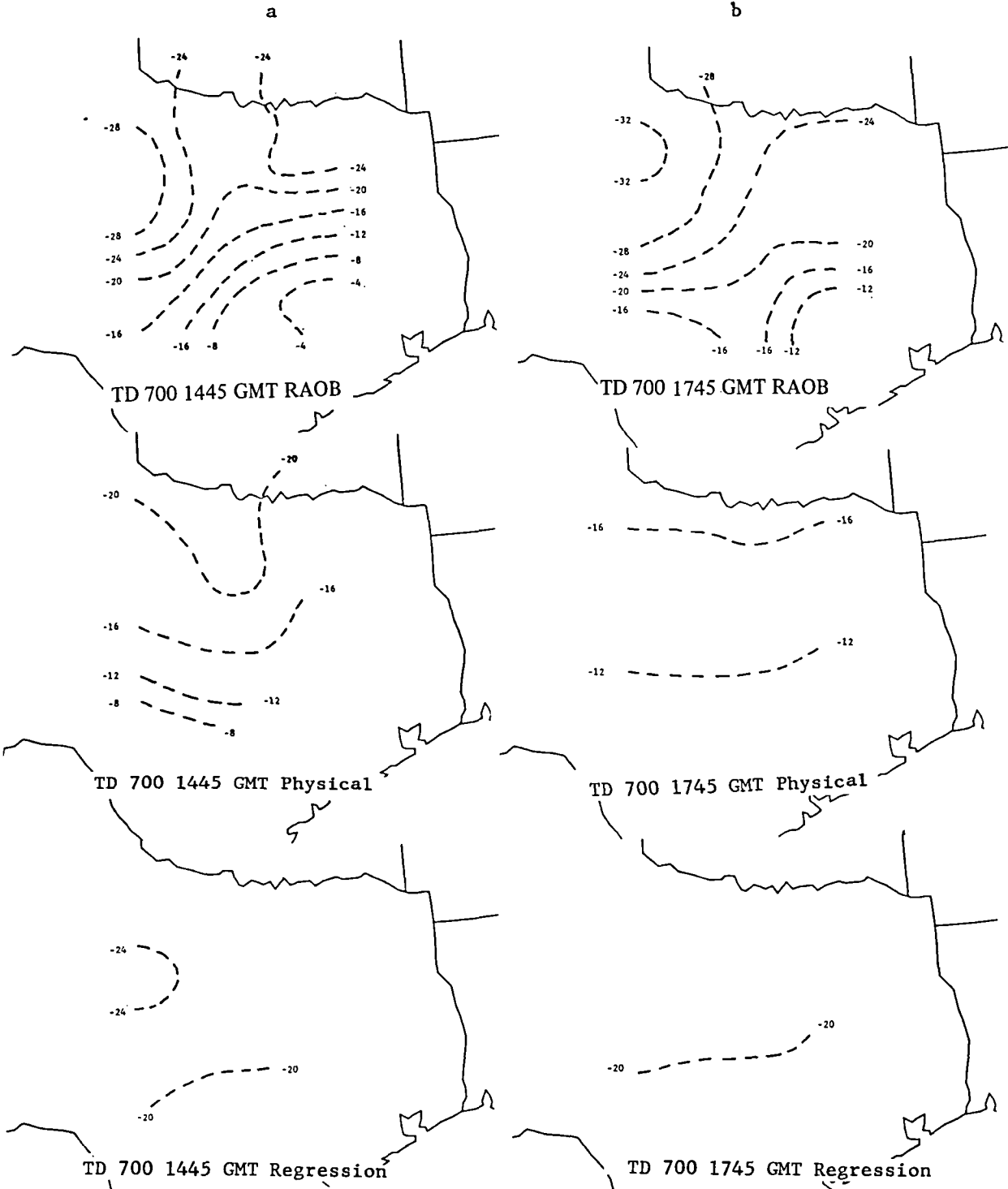
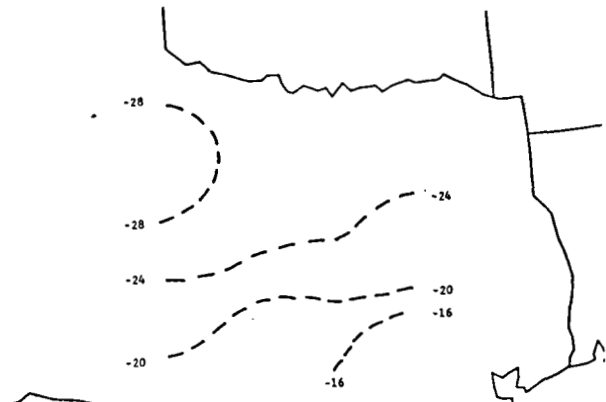


Figure 5-21. Same as in Figure 5-20 except for dewpoint temperature at 700 mb.

c

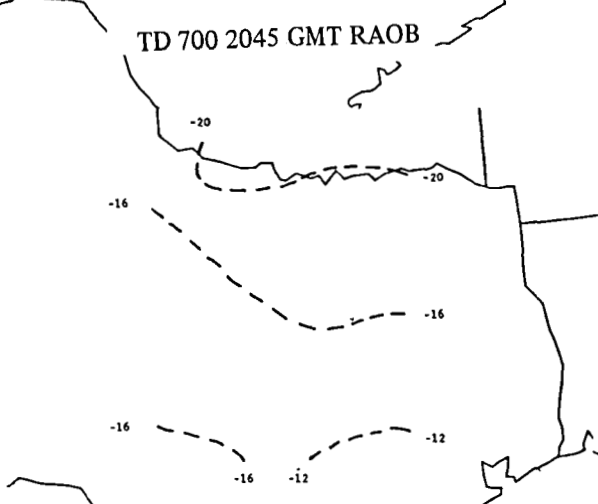


TD 700 2045 GMT RAOB

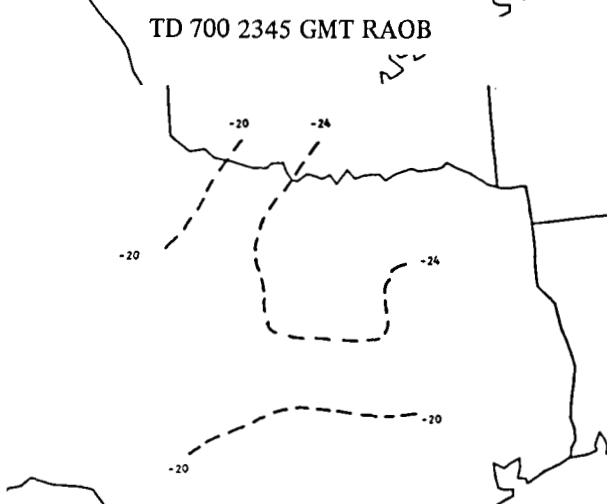
d



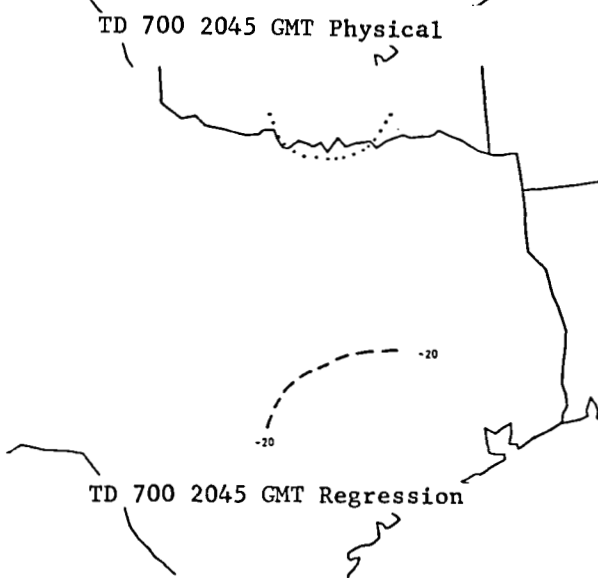
TD 700 2345 GMT RAOB



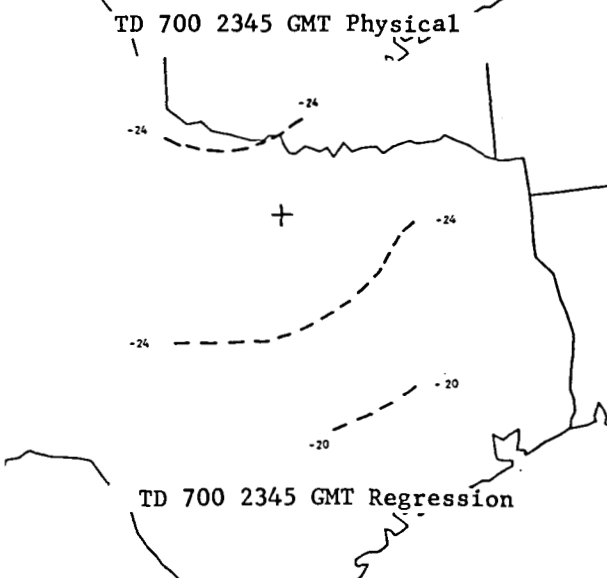
TD 700 2045 GMT Physical



TD 700 2345 GMT Physical



TD 700 2045 GMT Regression



TD 700 2345 GMT Regression

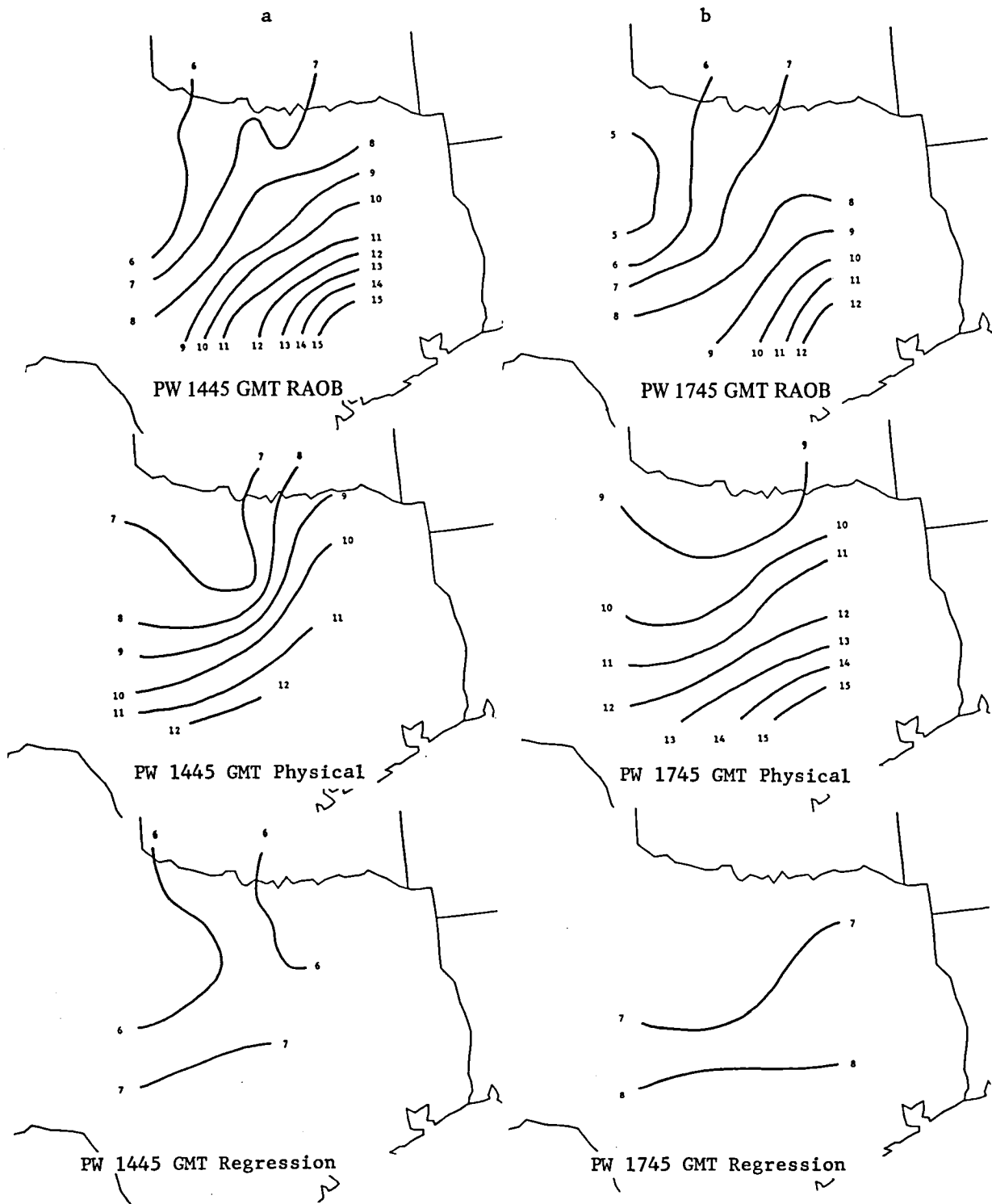


Figure 5-22. Same as in Figure 5-20 except for precipitable water.



Figure 5-22. (Continued)

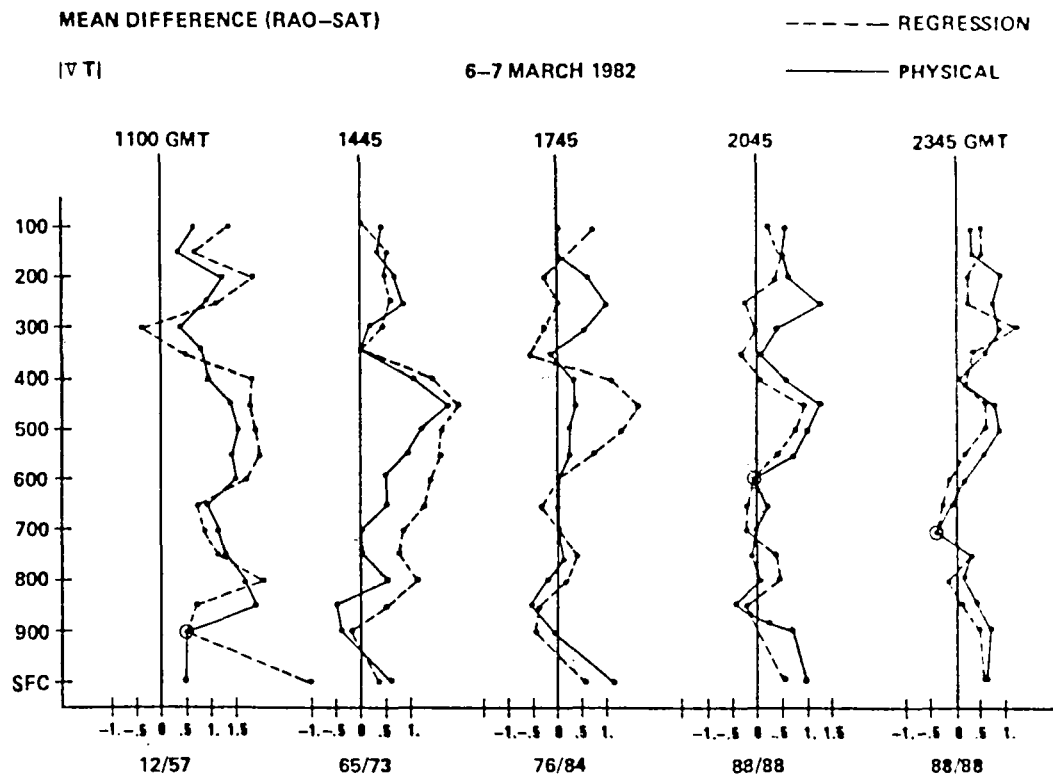


Figure 5-23. As in Figure 5-14 except for the magnitude of the temperature gradient in $^{\circ}\text{C}/100\text{km}$.

although the regression retrievals do not adequately describe the horizontal moisture structure over the mesoscale region. Temperature and height gradients for both satellite data sets present good representations of the mesoscale environment, except that their magnitudes were reduced by about 30 to 50 percent.

Biases in the satellite temperature and moisture profiles seem to be extremely dependent on the structure of the atmosphere. The strength and height of inversions greatly effect the vertical structure of a retrieved profile, and the magnitude of the biases at various levels. As the low-level temperature inversion broke down during the day on 6 March, the low-level temperature biases were substantially reduced.

Some of the biases presented in this study, and a fraction of the biases at various levels, may be due to RMS errors in the ground truth radiosonde data. An evaluation is underway to assess how these assumed radiosonde errors affect the mean and RMS differences calculated over the mesoscale grid region.

A major portion of these biases may be due to the

sampling aspect of the two measurement types. The radiosonde, is a point measurement, and detects atmospheric properties of a small volume. VAS soundings are often produced using average radiances over a large horizontal region (1000 km^2 to 5000 km^2), and therefore represent some type of spatial average. Bruce *et al.* (1977) have examined the atmospheric variability over various spatial scales, and claim that this sampling problem could explain discrepancies of about 1°C at most pressure levels. An evaluation of this problem is currently being conducted.

Despite some of the large discrepancies between the radiosonde and satellite-derived values, it is apparent that VAS sounding data can be very useful in describing the atmosphere. VAS sounding data in the 6 March 1982 case may not provide horizontal resolution similar to that of the mesoscale radiosonde network, although much more detail is presently available than was available routinely, with standard NWS radiosonde observations. Caution must be used in interpreting observable features in VAS data. Not all fluctuations in VAS data correspond to variations described by the ground truth data (at least in this study). More ground truth studies that represent a variety of atmospheric conditions are

needed to evaluate how well VAS soundings describe the atmosphere, to establish error statistics, and to better understand the most effective usages for VAS soundings, by taking full advantage of their most reliable characteristics.

5.3.2 GSFC Verification of VAS Regression Soundings of 6 March 1982

D. Chesters
R. A. Petersen
L. W. Uccellini

*Goddard Laboratory for Atmospheric Sciences
Goddard Space Flight Center
National Aeronautics and Space Administration
Greenbelt, Maryland*

T. H. Lee
*Computer Science Corporation
Silver Spring, Maryland*

A. Mostek
D. A. Keyser
W. Robinson
*General Software Corporation
Landover, Maryland*

5.3.2.1 "VAS Plus Surface" Regression Soundings

The VAS soundings by the Goddard Laboratory for Atmospheric Sciences (GLAS) are obtained by using the linear regression technique (discussed in Section 5.1), that uses VAS radiances plus conventional surface temperature and dewpoint data [called "VAS plus SFC" method, Lee *et al.* (1983)]. The March 6 regression coefficients were calculated with data from the synoptic dawn and dusk radiosonde observations, the airways surface reports, and the corresponding cloud-free VAS IR measurements within the selected region of the central United States. In addition, an estimate of the 1800 GMT upper-air sounding set was included in the training data to emulate diurnal variations of temperature and dewpoint. These soundings were generated by a linear interpolation between the 1200 GMT and 0000 GMT operational soundings, and the 1800 GMT surface data which influenced the lower portion of the estimated soundings. The 1200 GMT, 1800 GMT, and 0000 GMT sounding sets yielded a total of 50 coincident VAS/radiosonde/surface samples that were used to compute the regression coefficients. To reduce the skin temperature effects, the 3.9- μm window channel was also eliminated as a predictor. Throughout the training, sounding, and the evaluation processes, VISSR images

were exploited using the interactive VAS sounding system at GLAS in a "person-in-the-loop" mode to minimize cloud contamination.

5.3.2.2 Statistics of Retrieval Errors

A total of 112 retrieved temperature and dewpoint profiles were computed from the "VAS plus SFC" regression matrix at five different times on 6 March. The VAS retrievals were separated into two groups, which correspond to the AVE Special Network and the regular NWS radiosonde sites (Figures 5-8 and 5-9). The NWS data set is not completely independent, because approximately half of the samples (at 1200 and 0000 GMT) were used for computing the retrieval regression matrix.

An example of a time series of temperature and dewpoint profiles from radiosonde and VAS soundings is shown from 1130 to 2300 GMT 6 March for Henrietta, Texas (Figure 5-24). In this typical example for clear conditions, retrieval errors are only a few degrees for temperatures and dewpoints above the 850-mb level. The warming trend in the lower troposphere is well retrieved, but the early morning dryness at 700 mb is not captured. This should be expected since there are no VAS channels which are moisture-sensitive at 700 mb. The largest errors are found near the midday temperature inversion (around 900 mb) that occur in a layer that is too thin for the VAS channels to resolve. Inversion structures are always difficult to retrieve from infrared remote sensing techniques, due to limited vertical resolution. The AVE data also indicate a cool layer at 500 mb that the VAS retrievals under-estimate.

Statistical evaluations of the VAS retrievals at GSFC were conducted for three different sets of soundings. Basically the first set was accepted with little quality control and is termed the "minimum screening" set. The second set has "stringent co-location" criteria placed on *all the soundings* in an effort to assess the quality of the ground truth radiosonde data base. The third set consists of VAS soundings which are known to be "cloud-free."

5.3.2.2.1 Minimum Screening—Table 5-14 shows the statistics of ground truth and retrieval accuracy for temperature up to the 500-mb level and dewpoint up to the 700-mb level. The 49 samples from the AVE radiosonde Network and 63 samples from NWS radiosonde sites are selected with a minimum screening (i.e., avoiding the sites with bad radiosonde reports or those with extensive cloud cover). The VAS minus radiosonde differences

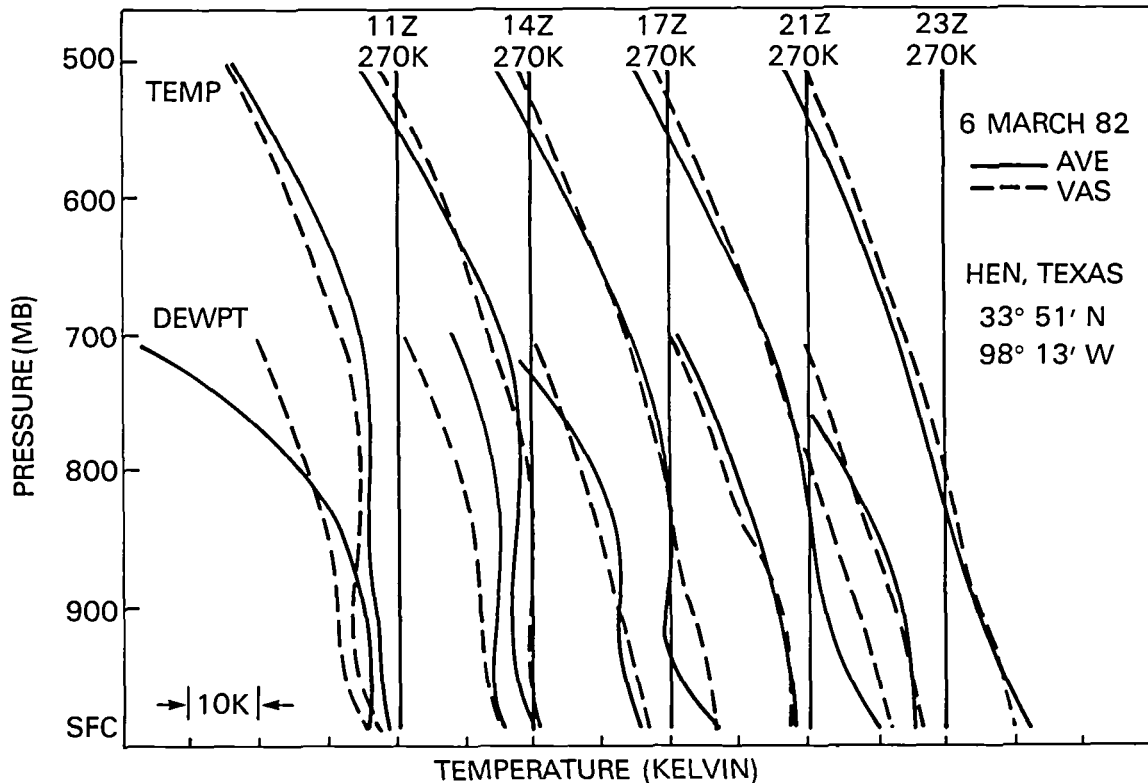


Figure 5-24. VAS/AVE profiles at HEN

are listed as mean errors, RMS residuals, and recovery rates (fractions of the variances retrieved by regression).

In general, the quality of VAS retrievals in the regular NWS radiosonde group are comparable to the results of the 1981 midsummer preconvective case studies (see Section 5.1). For this group, the absolute RMS accuracies are between 1.5 and 2.5°C for temperatures below the 500-mb level and for dewpoints below 850 mb. For the AVE Special Network group, the biases are noticeably higher and the boundary layer temperature and dewpoint retrievals are unrealistic. Nevertheless, the recovery rates are good, because of high variances in the ground truth. A detailed examination of individual VAS soundings reveals two possible sources of error, the discrepancy between radiosonde and airways reports of temperature and dewpoint at the surface, and cloud contamination. Therefore, two more groups of retrievals were created and analyzed to test the effect of each source of error.

5.3.2.2.2 Stringent Co-location—Many large discrepancies were found between the radiosonde surface temperature and dewpoint observations in the meso-β special

network and the surface reports from the closest FAA or NWS observing stations, used in the GSFC VAS retrievals. For example, at 1200 GMT 6 March, the closest available surface report to the radiosonde site at CRO is from HBR, which is located 1.02° in latitude, and 0.66° in longitude away, from CRO. For this case, the differences between the radiosonde and surface reports were -9.6°C and -12.4°C in temperature and dewpoint, respectively. A new test subset was created by removing 20 samples from the AVE group and two samples from the NWS group, for which the closest verifying surface stations are more than 75 km away from any radiosonde site. The improved match of surface temperature and dewpoint between the RAOB and the nearby surface reports result in better boundary temperatures and dewpoint retrievals. This is indicated in Table 5-15(a). The discrepancies between the surface data from operational stations and the meso-β network sites are large enough to impact the retrievals even if the radiosonde site and surface station are closely located. The underlying source of these significant discrepancies in the “ground truth” data set is unknown. The VAS retrievals in the lower troposphere are still poor, due to the sharp inversion in the boundary layer, especially above the snow cover in northern Texas.

Table 5-14
Residual Differences Between VAS and AVE Profiles on
6 March 1982 with Minimal Data Rejection Requirements

	Ground Truth (RAOB)				Retrieval Accuracy (VAS-RAOB)						
	AVE sites		NWS sites		AVE sites			NWS sites			
	mean	± dev	mean	± dev	mean	± dev	rate	mean	± dev	rate	
Temp (K)											
1000 mb	277.6	± 4.67	273.6	± 7.12	-.38	± 2.15	.79	.65	± 1.57	.95	
920	271.3	4.20	272.1	6.18	2.38	2.55	.63	.55	2.65	.82	
850	269.3	2.10	270.9	3.91	1.19	1.51	.48	.08	2.18	.69	
700	264.5	1.66	263.1	2.82	-.65	1.62	.02	-.07	1.70	.64	
600	256.1	1.89	256.0	2.81	.04	1.89	.00	-.22	1.82	.58	
500	245.8	3.24	247.6	3.66	2.36	2.68	.32	-.14	2.40	.57	
Dewpoint (K)											
1000 mb	268.7	± 3.91	264.9	± 4.07	-1.45	± 3.07	.38	-.11	± 1.60	.85	
920	265.1	2.48	264.0	3.67	-.89	2.37	.09	-.50	2.49	.54	
850	262.6	1.51	262.0	3.34	-1.23	1.71	-.28	-.57	2.77	.31	
700	249.2	5.91	250.7	5.16	1.18	5.56	.11	.08	4.91	.09	
Sample size	49		63		49			63			

5.3.2.2.3 Effect of Cloud Contamination—Many of the minimally screened retrievals were made around cloud edges or through holes within clouds. A few test retrievals were actually obtained for sites with a low overcast. Careful screening for high-cloud contamination and other overcast sites removed 11 and 18 samples from the AVE and NWS group, respectively. The residual errors for the cloud-free retrieval data set are not very different (Table 5-15(b)), except for some of the recovery rates. The apparent degradation of the recovery rate for low-level dewpoint retrievals, for the Special Network group, is due to a reduction in the corresponding original dewpoint variances. Examination of several individual profile retrievals show that there are little effects from partial high cloud contaminations, and that the “VAS plus SFC” retrievals at overcast sites are reasonably good (presumably due to the dominance of the conventional surface data as a statistical predictor of the lower troposphere).

5.3.2.3 Field Analyses and Comparisons

The AVE ground truth radiosondes and the VAS sound-

ings were objectively analyzed to generate constant-pressure contour charts of temperature and dewpoint over Texas, Oklahoma, and Kansas for all five times on 6 March, using the GEMPAK-Barnes analysis scheme (Koch *et al.*, 1983). Unfortunately, comparisons between VAS and radiosonde analyses are difficult because of the differences in data coverage between the two data sets. Due to the presence of clouds, the larger percentage of VAS soundings are outside the dense AVE Network area, particularly at the earlier times. On the other hand, the dense VAS soundings around the Kansas-Oklahoma boundary have very few ground truth observations for verification.

Figures 5-25 and 5-26 show examples of AVE and VAS 500-mb temperature and 850-mb dewpoint fields at 1700, 2000, and 2300 GMT for the AVE data, and 1730, 2030 and 2330 GMT, for VAS. At these times, VAS retrievals cover a large portion of the Special Network region. These analyzed VAS fields use cloud-free retrievals spaced at approximately 1° in latitude and in longitude, comparable to the approximately 1.5° separation of the AVE radiosonde reports in the Special Network.

Table 5-15
Residual Differences Between VAS and AVE Profiles on 6 March 1982
With (a) Close Surface Location and (b) Cloud-Free Requirements

	(a) Close Surface Location					(b) Totally Cloud-Free					
	Ground Truth		Retrieval Accuracy			Ground Truth		Retrieval Accuracy			
	mean	± dev	mean	± dev	rate	mean	± dev	mean	± dev	rate	
Temp (K)											
1000 mb	278.3	± 4.27	.20	± 1.83	.81	278.4	± 4.75	.54	± 2.23	.78	
920	271.7	3.84	2.88	2.56	.56	272.1	4.32	2.51	2.81	.58	
850	269.7	1.84	1.23	1.69	.16	269.8	1.90	1.14	1.51	.37	
700	264.6	1.57	-.55	1.42	.18	264.0	1.32	-.27	1.46	-.22	
600	255.9	1.68	.36	1.61	.08	255.4	1.16	.55	1.56	-.81	
500	246.0	3.18	2.41	2.55	.36	245.0	2.80	2.94	2.53	.18	
Dewpoint (K)											
1000 mb	268.6	± 4.22	-.76	± 2.67	.60	268.7	± 2.74	-1.79	± 2.64	.07	
920	265.3	2.95	.45	2.40	.34	264.9	1.75	-.82	2.23	-.62	
850	262.7	1.55	-1.13	1.73	-.25	262.6	1.38	-1.45	1.69	-.40	
700	248.4	6.01	2.05	5.60	.13	248.1	5.53	1.95	5.38	.05	
Sample size	29		29				38		38		

The AVE 500-mb temperature field (Figure 5-25) contains a pocket of cold air between northwestern Texas and southwestern Oklahoma, that moves across the Network over the next six hours. A moderately strong temperature gradient is present in the cloudy area to the southeast of this cold air. The VAS temperature field at 500 mb is 2° to 5°C warmer than the radiosonde analysis with the coldest air displaced northward of the AVE cold air center. The VAS soundings indicate a pocket of colder air that is moving east-northeast across Oklahoma (too far north for the AVE meso-β Network to verify). The AVE radiosonde data yields a significantly different 500-mb analysis. A distinct pocket of cold air is found moving southeast across Texas. This is a feature that was scarcely retrieved by VAS. A thermal gradient is present in the VAS field to the south of the cold air pocket, but it is weaker than the gradient in the AVE field. Due to cloud cover, no comparison between the gradients across eastern Texas can be made.

The AVE 850-mb dewpoint structure (Figure 5-26) ex-

hibits no strong signal or large gradients in the Special Network region, although it shows a larger scale structure, which is a function of the surrounding NWS sites. The time continuity of this field is extremely small, due to alternating wet and dry reports from Amarillo, Texas and Topeka, Kansas. In contrast, the VAS 850-mb dewpoints are characterized by a relatively smooth, temporally stable pattern with a distinct dry pocket across the northern and western part of the Meso-β Network at all three times. VAS dewpoint temperatures in this region are 3° to 5°C lower than the corresponding AVE values. A sharp moisture gradient is retrieved over the eastern half of the Meso-β Network at 2330 GMT. The VAS retrievals indicate that the dry slot also extended northeast into Oklahoma by 2330 GMT. Clearing skies permitted VAS retrievals at this time.

5.3.2.4 Discussion and Summary

Due to extensive cloud cover in the Special Network area early in the day, and flaws in the ground truth data,

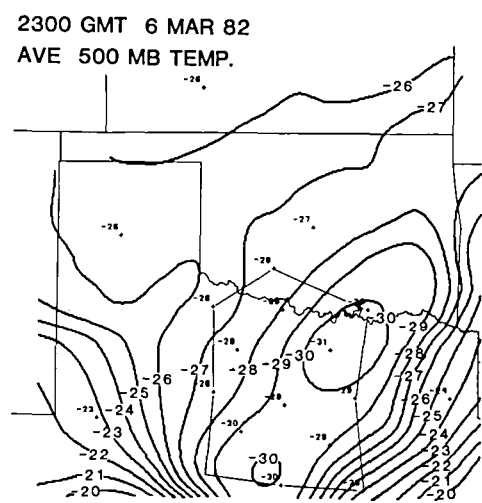
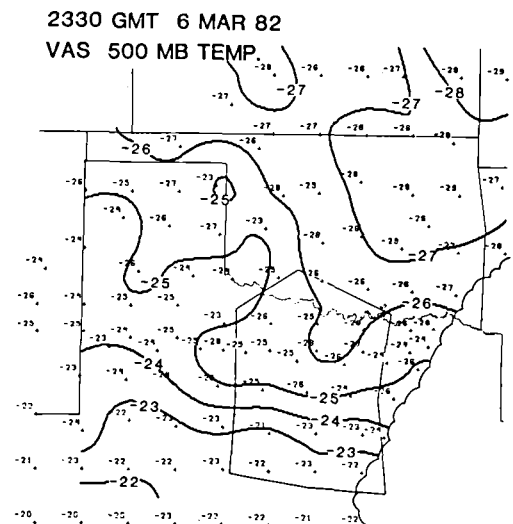
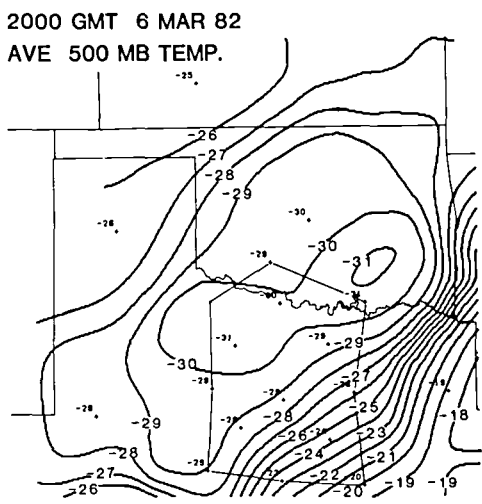
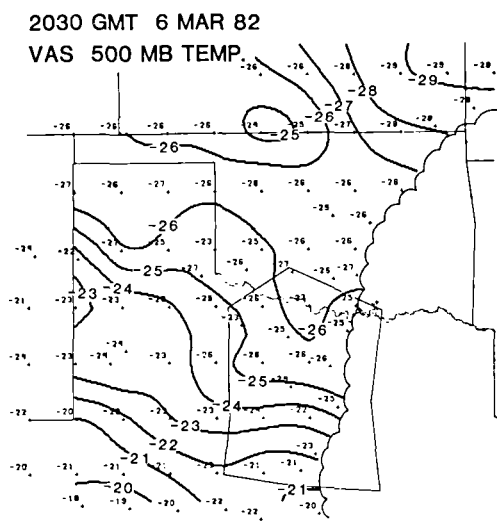
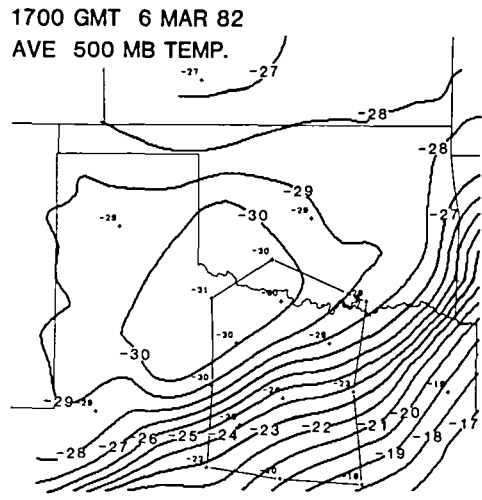
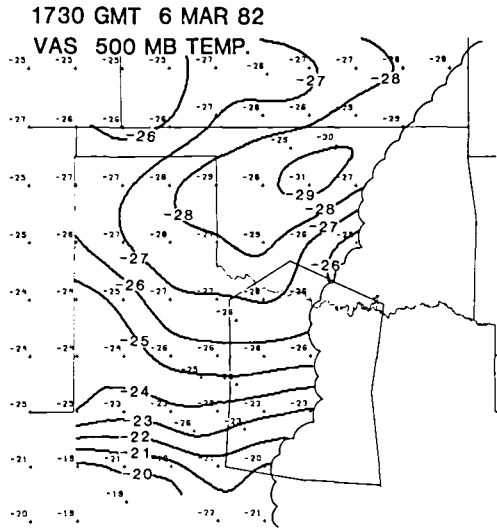


Figure 5-25. VAS/AVE fields of 500 mb temperature

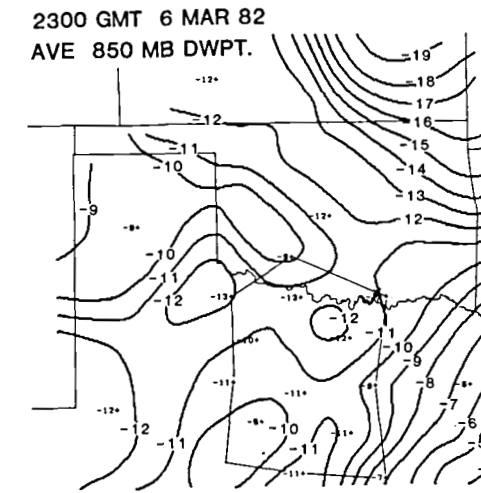
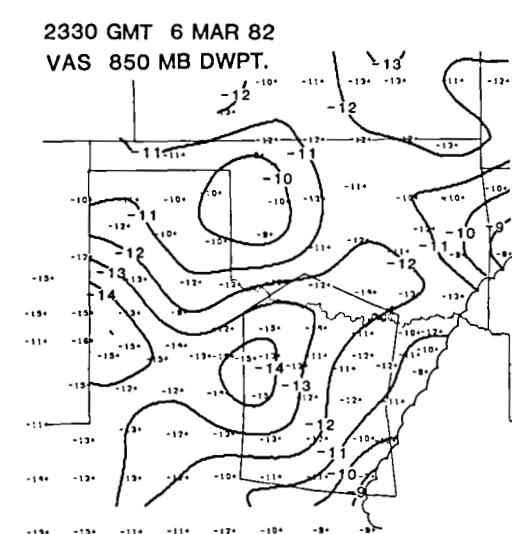
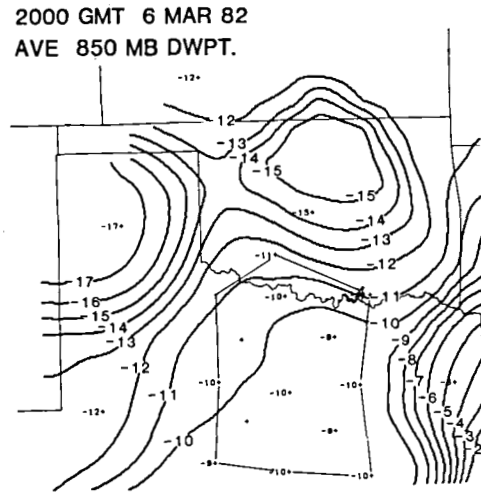
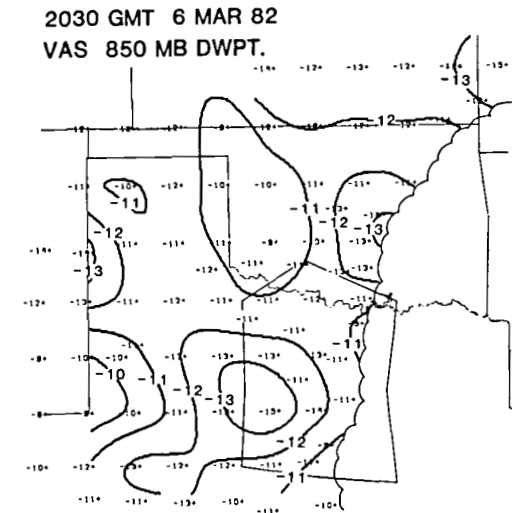
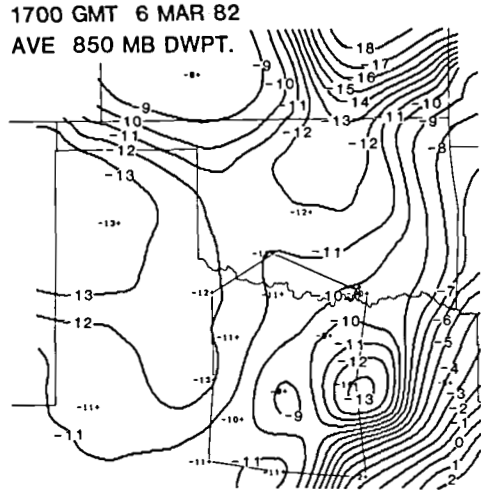
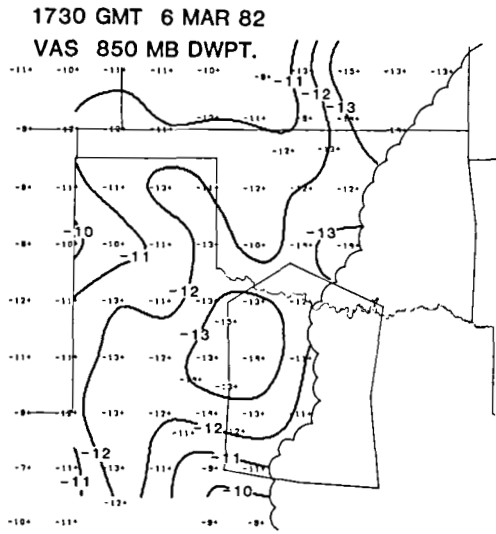


Figure 5-26. VAS/AVE fields of 850 mb dewpoint

6 March 1982 was not an ideal day for a VAS verification study. Despite these problems, the statistical analysis show that the quality of VAS soundings compare favorably to the NWS radiosondes, and that retrieval accuracies meet the VAS Demonstration requirements *when conventional surface reports were utilized in the retrieval algorithm*. The ancillary surface temperature and dewpoint replace the window channels as statistical predictors for the low-level retrievals, and help reduce the effects of skin brightness fluctuations from diurnal heating, high cloud contamination, and snow cover. In fact, the "VAS plus SFC" matrix even retrieves useful atmospheric profiles, in an area with low overcast. The "VAS only" matrix cannot infer any reasonable profile under the same conditions.

The 500-mb temperature and 850-mb dewpoint analyses reveal that there are definite limitations to the statistical retrieval procedure, as well as deficiencies in the ground truth data sets. The VAS soundings failed to retrieve the 850 to 920-mb temperature inversion and a cold pocket at the 500-mb level. The unexpected problems that were encountered were, *large differences between the special network RAOBs and hourly surface measurements, and the lack of surface stations near the sounding sites in some cases*. These differences have a significant impact on the evaluation of the accuracy of the VAS temperature and dewpoint retrievals in the boundary layer, since the GLAS retrieval algorithm depends heavily upon surface data. The quality assurance of the "ground truth" AVE Network data will have to be reviewed in order to rectify the large differences in surface reports before a more accurate "error" analysis for the VAS Special Network soundings can be made.

5.3.3 UW-NESDIS (CIMSS) Special Network VAS Evaluation

C. Hayden
*Cooperative Institute for Meteorological
Satellite Service
National Environmental Satellite
Data Information Service
National Oceanic Atmospheric Administration
U.S. Department of Commerce*

The March 6 Special Network experiment was indeed special to the NESDIS Development Laboratory (DL). Not only were the radiances for the five dwell sounding periods of that day processed with particular care, but the retrievals were used in further studies of their value

to data assimilation in a major research effort that will be discussed here. The DL processed all of the data using two methods. These methods differed in two aspects. Method-A discarded measurements that were judged to be cloud contaminated. Method-B attempted a radiance correction by N-star or filtering. Method-A retrieved moisture as a relative humidity estimate. Method-B attempted to retrieve the absolute moisture. Results of the two methods were compared in order to determine an "official" set for distribution. Method-A was selected chiefly on the basis that this method employed the current "operational" algorithm used to provide daily data to the National Severe Storms Forecast Center (NSSFC) in Kansas City. In terms of retrieval quality, there was seemingly very little basis to differentiate between the two methods.

5.3.3.1 Ageostrophic Wind

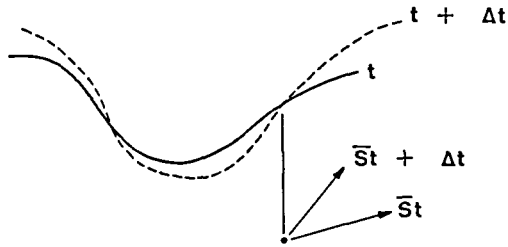
The factors involved with this experiment suggested an investigation of the "time-continuity" application of the VAS data. First, the weather was interesting and rapidly changing. Second, the cloud problems did not appear to be too formidable. Third, the mesonet radiosondes offered some prospect of verification. Consequently, we have used these data to derive both gradient and ageostrophic wind estimates. The latter involves a time change and (hopefully) is closer to the real wind. One assumes that an accurate ageostrophic wind would be useful to the numerical forecast modeler.

Figure 5-27 schematically shows the approach. In essence, the time rate of change of the mass field (as determined from the temperature observations) is used to calculate the isallobaric wind, which modifies the gradient wind. Conceptually, the calculation in practice is quite difficult because of strong dependence on the accuracy of the evaluation of curvature and its time derivative. Since this delicate matter was the object of a considerable amount of research, it is instructive to go into some of the details of the computation here.

The first step of this procedure is the objective analysis of the geopotential to a regular grid. It is important that the grid mesh is relatively fine, since the grid will be used to determine the first and second derivatives necessary in the calculation of the wind. It is most desirable to have the wind estimates representative of a fairly small area. Through trial-and-error with the standard 2-pass Barnes objective analysis scheme, we decided on a procedure using a gridlength of 0.8° in latitude, with

Quasi-Geostrophic wind Adjustment

$$\bar{V} = \bar{V}_g + \bar{V}_{ag}$$



$$\bar{V}_{ag} = \frac{1}{f} \bar{k} \times \left\{ \frac{\partial \bar{V}_g}{\partial t} + V_g \frac{\partial \bar{V}_g}{\partial s} \right\}$$

$$\bar{V}_{ag} = \frac{1}{f} \frac{\partial \bar{V}_g}{\partial t} \bar{k} \times \bar{S} + \frac{V_g^2}{f} \bar{k} \times \left\{ \frac{1}{V_g} \frac{\partial \bar{S}}{\partial t} + \bar{S} \cdot \nabla \bar{S} \right\}$$

$$(1) \qquad (2) \qquad (3)$$

(1) + (2) = isallobaric wind

(3) = gradient + diffluent adjustment

Figure 5-27. Schematic representation of the wind components calculated in this study

a first guess background field derived from time interpolated Limited Area Fine Mesh (LFM) analyses (actually a 1200 GMT analysis and 12 hour forecast). The influence of the background field is mostly cosmetic, preventing the analysis from becoming noisy in areas that are sparse in data coverage. Usage of the Barnes analysis was followed by the application of a smoother, designed to remove all wavelengths less than 500 km.

The second step in this procedure is the choice of a finite difference algorithm, to determine differential properties. We have used a 25-point operator which is equivalent to a local least squares polynomial fit to a surface which allows analytic estimates of the derivatives. Therefore, the desirability of a fine gridmesh is obvious. The winds derived in this experiment are in a sense representative of a 4° by 4° latitude-longitude area.

The third step is the description of the algorithm. We found it to be appropriate to break the computation into several parts which could be examined and diagnosed separately. The geostrophic component, a gradient correction, a time dependent curvature correction, and a time dependent speed correction, each were examined independently, to ferret out any computational difficulties and, more importantly, to ensure

temporal consistency in the geopotential analyses. The qualitative assessment of the corrections influenced the final determinations of step 1 and step 2. A memorandum detailing the algorithm is included in Section 5.3.3.2.

Given the relatively uniform coverage of the special radiosonde network, it seemed appropriate to treat the geopotential reported by these stations in the same way as the VAS (i.e., to analyze to a regular grid and derive geostrophic gradient and geostrophic winds). The representation of the geopotential at 500 mb as analyzed from the radiosondes at 1200, 1500, 1800, and 2100 GMT is shown in Figure 5-28. The continuity in the movement of the sharp trough over Texas is evident, although it is far from uniform. In particular, at 2100 GMT, there is an abrupt deepening and southwesterly shift. This same behavior has been noted (suspiciously) in the VAS representation of the geopotential, before the special radiosondes were available. Results from the VAS are shown in Figure 5-29.

The first three columns of Table 5-16 compare (in terms of mean difference, RMS difference, and correlation coefficient) the observed wind speeds at four levels, with the wind speeds derived from the analyzed geopotential. Several conclusions can be drawn from these numbers. First, the geostrophic approximation is generally the best, and is slightly better than the gradient (except at 300 mb), and significantly better than the ageostrophic estimate. This result is somewhat surprising and is certainly disappointing, since the synoptic regime would seem ideal for demonstrating the value of the second order corrections to the geostrophic estimate. With respect to the gradient correction, the largest changes were a reduction in the velocity in the area of the trough over the special network (Figure 5-28). Unfortunately, in this situation, the geostrophic approximation has already provided an underestimation. This deficiency could be the result of oversmoothing that is implicit in the 25-point finite differencing. If this is true, a different formulation could yield a better comparison. This clearly falls in the category of "tweaking" the technique to achieve the desired result¹. The overriding conclusion is that,

¹The gradient experiment was repeated using a gridspacing of 0.6° for the objective analyses. This reduced the effective areal extent of the 25 point differencing from a 4 by 4 degree to a 3 by 3 degree area. Comparison of the derived with observed winds were essentially unchanged; slightly better at high levels and slightly worse at low levels. The slow "bias" was not significantly affected.

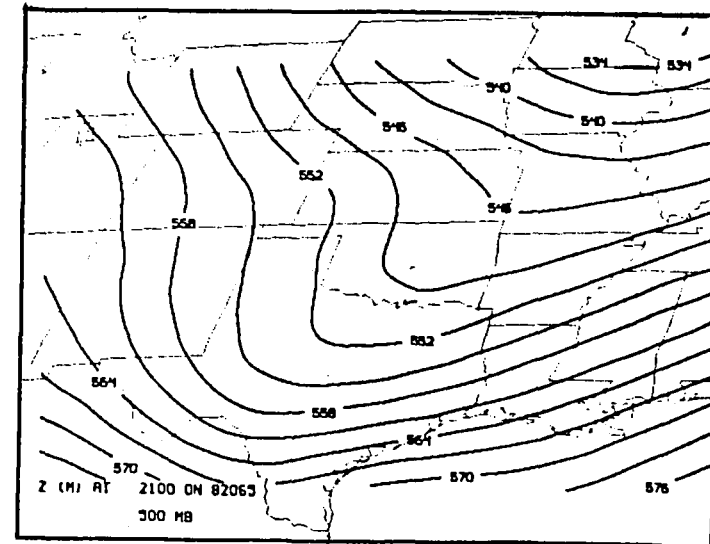
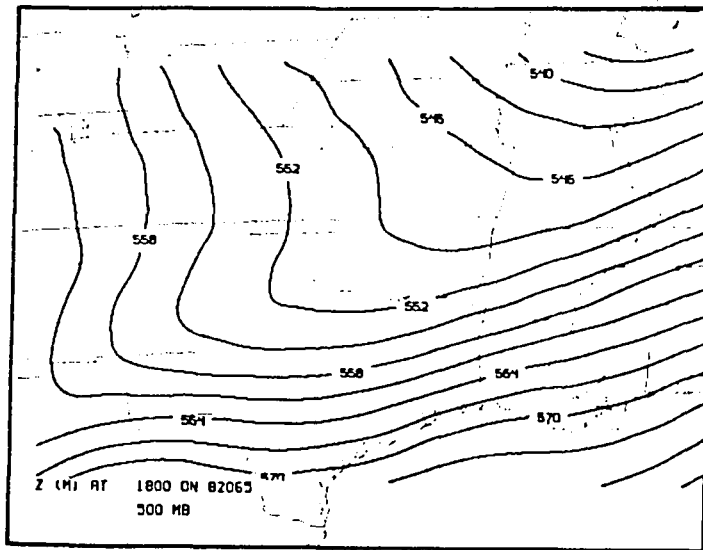
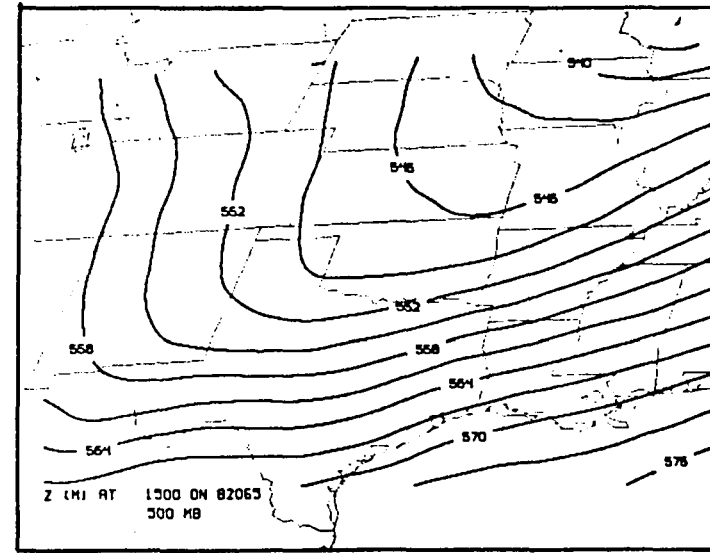
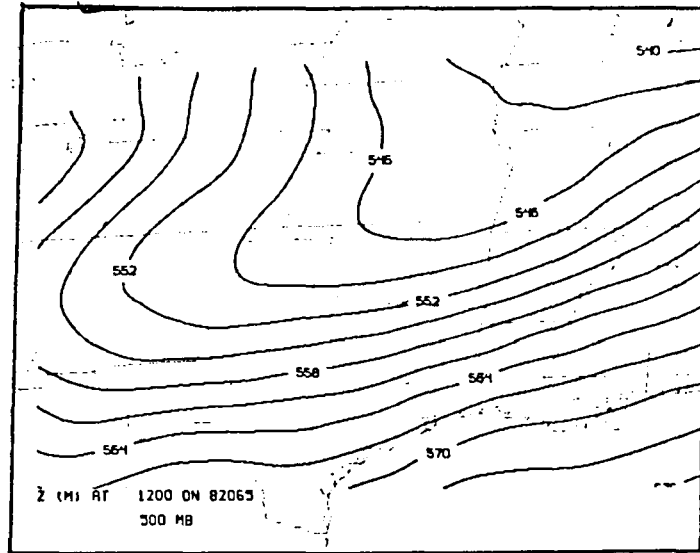


Figure 5-28. 500 mb geopotential analyses obtained from the special network radiosondes at 1200, 1500, 1800, and 2100 GMT, 6 March 1982.

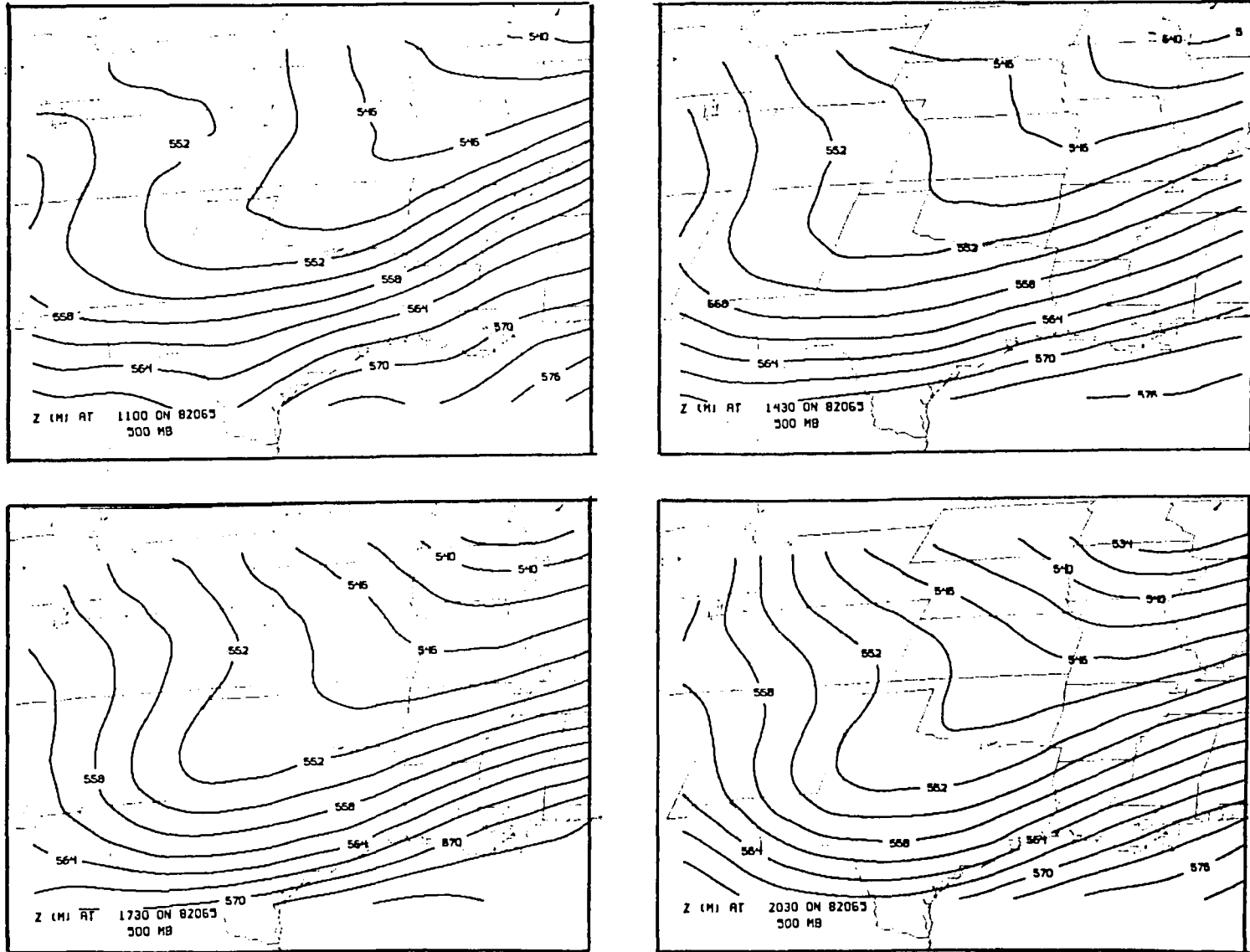


Figure 5-29. 500 mb geopotential analyses derived from the VAS temperature and moisture profiles and conventional surface observations at 1130, 1430, 1730, and 2030 GMT March 1982.

in this situation, the gradient correction cannot easily be shown to improve over the geostrophic. In the case of the ageostrophic correction, the largest changes are to further reduce the mean wind speed. Therefore, the conclusions drawn for the gradient correction, are true for the ageostrophic also. Nevertheless, as the degradation associated with the gradient correction is small, that associated with the ageostrophic is large at low levels. One might wonder if the failure is aggravated by an excessively large time difference (3 hours) in measuring the change in the geostrophic wind. This might be a contributing factor, but the isobaric changes are quite coherent (spatially), and look to be qualitatively reasonable. Apparently, the real is not behaving according to the chosen formulation.

Scatter plots of measured, versus gradient winds for the radiosonde are shown in Figure 5-30. The slow bias at

low levels is obvious. At high levels, the scatter is seen to increase markedly at higher wind speeds. In some cases, one is sorely tempted to question the rawinsonde. However, the exclusion of one or two of the outlying points does not significantly alter the conclusions of the study.

The rightmost two columns of Table 5-16 show the comparisons between the measured winds and those estimated from the satellite analyses. The results can be viewed as being either good or bad. On the optimistic side (except at the lowest level), the VAS gives an estimate of the gradient wind which is as good as can be derived from the radiosonde (the radiosonde has the advantage here insofar as the verification is established at the radiosonde measurement where, in several cases, there is no satellite data because of cloud problems). This is an important result since it implies that *the*

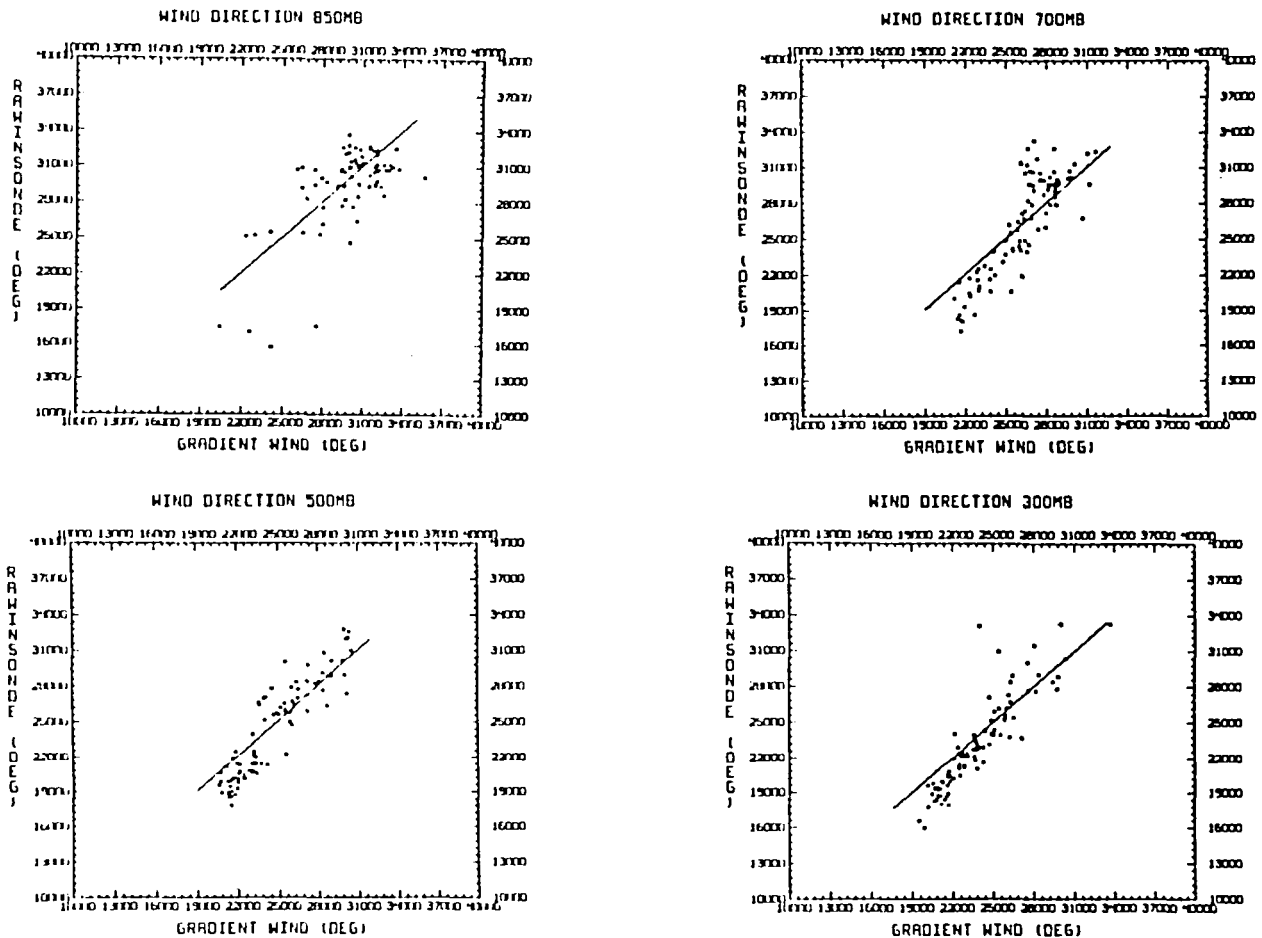


Figure 5-30. Scatter diagram of the rawinsonde speed observations compared to values derived from the geopotential analyses of the radiosondes using a gradient wind approximation. All time periods shown in Figure 5-28 are included.

Table 5-16
Wind Speeds Derived from Geopotential Analyses of the VAS and
Radiosonde Data Compared with Winds Measured by the
Rawinsonde Soundings at 1430, 1730, and 2030 GMT 6 March 1982

Level	Radiosonde			VAS	
	Geostrophic	Gradient	Ageostrophic	Gradient	Ageostrophic
mean ($m s^{-1}$)	3.9	3.8	4.2	4.8	4.8
850 RMS ($m s^{-1}$)	4.7	4.6	5.1	5.8	5.9
CC (%)	60	59	38	17	18
mean ($m s^{-1}$)	3.6	4.1	5.5	4.0	4.6
700 RMS ($m s^{-1}$)	5.3	5.8	7.6	5.8	6.4
CC (%)	59	54	28	57	55
mean ($m s^{-1}$)	1.9	3.4	4.0	3.5	3.1
500 RMS ($m s^{-1}$)	8.6	8.8	10.0	8.8	9.1
CC (%)	71	72	66	72	70
mean ($m s^{-1}$)	-4.0	1.1	0.3	1.1	0.8
300 RMS ($m s^{-1}$)	14.8	12.1	13.2	12.7	14.2
CC (%)	74	74	71	68	60

satellite can measure mid-tropospheric geopotential gradient with an accuracy comparable to high density radiosondes. On the pessimistic side, the satellite does not represent the real wind very well. This may not be important in application. For example, if an analysis forecast scheme uses wind observations through a dynamic constraint (e.g., optimum interpolation using gradient statistics), a good gradient estimate may be preferable to a real wind. The satellite does not appear to be capable of providing a good ageostrophic component by this method, therefore its utility in small scale dynamics is not demonstrated.

Table 5-17 compares wind directions derived from the geopotential analyses, with directions observed using the rawinsondes. What was previously stated, concerning wind speed can be repeated in regards to the direction. The gradient approximation is a fairly respectable representation. This is significantly degraded by attempting an ageostrophic correction. Also, results achieved from the satellite-derived analyses are comparable to those obtained with the high density radiosondes. (VAS ageostrophic results are not presented in the table because routine McIDAS operating maintenance destroyed a number of required files whose

recreation exceeded the available energy of this experiment.) The statistics do not show the bias that is obvious in the case of wind speed, but this is misleading as seen in the scatter diagram of Figure 5-31. The gradient winds are too southerly in northerly flow, and too northerly in southerly flow (ahead of the trough). In essence, they portray a trough of broader amplitude than the actual winds, and therefore are biased to a "smoothness", just as the speeds are. The nagging suspicion remains that the results are partly a reflection of the selected smoothing and finite differencing involved in this experiment, but further tightening (beyond that mentioned in the footnote) is not justified by the data spacing of either the satellite or radiosonde. Also, there is a feeling that the statistics paint an overly gloomy picture. Figure 5-32 shows that both radiosonde and satellite show an abrupt backing of the wind, associated with a sharp increase in speed, over a relatively short distance in the area of the special network. The two data types show this phenomenon in slightly different locations, which makes the statistical comparison unflattering.

The conclusions to be drawn from this study are, to some degree, a reaffirmation of well-known facts. As

Table 5-17
Wind Directions Derived From Geopotential Analyses of the VAS and
Radiosonde Data Compared to Winds Measured by Rawinsonde

Level	Rawinsonde		VAS	
	Gradient	Ageostrophic	Gradient	
850	mean (degrees)	-5	9	15
	RMS (degrees)	27	61	32
	CC (%)	67	40	62
700	mean (degrees)	-2	-5	9
	RMS (degrees)	24	24	28
	CC (%)	86	84	79
500	mean (degrees)	-5	11	4
	RMS (degrees)	19	45	20
	CC (%)	92	52	90
300	mean (degrees)	-7	-2	-4
	RMS (degrees)	21	26	25
	CC (%)	89	77	90

Petterssen (1956) remarked many years ago, "Caution should . . . be exercised in using the gradient-wind formula, except where conditions are favorable for obtaining reliable results; elsewhere it is usually preferable to use the geostrophic-wind relationship." An even stronger caveat should be raised with regard to ageostrophic corrections. It is encouraging that the VAS geopotential analyses can produce a gradient representation which is equivalent to that obtained from the dense radiosonde network. At the same time, it is discouraging that the representation is smoother than that given by the wind observations themselves. Finally, it should be noted that one cannot put too much stock into the absolute numbers given in this report (as opposed to the relative comparisons of the dynamic methods and the bias trends). The wind observations, as shown by the wind speeds plotted in Figure 5-32, are quite variable over a very small scales. Clearly, this variation cannot be achieved from geopotential analyses of the scale, dictated by the spatial distribution of the thermal observations themselves.

5.3.3.2 Time Coupling of Geopotential Analyses

Two strategies were developed to allow for the adjustment of geopotential analyses at two time periods, in

order to permit dynamic consistency in terms of potential vorticity. In the first scheme, the mean and variance of the potential vorticity is forced, through least squares adjustment, to be the same in the two analyses. In the second scheme, forecast and hindcast of potential vorticity from the two analyses are adjusted to be equal at the midpoint time. The primary difference in the latter scheme is that it permits a phase change, as well as an amplitude change in the adjustments of the geopotential.

This study is discussed in detail in Lewis *et al.* (1983), and will not be dealt with in detail in this document. The result was that the second method proved to be superior, and made meaningful adjustments to the analyses. The changes could be verified by subjective evaluation of resultant omega fields in data poor areas.

5.3.3.3 Differential Properties Algorithm

Winds which accompany the VAS temperature retrievals are derived from geopotential heights analyzed at constant pressure levels. The height data used to construct

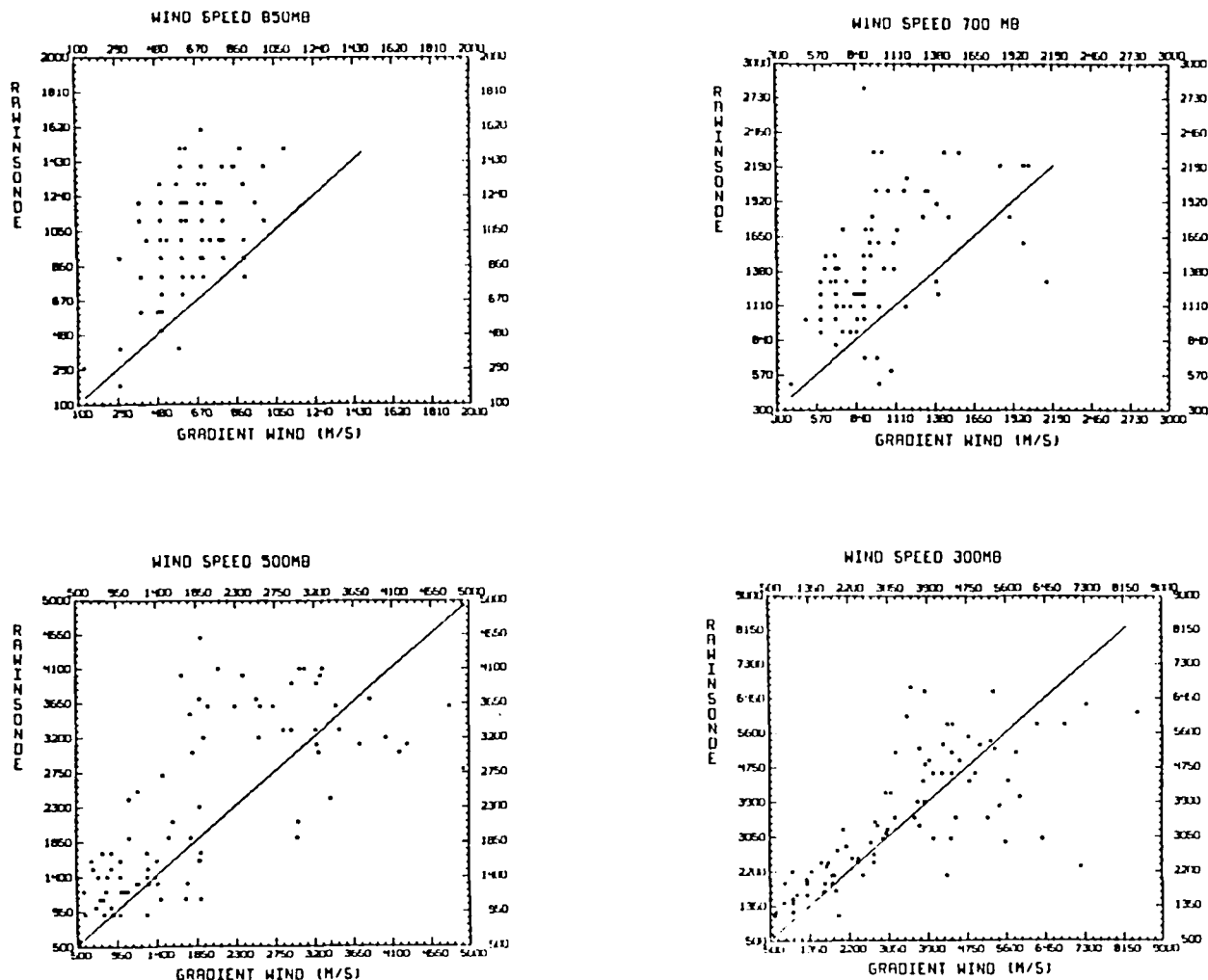


Figure 5-31. Same as Figure 5-30 except for wind direction (all values have been biased by 40 degrees to avoid problems at 360/0).

the analyses are provided from the VAS temperatures and mixing ratios. The lower reference level is a surface height estimated from a topography file, and a surface pressure produced from objective analyses of mean sea level temperature and 1000-mb heights. The latter are based on conventional surface observations. Several options may be exercised in obtaining wind estimates, all are based on the expression:

$$\left(\frac{d\bar{V}}{dT}\right)_H = \frac{\partial \bar{V}}{\partial T} + \bar{V} \cdot \nabla \bar{V} + \omega \frac{\partial \bar{V}}{\partial z} + \bar{F} \quad (1)$$

$$= f\bar{V} \times \hat{k} - f\bar{V}_g \times \hat{k}$$

where \bar{V}_g refers to the geostrophic wind, and T represents time.

Thus

$$\bar{V} = \bar{V}_g + \frac{1}{f} \hat{k} \times \left[\frac{\partial \bar{V}}{\partial T} + \bar{V} \cdot \nabla \bar{V} \right] \quad (2)$$

where the last two terms represent the isalobaric and gradient corrections, respectively. The quasi-geostrophic assumption is made to replace V on the right-hand side, by \bar{V}_g . Introducing the tangent vector \hat{t} :

$$\bar{V} = \bar{V}_g + \frac{1}{f} \hat{k} \times \left[\frac{\partial}{\partial T} \bar{V}_g \hat{t} + \bar{V}_g \cdot \nabla \bar{V}_g \hat{t} \right]. \quad (3)$$

In the program which computed the VAS winds, equation 3 was broken down into the terms:

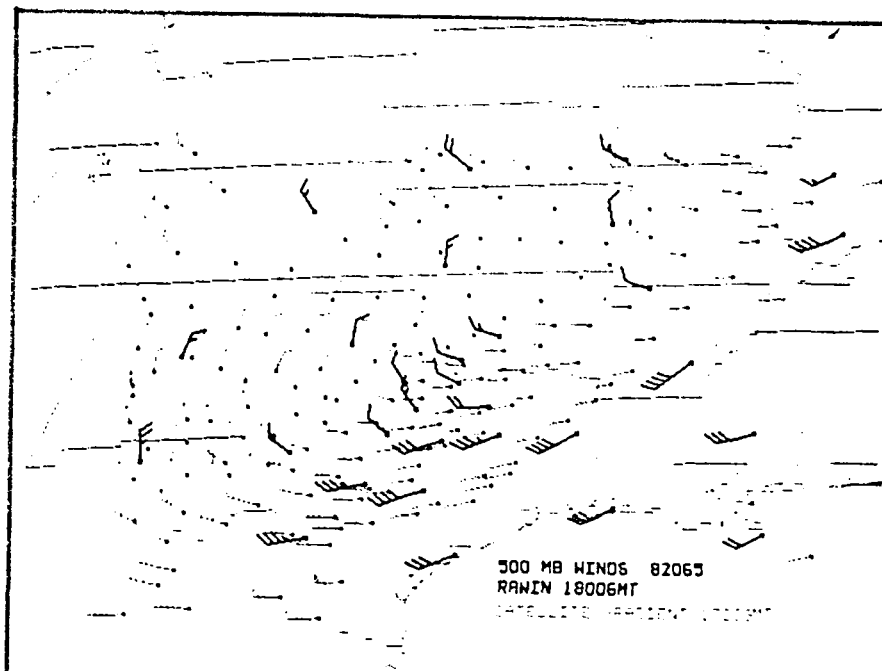
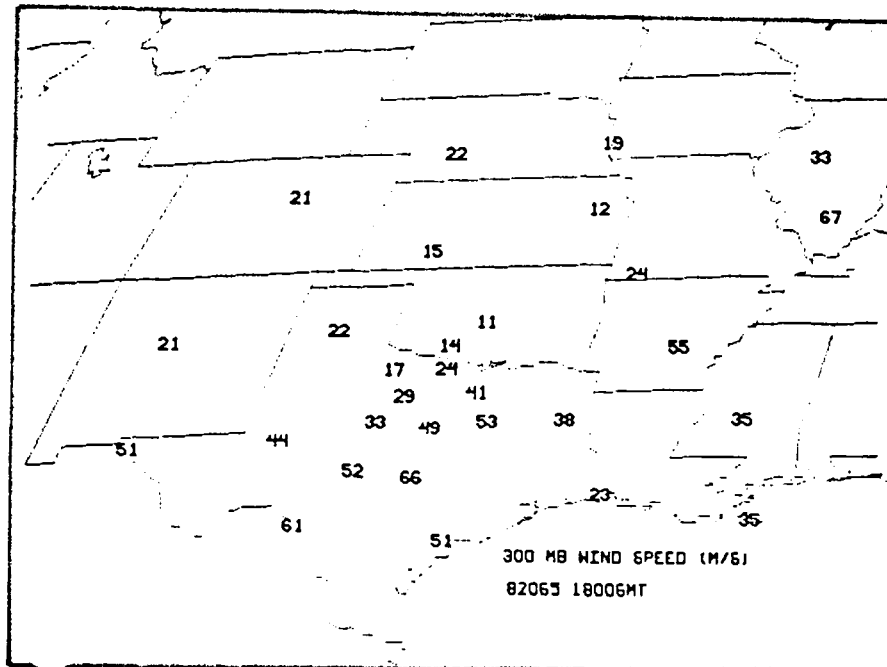


Figure 5-32. Top: 300 mb wind speeds for the special network rawinsondes at 1800 GMT, 6 March 1982. Bottom: wind barbs representing the satellite-derived gradient winds and the special network rawinsondes (bold) at 500 mb, 1800 GMT, 6 March 1982.

$$\bar{V} = \bar{V}_g + \frac{1}{f} \frac{\partial V_g}{\partial T} \hat{k} \times \hat{t}$$

(a) (d)

$$+ \frac{1}{f} V_g^2 \hat{k} \times \left[\frac{1}{V_g} \frac{\partial \hat{t}}{\partial T} + \hat{t} \cdot \nabla \hat{t} \right]$$

(c) (b)

(4)

(a) geostrophic component; (b) gradient correction; (c) time dependent curvature correction; (d) time dependent speed (normal) correction. Each of these can be displayed independently, or in conjunction with any other(s) using the flag option. For example:

1 → (a)

10 → (b)

100 → (c)

1000 → (d)

11 → (a)+(b) = gradient wind

1100 → (c)+(d) = isallobaric wind, etc.

i) Gradient algorithm

$$\begin{aligned} \hat{t} &= \frac{1}{V_g} (u_g \hat{i} + v_g \hat{j}) = \frac{1}{D} \left(\frac{\partial z}{\partial y} \hat{i} + \frac{\partial z}{\partial x} \hat{j} \right) \\ D &= \left[\left(\frac{\partial z}{\partial y} \right)^2 + \left(\frac{\partial z}{\partial x} \right)^2 \right]^{1/2} \\ \hat{t} \cdot \nabla \hat{t} &= \frac{1}{D} \left(\frac{\partial z}{\partial y} \hat{i} + \frac{\partial z}{\partial x} \hat{j} \right) \cdot \left(\frac{\partial}{\partial x} \hat{i} + \frac{\partial}{\partial y} \hat{j} \right) \\ &= \frac{1}{D} \left[\left(-\frac{\partial z}{\partial y} \hat{i} + \frac{\partial z}{\partial x} \hat{j} \right) \right] \end{aligned} \quad (5)$$

After a little algebra,

$$\begin{aligned} & \frac{1}{D^2} \left[\frac{\partial z}{\partial y} \frac{\partial^2 z}{\partial x \partial y} - \frac{\partial z}{\partial x} \frac{\partial^2 z}{\partial y^2} - \frac{1}{D} \frac{\partial z}{\partial y} E \right] \hat{i} \\ & - \frac{1}{D^2} \left[\frac{\partial z}{\partial y} \frac{\partial^2 z}{\partial x^2} - \frac{\partial z}{\partial x} \frac{\partial^2 z}{\partial x \partial y} - \frac{1}{D} \frac{\partial z}{\partial x} E \right] \hat{j} \end{aligned} \quad (6)$$

where

$$E = \frac{\partial z}{\partial y} \frac{\partial D}{\partial x} - \frac{\partial z}{\partial x} \frac{\partial D}{\partial y}$$

Using the program notation

$$\hat{t} \cdot \nabla \hat{t} = \text{curv} \hat{i} + \text{curv} \hat{j} = \hat{C} \quad (7)$$

The sign of the curvature is derived from $\hat{C} \cdot \hat{n}$

$$\begin{aligned} \hat{C} \cdot \hat{n} &= \hat{C} \cdot \hat{k} \times \hat{t} = (C_i \hat{i} + C_j \hat{j}) \cdot \hat{k} \\ &\times \left(\frac{\partial z}{\partial y} \hat{i} + \frac{\partial z}{\partial x} \hat{j} \right) / D = \frac{1}{D} \left[C_i \frac{\partial z}{\partial x} + C_j \frac{\partial z}{\partial y} \right] \end{aligned} \quad (8)$$

(7) and (8) are combined to give the signed curvature which is used to compute the total gradient wind components from

$$U_{gr} = \frac{2f u_g}{f + (f^2 + 4gCD)^{1/2}} \quad (9)$$

and similarly for V_{gr} with the restriction that the radical is greater than or equal to 0. The gradient correction (b, found in (4)) is obtained by subtracting the geostrophic components.

Note: All derivatives are evaluated by an algorithm which is equivalent to doing a least squares quadratic fit to a 5 by 5 array of gridpoints, centered on the "wind" location. The derivatives $\partial/\partial x$; $\partial/\partial y$; $\partial^2/\partial x \partial y$; and $\partial^2/\partial x^2$; $\partial^2/\partial y^2$ are in essence the coefficients of the quadratic.

ii) Isallobaric algorithm

The isallobaric wind correction is computable if more than one time level of height analyses are available. In the VAS wind program, the time derivative is evaluated as a simple centered difference between two time periods. Thus

$$\frac{\partial \hat{t}}{\partial T} = \frac{\partial}{\partial T} \left[\frac{-\frac{\partial z}{\partial y} \hat{i} + \frac{\partial z}{\partial x} \hat{j}}{D} \right]$$

$$= -\frac{1}{D^2} \left[\frac{\partial}{\partial T} \left(\frac{\partial z}{\partial y} \right) D - \frac{\partial z}{\partial y} F \right] \hat{i} \quad (10)$$

$$+ \frac{1}{D^2} \left[\frac{\partial}{\partial T} \left(\frac{\partial z}{\partial x} \right) D - \frac{\partial z}{\partial x} F \right] \hat{j}$$

where

$$F = \frac{\partial}{\partial T}(D) = \frac{D_+ - D_-}{\Delta T}$$

$$\frac{\partial}{\partial T} \left(\frac{\partial z}{\partial x} \right) D = \frac{D_- \left(\frac{\partial z}{\partial x} \right)_+ - D_+ \left(\frac{\partial z}{\partial x} \right)_-}{\Delta T}$$

where + indicates a later sample and - indicates an earlier sample.

For the time dependent curvature adjustment (c, found in (4))

$$\bar{V}_c = \frac{V_g^2}{f} \hat{k} \times \frac{1}{V_g} \frac{\partial \hat{t}}{\partial T}$$

recalling that

$$V_g = \frac{g}{f} D$$

$$\bar{V}_c = -\frac{g}{D_m f^2} \left[\frac{\partial}{\partial T} \left(\frac{\partial z}{\partial x} \right) D - \frac{\partial z}{\partial x} F \right] \hat{i} \quad (11)$$

$$- \frac{g}{D_m f^2} \left[\frac{\partial}{\partial T} \left(\frac{\partial z}{\partial y} \right) D - \frac{\partial z}{\partial y} F \right] \hat{j}$$

where

$$D_m = \frac{D_+ + D_-}{2}$$

Finally, for the normal component term:

$$\frac{1}{f} \frac{\partial V_g}{\partial T} \hat{k} \times \hat{t} \quad (12)$$

$$\bar{V}_d = -\frac{g}{D_m f^2} F \left[\frac{\partial z}{\partial x} \hat{i} + \frac{\partial z}{\partial y} \hat{j} \right]$$

note that these components cancel the second terms in (1) as they obviously should. This separation is only for illustrative purposes.

METEOROLOGICAL ASSESSMENT OF VAS IN MONITORING THE PRE-CONVECTIVE ENVIRONMENT FOR SEVERE LOCAL STORMS

Although it was recognized that the VAS data should be applied to a wide variety of important meteorological phenomena (including convective storms, heavy precipitation associated with extratropical cyclones and tropical storms), the assessment portion of the VAS Demonstration was designed to emphasize the severe convective storm problem. Specifically, the main goal of the VAS assessment was to determine if VAS data could be used to accurately measure the magnitude and extent of convectively unstable air masses prior to the outbreak of severe storms. The following section describes the results from the VAS assessment activities at GSFC and UW.

Research groups at GSFC and UW conducted detailed case studies for those situations in which VAS data was collected prior to the development of intense convective storm systems. Furthermore, a concerted effort was made at UW to produce VAS images and sounding for real time application at NSSFC in Kansas City. This effort was designed to determine if VAS data could be presented to a forecaster in a timely manner, for use in mesoscale prediction. The NESDIS team at UW also produced soundings for model impact studies conducted at NMC.

6.1 GSFC Assessment

L. W. Uccellini
D. Chesters
R. A. Petersen

*Goddard Laboratory for Atmospheric Sciences
Goddard Space Flight Center
National Aeronautics and Space Administration
Greenbelt, Maryland*

A. Mostek
D. A. Keyser
W. D. Robinson
*General Software Corporation
Landover, Maryland*

The VAS Demonstration research effort at GSFC was performed in three phases. Phase 1 was directed toward

the study of simulated VAS radiances to determine the extent to which VAS could detect convective instability under optimal conditions. Phase 2 was based solely on a detailed study of the utility of VAS imagery in severe storm environments. Phase 3 was directed toward a statistical validation of VAS soundings based upon regression (discussed in Section 5.1) and case studies of severe weather events for which the VAS imagery and soundings were acquired.

6.1.1 Phase 1 of GSFC Research Effort: Prelaunch VAS Simulation Study

The results from the VAS simulation experiment are found in the paper by Chesters *et al.* (1982), that describes a controlled sounding *simulation* experiment to demonstrate the ability of VAS to detect convective instability under optimal conditions, and test the sensitivity of residual errors in VAS regression retrievals to “local” statistical conditioning. The results of this experiment indicate that:

- In the troposphere temperature profile residual errors are $\pm 2^{\circ}\text{C}$ and corresponding mixing ratio residuals are $\pm 2 \text{ gm kg}^{-1}$.
- Retrievals done with regression matrices conditioned with “local” weather statistics have smaller residual errors than those conditioned with “global” data. These results are due to the better resolution of ambiguities in vertical structure, in favor of the most probable structure derived from a “local” statistical database.
- Horizontal and vertical temperature and moisture structures are retrieved in the lower troposphere. Potentially unstable air is recovered from simulated VAS radiances. Nevertheless, the absolute magnitude of the retrieved potential instability is significantly underestimated by the remote sounding process, which reflects the lack of vertical resolution in the 12 VAS channels.

- VAS was capable of retrieving vertically-integrated meteorological parameters, such as precipitable water and geopotential thickness using “locally” conditioned regression coefficients.

The VAS simulated soundings showed the same limitations in absolute accuracy and vertical resolution that occur with other passive infrared satellite instruments. This result implies that even in these optimally simulated soundings, the incorporation of a “local” radiosonde database would be needed for computing the retrieval matrix, and that conventional surface data would have to become a part of VAS data processing in order to make the lower-tropospheric retrievals more accurate.

6.1.2 Phase 2 of GSFC Research Effort: Assessment of VAS Imagery

The results of the image analyses can be found in the journal papers by Chesters *et al.* (1983) and Petersen *et al.* (1983A; 1983B) as well as in several conference preprints (Petersen and Mostek, 1982; Petersen *et al.*, 1982, 1983A, 1983B). This research effort was designed to determine if VAS moisture images could be used to delineate upper- and lower-level moisture fields, and if a combination of VAS moisture images could be used to infer convective instability where mid-level dry air overlays low-level moist air masses. Two cases were selected to test the usefulness of the VAS moisture images (July 13, 1981 and July 20, 1981), for which severe storms developed in relatively clear air during a VAS observing period.

Surface, upper-air, and radar maps for 13 July 1981 are shown in Figure 6-1. At 1200 GMT, a weak surface wave is slowly drifting from eastern Colorado toward Nebraska along a stagnant surface front that extends through northern Illinois into southern Michigan. Precipitation over the Midwest is confined to several regions of thunderstorms in South Dakota, eastern Iowa, and in the Texas-Louisiana coastal area. The 850-mb analysis is dominated during the 12-hour period by a broad anticyclone centered over Alabama, producing a broad band of weak southerly flow, west of the Mississippi River. To the northeast of the Great Lakes, a short wave was rapidly propagating southeastward toward Maine, as a moderately intense jet streak propagated southeastward across New York State by 0000 GMT. Over the Mississippi Valley and the Great Plains, the 250-mb flow pattern remained weak and disorganized south of a major upper-level ridge. By 1800 GMT,

surface temperatures rose well above 30°C. Dewpoint temperatures surpassed 20°C over almost the entire southeastern portion of the country. The area of thunderstorms originally located over Iowa weakened as it approached northern Illinois. The precipitation in the Dakotas moved northward and diminished. Thunderstorms along the Gulf continued to strengthen, as numerous other areas of rain developed east of the Mississippi. By 0000 GMT, radar reports showed isolated thunderstorms over much of the western Mississippi Valley. One aspect that was of particular interest to this study was the 1678 m (55,000 ft) high storms which developed in less than 2 hours over eastern Iowa, in an area devoid of any particularly strong, large-scale dynamical forcing, and approximately 150 km ahead of the weak surface front. The three-hourly visible images, shown in Figure 6-2, verify the progress of the precipitation activity already shown on the radar summaries, and illustrate the banded structure of the convection in Oklahoma and Kansas.

Chesters *et al.* (1983) describes the application of a “split window” technique for measuring low-level (1000–700 mb) water vapor fields for the 13 July 1981 case. The differential water vapor absorption between the 11 and 12- μm infrared channels is the basis of the split window, which makes it possible to separate the surface and atmospheric radiance contributions within each image field-of-view. The average air brightness temperature, determined at radiosonde sites, allows the further separation of atmospheric emission and absorption terms. A simply parameterized algorithm was developed from a single-layer model for the split window radiances to calculate the vertically-integrated water vapor content (measured in gm cm^{-2}) of the lower troposphere.

A time sequence of four VAS split window images taken every three hours over the United States on 13 July 1981 (Figure 6-3), shows subsynoptic and mesoscale details at 15-km horizontal resolution that evolve continuously during the 8 h period. These images reveal that the background surface temperature variations are effectively eliminated. Several areas of enhanced low-level water vapor developed into convective cloud formations as indicated in the sequence of low-level water vapor fields. Convection in Oklahoma at 2100 GMT developed in a pre-existing band of low-level moisture that became evident 3 to 6 h before the convective clouds began to form. The convection that developed in Iowa after 2100 GMT also occurred in a maximum of the low-level moisture.

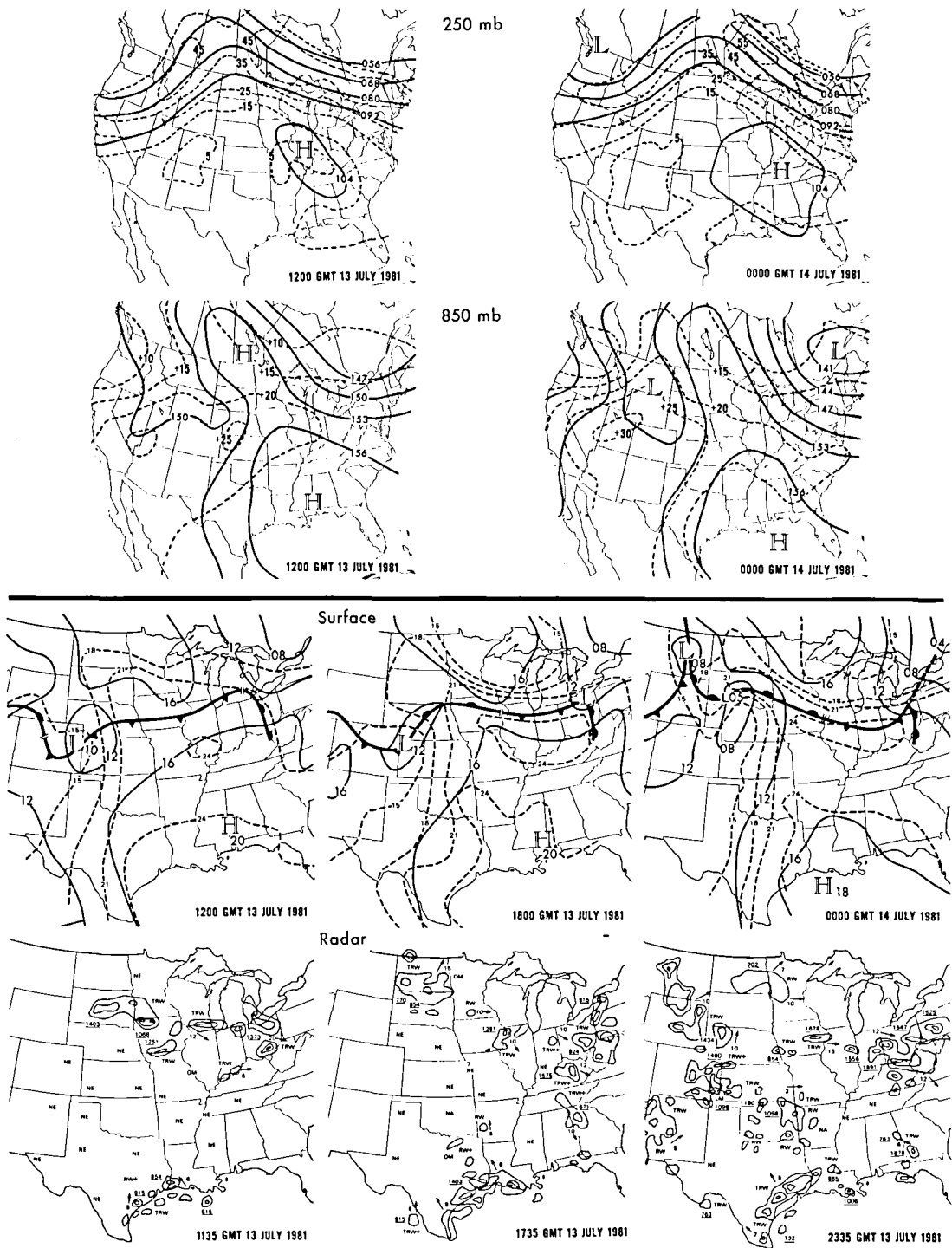
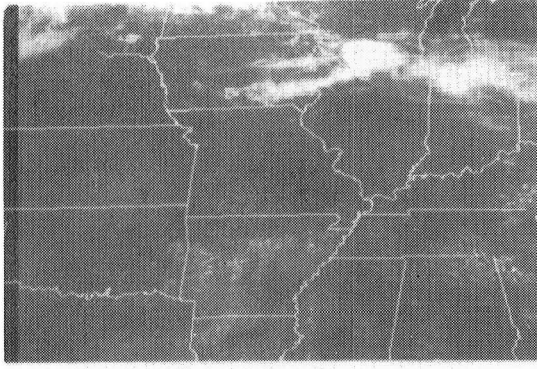
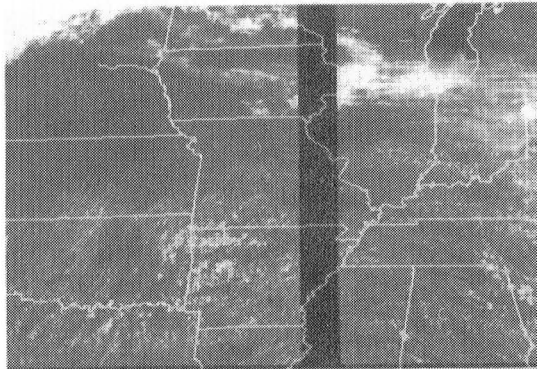


Figure 6-1. Upper Air, Surface, and Radar Maps for July 13, 1981

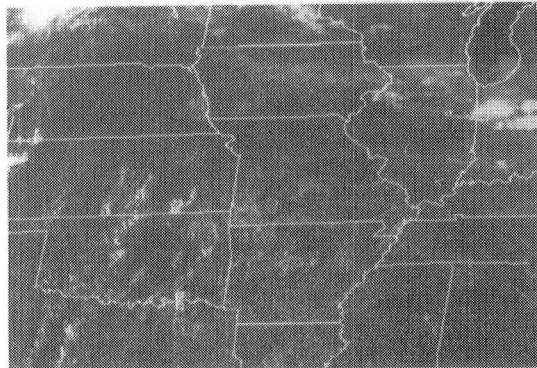
1500 GMT



1800 GMT



2100 GMT



2300 GMT

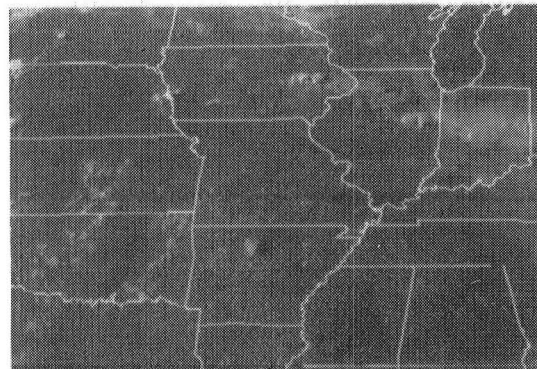
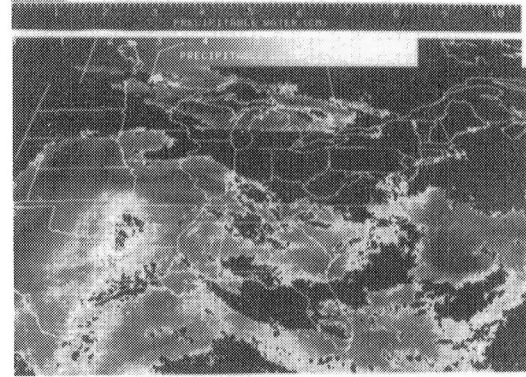


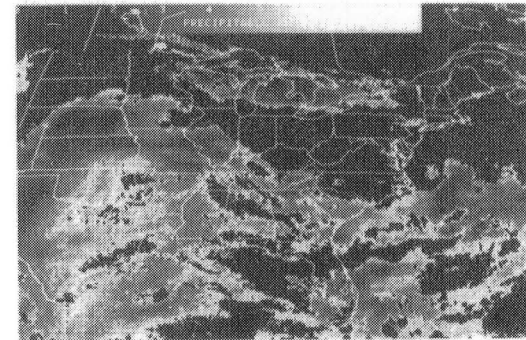
Figure 6-2. Three-hourly VAS Visible Images for July 13, 1981

Split window - Low Level Moisture

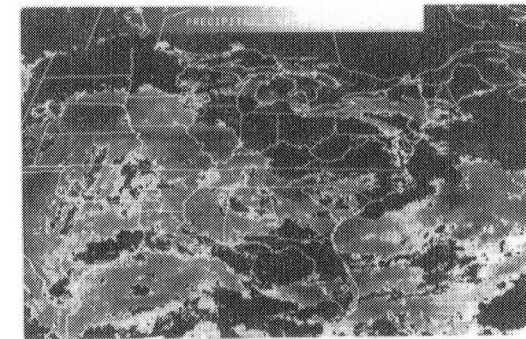
1500 GMT



1800 GMT



2100 GMT



2300 GMT

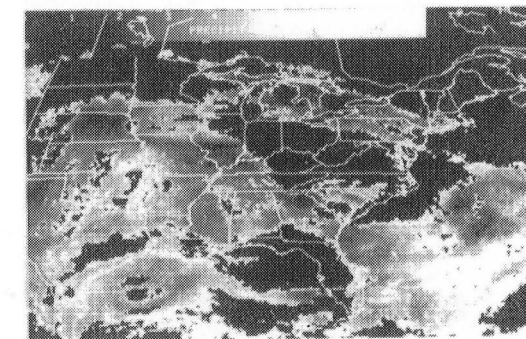


Figure 6-3. Three-hourly Sequence of VAS Split Window Images for July 13, 1981

Precipitable water estimates were verified using independent radiosonde measurements taken twelve hours after the initial air temperature determination. An accuracy of $\pm 1.0 \text{ g cm}^{-2}$ was established over a range of 1.7 to 5.5 g cm^{-2} . Unresolved clouds make up a large

portion of the error. The cloudlike patterns of excessive water vapor are readily identified in the images and can be easily avoided (dark areas in Figure 6-3). Spot verifications of the VAS-derived water vapor field were made against individual radiosonde reports for this case (Chesters *et al.*, 1983). For example, the radiosonde soundings from Salem, Illinois, at 1200 GMT on 13 July and 0000 GMT on 14 July 1981, shown in Figures 6-4(A) and (B), verify that significant drying occurred within several layers below 600 mb in south-central Illinois, even though the surface dewpoint readings remained nearly constant. The drying is also numerically verified by the spot values of precipitable water computed at the collocated VAS and radiosonde observations (listed on Figures 6-4(A) and (B)). Therefore, the VAS split window can differentiate those areas in which the water vapor extends over a deep layer and is more able to support convective cells, from those areas in which the water vapor significantly decreases immediately above the earth's surface and is therefore less able to support convection. This conclusion is supported by other examples presented and discussed by Chesters *et al.* (1983).

The image analysis research for the July 13th case was also used to determine the extent to which VAS can delineate those regions where the moist lower-tropospheric air mass is capped by dry air in the middle to upper troposphere, and relate this vertical moisture distribution to convectively unstable air masses (see Petersen *et al.*, 1983). The $6.7\text{-}\mu\text{m}$ infrared observing channel of VAS was chosen to monitor mid-tropospheric moisture. While the weighting function for the $6.7\text{-}\mu\text{m}$ channel peaks near 400 mb, the transmittance weighting function extends approximately from 200 to below 700 mb. When the atmospheric water vapor is distributed uniformly, observations from this channel represent an estimate of the total integrated water vapor content in the upper and middle troposphere. The precise altitude of a single layer of excess moisture cannot be determined from this channel alone, since the amount of radiation received by the satellite is a function of both water vapor content and temperature. Therefore, differing amounts of water vapor and varying temperature can give almost identical radiometric signals to the spacecraft. Nevertheless, the interpretation of the satellite image is unambiguous in areas where little or no water vapor is present, since the warm low-level temperature is observed through the dry mid-level air to provide a distinct and sharply contrasting signal. As the water vapor content in the upper troposphere decreases, the level at which this channel's weighting

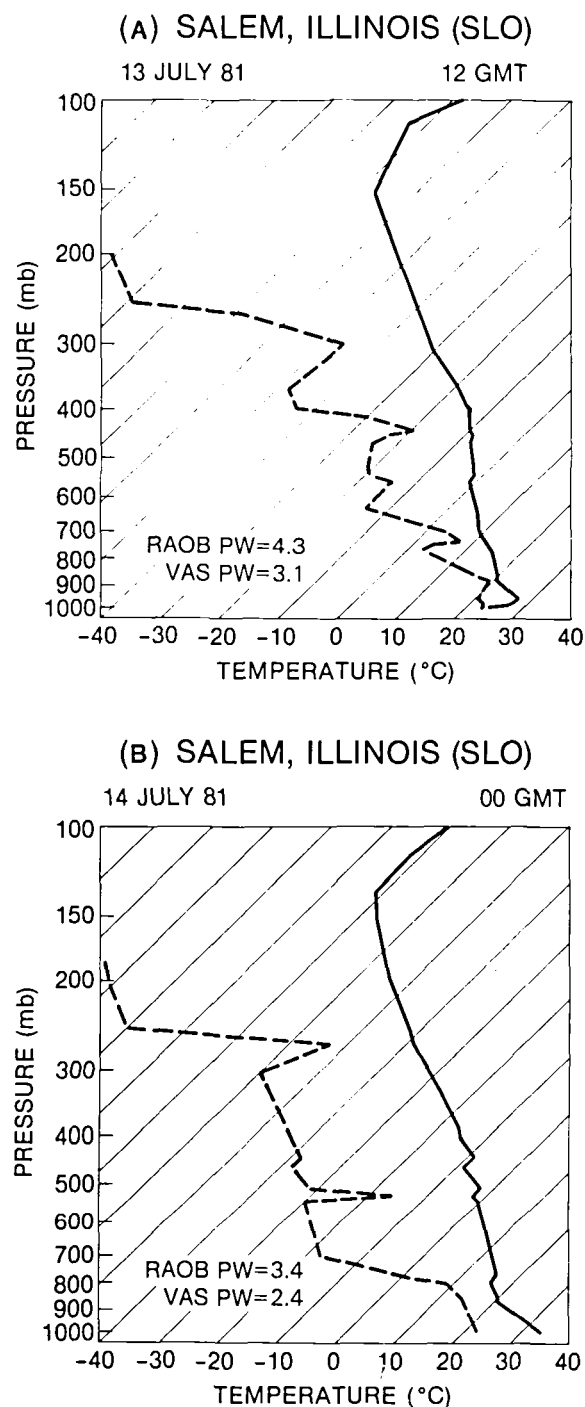


Figure 6-4. Radiosonde Soundings for Salem, Illinois

6.7 micron - Middle Level Dryness

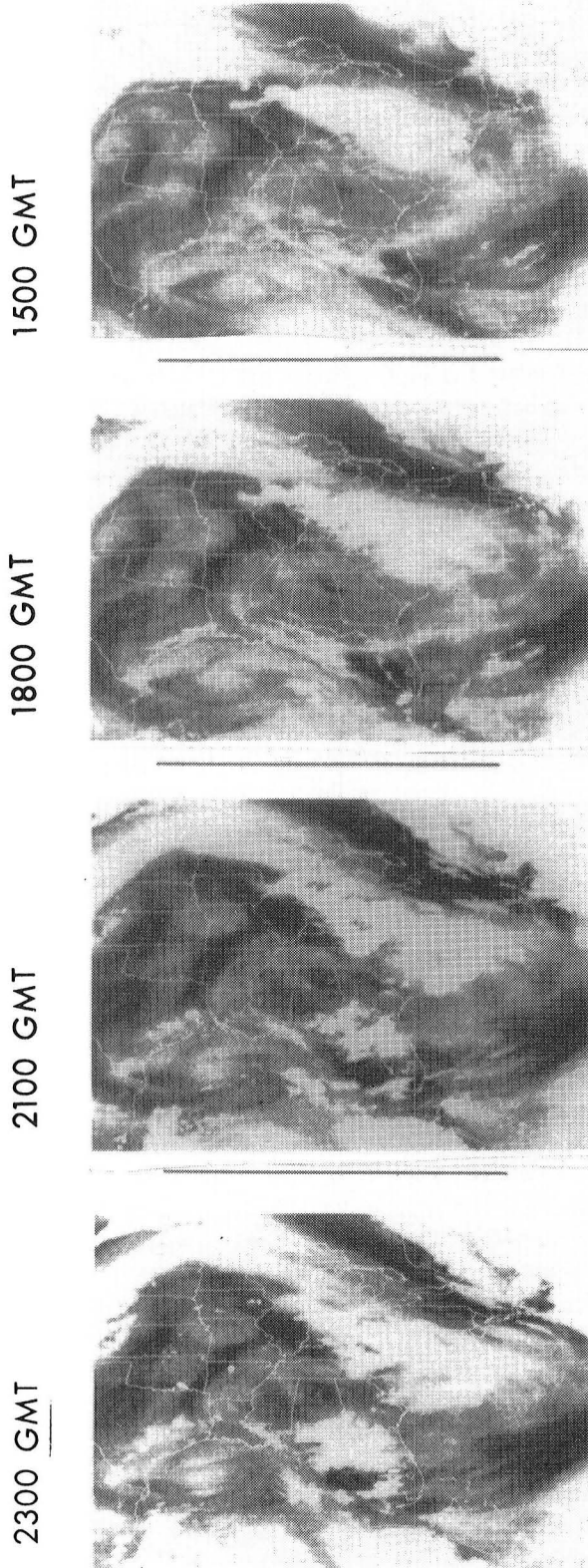


Figure 6-5. Sequence of 6.7 μm moisture Images for July 13, 1981

function peaks, shifts downward significantly. Consequently, a strong warm signature on the imagery, represents dry conditions throughout a deep layer extending downward to 700 mb.

The sequence of moisture images from the 6.7- μm channel is shown in Figure 6-5 for the 13 July 1981 case. The mid to upper-level water vapor fields over the central United States reveal remarkable structure within the "clear air" as observed by the visible channel (Figure 6-2). A cyclonic vortex located over the Colorado-Kansas region at 1500 GMT, and imbedded within a generally anticyclonic flow field (Figure 6-1), slowly moves north-northeastward during the day and dissipates. The 6.7- μm channel also reveals distinct bands of mid-level dryness that are located directly above the low-level moisture maxima in Iowa, Kansas, and Oklahoma, as derived from the split window. These observations confirm the radiometric independence of the VAS measurements in these spectral bands. The convection that developed in these areas (denoted by the "white clouds" in Figure 6-5 and black "cloud contaminated" pixels in Figure 6-3), developed as the dry air aloft, moved over the regions marked by low-level moisture maximum. Consequently, the VAS images delineate areas where the potential for convective instability is enhanced by differential moisture advectations prior to the onset of the convective storms. Point-by-point measurements made for this case, confirm that the air masses were convectively unstable where dry air overlays the moist air, as inferred from the VAS imagery.

The second case study of the outbreak of severe convection for which VAS imagery was available is the 20 July 1981 case (see Petersen *et al.*, 1984; Smith *et al.*, 1982), which traces the evolution of two distinct areas of convection that developed during the daylight hours. Although little large-scale dynamical forcing existed on 13 July, the 20 July 1981 case is characterized by a moderately strong baroclinic zone and jet streak, and a progressive surface cold front that initiated a very intense organized convective system. Throughout the day, a 500-mb short wave moved toward the Mississippi Valley, with strong cold advection ahead of a jet streak, propagating from Wyoming into Nebraska (Figure 6-6). At the surface, a cold front, extending from central Colorado to a diffuse low pressure system over Michigan, was beginning to drift slowly southward. The frontal boundary separated the warm moist air that was being transported northward over the south-central United States (dewpoint temperatures soon exceeded

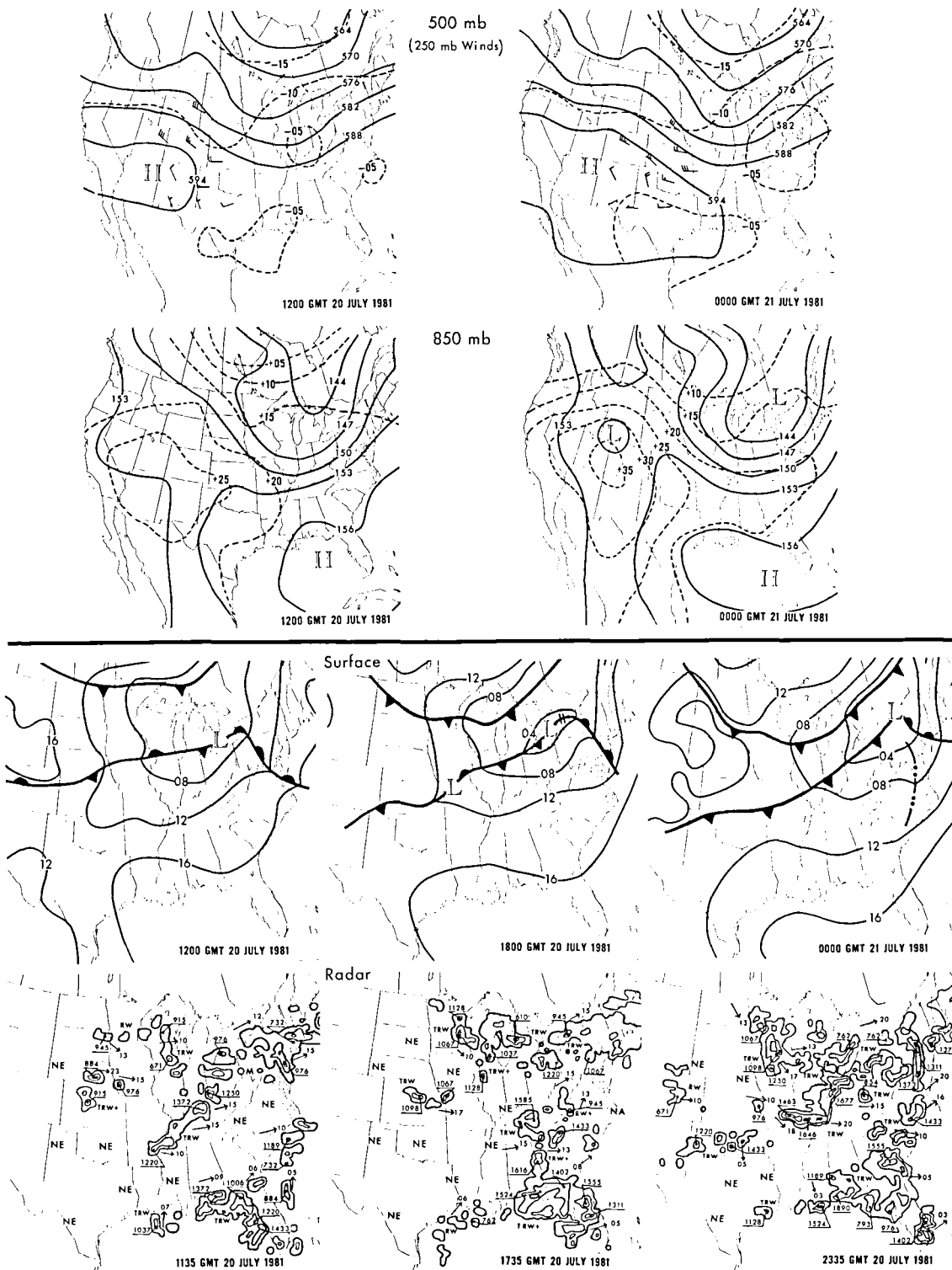


Figure 6-6. Upper Air, Surface, and Radar Maps for July 20, 1981

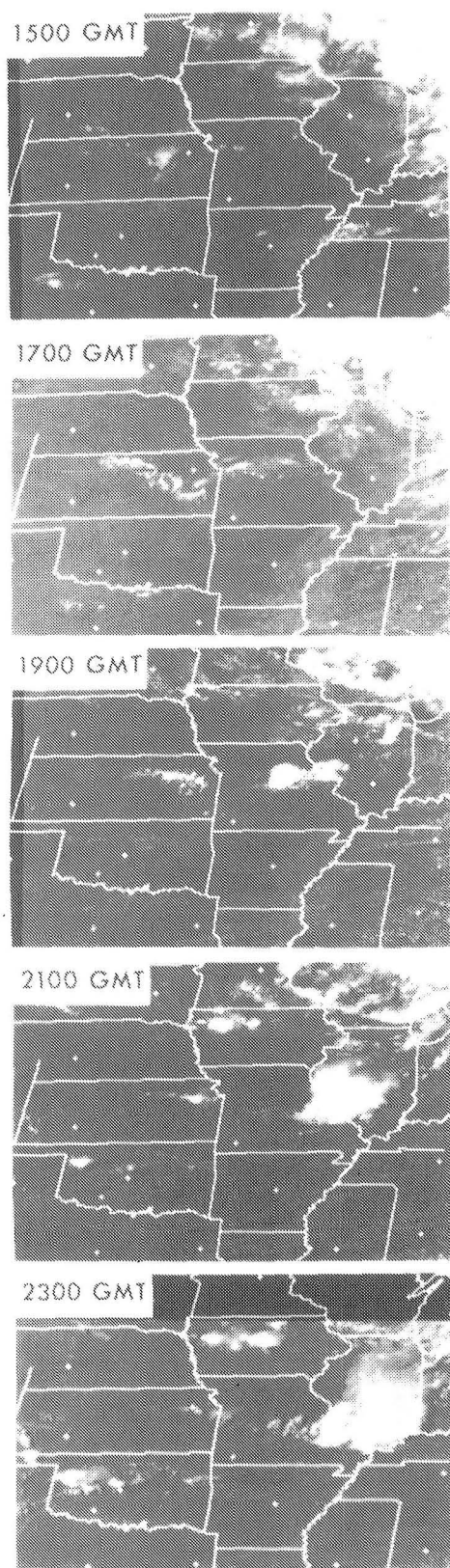


Figure 6-7. VAS Visible Imagery for July 20, 1981

25°C over central and southern Missouri), from the significantly cooler and drier air mass to the north. By 1800 GMT, an isolated, short-lived convective cell formed in north-central Illinois, followed by the development of a group of massive thunderstorms over central Missouri (see Figure 6-6), that moved southeastward throughout the afternoon. Later in the day, a second line of thunderstorms formed across Oklahoma. The explosive development of the thunderstorms in Missouri and Oklahoma is also depicted in the visible imagery in Figure 6-7. Although surface dewpoints over Oklahoma were less than those measured farther to the east, temperatures in excess of 40°C provided an ample energy source to support the convective storms.

A time sequence of split window low-level water vapor images produced with an average layer temperature representative of the area south of the cold front is shown in Figure 6-8. The solid black areas on the images are regions of obvious cloud cover, or are areas where moisture estimates could not be made since the boundary layer air temperature was much colder than that estimated for the south-central United States (e.g., the black areas north of the cold front in Iowa). The split window precipitable water imagery at 1500 GMT (Figure 6-8) shows two moisture wedges, one over south-central Nebraska and eastern Kansas, the other extends across northern Missouri into north-central Illinois. By 1700 GMT, the overall moisture patterns gradually moved eastward. While retaining their basic shapes, the magnitude of the low-level moisture maxima increased over northern Missouri from 1500 GMT. This increase in brightness was primarily due to the presence of scattered low clouds, that are evident on the 1-km visible imagery (Figure 6-7). While the cloud contamination invalidates the quantitative measurement of precipitable water in this area (Chesters *et al.*, 1983), the split window and visible data provide the strong and meaningful low-level moisture image needed to infer a potential for convective instability in the image overlay procedure.

A second low-level moisture maximum protruding northwestward over the cloud-free regions of northern Oklahoma becomes more pronounced by 1900 GMT. Again, the low-level moisture maxima are divided by narrow bands of dryness (one reaches across southern Iowa into southern Nebraska and northern Kansas, and another extends westward from southern Missouri into southeast Kansas). This is a mesoscale structure that cannot be resolved using the operational radiosonde data alone.

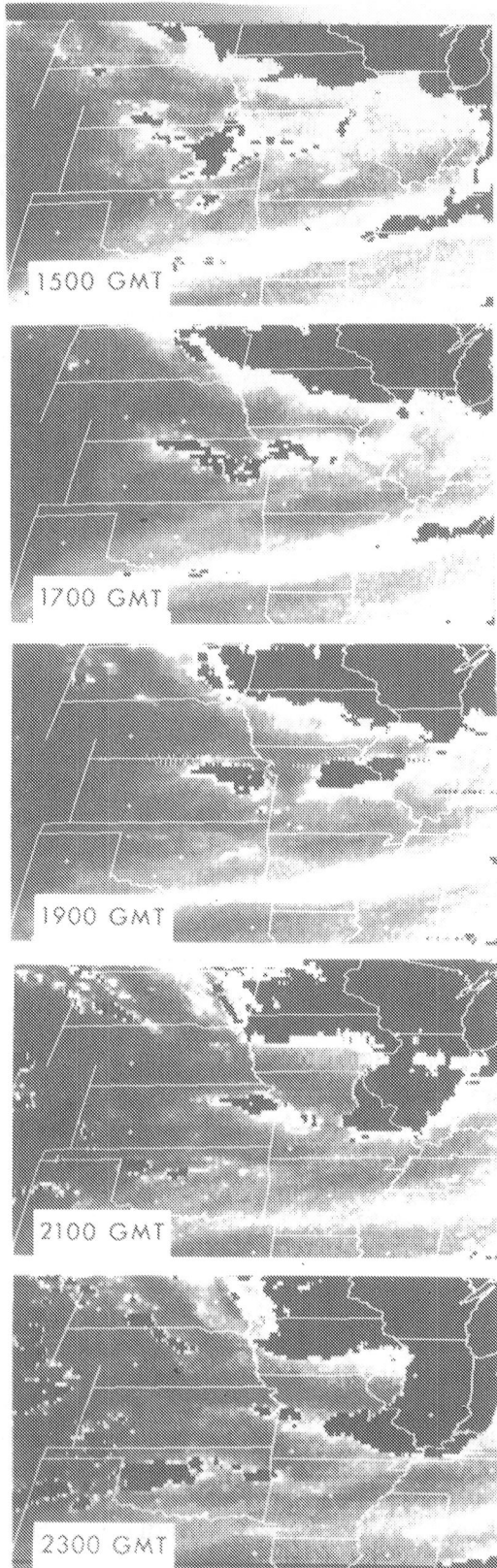


Figure 6-8. Split window-low level water vapor images for July 20, 1981

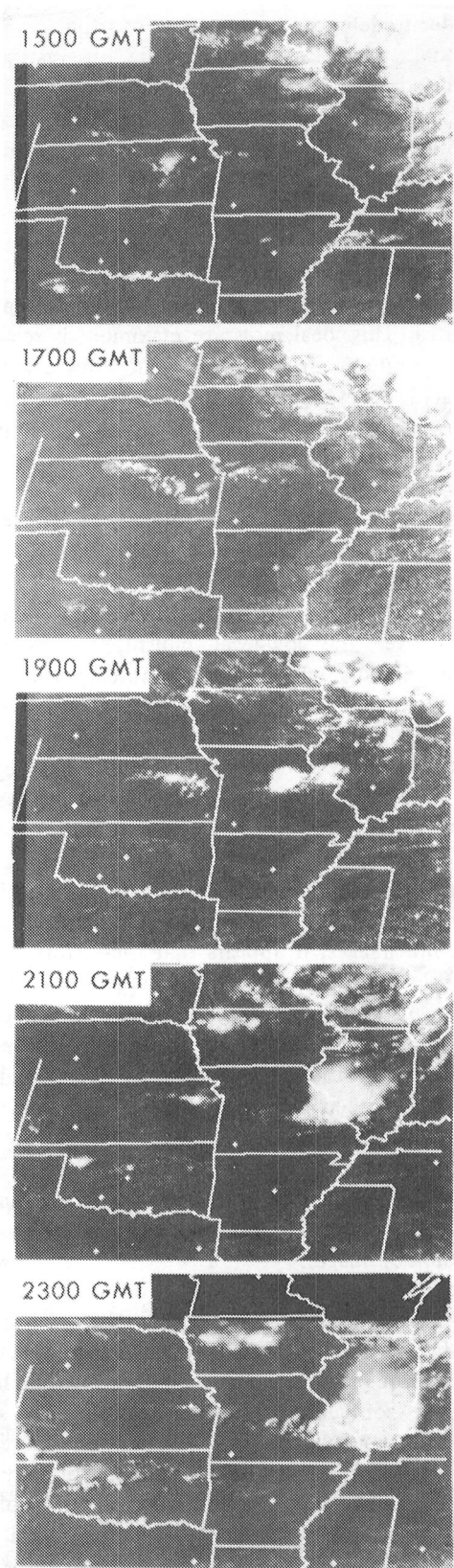


Figure 6-9. 6.7 μm Middle Level Dryness

In order to delineate specific areas of strong convective potential, these low-level moisture observations are contrasted with the distribution of mid-level dryness measured by the 6.7- μm infrared channel (Figure 6-9). At 1500 GMT, a continuous band of dry air associated with the polar jet approaching the mid-level short wave, was curving from western South Dakota, across Nebraska and Iowa into southern Wisconsin. The spatial continuity of this dry belt is interrupted by a moist signal over northeastern Kansas and eastern Nebraska. This local moisture maximum is related to an evaporated cirrus shield from convection that dissipated in east-central Nebraska and northeastern Kansas, prior to 1200 GMT. As such, the deep layer of mid-level dryness should be considered as a single, continuous, elongated feature, extending from Montana, across Nebraska and northern Missouri toward Wisconsin.

After 1700 GMT, the mid-level moisture minimum moved over the low-level moisture maximum in northern Illinois, with convection developing along the edge of the mid-level dryness wedge. This particular convection was short-lived, moving eastward and then weakening after being overtaken once again by the moist mid-level air to the west. The most intense convection of the day began to develop at 1700 GMT, apparently ahead of the upper-level dryness boundary in northern Missouri. Viewing the spatial continuity present in a time lapse sequence of a more frequent set of 6.7- μm images, it appears that these storms did in fact form at the intersection of the mid-level dryness and low-level moisture signals. While the mid-level dryness bands that were noted in other cases often had distinct edges, the boundary of the deep mid-level dryness is masked by the aforementioned evaporated cirrus. *It must be noted that much of the value of using the 6.7- μm imagery to delineate mid-level dryness, lies not only in the individual images themselves, but also in the continuity of features observed through a succession of images.*

By 1900 GMT, a second area of mid-level dryness (that extended from the Texas panhandle across Kansas) became more pronounced. Although this feature has an elongated configuration (similar to the dry streak aligned with the high-speed flow around the short wave trough), this dryness wedge is situated normally with the mid-tropospheric flow, and away from the polar jet streak. Analysis of the upper-level radiosonde wind reports at 1200 and 0000 GMT, indicate that this band of intensifying mid-level dryness appears to be the con-

sequence of strong subsidence, associated with substantial along-stream velocity convergence, near the 250-mb level (note the winds shown in Figure 6-6). The magnitude of this mid-level drying is evident when comparing the 1200 and 0000 GMT radiosonde soundings in this area, where dewpoints above 750 mb decrease by as much as 25°C during this period (not shown).

The sequence of combined "split window" and 6.7- μm channel images show that the upper-level dryness over Oklahoma is moving rapidly toward the south and the east, as the low-level moisture is stationary or moving slowly toward the north and west (Figure 6-8). *This sequence provides evidence that VAS images can be used to infer the differential moisture advections that contributed to the development of a convectively unstable air mass, suitable for the development of severe convective storms.*

An alternative display of the intensification of the vertical moisture gradient over Kansas and Oklahoma is shown in Figure 6-10. The display was obtained by multiplying scaled low-level moisture values at each pixel (m_L), by the magnitude of the upper-level dryness ($1-m_U$), where m_L and m_U range from 0 to 1. The product $m_L(1-m_U)$ represents a measure of the vertical moisture gradient, that is displayed in an image format. This approach guarantees that the mid-level dryness extends through a deep layer of the troposphere, i.e., it ensures that the split window moisture is not being observed by the 6.7- μm channel. The sequence of 2-hourly images in Figure 6-10, isolates the effects of the differential moisture advection. In northwestern Oklahoma, the image changes in its intensity between 1700 and 2100 GMT, indicating that the vertical moisture gradients are increasing with time as the dry air moves over the moist lower troposphere. The image sequences in Figure 6-8 and 6-9 show that, for this case, the convection developed when the dry air overlays the extremely warm and moist low-level air below, first over western Oklahoma (after 1900 GMT) and then throughout the entire central region of the state (after 2100 GMT). As in previous cases that were studied, the preferred region for convective development was near the edges of the dry slots in the middle and upper troposphere. Not only is convective instability implicated in regions where the dry air is superimposed over low-level moisture, but the probable decrease in subsidence along the edges of these dry wedges may also allow a mechanism for an easier release of this instability.

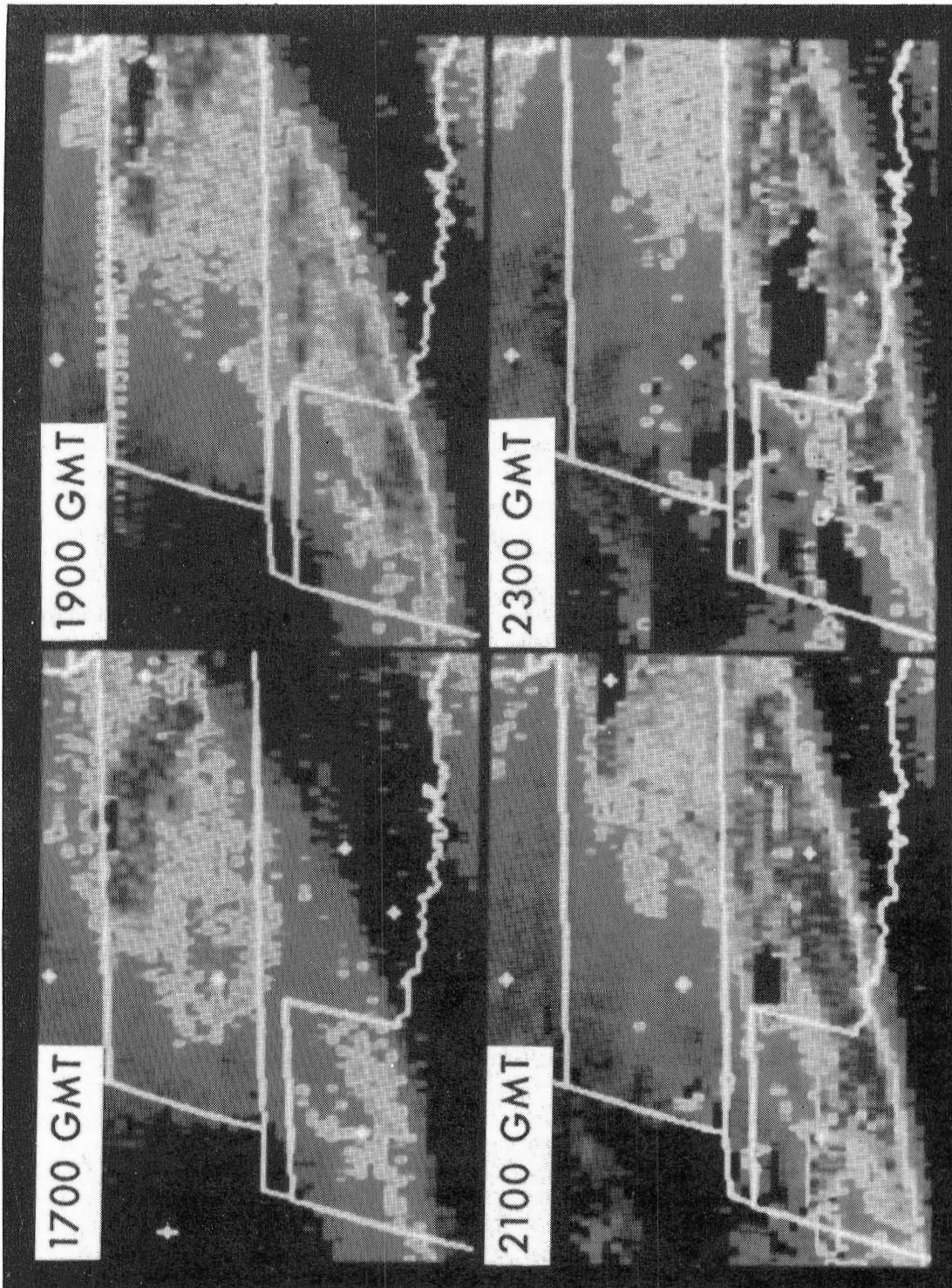


Figure 6-10. Two-hourly vertical moisture gradients over Kansas and Oklahoma on 20 July 1981

Analyses of these cases point to the ability of the VAS instrument to delineate meteorologically meaningful patterns of low-level moisture and mid-level dryness, and to the utility of the image overlay and multiplication procedures for isolating (in near real time) regions of convective instability in a rapidly changing environment. Mesoscale moisture patterns for the upper and lower troposphere are obtained in clear, and cloudy areas, and in a variety of baroclinic and barotropic environments. *The image sequences from both cases show that the VAS moisture channels can be used to infer differential moisture advection that convectively destabilize the atmosphere. The image analyses also reveal that there is a distinct preference for convection development along the edges of the upper-level dryness wedges in areas of plentiful low-level moisture, and within an area of mid-level dryness as it moves over a low-level moisture maximum in the vicinity of surface forcing.* The technique of superimposing the mid-level dryness pattern over the low-level moisture field proves extremely useful in isolating regions of potential convective instability.

The moisture patterns observed by VAS have a mesoscale structure and a temporal evolution that cannot be resolved fully, using the conventional radiosonde database. Point-by-point comparisons between radiosonde and the VAS moisture images confirm the dry and moist regions, and indicate that convective instability exists where VAS measures the dry air overlaying moist air masses. Direct confirmation of the mesoscale patterns and temporal evolution of the images is not possible. Nevertheless, the persistence of convective development along these thermodynamically meaningful interfaces provide convincing evidence for their existence and usefulness.

The results also indicate several precautions which must be observed when using the VAS data: 1) Unresolvable low clouds can easily contaminate the low-level precipitable water estimates. Although this can restrict the quantitative use of the split window technique, the procedure is still applicable for qualitatively isolating areas of large low-level water vapor content. 2) Although most upper-level jet streaks tend to be accompanied by bands of dry air observed in the 6.7- μm imagery (e.g., Ramond *et al.*, 1982), meteorologically significant elongated dryness patterns can also develop and persist that are not related to a jet maximum and are not parallel to the upper-level flow. Therefore, care must be taken when relating these streaked, mid-level dryness patterns to upper-level flow regimes. The overlay of upper-level radiosonde reports on the imagery

becomes particularly useful in this respect. 3) Thin layers of cirrus or moisture from evaporated cirrus can often effectively mask a deep layer of dryness throughout the remainder of the troposphere. In this case, evaporated cirrus blowoff from previous convection, obscured the precise timing of the mid-level dryness/low-level moisture interface over Missouri. This difficulty can be overcome, to some degree, by viewing time sequences of images rather than focusing attention on a single time period.

Since this study relied almost exclusively on short-interval satellite data, the results have immediate potential for near real-time forecast application. The full utilization of the information from VAS can only be realized when used jointly with all forms of conventional data. Therefore, future development must also incorporate data from a variety of sources, including detailed analyses of surface observations and derived parameters (such as surface divergence and moisture divergence), to more completely relate the processes that act to destabilize the atmosphere and those that act to release the instability and initiate the storm systems.

6.1.3 Phase 3 of GSFC Research Effort: Assessment of VAS Retrievals for Pre-Storm Environments

Temperature and dewpoint profiles were retrieved from all of the VAS channels and thoroughly verified for the two July 1981 cases. The main intent of this phase of the research effort was to determine whether the information seen in the multispectral images could be quantified and used to effectively analyze a preconvective environment. Section 5.1, and Lee *et al.* (1983) describe the linear, "ridge" regression scheme, that combines VAS and surface observations, and was used to produce VAS soundings in the case studies described below. We now address the meteorological application of the VAS retrievals, specifically, in a case study mode to determine the extent that VAS can improve the temporal and spatial resolution over conventional data.

July 13, 1981:

In order to survey the setting for the isolated convection that develops near the stationary front over Iowa on 13 July 1981, the VAS retrieval domain was chosen to encompass most of the central plains. This area is well-suited for VAS soundings since the preconvective environment was relatively cloud free. The VAS retrievals were first computed on a 1° by 1° grid. The cloud contaminated retrievals were then eliminated

and the person-in-the-loop interactive approach was used to derive soundings at clear sites (as determined from the visible imagery), near partly cloudy to cloudy areas. The number of retrieval sites vary from 132 at 1202 GMT to 171 at 1802 GMT. A GEMPAK-Barnes objective analysis (Koch *et al.*, 1983) was performed on the data to generate a regularly spaced grid at $1/2^\circ$ resolution.

The sensitivity of VAS retrievals to potentially harmful predictors was tested by selectively eliminating either noisy channels (1, 2 and 3), or skin-sensitive window channels (8 and 12). The removal of channel 12 caused a marginal overall bias in the retrieved fields (Lee *et al.*, 1983). The elimination of more predictors generally resulted in an obvious degradation of the retrieved parameters, except at the lowest levels where the surface predictors dominate the retrievals. In the final analysis, all 12 channels, and surface temperature and dewpoints, were used in the regression retrieval scheme.

The time sequences of 850-mb temperature and dewpoint analyses, both show striking temporal continuity in the mesoscale structure of the thermal fields (Figure 6-11). A wedge of warm air extending from the west through Omaha in the radiosonde based analysis, is further refined in the VAS analysis reaching eastward along the Iowa-Missouri border. A comparison between an analysis of radiosonde and VAS data (Figure 6-11E) shows a marked increase in the detail of the thermal structure near the surface frontal zone, while maintaining excellent correlation at radiosonde observation points. The VAS retrievals display a systematic warming and cooling ahead of, and behind the front, respectively, on a scale not resolvable with the RAOB network.

Analyses of 850-mb retrieved dewpoints (Figure 6-11) show important details beyond the resolution limits of the conventional radiosonde network. A moisture maximum can be traced eastward across Iowa during the 5 hour period (Figure 6-11). A second maximum is intruding into southwestern Missouri and eastern Kansas from Oklahoma. These two moisture maxima are divided by a band of drier low-level air extending southeastward from Nebraska through central Missouri. Comparisons with 0000 GMT radiosonde analyses (Figure 6-12) illustrate the increased horizontal resolution present in the VAS observations. The VAS retrievals isolate a distinct moisture maximum in southeastern to east-central Iowa, where the convection developed by 0000 GMT. Additionally, this moisture maximum, the band of lower dewpoints across Missouri, and the second moisture regime extending northeast from

northeast Oklahoma into central Kansas, all agree with the low-level water vapor images presented earlier.

To test the ability of VAS to resolve vertical temperature and moisture structure in this case, a vertical cross-section of θ_e , retrieved along 41 degrees north latitude (across Iowa) is shown in Figure 6-12 for 2100 GMT. The large boundary layer values of θ_e correspond with the moisture maximum observed using the split-window technique (Figure 6-3). The minimum value of θ_e near the 600-mb level agrees with the dry slot observed using the $6.7\text{-}\mu\text{m}$ channels (Figure 6-5). The decrease of θ_e with height in this region is indicative of a convectively unstable pre-storm environment in Iowa. Although the vertical gradients are much weaker than would be expected from radiosonde observations, the cross-section clearly indicates a significant decrease of θ_e with height, and substantiates the convective instability qualitatively inferred from the combined image overlay procedure previously discussed.

July 20, 1981:

Soundings across the central plains were derived from 1200 GMT 20 July to 0000 GMT 21 July using the linear regression technique. Statistical training was based on 50 radiosonde sites across the eastern half of the country (26 from 1200 GMT and 24 from 0000 GMT), to provide an adequate sample size for the correlation coefficient matrix calculation. The selection of suitable clear radiosonde sites was done with visible imagery. Small adjustments in radiosonde locations and data were made when sites were located on the edge of cloud cover.

Radiances from 11 VAS channels, supplemented by conventional surface temperature and dewpoint reports, comprise the statistical predictors used in the regression procedure. Channel 12 was not applied to this study because of several missing scan lines at certain observation times. Analyses physically show that reasonable soundings for this case are still produced when channel 12 is excluded from the matrix calculation.

Satellite retrievals of temperature, dewpoints, and the other parameters were obtained at approximately 100 km intervals over a domain extending from 29 to 48° N and 86 to 103° W. The number of retrieval sites varied from 192 at 1202 GMT, to 225 at 2102 GMT for this case.

The VAS derived precipitable water (PW), and lifted index (LI) are discussed for this case. Temperature and

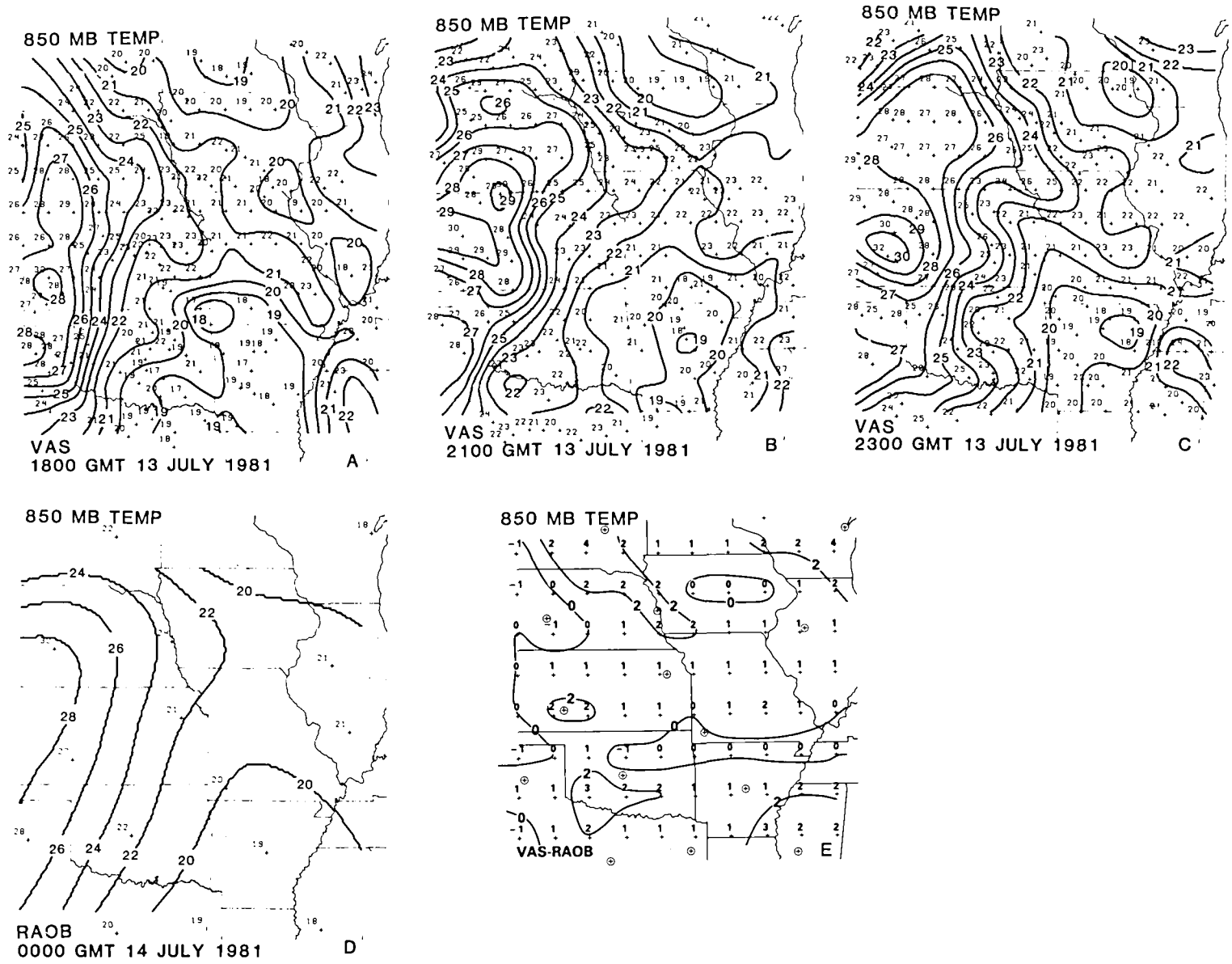


Figure 6-11. Time Sequence of 850 mb Temperature and Dewpoint analyses with RAOB comparisons at 0000Z for 13 July 1981

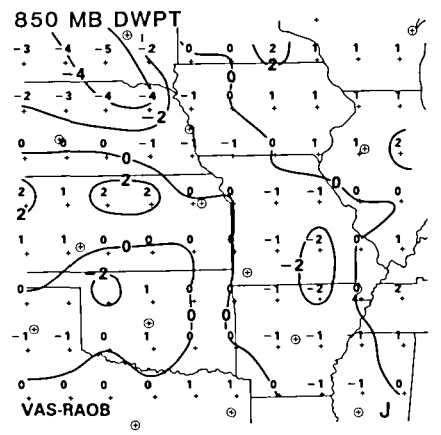
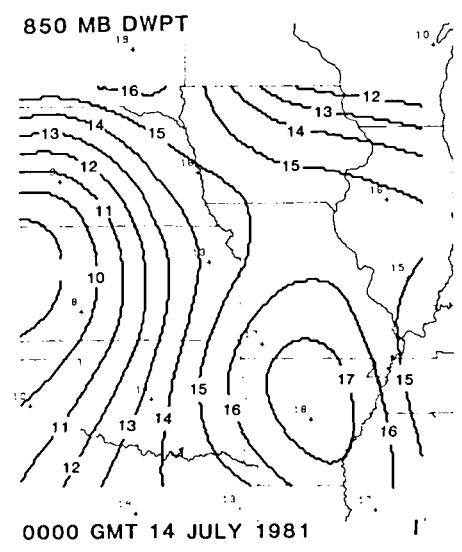
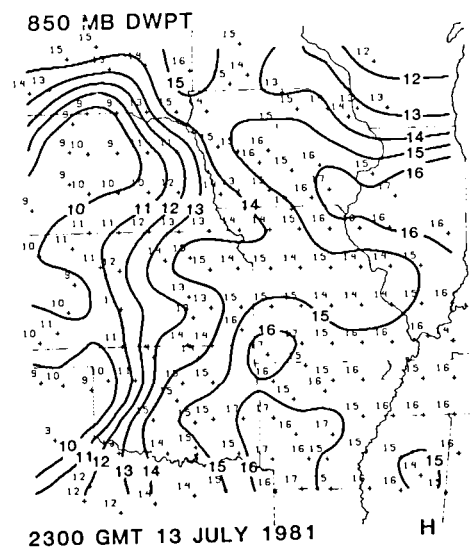
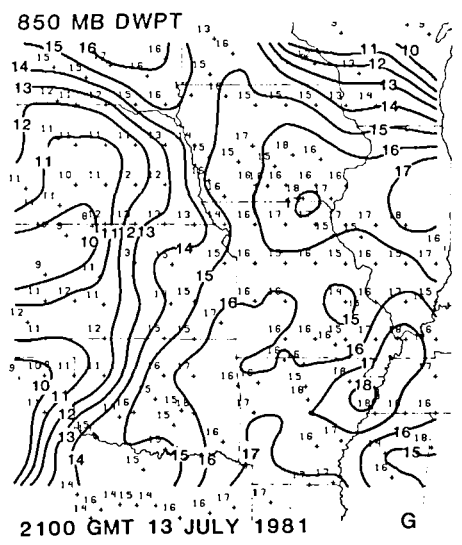
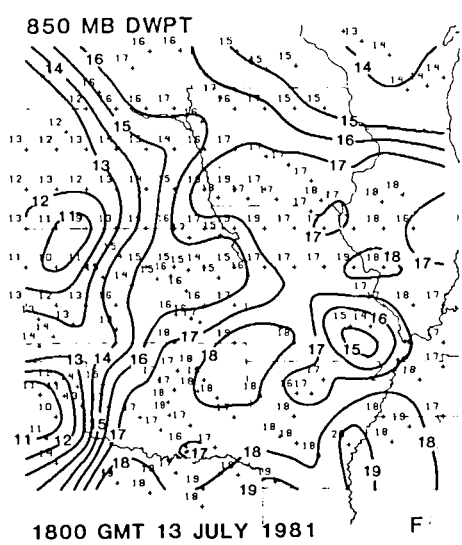


Figure 6-11. (Continued)

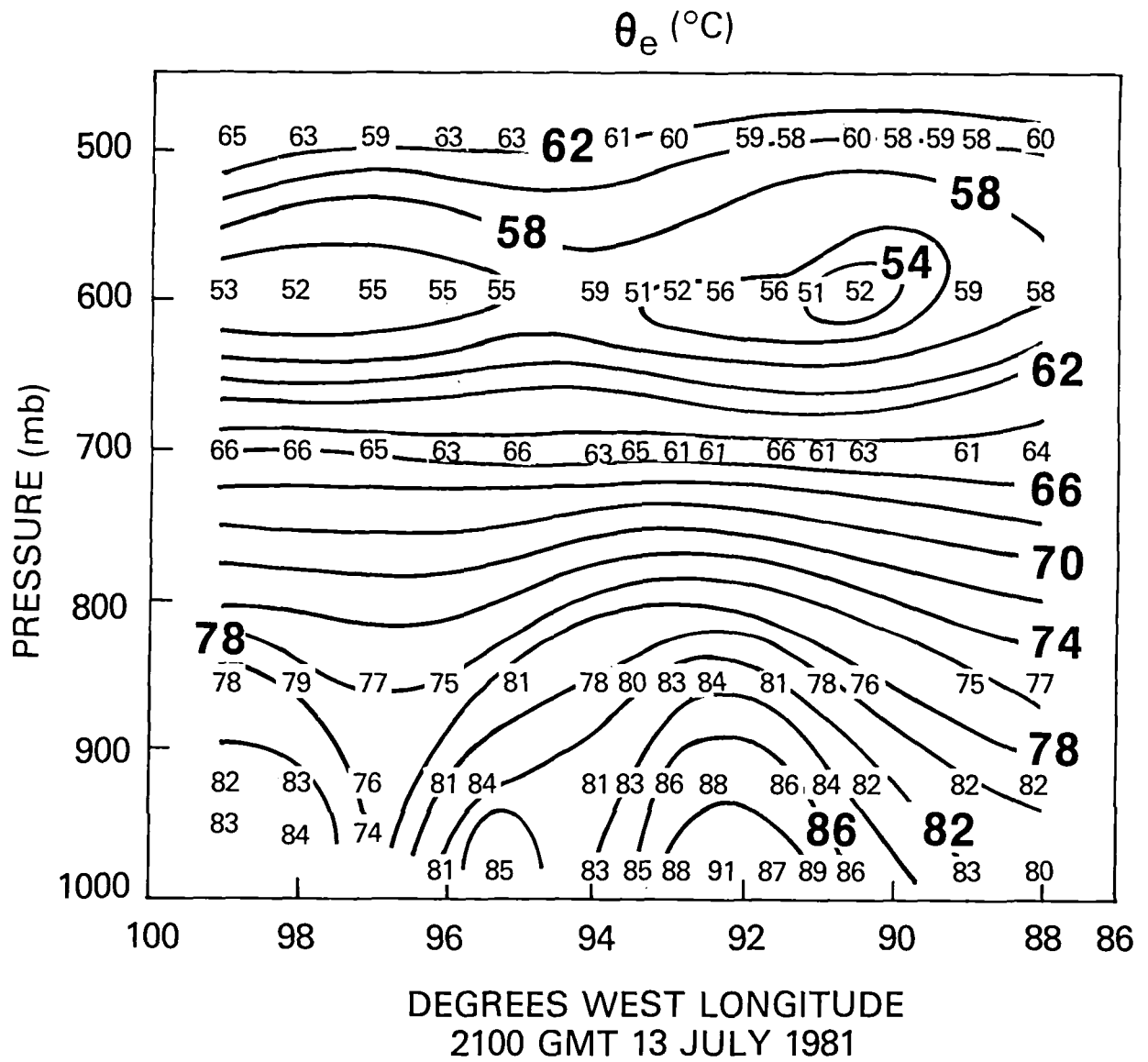


Figure 6-12. Vertical Cross Section of θ_e From South Dakota through Southern Illinois.

dewpoint fields are discussed by Petersen *et al.*, (1983). In general, the LI fields appear to be more consistent, spatially and temporally, and agree better with the 1200 and 0000 GMT radiosonde values, than either the Showalter, or totals-totals indices (not shown). The precipitable water retrievals also display good spatial and temporal consistency.

The VAS derived PW field displayed in Figure 6-13, shows a moisture wedge across northern Missouri at 1500 GMT, that slowly moved southeastward as significantly drier air moved in from the northwest. The convection that was initiated at 1800 GMT over Missouri (Figure 6-6), developed along the strengthening moisture gradient as it moved southeastward. The precipitable water retrievals over Missouri are consistent with the split window moisture image (Figure 6-8) that displays similar temporal evolution of the moisture field, prior to the onset of convection.

Retrievals of LI (Figure 6-14) indicate increasing destabilization across northern and central Missouri between 1200 and 1800 GMT, with values decreasing to -4 and -5, over the area in which the severe convection rapidly developed around 1900 GMT (Figure 6-6). Again, the decreasing LI derived from the VAS soundings, confirm the destabilization process inferred from VAS moisture images, where mid-level dry air measured by the 6.7- μm channel (Figure 6-9), rapidly moved over the low-level moisture maximum observed in the VAS split window (Figure 6-8). Analyses of the PW and the LI indicate that an increase in moisture and a decrease in convective stability immediately preceded the onset of convection. The VAS measurements also reveal that moisture in the region rapidly decreased, and the convective stability rapidly increased as the storms moved to the east, and cooler drier air moved in from the northwest.

The VAS PW fields (Figure 6-13) reveal a moisture maximum that extend across Arkansas and southeast Oklahoma at 1500 GMT, and slowly expanded northwestward, until it broke off into a separate moisture maximum in southwest Oklahoma by 1800 GMT. The LI (Figure 6-14) shows that the Oklahoma area is generally marked by negative values, indicating a large area of convective instability that becomes more pronounced by 2300 GMT. The increasing moisture and negative values of LI in Oklahoma are consistent with the image analysis for this region. The combination of moisture images were used to infer a region of convective instability within which convective storms developed rapidly. Analysis of the VAS derived θ_e for this region also indicate increasing convective instability between 1500

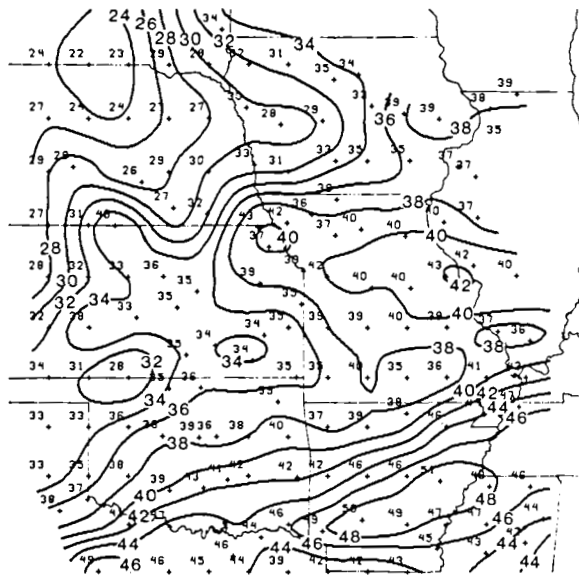
and 2300 GMT, as θ_e decreased steadily above 750 mb (as drier air observed in the 6.7- μm channel moved over Oklahoma), while θ_e increased slightly below 850 mb.

6.1.4 Summary of GSFC Research Effort

Analyses of the VAS data from the 13 and 20 July 1981 case studies indicate that the VAS offers a meso-scale data base, suitable for the analysis of severe storm situations in which the pre-storm conditions generally remain clear to partly cloudy. A split window technique (Chesters *et al.*, 1983) was derived to produce images of low-level water vapor. Upper to middle-tropospheric water vapor can be effectively monitored by the 6.7- μm water vapor channel. The VAS imagery depicts meso-scale moisture patterns for the upper and lower troposphere with a structure that cannot be resolved fully (nor verified) with the conventional radiosonde data base. The technique of overlaying the 6.7-micron upper tropospheric VAS moisture channel with the VAS split window low-level moisture field has proven useful in delineating regions where dry air overlies moist air, indicating a potential for convective instability (dry air over moist air) within which intense convection develops rapidly. The image analyses show a strong tendency for thunderstorm development along the edges of mid-level dry bands, often at a scale that is not resolvable using conventional radiosonde data. Not only is convective instability implicated in regions where this dry air is superimposed over low-level moisture, but the probable decrease in subsidence along the edges of the upper-level dry wedges might, in some circumstances, indicate a dynamic mechanism which acts to release the instability. The temporal evolution of the moisture fields, clearly evident when "looping" time sequences of VAS images, also provides a measure of the differential moisture advection which acts to destabilize the atmosphere, making it more conducive for the development of severe convective storms.

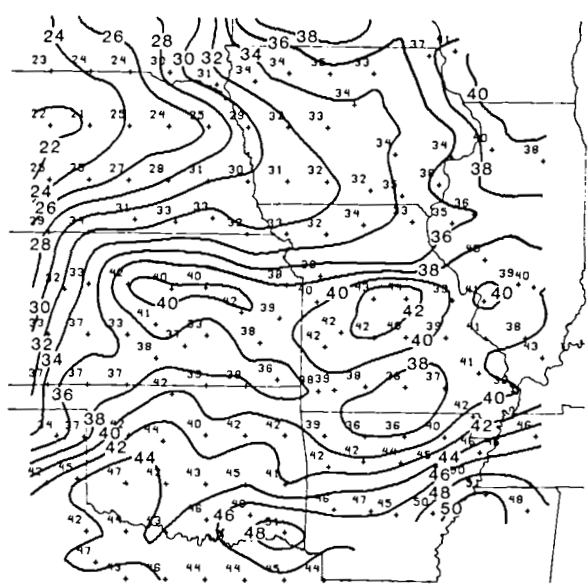
The 13 and 20 July 1981 cases were also analyzed quantitatively, using a regression sounding algorithm, to produce temperature and moisture profiles and other parameters. The results reflect the qualitative information gleaned from the VAS imagery. Regions of upper-level drying over low-level moisture can be delineated. Coherent mesoscale structure is observed within the temperature, dewpoint, θ_e , precipitable water, and lifted index fields, in space and time. The tendencies of precipitable water and LI, and cross sections of θ_e derived using VAS, reveal that regions of convective instability can be inferred from the moisture imagery and related to quantitative measures derived from VAS radiances.

VAS PRECIP. WATER



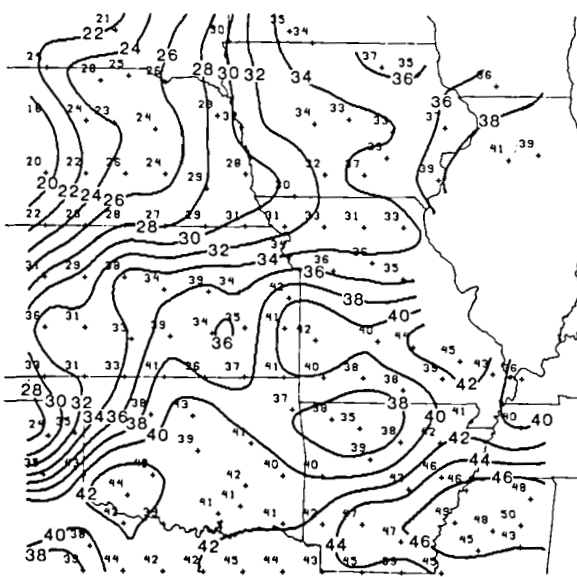
1502 GMT 20 JUL 81

VAS PRECIP. WATER



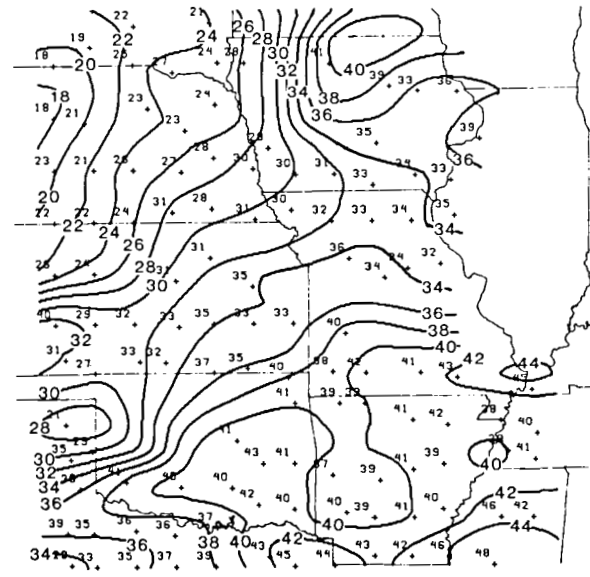
1802 GMT 20 JUL 81

VAS PRECIP. WATER



2102 GMT 20 JUL 81

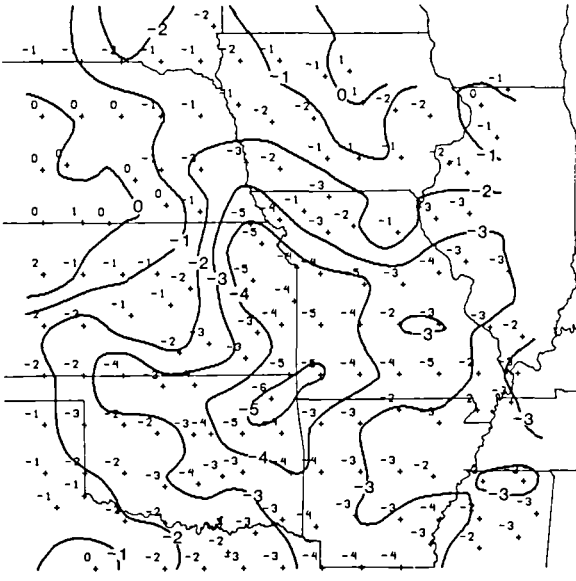
VAS PRECIP. WATER



2301 GMT 20 JUL 81

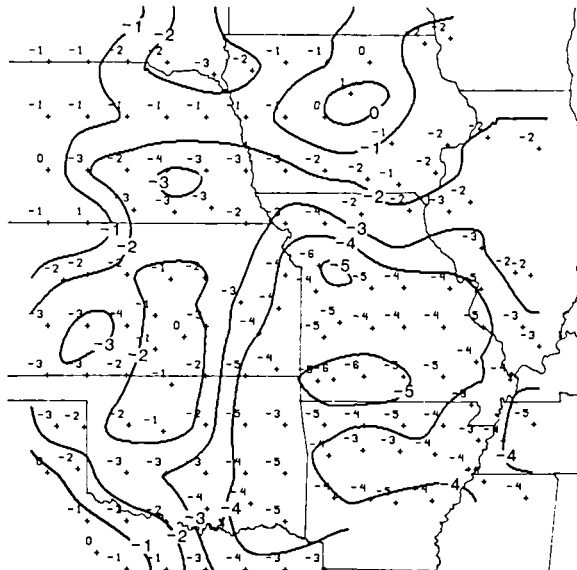
Figure 6-13. VAS Derived Precipitable Water for 20 July 1981

VAS LIFTED INDEX



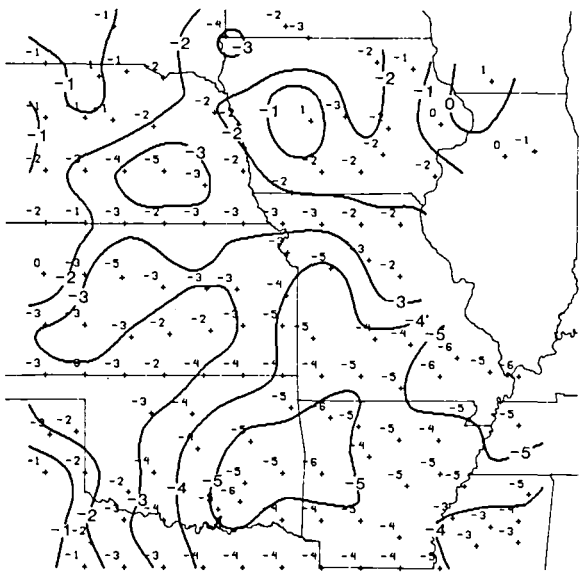
1502 GMT 20 JUL 81

VAS LIFTED INDEX



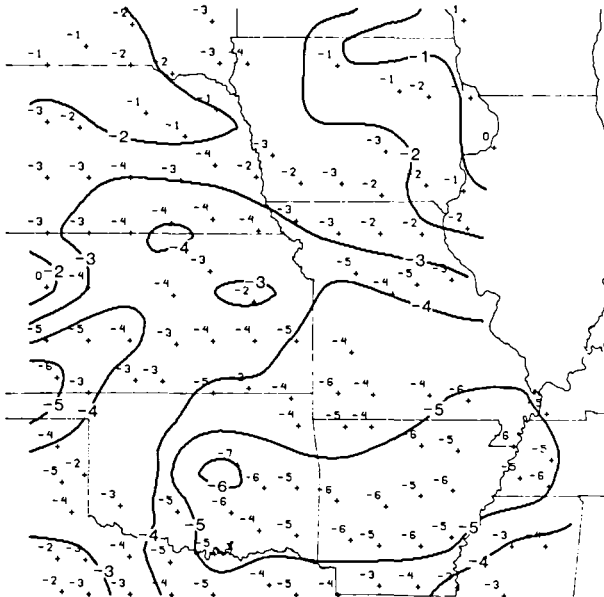
1802 GMT 20 JUL 81

VAS LIFTED INDEX



2102 GMT 20 JUL 81

VAS LIFTED INDEX



2301 GMT 20 JUL 81

Figure 6-14. VAS Derived Lifted Index for 20 July 1981

Since the sounding methods used at GSFC to convert VAS radiances into meteorological parameters are heavily dependent on the use of conventional data bases, we are not advocating the substitution of VAS for radiosonde or surface reports. We feel that the VAS has great potential for filling the temporal and spatial data gaps that currently exist within the conventional data base, providing a means of better study and better prediction of severe local storms.

Several problems have been encountered when using the VAS data that can restrict its applicability, even in a *case study* mode. Perhaps the greatest obstacles in working with the VAS data are those clouds with small dimensions (less than 30 km), and cirrus clouds which are not effectively detected by the VAS infrared channels. Clouds interfere with quantitative estimates of low-level water vapor using the split-window technique, the training required for the regression scheme, the derivation of the sounding, and the spatial and temporal continuity of the analysis. Therefore, cloud cover limits the applicability of VAS in certain situations, and necessitates the use of a person-in-the-loop approach, using visible data for quality assurance. This adds to the time, and the computer resources needed to construct a data base.

A second problem revolves around the limitations of the regression approach used in our research. In order to produce the VAS soundings for mesoscale analyses using a statistical retrieval method, all "local" cloud-free radiosondes must be used to stabilize the construction of the regression coefficients. The twice-a-day (dawn and dusk) radiosonde/VAS radiance statistical training does not include any radiosonde data during the peak heating period. Therefore, potentially there is a problem of over-sensitivity to the skin temperatures observed by the short-wave window channel. This appears to be small in these cases, due to its reduced role in the presence of better correlated predictors such as the surface data and the other less skin-sensitive window channels. Quantitative assessment of diurnal variation in retrievals were not possible for the summer convective cases, given the absence of ground truth data around local noontime.

A third problem with a regression approach is that there is no "universal" regression coefficient set, and different matrices must be created specifically for each kind of space-time interpolation. Another major constraint in applying the regression method to mesoscale studies is finding a sufficient number of high quality

ground truth data to establish a statistically significant correlation. Therefore, the quality control of the data base, particularly the coincident data set, is very important for eliminating large individual errors from the small data base available for mesoscale training. The main sources of error in this purely statistical approach to mesoscale satellite sounding come from the scarcity of upper-air data in space and time, from observations and interpolation error in radiosonde and surface reports, from VAS instrument noise and calibration errors, and from cloud contamination in the observed radiances.

6.2 UW ASSESSMENT

W. Smith
C. Hayden
P. Menzel

*Cooperative Institute for
Meteorological Satellite Studies
National Environmental Satellite
Data Information Service
National Oceanic and Atmospheric Administration
U.S. Department of Commerce*

6.2.1 Nowcasting Applications to Severe Weather Forecasting

At the UW/CIMSS, particular emphasis has been placed on the use of VAS MSI and DS data for nowcasting, in particular, the short-term forecasting of severe convective weather. Algorithms were developed to derive moisture, surface temperature, and stability parameters in real time from MSI data (Smith and Zhou, 1982). Alternatively, these parameters can be calculated more precisely from complete sounding retrievals (Smith, 1983), at the expense of the timeliness and geographical coverage of the results.

The VAS 6.7- μm water vapor imagery has been found to be the single most useful forecast aid provided to the forecaster by VAS. The VAS water vapor imagery greatly improved the delineation of the position and intensity of large scale weather systems, as well as revealing the location of baroclinic boundaries between ascending (wet) and descending (dry) air where mesoscale weather producing systems develop. Figure 6-15 is a good example of the added capabilities available to the forecaster in the 6.7- μm imagery. Note the better definition of the cyclones, (especially over the North Atlantic Ocean) in the water vapor imagery (Figure 6-15b), than that provided by the visible/infrared

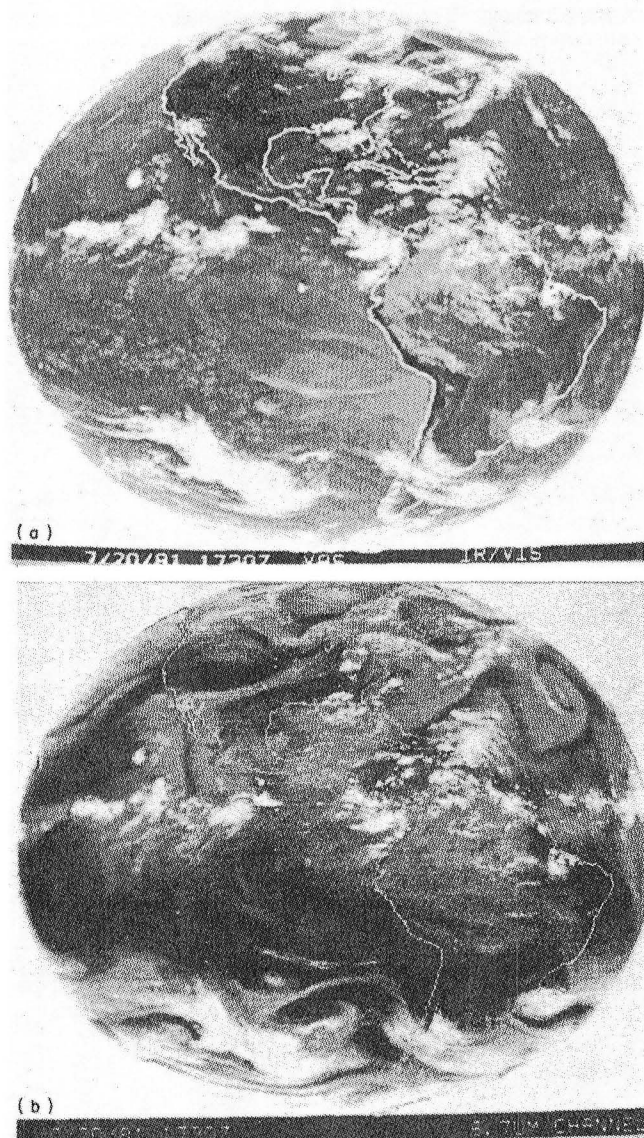


Figure 6-15. Full disk images obtained on 20 July 1981 between 1730 and 1800 GMT: (a) $11\ \mu\text{m}$ window and (b) $6.7\ \mu\text{m}\ \text{H}_2\text{O}$.

cloud imagery (Figure 6-15a). Also note the delineation of a narrow band of moisture across the United States, stretching from the Great Lakes into southern California. Tornadoic storms developed along the northern boundary of the moisture band several hours after the time of these images.

For nowcasting the development of intense weather phenomena, it is useful to combine contour analyses of important meteorological variables with the cloud and water vapor imagery (Smith *et al.*, 1982). A simple but

very useful type of display is the contour analysis of surface dewpoint overlying the $6.7\text{-}\mu\text{m}$ water vapor imagery. In this display, the intersections of axes of tongues of warm moist air at the surface, and dry intrusions aloft can be isolated. These intersections often pinpoint the centroid of convectively unstable air. A more complicated but useful type of display from VAS soundings, is an overlay of the contour analyses of total precipitable water (dominated by low-level moisture) and the isotachs of 300-mb gradient wind over the VAS $6.7\text{-}\mu\text{m}\ \text{H}_2\text{O}$ image. An example of this display is shown in Figure 6-16. An intersection between the axes of a low-level moisture tongue and an upper-level dry slot is seen over the state of Alabama at 1500 GMT. It should be noted that the location of this convectively unstable air column is in the exit region of the upper-level jet core, as defined by the isotachs of 300-mb gradient wind. (The streamlines are parallel to the moist/dry boundary southerly circulation in the $6.7\text{-}\mu\text{m}$ imagery.) Because of the forcing of a lower-level southerly circulation under the exit region of the upper-level westerly jet (Uccellini and Johnson, 1979), the continued advection of warm and moist gulf air would be expected to continue to destabilize the air over Alabama.

The time rate of change of stability is viewed through contour analyses of a stability index (such as the lifted index or the total-totals index), over the infrared cloud imagery. The contour analyses isolate the areas where the most severe convection can be expected to occur within the next few hours. The infrared cloud imagery monitors the growth of the convective clouds. Figure 6-17 shows these displays for the convectively unstable Alabama situation (noted above). Rapid destabilization, as indicated by increases in the total-totals index, precedes the development of intensive convective clouds. On this particular day, an outbreak of severe weather occurred over Alabama and western Georgia shortly after the time of the last VAS observations (2100 GMT). Eighty percent of the severe weather was confined to the geographical area outlined by the 69 total-totals contour observed at 2100 GMT (Figure 6-17C).

Effective display of VAS information is being studied to help the forecaster to better concentrate the geographical boundaries of severe weather watch boxes. An example of how this objective might be achieved is shown in Figure 6-18, which shows a severe weather watch box issued at 1830 GMT by the National Severe Storms Forecast Center (NSSFC). At that time, radar

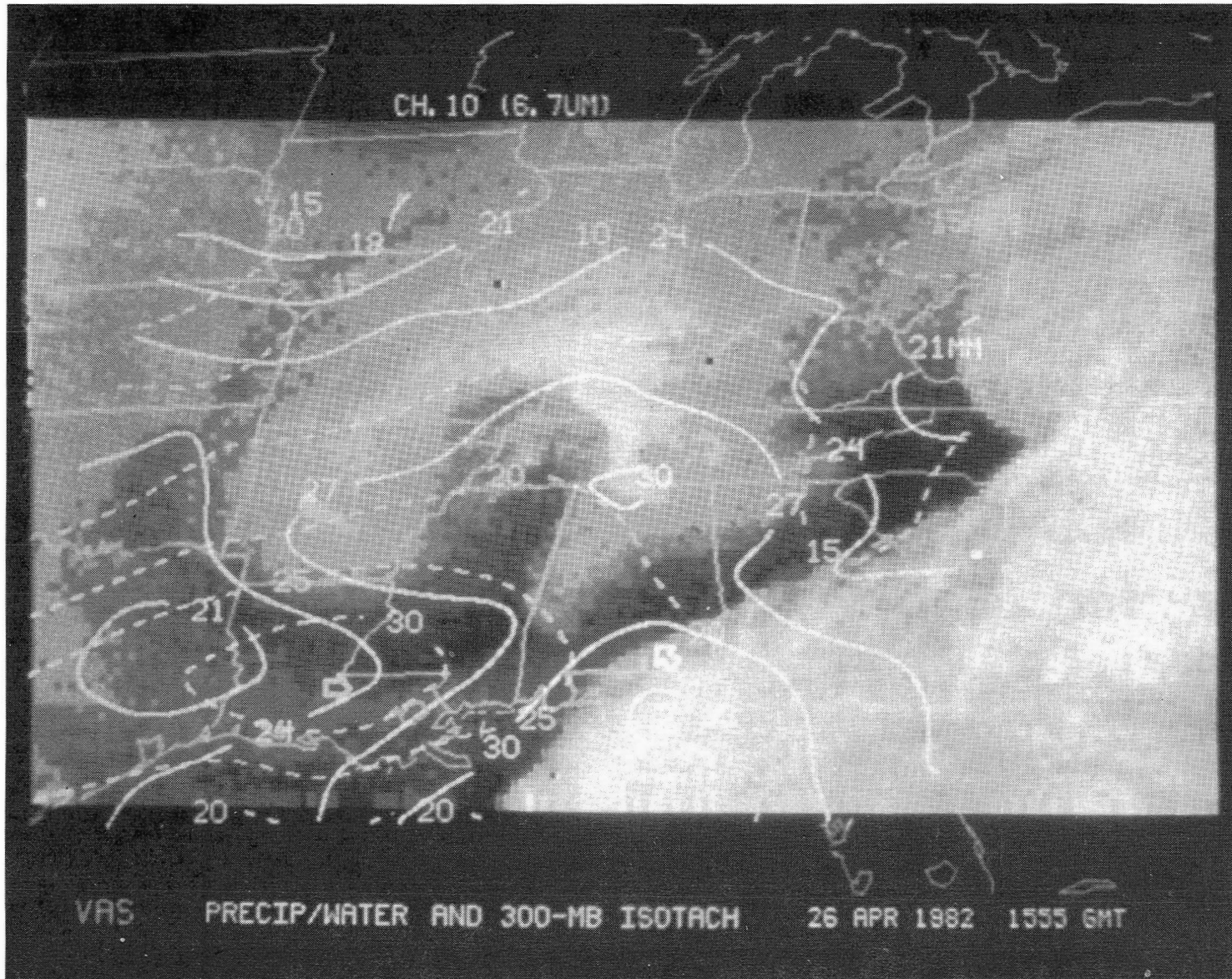


Figure 6-16. Analyses of VAS total precipitable water (solid, contour interval 3 mm) and VAS 300 mb gradient wind isotachs (dashed, contour interval 5 ms⁻¹) over 6.7 μm water vapor image for 26 April 1982, 1555 GMT.

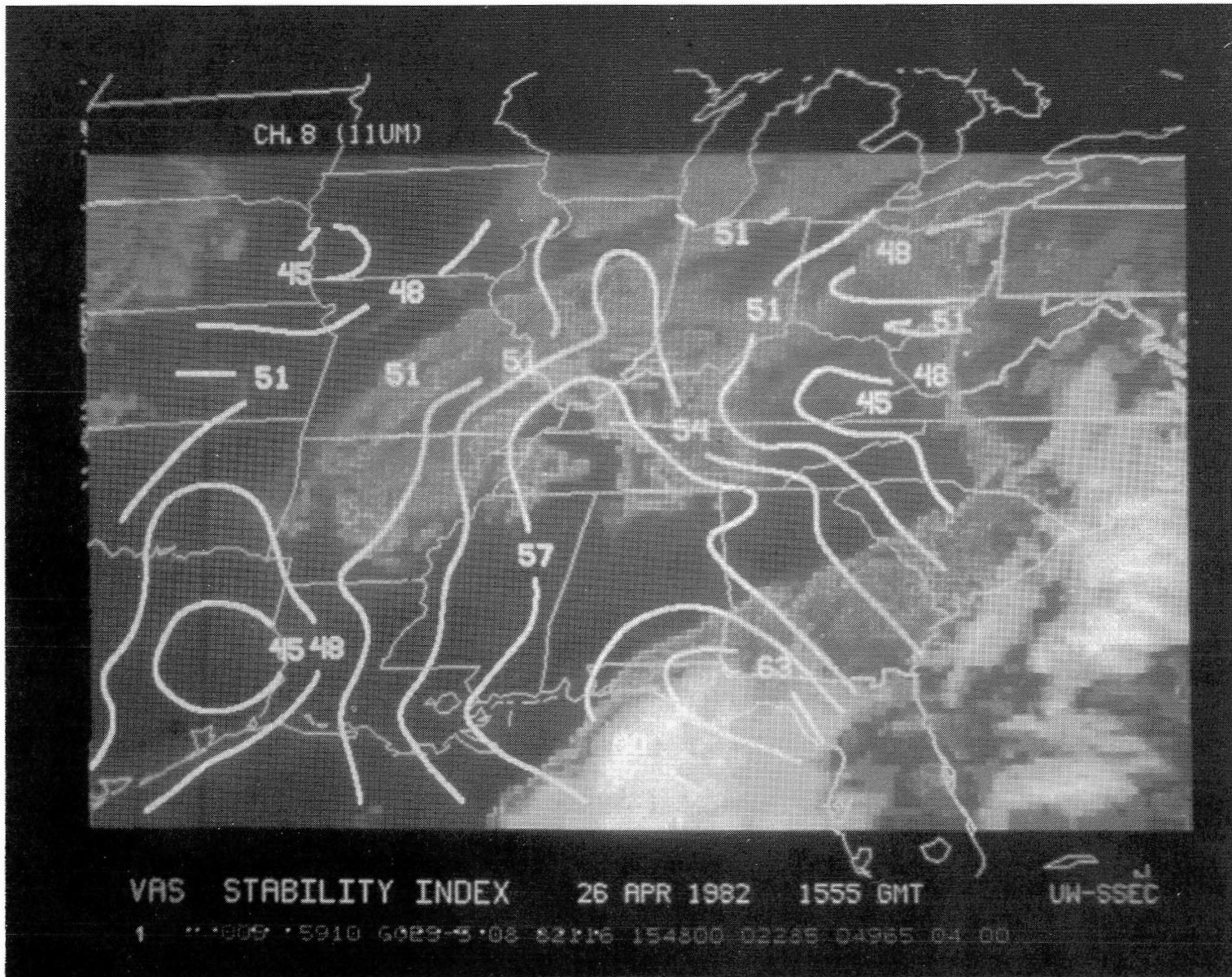


Figure 6-17a. Analysis of VAS Total-totals Index over infrared image for 26 April 1982, 1555 GMT.

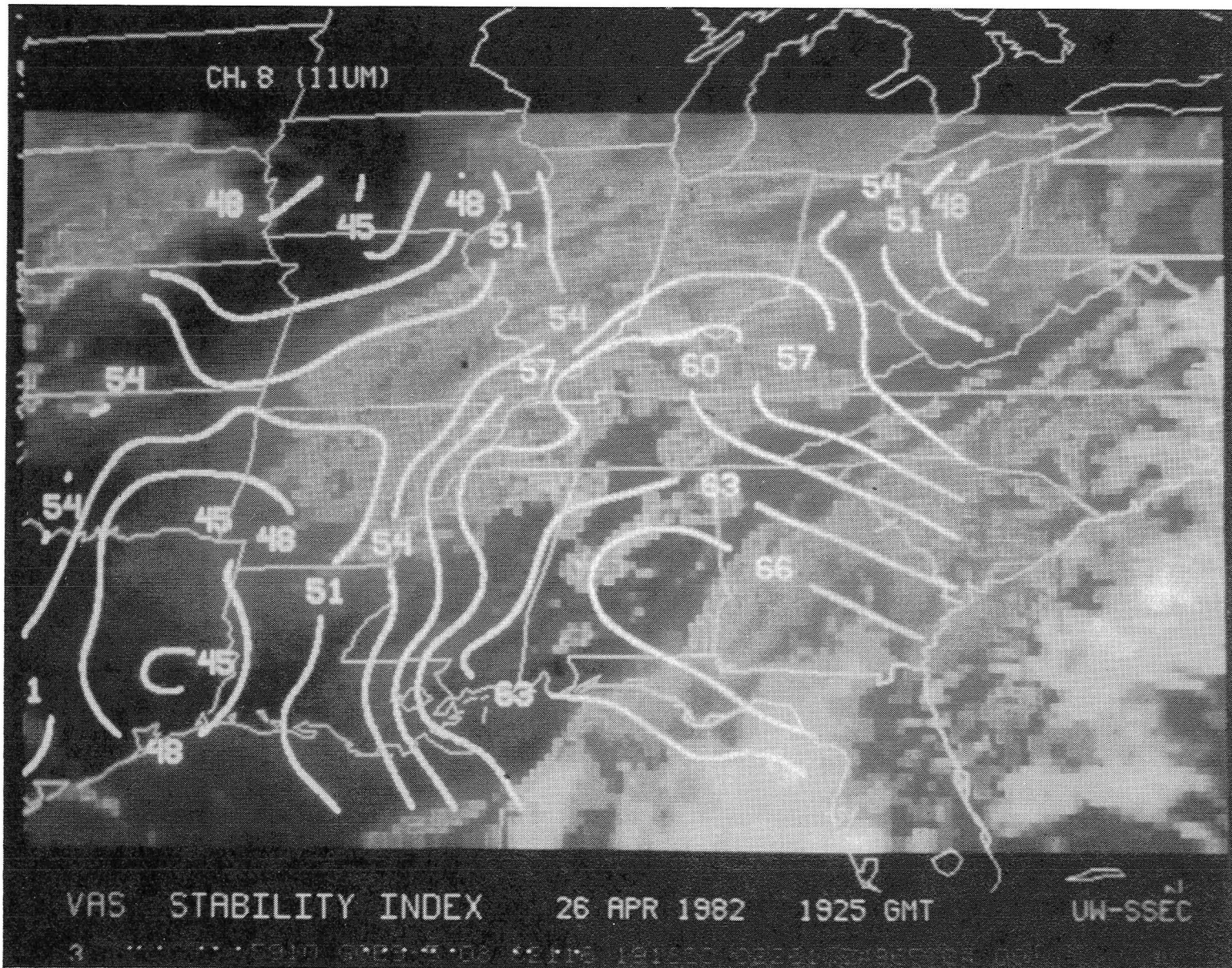


Figure 6-17b. Same as Figure 6-17a except for 1925 GMT.

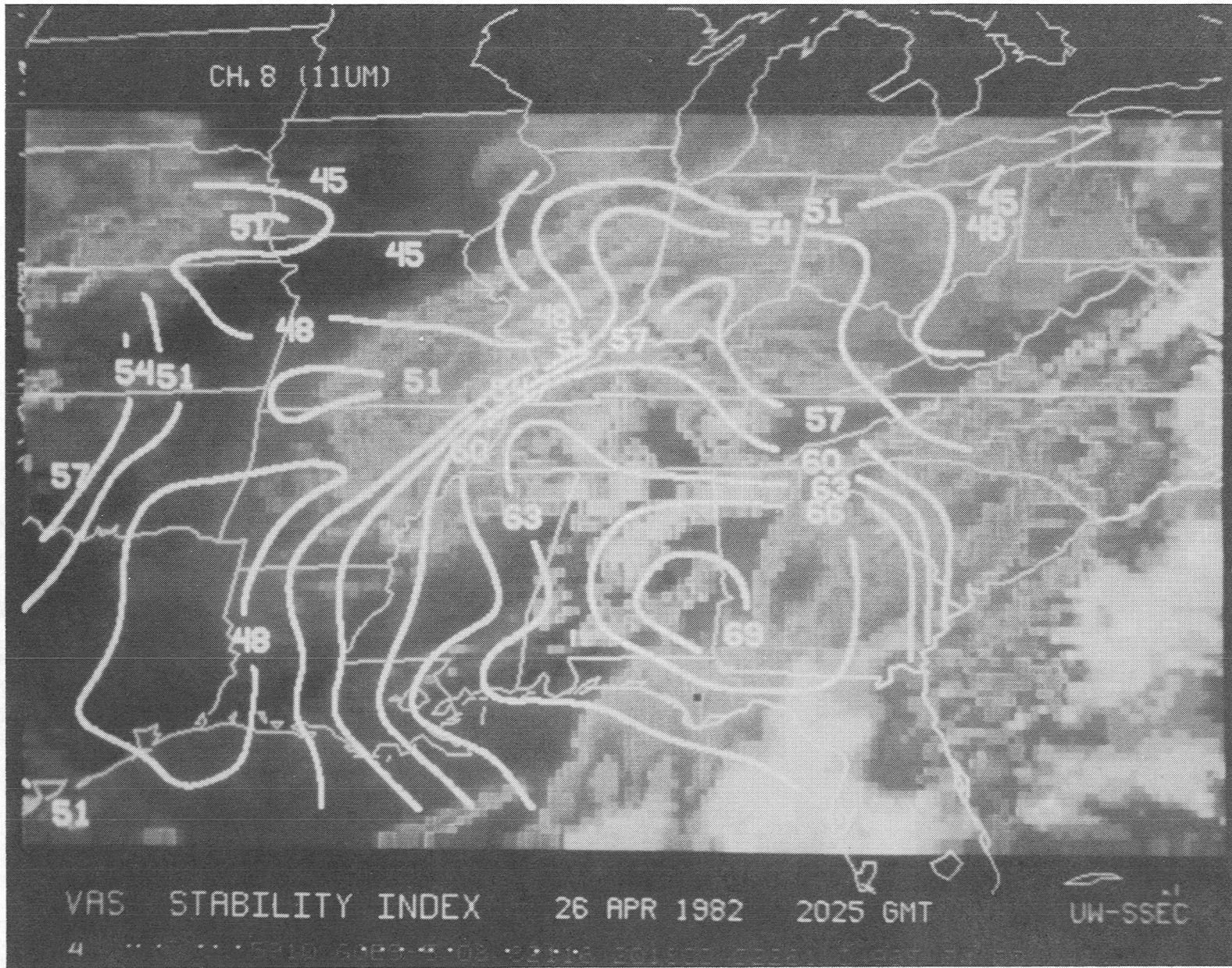


Figure 6-17c. Same as Figure 6-17a except for 2025 GMT.

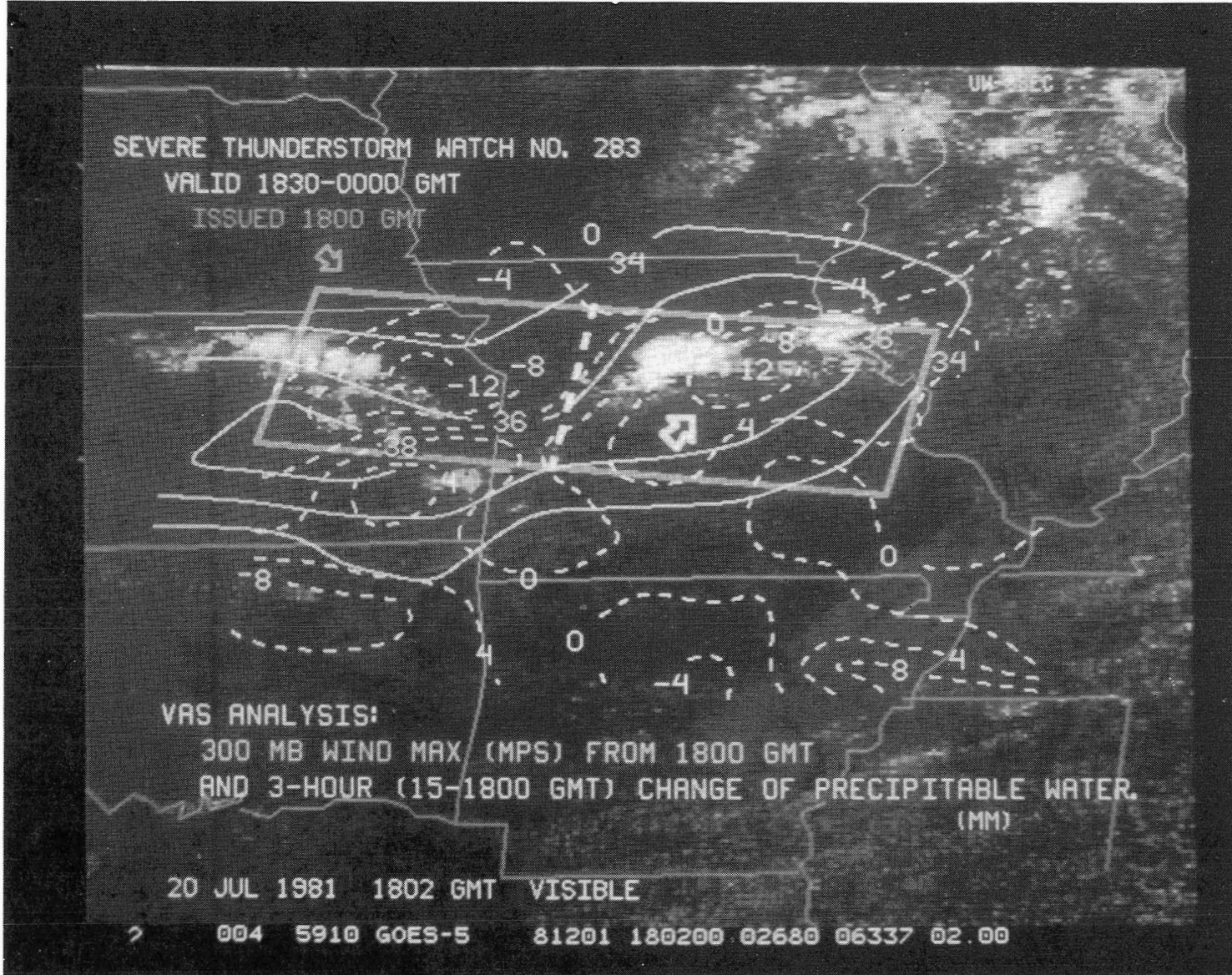


Figure 6-18. Analyses of VAS 300 mb gradient wind isotachs (solid, contour interval 2 ms^{-1}) from 1800 GMT and change of total precipitable water (1500-1800 GMT, dashed, contour interval 4 mm) with NSSFC Watch Box No. 283 over visible imagery at 1800 GMT 20 July 1981.

and satellite imagery revealed intense convection along a line stretching from eastern Kansas across Missouri and into western Illinois. Therefore, a very large rectangular watch area was issued to cover the entire region of active convection. The VAS derived total precipitable moisture content observed during the day showed large decreases in moisture occurring over the western portion of the watch area and large increases in the eastern section during the three hours prior to the time that the severe weather watch box was issued. As would be expected, the convection in the west dissipated since its low-level moisture supply was depleted, whereas the convection in the eastern portion exploded rapidly and produced tornadoes and other severe weather in the St. Louis, Missouri metropolitan area by 2100 GMT. If confidence was placed in the VAS data, the watch area could have been reliably limited to the eastern one-third of the area, greatly reducing the "false-alarm" region.

An intense effort is now underway to introduce the VAS nowcasting capabilities into the NSSFC operation. Imagery and quantitative products are made available to the NSSFC on a Man-computer Interactive Data Access System (McIDAS) terminal (Suomi *et al.*, 1983) that is connected by phone line to the University of Wisconsin. A preliminary assessment of the activity has been given by Anthony and Wade (1983).

6.2.2 Objective Estimation of Severe Weather Probability

Keller and Smith (1983) have developed an objective statistical technique for depicting the probability of severe weather occurrences six to twelve hours beyond the time of the surface and upper air observations that have been used. Gridpoint analyses of tropospheric temperatures, dewpoints, and winds are used to calculate stability and dynamic (e.g., winds and wind shears) predictors. A non-linear "tabular regression" technique is used to evaluate eight different predictors, individually and in combination, in order to produce an optimal decision tree prediction algorithm. The original work (Keller, 1982) was performed using radiosonde and NOAA-6 polar orbiting satellite soundings. It has been shown that forecasts of severe weather using the higher resolution satellite soundings, resulted in "threat" scores that were equal to, or slightly higher than the "threat" scores of forecasts made from radiosonde data. The technique has been applied to the VAS real time sounding data produced by the CIMSS at the University of Wisconsin during 1982/83, demonstrating its

operational utility for monitoring severe weather potential throughout the day.

Figure 6-19 shows a schematic of the tabular regression algorithm formulated for the eight predictors, that were the most useful of the many predictors that had been investigated. These eight predictors are the Showalter index, 850- to 500-mb wind shear, 8-hour 850-mb temperature advection, 500-mb wind speed, 850-mb wind speed, 300-mb wind speed, 8-hour advective change of Showalter index, and 8-hour 500-mb temperature advection. The probabilities for each predictor pair class were determined from a sample of independent data sets and severe weather verification observations obtained during 1980/81, and updated with severe weather situations observed during subsequent years.

An example of an application of the tabular regression technique to VAS data is shown in Figure 6-20. The case is May 21, 1982, when severe weather occurred over Texas, Arkansas, Kentucky, and Tennessee. Severe weather probabilities were produced in real time from VAS data observed at 1400, 1500, 1600, and 1900 GMT, which are all prior to the severe weather occurrences.

The area forecast that has a 20 percent or greater probability of severe weather at 1400 GMT is unchanged throughout the day. This feature demonstrates the consistency of the VAS data and the tabular regression estimates. As shown, many severe weather reports occurred from Arkansas to Tennessee in the area of persistently high probability on the basis of all data sets. The probability values of Texas show a large increase with time. Low values at 1400 GMT increased to values well over the 20 percent threshold by 1900 GMT. There were several tornado, hail, and severe wind reports within the six hour period following the 1900 GMT probability estimate.

This technique is under continual refinement in the updating of the statistical data base and in the investigation of other predictors. The inclusion of VAS observations of the time rate of change of the predictors is expected to significantly improve the skill of the tabular regression technique.

6.2.3 Application to NMC Limited Area Numerical Forecasts

Soundings from geostationary satellites offer a unique

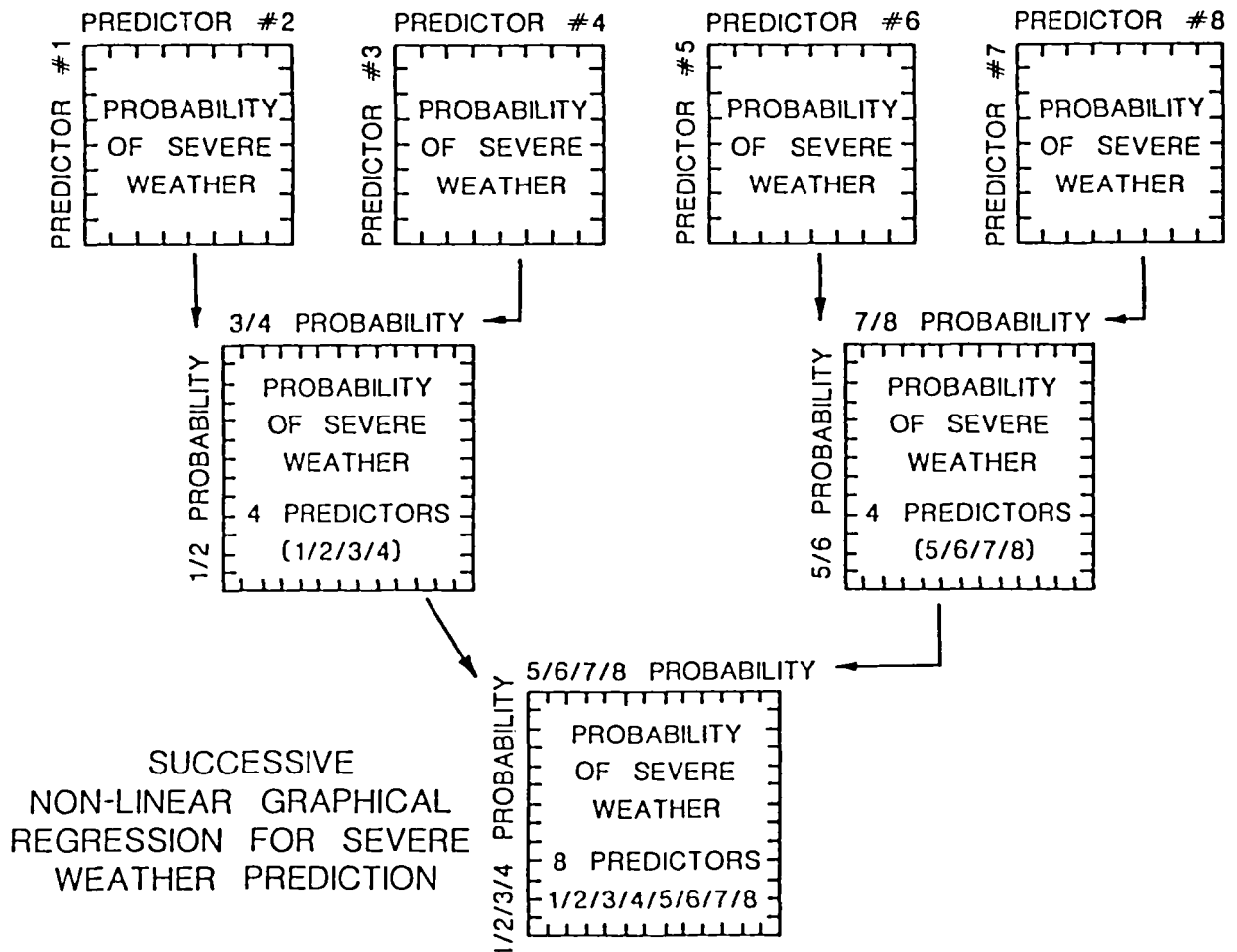


Figure 6-19. Graphical Regression Flow Chart

advantage over those from polar orbiting satellites with regard to their use in limited area numerical forecast models. The soundings over the region of interest can be obtained in a synoptic manner, all at approximately the same time, whereas there is a 110 minute time gap between polar orbits. During the winter of 1981-1982, soundings were produced by the UW/CIMSS over the North Pacific Ocean from the GOES-West VAS in order to study their impact on National Meteorological Center (NMC) Limited area Fine Mesh (LFM) analyses and forecasts. Six cases were chosen at random for evaluation by the NMC. The methods of analysis and results, (details of which are given in a report by O'Lenic (1982)), are summarized here.

Important features of sounding retrievals are:

- They were produced in a latitude belt 35-55°N from VAS Dwell Sound (DS) data obtained during a one-hour period beginning at 1030 GMT.

- The algorithm used was that described by Smith (1983) and utilized an LFM 12 hour forecast valid at the time of the data for a first guess in the retrieval process.
- An NMC 12 hour forecast 1000 mb height field was used as a reference level to construct geopotential heights at the mandatory levels from the radiance derived temperature profiles.

Important characteristics of the NMC evaluation are:

- "VAS" analyses were constructed by taking conventional 1000-mb geopotential analyses (i.e., analyses of forecast and conventional data) and the VAS geopotential thickness observations.
- The conventional analyses, called "NOVAS" analyses, were computed with the "VAS" analyses.

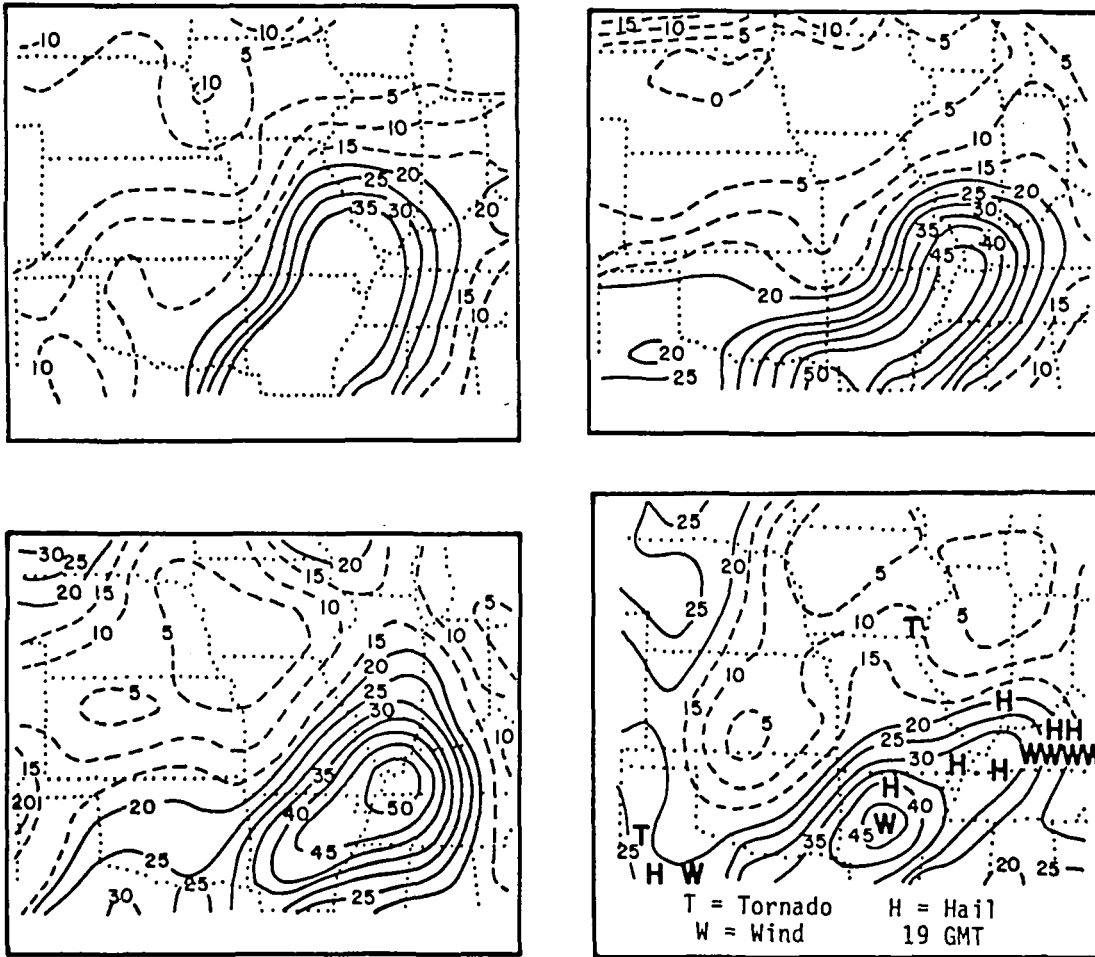


Figure 6-20. Forecasts of severe weather probability using VAS soundings from 1400, 1500, 1600 and 1900 GMT on 21 May 1982, valid 3 to 9 hours after the VAS observation time.

- Numerical forecasts, to 24 hours, achieved with the LFM were conducted using the “VAS” analyses as initial conditions and these were compared with the operational “NOVAS” LFM forecasts.

The results of the randomly selected six cases can be summarized as follows:

- At 500 mb, the VAS data exerted a considerable influence on the geopotential analyses (VAS and NOVAS analysis differences being as much as 90 meters at the 500-mb level and 300 meters at the 300-mb level).
- Two out of the six VAS forecasts were a very significant improvement over the NOVAS forecasts. In one of the six cases, VAS data introduced large and complex changes to the NOVAS

analysis, yet the VAS forecast showed little improvement to the NOVAS forecast which was satisfactory.

- None of the six VAS forecasts conducted exhibited reduced accuracy as compared to the NOVAS forecasts.

An example of one of the cases for which the VAS data greatly improved the LFM forecast is shown in Figure 6-21. As can be seen from Figure 6-21a and 6-21b, the VAS data modified the LFM analysis greatly in the eastern Pacific by intensifying the amplitude of the trough in the vicinity of 50°N, 160°W. This alteration of the analysis over the Pacific greatly impacted the 24 hour forecast for the west coast of the United States. As can be seen, the errors in the 500-mb forecast along the West Coast were reduced from values in excess of 120 meters (6°C), to below 60 meters (less

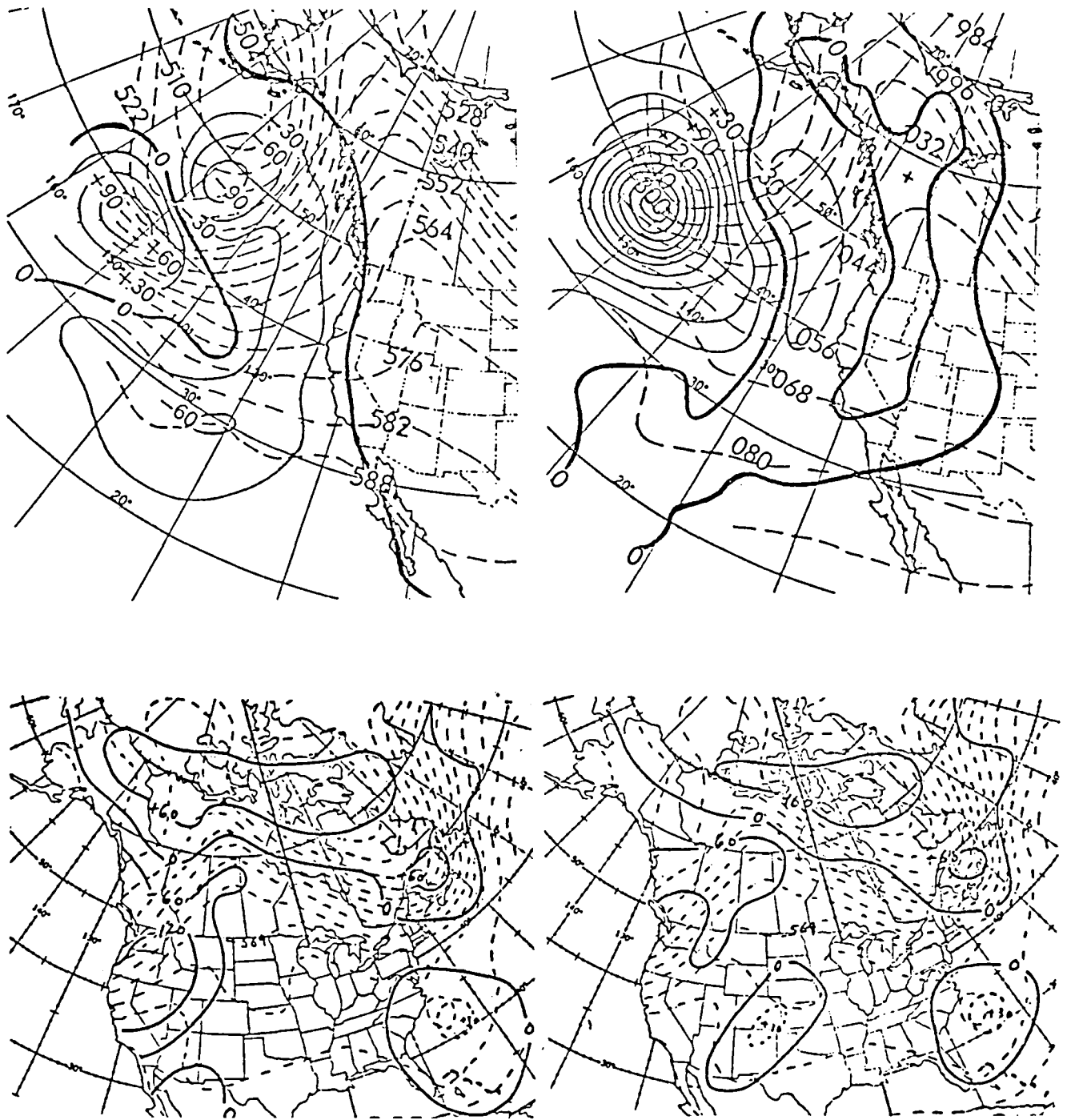


Figure 6-21. SAT-minus-NOSAT LFM height analysis differences (solid lines, 30 meter intervals) with NOSAT analysis contours (dashed lines, intervals of 60 meters at 500 mb and 120 meters at 250 mb) for 10 November 1981 case; (a) for 500 mb and (b) for 250 mb. (c) NOVAS 500 mb height errors (solid lines) for 48 hour LFM forecast valid 1200 GMT, 12 November 1981. Verifying 500 mb analysis contours are dashed at 60 meter intervals. (d) VAS 500 mb height errors (solid lines) for 48 hour LFM forecast valid 1200 GMT, 12 November 1981. Verifying 500 mb analysis contours are dashed at 60 meter intervals.

than 3°C). These reductions in the 24 hour forecast imply that larger error reductions would have occurred for longer range forecasts (36-72 hour forecasts) for the central and eastern United States.

6.2.4 Tropical Storm Trajectory Forecasting

Studies have indicated that the deep layer mean wind field around a tropical cyclone is one of the best indicators of the storm's steering current (Chan and Gray, 1982). One of the main goals of the UW/CIMSS VAS research program is to develop a method of deriving a steering current analysis, from VAS imagery and soundings, in order to improve forecasts of hurricane movement.

A technique has been developed (Velden, Smith, and Mayfield, 1983) for amalgamating three complementary wind estimates from VAS: upper and lower-tropospheric level cloud drift winds (Mosher, 1979) with improved cloud height assignments based on CO₂ radiance observations (Menzel *et al.*, 1983), mid-level water vapor motion derived from hourly interval 6.7 μm imagery (Mosher and Stewart, 1981), and gradient winds derived for all tropospheric mandatory levels in cloud-free areas. The combined wind set consisting of gradient, cloud-drift, and water vapor motion winds is edited to provide a self-consistent data set for three levels (approximately 850 mb, 500 mb, and 200 mb). A pressure weighted average is computed to yield a deep layer (850-200 mb) mean wind analysis. This final

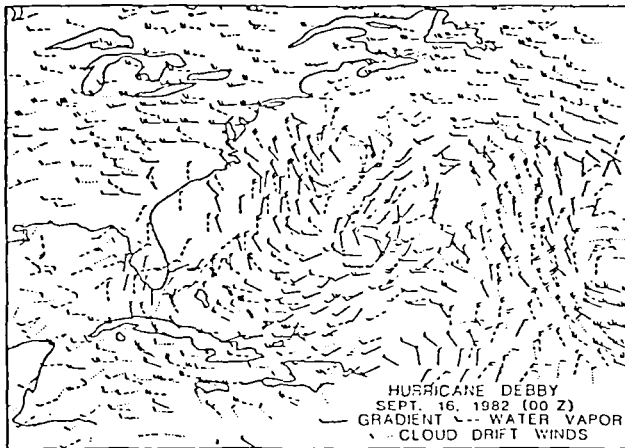


Figure 6-22. Final combined wind set (mid level) consisting of VAS and TIROS gradient (solid) winds, water vapor motion (dashed) winds and cloud drift (dotted) winds for Hurricane Debby.

set provides complete coverage of the storm's environment. Figure 6-22 shows an example of an analysis of the deep layer mean wind derived from VAS observations of Hurricane Debby. The figure also shows 500-mb aircraft dropwindsonde observations for comparison. Deep layer mean wind analyses have been derived for all the time periods processed around Hurricane Debby, for comparisons with conventional atmospheric analyses of the North Atlantic Ocean area, that is virtually void of conventional observations. The forecast utility of greatly enhanced wind observations over this area is being assessed. Testing and numerical comparisons are being done with the National Hurricane Center (NHC) operational SANBAR (SANDers BARotropic model) (Sanders *et al.*, 1975). While waiting for the results of this research, a simpler trajectory forecasting procedure has been tested at the UW/CIMSS.

As may be seen in Figure 6-23 from the locations of Hurricane Debby at six hour intervals beginning at 0000 GMT on 16 September 1982, the tropical cyclone follows the VAS derived deep layer mean wind analysis streamlines (from 0000 GMT on 16 September 1982 data) fairly closely, out to 72 hours. Greater deviations from the streamline pattern can obviously be expected at longer durations from the analysis time since the streamline fields are constantly changing with time. This streamline field serves as a good approximation of the steering current and subsequent short range storm track forecast. Assuming that the deep layer mean wind steering current theory holds, and also that the abundance of wind data in a normally data sparse region would improve the analysis, a simple trajectory model was developed to test on the Hurricane Debby data. Although it is recognized that trajectory forecasting of tropical cyclone movement is not a new concept, the method was employed using the VAS derived deep layer mean wind analyses from Hurricane Debby to assess the accuracy of the streamline field as an approximate steering current, and as an initial analysis for more sophisticated forecast models. The streamlines are given by the solution to the following equations:

$$dx/dt = u(x, y)$$

$$dy/dt = v(x, y)$$

These equations are solved numerically by using the Adams method (Hildebrand, 1962). This method assumes that $u(x, y)$ and $v(x, y)$ vary linearly between mesh points on the grid analysis and results in the following formula for the path:

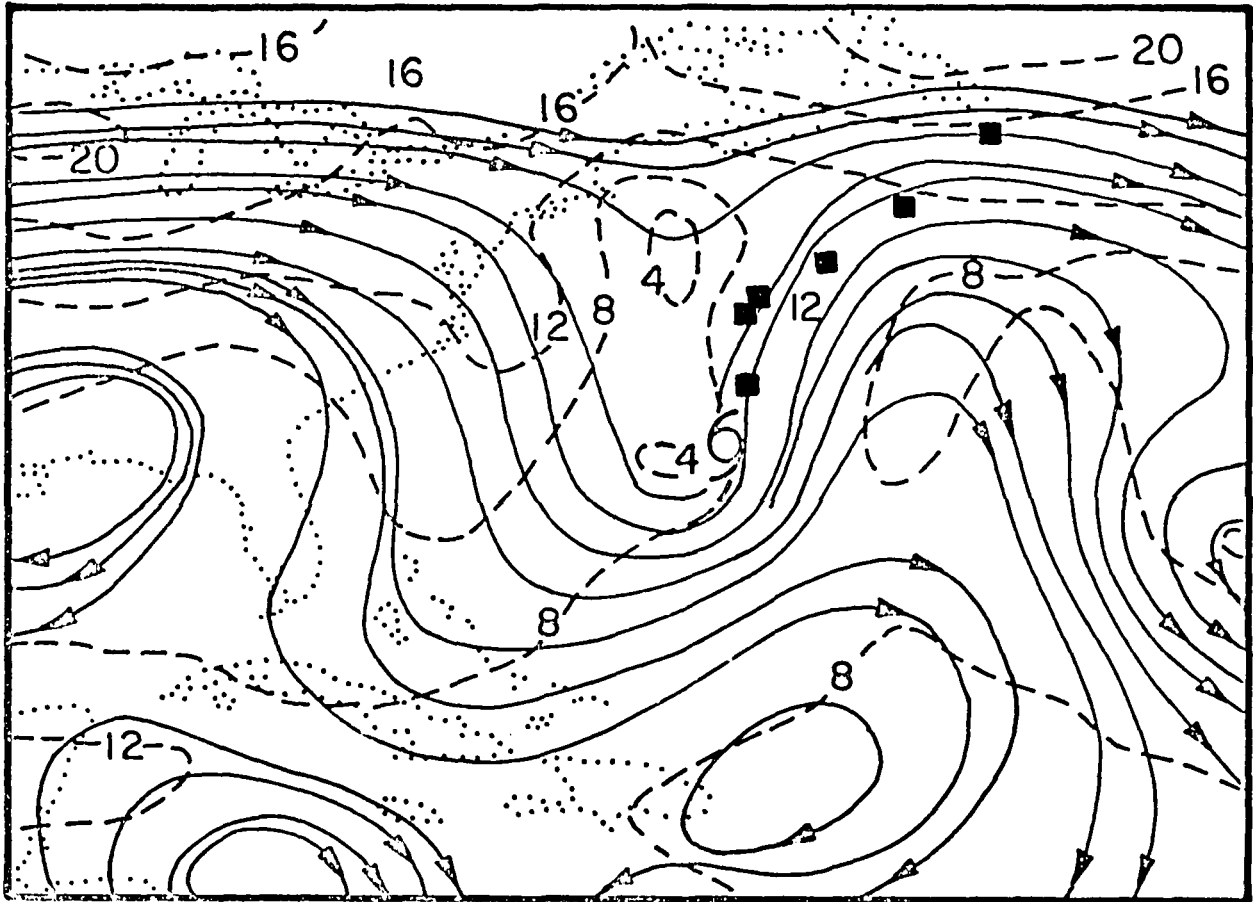


Figure 6-23. Composite 850-200 mb mean wind analysis for Hurricane Debby at 0000 GMT 16 September 1982, streamlines (solid), isotachs (dashed at 4 m/s interval) and blocks (storm track, every 12 hours).

$$x_{k+1} = x_k + hU_k + \frac{h}{2}(U_k - U_{k-1})$$

$$y_{k+1} = y_k + hV_k + \frac{h}{2}(V_k - V_{k-1})$$

where (x_k, y_k) and (x_{k-1}, y_{k-1}) are the previous positions of the source point with corresponding velocities (U_k, V_k) and (U_{k-1}, V_{k-1}) , and h is the time step. The velocity components at an arbitrary point in the grid analysis field are found using bi-linear interpolation.

In Table 6-1 comparisons are shown of mean forecast errors (MFE) for several different operational models used by NHC, the official forecasts, and the VASTRA (VAS TRAjectory) model for selected cases from Hurricane Debby when VAS deep layer mean wind data were available. Initial positioning error (Neumann and Pelissier, 1981) was removed from the MFE in all cases. From Table 6-1, it can be seen that the VASTRA forecasts compare favorably with the official

forecasts and the other operational models, especially at 24-48 hours. Although it is recognized that these data represent only one case study, it is believed that the good quality and improved density of wind data over the oceanic regions are at least in part responsible for the encouraging results. Nevertheless, the numerical impact of the data itself will ultimately be determined by the SANBAR numerical comparisons. Qualitative assessments of the forecast storm tracks from tropical cyclones Alicia and Barry of 1983 have also been encouraging.

An effort is currently underway to use actual trajectory analyses from consecutive deep layer mean wind analyses in a numerical model. In order to generate the initial winds for the barotropic model (SANBAR), the sequence of previous wind analyses will be used to augment the field at the initial time ($t=0$), in effect, an extrapolation of the analyses to $t=0$ in order to fill in the data void areas. These ideas have been successfully applied to VAS geopotential data in conjunction with

Table 6-1
Comparisons of MFE (nm) for Selected Cases
During Hurricane Debby of 1982 (Official and MFM
Forecasts are not Issued for 36 and 72 h, Respectively)

Model	Forecast Intervals (h)									
	12	(# of cases)	24	(# of cases)	36	(# of cases)	48	(# of cases)	72	(# of cases)
Official Forecasts	59	(11)	148	(11)	—	—	283	(10)	232	(7)
VASTRA	81	(11)	144	(11)	—	—	235	(10)	310	(7)
NHC 67	56	(9)	102	(9)	185	(9)	264	(8)	186	(6)
NHC 72	70	(9)	134	(9)	186	(9)	223	(8)	380	(6)
HURRAN	85	(9)	196	(9)	306	(9)	389	(8)	279	(6)
CLIPER	76	(9)	177	(9)	284	(9)	344	(8)	280	(6)
VASTRA	79	(9)	131	(9)	174	(9)	229	(8)	319	(6)
NHC 73	62	(8)	133	(8)	152	(7)	231	(7)	504	(5)
SANBAR	87	(8)	197	(8)	312	(7)	403	(7)	637	(5)
VASTRA	76	(8)	133	(8)	184	(7)	226	(7)	327	(5)
MFM	57	(4)	92	(4)	128	(4)	190	(4)	—	—
VASTRA	59	(4)	95	(4)	149	(4)	214	(4)	—	—

quasi-geostrophic models (Lewis *et al.*, 1983). In the context of hurricane tracking, the barotropic constraint of absolute vorticity conservation will be used to couple the wind fields in time.

Continued research into hurricane track forecasting using the VAS deep layer mean wind analyses in the SANBAR model and the complete VAS sounding and wind data sets in primitive equation forecast models is also underway at the UW/CIMSS.

6.2.5 Sea Surface Temperature (SST) Determination

The UW/CIMSS derives sea surface temperature from VAS multispectral data using the "split window" tech-

nique (Prabhakara *et al.*, 1974) and has tested the results against sea surface temperature reports from NOAA fixed buoys as ground truth and SST determinations from the AVHRR. A total of 264 satellite-buoy matches show no bias, and an RMS difference of 1.25°C when the VAS SST is derived from the 11 and 12- μm channels. Also, eleven coincident VAS-AVHRR-buoy matches show VAS SST's to be comparable to SST's derived from the AVHRR.

The method of multispectral SST determination using infrared data requires that only cloud-free fields of view are used. Therefore, it is necessary to have rigid tests for whether the field-of-view of the observation is cloud free. The most rigid test for clouds over the

Oceans is a visible albedo test, since in cloud free areas remote from sunglint, the albedo due to the reflectance from the oceans and atmosphere, is generally less than eight percent. Only the VAS data collected during the day, when the visible albedo test can be performed, are chosen for this study. Several cases using infrared data during the night have been attempted. The results indicate that the cloud threshold tests that are based on infrared data only, are inadequate.

The visible detectors on the GOES satellite are photomultiplier tubes (PMT) and are sensitive to radiation in the .5- to .7-micron wavelength band. Figure 6-24 shows the count to reflectance conversion for the GOES-5 visible signal. This calibration curve was determined by adjusting the measured laboratory response curve to observed reflectances of dark space and bright surfaces (White Sands, New Mexico). The nonlinear A/D conversion of the PMT signal is advantageous for detecting small amounts of cloud, since this is more sensitive to low count values (low reflectances) than high. This nonlinear A/D conversion produces maximum accuracies within 6 bits available since the noise increases with the square root of the brightness.

NOAA's regularly reporting fixed buoys were used for matchups, to evaluate the quality of the VAS derived SST's. Observations from these buoys are available once every three hours. Laboratory tests indicate that the buoys are capable of providing temperatures within one standard deviation of less than $\pm 0.2^{\circ}\text{C}$. Buoy observations of SST are much more reliable than merchant ship observations (of SST), because the buoys are subjected to rigorous quality control. Studies of buoy observations versus ship observations of SST have shown that ship's observations are $0.2 \pm 5.1^{\circ}\text{C}$ greater than those of buoys (Tabata, 1978).

VAS SST data used for matchups is obtained by averaging all cloud free infrared observations within a three by three array, centered at the buoy location. Only daytime data were used. The buoy report SST's every three hours, so that the largest time difference between buoy and satellite observations is one and one-half hours. During the period of July 22 to October 13, 1982, the split window algorithm (Bates, 1983) displayed in Figure 6-25 had a bias (i.e., mean satellite-buoy difference) of zero, and a root mean square error (RMSE) of 1.25°C , for 264 matches. The low values of RMSE in the two channel algorithm is very encouraging. The low bias for the two channel algorithm suggests that the original sample of ship data used to calculate the algorithm was quite representative.

During this time period, there were also found to be eleven coincident (± 2 hours) SST matches between VAS, AVHRR, and the fixed buoys. These results show a mean bias for VAS (i.e., VAS SST minus buoy SST) of -0.06°C , with a standard deviation of 0.91. The mean bias for AVHRR was -1.04°C , with a standard deviation of 1.37. The relatively high bias for the AVHRR may be attributed to volcanic aerosol contamination from the El Chichon eruption. If this volcanic aerosol is treated as another source of instrument noise, the AVHRR split window algorithm would amplify this noise to approximately twice the amount that the VAS algorithm does (Barton, 1983).

The evaluation of monthly mean SST's from VAS for March 1982 showed good agreement with climatological SST's of Reynolds (1982). For this study, only VAS data from the GOES-East satellite, located at 0°N , 75°W were available. Because of the satellite's fixed location, two separate regions were chosen for monthly

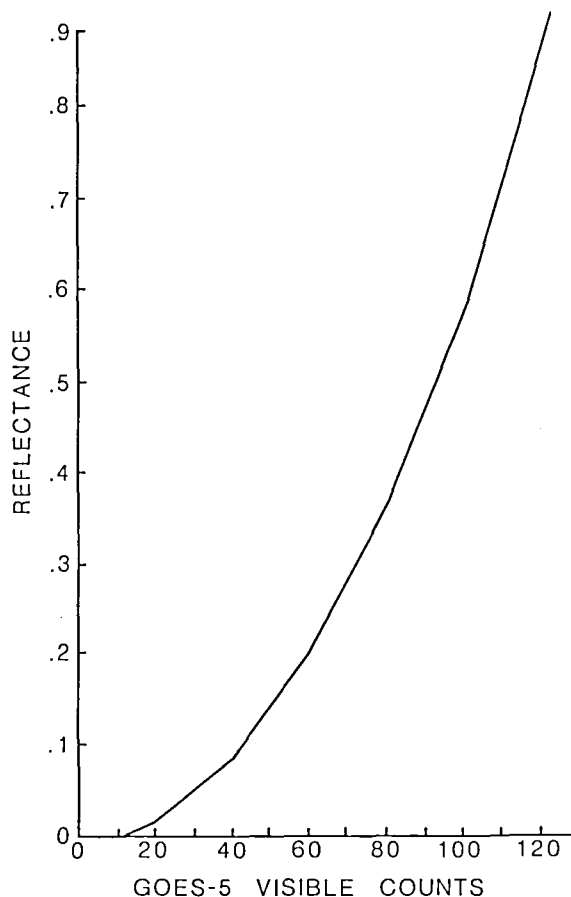


Figure 6-24. Count to reflectance conversion for GOES-5

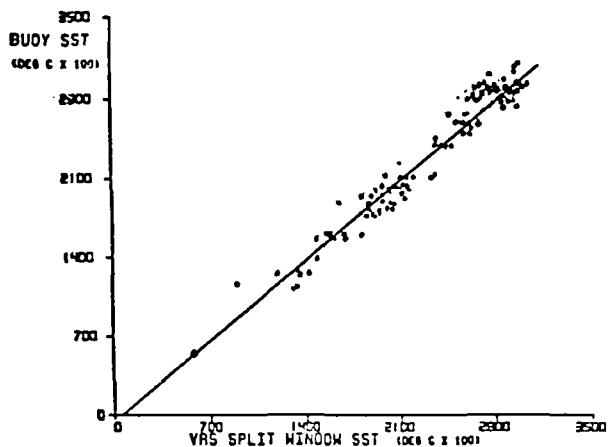


Figure 6-25. Scatter diagram of 2 channel VAS/buoy SST matches.

analysis; one in the North Atlantic Ocean extending from 45°N, 80°W to 20°N, 50°W and the other in the equatorial Pacific Ocean extending from 10°N, 115°W to 30°S, 75°W. Although VAS MSI data is available every hour on weekdays during normal operation, we chose to analyze SST's at 1730 and 2030 GMT to establish a balance between the cost and practicability of processing large amounts of data, and the desire to eliminate the diurnal effects of cloudiness and sunglint. Initial comparisons of the monthly data density between VAS and AVHRR show that of the main advantages to VAS MSI data are the abilities to reduce the diurnal contamination by cloudiness, especially in the stratus areas off the west coasts of continents, and the ability to eliminate the data loss in areas of sunglint in the tropics inherent in the sun-synchronous satellites.

The procedures for regional analysis are similar to those described for the VAS buoy matches. Each SST target area consists of a three by three infrared pixel array. The coincident visible data for each IR pixel are analyzed and if two or more of the IR pixels are found to be cloud free, then the brightness temperatures for each of the channels are averaged to compute a SST. Additional quality control checks on the data include tests for frozen water ($SST < -2^{\circ}C$), land, and missing data. Subjective tests include a check on satellite navigation accuracy as well as a gross check on VAS SST field homogeneity. Less than 5 percent of the total data that were analyzed, were subjectively edited out.

The monthly mean SST fields from VAS shown in Figure 6-26 were produced by objectively analyzing each individual time period, at a one degree grid interval period, using a first guess, the Reynolds climatology,

to eliminate unrealistic data extrapolation in areas of large data voids. The complete data set was then averaged to produce the monthly mean VAS SST. This monthly mean VAS SST was then compared with the Reynolds 1982 SST climatology to construct monthly anomaly fields. In the eastern equatorial Pacific, the areas of coastal and equatorial upwelling are clearly evident as are warm tongues of water extending south from Central America and southeastward in the South Pacific toward Chile. The anomaly field is quite weak throughout this area, with no anomaly exceeding 2°C. In the North Atlantic, the tight gradient of the Gulf Stream is quite visible, but the anomalies are greater with the VAS SST's averaging warmer than climatology throughout the region.

6.2.6 Specifying Heights and Velocities of Cloud Motions

UW/CIMSS has been achieving qualitative height assignments and quantitative velocities with the carbon dioxide (CO₂) slicing method. This technique uses sequences of half hourly CO₂ channel images (spectral bands 3, 4, and 5, at 703, 715, and 751 cm⁻¹) for tracking clouds at high (351 to 100 mb), middle (651 to 350 mb), and lower (sfc to 650 mb) levels. This CO₂ slicing improves cloud-vector determinations (because the individual cloud elements are tracked at a given altitude), and it indicates the height assignment of the cloud-wind vector. Good agreement with radiosonde wind observations at 200, 400, and 700 mb was found. Errors in the cloud-motion wind velocity are expected to be minimized, because apparent motions caused by higher level clouds overlaying lower level clouds are not observed.

Radiances from CO₂ spectral bands 3, 4, and 5 have been used to specify cloud-top pressures (see Menzel *et al.*, 1983). The CO₂ absorption method determines cloud-top pressures from the ratio of differences in cloud produced radiances and corresponding clear air values for the CO₂ absorption spectral bands. The method does not depend on fractional cloud cover or cloud emissivity, in fact the effective cloud amount is a byproduct of the calculations. Several comparisons of cloud heights, determined by using different techniques, have been made over several different cloud types. Comparisons of CO₂ heights with radiosonde observations for several case study days were within 50-mb rms with no discernible bias; comparisons with stereo cloud height determinations were within 30-mb rms with no discernible bias; and comparisons with bispectral cloud heights were within 100-mb rms with the

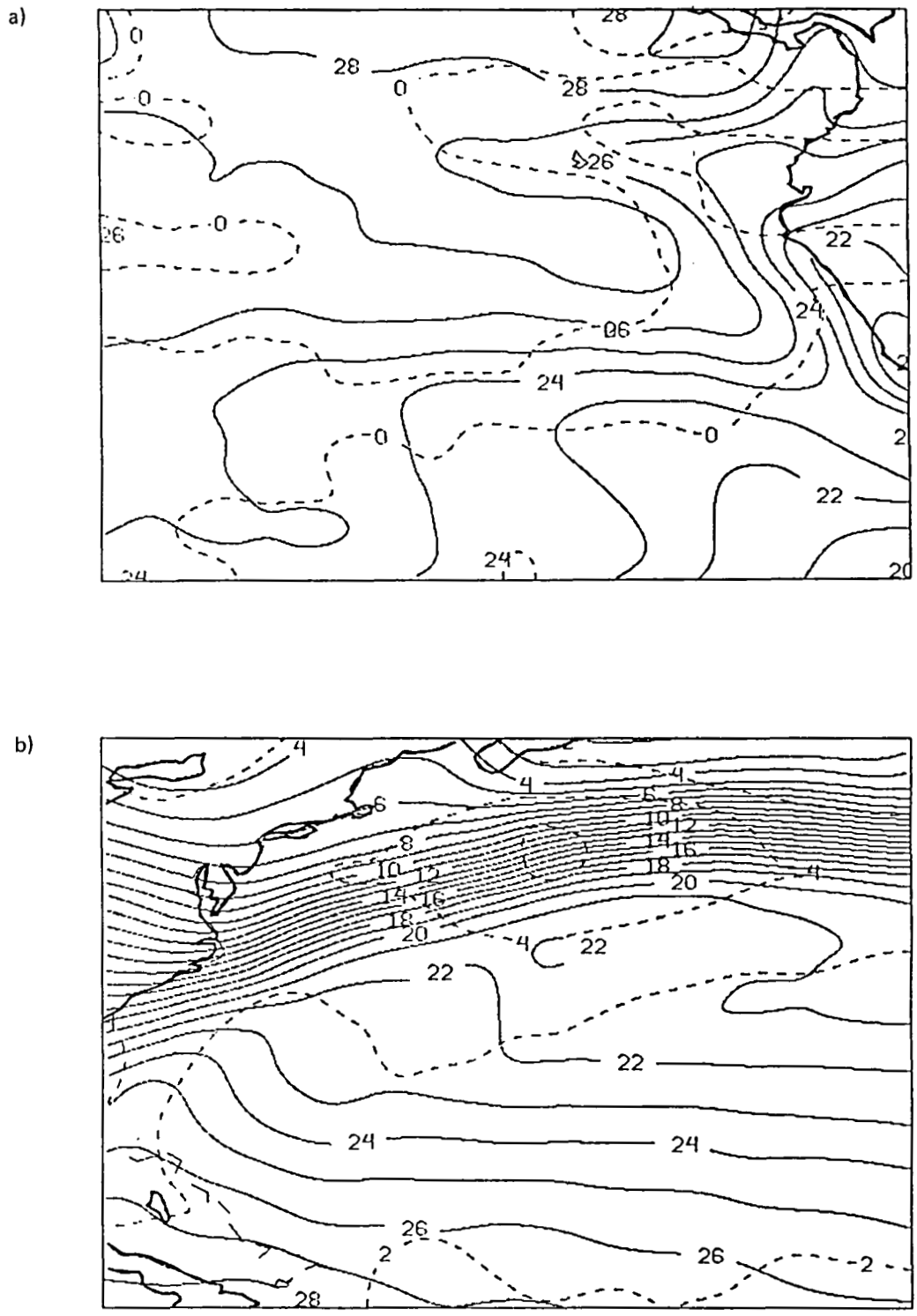


Figure 6-26. Monthly mean for March 1982 VAS SST fields (solid) and anomaly with respect to Reynolds (1982) SST climatology (dashed) in the eastern Pacific (a) and North Atlantic Ocean (b).

bispectral heights biased about 30 mb too low in altitude. This last comparison indicates the difficulty that the bispectral technique has with cirrus clouds. Cloud heights are estimated too low because the infrared window senses radiation from within and below the thin clouds. Therefore the brightness temperature is an overestimate of the cloud temperature. CO₂ derived cirrus cloud heights show good reliability to within 50-50-mb rms. Figure 6-27 dramatizes this fact. CO₂ and bispectral heights are plotted along a cirrus anvil blowing of the top of a thunderstorm (1348 GMT, 14 July 1982) over Missouri. As one moves away from the dense cumulus clouds toward the thin cirrus, the CO₂ absorption method maintains high altitudes, while the

bispectral method frequently underestimates the altitude by varying amount, depending on the thinness of the cirrus clouds.

The CO₂ technique has been applied routinely (in the fall of 1983) to multi-spectral imaging (MSI) data with VAS spectral bands 3, 4, 5, and 8, over the Atlantic Ocean to produce heights and velocities of cloud motion winds in the region of interest to the National Hurricane Center (see Section 6.2.4). Applications to global circulations are being investigated. The operational utility of these data is currently being assessed under the auspices of the NOVA (NOAA VAS Assessment) program.

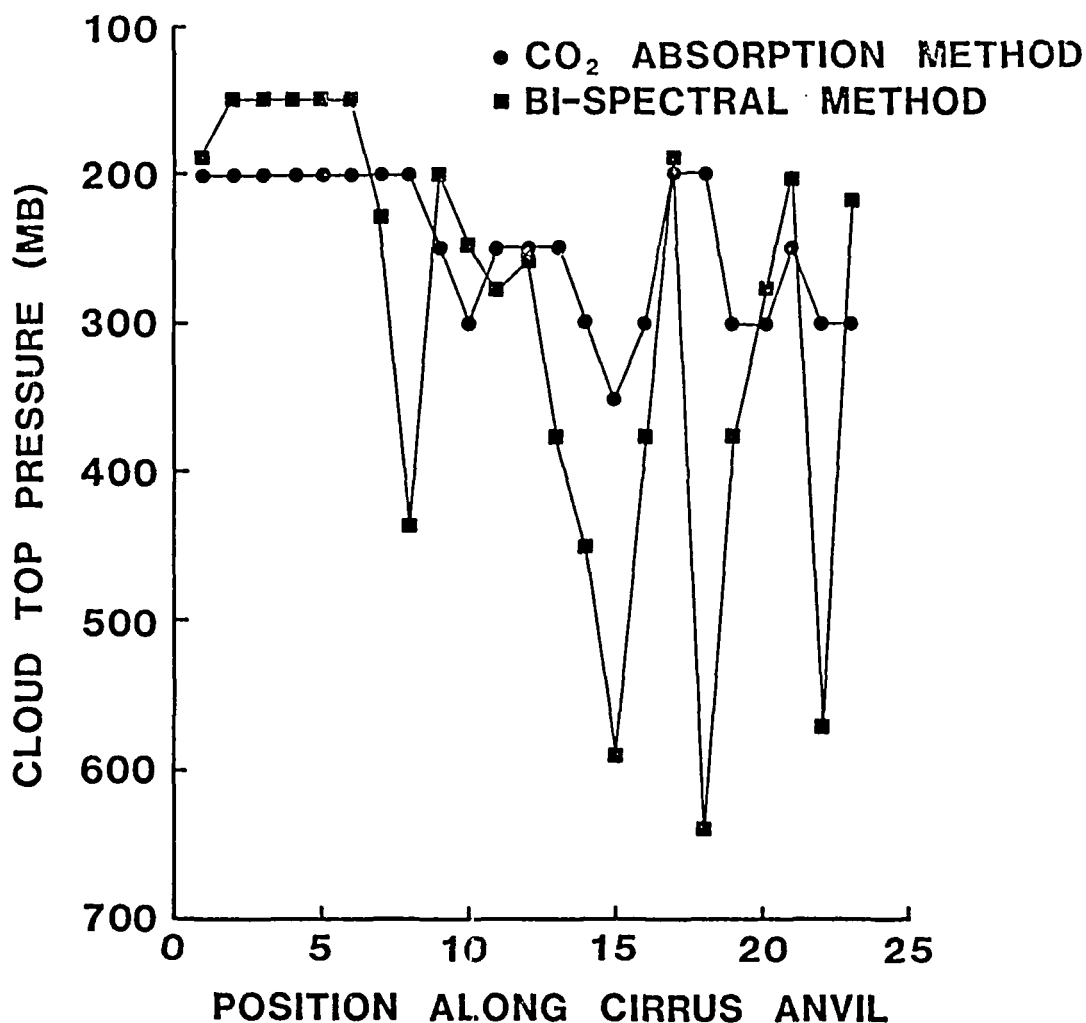


Figure 6-27. Bispectral and CO₂ absorption cloud top pressures (mb) plotted versus the position along the cirrus anvil emanating from the thunderstorm over Missouri and Kansas at 1348 GMT 14 July 1982.

VAS DATA AVAILABILITY

7.1 INTRODUCTION

H. Montgomery
D. Endres
G. Wolford
*Goddard Space Flight Center
National Aeronautics and Space Administration
Greenbelt, Maryland*

P. Menzel
*Cooperative Institute for Meteorological
Satellite Studies
National Environmental Satellite
Data Information Service
National Oceanic and Atmospheric Administration
U.S. Department of Commerce*

G. Hunnolt
*National Environmental Satellite Data
Information Service
National Oceanic and Atmospheric Administration
U.S. Department of Commerce
Camp Springs, Maryland*

Data have been archived for the VAS instruments on GOES-4, GOES-5, and GOES-6 during the VAS Demonstration time frame (September 1980 to October 1983). For GOES-4, data were collected for various periods between September 24, 1980, and January 19, 1982. For the VAS Demonstration, data were collected from GOES-5 for the period June 8, 1981 to October 1983. For GOES-6, data were collected during the period from May 17-24, 1983 for the VAS Demonstration. GOES-4 was initially located at 98°W longitude and subsequently moved to 135°W longitude during February 1981. GOES-5 was initially located at 85°W longitude and moved to 75°W longitude during August 1981. GOES-6 was placed at its final operational position of 135°W longitude at launch.

During much of this period, data have been archived at both UW and GSFC. UW has been archiving the data on a routine basis, whereas GSFC has been archiving data on a call-up basis only. The primary archive of VAS data is UW/SSEC, since NOAA/NESDIS has con-

tracted with them to maintain a VAS data base for the user community.

The remainder of this chapter will describe in more detail the characteristics of the data that is available, and how to obtain it.

7.2 DATA DESCRIPTION

The data were collected in one of three modes: dedicated, interrupt, and TVM. These modes are described in Section 2.5. For a short period of time, only the MSI data were transmitted in the TVM. This was a precursor to the full TVM which allows multispectral imaging and dwell sounding.

Figure 7-1 shows the time periods when VAS data were being acquired and archived from GOES-4, 5, and 6. This figure is intended to give a gross indication of the data collection periods, and should not be used to determine whether data were acquired on specific days. Sections 7.3 and 7.4 address this question.

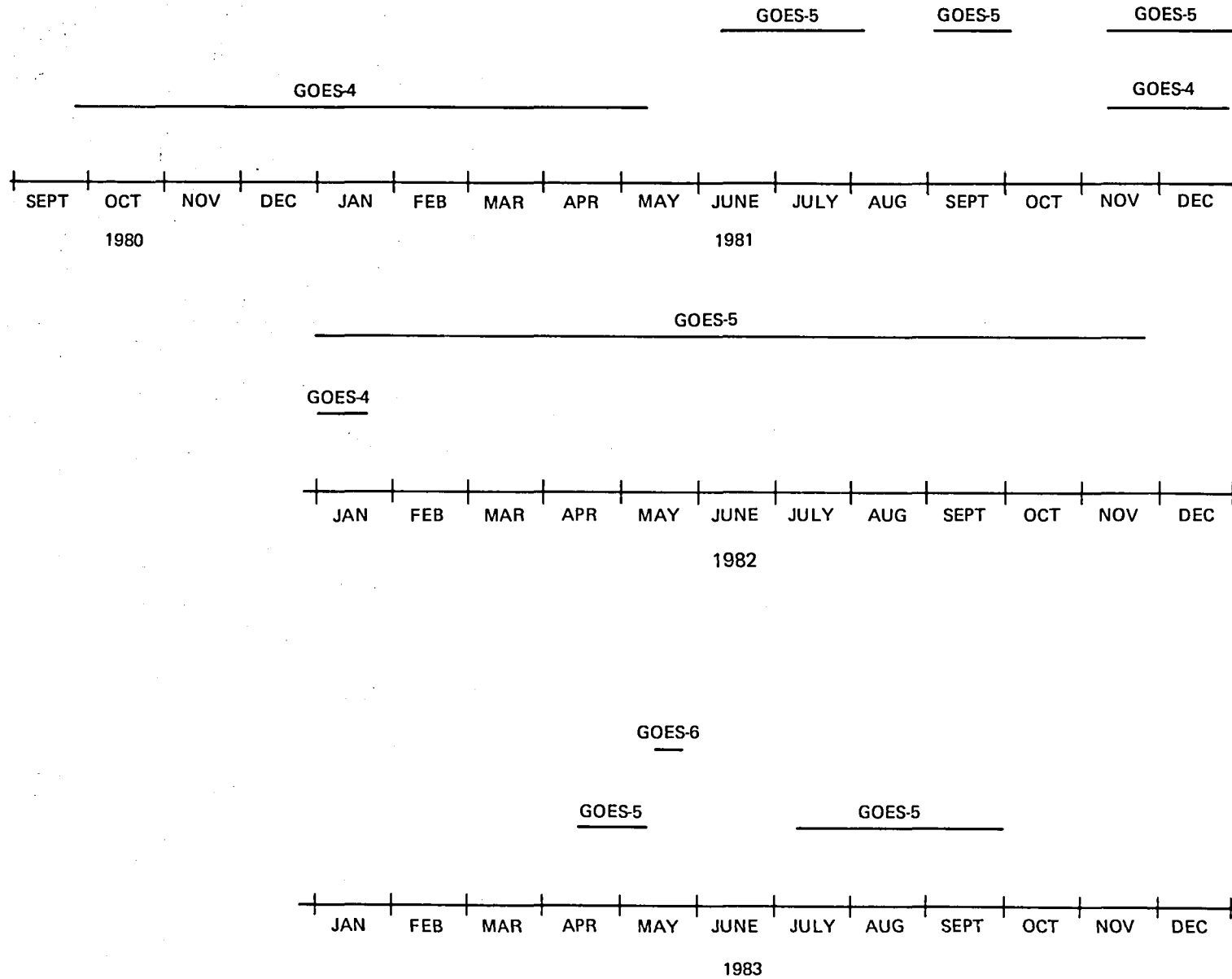


Figure 7-1. Calendar of VAS Data Acquisition

During the periods shown in Figure 7-1, VAS data acquisition was performed in one of the three modes mentioned above. In each mode, different data acquisition schedules were followed depending on the meteorological requirements. Tables 7-1 through 7-6 present the primary schedules that were used. Tables 7-1 and 7-2 present schedules that were used in the dedicated data collection mode. Tables 7-3 and 7-4 give schedules used in the interrupt mode, and Tables 7-5 and 7-6 give

schedules used in the TVM mode. These tables represent nominal schedules. The specific schedule, as dictated by operational constraints, is imbedded in the archived data.

These tables are intended to be used with the specific day-by-day data availability information given in Sections 7.3 and 7.4.

**Table 7-1
VAS Dedicated Normal Operation (NO) and
Severe Storm Day (SSD) Schedule**

TIME (GMT)	ACTIVITY	TIME (GMT)	ACTIVITY
11:30	Full MSI (7-8-10-12)	18:00	DSR
12:00	DSR	19:00	DIR
13:00	DIR	19:30	DIR
13:30	DIR	20:00	DIR
14:00	DIR	20:30	Full MSI (7-8-10-12)
14:30	Full MSI (7-8-10-12)	21:00	DSR
15:00	DSR	22:00	RDI
16:00	DIR	22:15	RDI
16:30	DIR	22:30	RDI
17:00	DIR	22:45	RDI
17:30	Full MSI (7-8-10-12)	23:00	DSR
		24:00 OR 0000	End Test

Full MSI (4 bands) - Multispectral imaging with specified bands (band 8 uses large detector) for full earth disc.

DSR - Dwell sounding regional coverage (55°-20°N)

DIR - Dwell imaging regional coverage (55°-20°N)

RDI - Rapid dwell imaging (43°-27°N)

Table 7-2
VAS Dedicated Cooperative Convective Precipitation
Experiment (CCOPE) Schedule

TIME (GMT)	ACTIVITY	TIME (GMT)	ACTIVITY
12:00	Full MSI (7-8-10-12)	18:30	DI
12:30	DSR	18:45	DI
13:30	DI	19:00	DI
13:45	DI	19:15	DS
14:00	DI	19:45	Full MSI (7-8-10-12)
14:15	Full MSI (7-8-10-12)	20:15	DI
14:45	DS	20:30	DI
15:30	DI	20:45	DI
15:45	DI	21:00	DS
16:00	DI	21:45	DI
16:15	DS	22:00	DI
16:45	DI	22:15	DI
17:00	DI	22:30	DS
17:15	DI	23:00	DI
17:30	DI	23:15	DI
17:45	DS	23:30	DI
		23:45	DSR
		00:35	End Test

DSR - Dwell sounding regional coverage (55° -20°N)
DI - Dwell imaging (52°-36°N)
DS - Dwell sounding (52°-36°N)
Full MSI (4 bands) - Multispectral imaging with specified bands (band 8 uses large detector) for full earth disc

**Table 7-3
VAS Interrupt Special Network (SN) Schedule**

<u>Time (GMT)</u>	<u>Activity</u>
1100	DS
1130-1430	Normal VISSR Operations
1430	DS
1500-1730	Normal VISSR Operations
1730	DS
1800-2030	Normal VISSR Operations
2030	DS
2100-2330	Normal VISSR Operations
2330	DS
2400-0230	Normal VISSR Operations
0230	DS
0300-0530	Normal VISSR Operations
0530	DS
0600-0830	Normal VISSR Operations
0830	DS
0900-1100	Normal VISSR Operations
1100	DS
DS - Dwell sounding (42°-24°N)	

Table 7-4
VAS Interrupt Hurricane Day (HD) Schedule

Time (GMT)	Activity
1130	DS
1200-1430	Normal VISSR Operations
1430	DS
1500-1730	Normal VISSR Operations
1730	DS
1800-2030	Normal VISSR Operations
2030	DS
2100-2330	Normal VISSR Operations
2330	DS
2400-0230	Normal VISSR Operations
0230	DS
0300-0530	Normal VISSR Operations
0530	DS
0600-0830	Normal VISSR Operations
0830	DS
0900-1130	Normal VISSR Operations
DS - Dwell sounding (40°-23°N)	

**Table 7-5
Transparent VAS 16-Hour Routine Operation (RO(16)) Schedule**

Time (GMT)	Activity	Time (GMT)	Activity
1031	MSI (7-8-12)	1748	DI (North)
1048	DS (North)	1801	Full MSI (7-8-10)
1101	MSI (7-8-10)	1831	MSI (7-8-12)
1118	DS (South)	1848	DI (North)
1131	MSI (7-8-12)	1901	MSI (7-8-10)
1148	DI (North)	1918	DI (South)
1201	Full MSI (7-8-10)	1931	MSI (7-8-12)
1231	MSI (7-8-12)	1948	DS (North)
1248	DI (North)	2001	MSI (7-8-10)
1301	MSI (7-8-10)	2018	DS (South)
1318	DI (South)	2031	MSI (7-8-12)
1331	MSI (7-8-12)	2048	DI (North)
1348	DS (North)	2101	Full MSI (7-8-10)
1401	MSI (7-8-10)	2131	MSI (7-8-12)
1418	DS (South)	2148	DI (North)
1431	MSI (7-8-12)	2201	MSI (7-8-10)
1448	DI (North)	2218	DI (South)
1501	Full MSI (7-8-10)	2231	MSI (7-8-12)
1531	MSI (7-8-12)	2248	DS (North)
1548	DI (North)	2301	MSI (7-8-10)
1601	MSI (7-8-10)	2318	DS (South)
1618	DI (South)	2331	Full MSI (7-8-12)
1631	MSI (7-8-12)	0001	Full MSI (7-8-10)
1648	DS (North)	0031	MSI (7-8-12)
1701	MSI (7-8-10)	0048	DI (North)
1718	DS (South)	0101	MSI (7-8-10)
1731	MSI (7-8-12)	0118	DI (South)
		0131	MSI (7-8-12)
		0148	DS (North)
		0201	MSI (7-8-10)
		0218	DS (South)
		0231	Full MSI (7-8-12)
		0300	Normal VISSR Operations

MSI (bands) - Multispectral imaging with specified bands for a partial Earth disc (Top of disc to 42°S)

Full MSI (bands) - Multispectral imaging with specified bands for a full Earth disc

DS (North) - Dwell Sounding (49°-36°N)

DS (South) - Dwell Sounding (36°-26°N)

DI (North) - Dwell imaging (44°-27°N)

DI (South) - Dwell imaging (27°-14°N)

**Table 7-6
Transparent VAS Hurricane Research Day Schedule B (HRDB)**

Time (GMT)	Activity	Time (GMT)	Activity
1031	MSI (7-8-10)	1948	DS (Bottom)
1048	DS (Top)	2001	MSI (3-4-8)
1101	MSI (7-8-10)	2018	MSI (3-4-5-8)
1118	DS (Middle)	2031	MSI (3-4-8)
1131	MSI (7-8-10)	2048	MSI (3-4-5-8)
1148	DS (Bottom)	2101	Full MSI (7-8-10)
1201	Full MSI (7-8-10)	2131	MSI (7-8-10)
1231	MSI (7-8-10)	2148	DS (Top)
1248	DS (Top)	2201	MSI (7-8-10)
1301	MSI (7-8-10)	2218	DS (Middle)
1318	DS (Middle)	2231	MSI (3-4-8)
1331	MSI (7-8-10)	2248	DS (Bottom)
1348	DS (Bottom)	2301	MSI (3-4-8)
1401	MSI (3-4-8)	2318	MSI (3-4-5-8)
1418	MSI (3-4-5-8)	2331	MSI (3-4-8)
1431	MSI (3-4-8)	0001	Full MSI (7-8-10)
1448	MSI (3-4-5-8)	0031	MSI (7-8-10)
1501	Full MSI (7-8-10)	0048	DS (Top)
1531	MSI (7-8-10)	0101	MSI (7-8-10)
1548	DS (Top)	0118	DS (Middle)
1601	MSI (7-8-10)	0131	MSI (3-4-8)
1618	DS (Middle)	0148	DS (Bottom)
1631	MSI (7-8-10)	0201	MSI (3-4-8)
1648	DS (Bottom)	0218	MSI (3-4-5-8)
1701	MSI (3-4-8)	0231	MSI (3-4-8)
1718	MSI (3-4-5-8)	0300	Normal VISSR Operations
1731	MSI (3-4-8)		
1748	MSI (3-4-5-8)		
1801	Full MSI (7-8-12)		
1831	MSI (7-8-10)		
1848	DS (Top)		
1901	MSI (7-8-10)		
1918	DS (Middle)		
1931	MSI (7-8-10)		

MSI (3 bands) - Multispectral imaging with specified bands for partial Earth disc (Top of disc to 42°S)

MSI (4 bands) - Multispectral imaging with specified bands (band 8 uses large detector) for partial Earth disc (Top of disc to 12°S)

Full MSI (bands) - Multispectral imaging with specified bands for full Earth disc

DS (Top) - Dwell sounding (45°-31°N)

DS (Middle) - Dwell sounding (31°-20°N)

DS (Bottom) - Dwell sounding (20°-10°N)

7.3 UW/NOAA VAS DATA ARCHIVE

7.3.1 Data Availability

Table 7-7 lists all the VAS data available at the University of Wisconsin/SSEC through September 1983. The mode of operation, type of support, satellite name, satellite location, and the approximate latitudinal extent of dwell soundings (where applicable) are also given in this table. Table 7-8 lists the various types of support corresponding to the abbreviations in Table 7-7.

In order to establish whether VAS data are available for a particular user's need, the following procedure is recommended:

1. Check Figure 7-1 to determine if any data were archived for the period of interest.
2. Check Table 7-7 to determine whether data were archived on the particular day(s) of interest.
3. Check geographic coverage defined in Table 7-7 to see if the available data is located in the area of interest.
4. Using the "mode of operation" and "type of support" listed in Table 7-7, and the corresponding schedules given in Tables 7-1 through 7-6, determine if the available data are compatible with the user's requirements.

If acceptable data has been located, use the procedure given in the following section to order it.

7.3.2 How to Order UW/NOAA Data

The Satellite Data Services Division (SDSD) of the NOAA/NESDIS National Climatic Data Center has contracted with the Space Science and Engineering Center (SSEC) of the University of Wisconsin for the maintenance of a data base of Mode AA VAS data, and Mode A VISSR data received from NOAA/NESDIS GOES satellites. SDSD maintains an overall data base, of environmental satellite data and derived products, of which the VAS data is one important element. The environmental satellite data base, is an element of the overall national environmental data base managed by NOAA/NESDIS.

Users must note that the VAS data available from SDSD are calibrated radiance values. Atmospheric soundings (vertical profiles of atmospheric parameters, such as temperature and humidity) computed from VAS data are *not* available from SDSD at this time. Users interested in VAS-derived sounding products should contact SSEC directly by calling (608) 262-0544.

Users may obtain visible data to accompany VAS multi-channel IR data from SDSD as part of SDSD's normal service (also contracted with SSEC, to provide Mode A VISSR format data to users). The Mode A data includes visible data and one IR channel, normally the window channel, although the 6.7-micrometer IR channel is substituted for the window channel data at certain times. Delivery of VAS data will require at least one month (longer periods are needed for large orders). Information concerning the price of VAS data is available from SDSD. Detailed tape format documentation will be provided with the data.

Users may obtain further information concerning VAS or VISSR data available from SDSD and may place orders for data by contacting SDSD user services at (301) 763-8111 (FTS763-8111) or by writing:

Satellite Data Services Division
National Climatic Data Center
World Weather Building, Room 100
Washington, DC 20233

To request data, users must provide the following information:

1. Date, time, and geographic area of interest. Users are encouraged to consult SDSD to obtain specific information concerning the VAS data that are available. The information in this chapter is intended to be a summary of the available coverage. Day-to-day variations exist that may effect the user. The geographic area must be specified by the latitude and longitudes of four corners of a rectangle. The West-East extent is restricted to a maximum of about half the Earth disc along the equator. The North-South extent is limited by the data that are available.
2. Desired tape density (1600 or 6250 bpi).

Data from all of the IR channels programmed for use at the time are provided with the data. The user must verify that data from the channels desired are available at the time desired for the area desired, by consulting with SDSD.

Table 7-7
Catalogue of VAS Data Gathered at the University of Wisconsin
1980-1983

	Day	Sounding Coverage	Day	Sat	Loc (°W)	Type of Support	Mode of Op	Archived	Comments
1981	2 Jan	na	2	4	98	CO	D	2040-	year incorrect @ S/DB
	5	na	5	4	98	CO	D	1800-2149	
	6	25-55°N	6	4	98	S	D	1230-2149	soundings archived
	7	25-55°N	7	4	98	S	D	1230-1749	soundings archived
	8	25-55°N	8	4	98	S	D	1230-1749	soundings archived
	9	25-55°N	9	4	98	S	D	1230-2119	soundings archived
	12	25-55°N	12	4	98	S	D	1230-2119	soundings archived
	13	25-55°N	13	4	98	S	D	1230-2119	soundings archived
	14	25-55°N	14	4	98	S	D	1230-2119	soundings archived
	15	na	15	4	98	CO	D	1230-2119	checkout of S/DB
	16	na	16	4	98	CO	D	1230-2119	checkout of S/DB
	19	25-55°N	19	4	98	S	D	1230-2119	calibration paper
	20	25-55°N	20	4	98	S	D	1230-0156	soundings archived
	22	na	22	4	98	CO	D	1702-2156	checkout of S/DB
	23	na	23	4	98	CO	D	1230-2156	checkout of S/DB
	27	na	27	4	100	CO	D	1745-1903	start drifting GOES-4 to 135°W
	29	na	29	4	104	CO	D	1700-1831	checkout of S/DB
	30	na	30	4	106	CO	D	1445-2300	checkout of S/DB
	2 Feb	na	33	4	112	CO	D	1230-2155	checkout of S/DB
	3	na	34	4	114	CO	D	1230-2155	checkout of S/DB
	4	na	35	4	116	CO	D	1230-2155	checkout of S/DB
	5	na	36	4	118	CO	D	1730-1838	checkout of S/DB
	6	na	37	4	120	CO	D	1230-2212	antenna probe
	9	na	40	4	126	CO	D	1230-2156	problems with S/DB ⁽¹⁾
	10	na	41	4	128	CO	D	1230-2156	problems with S/DB ⁽¹⁾
	11	na	42	4	130	CO	D	1230-2156	problems with S/DB ⁽¹⁾
	12	na	43	4	132	CO	D	1230-2156	problems with S/DB ⁽¹⁾
	17	na	48	4	135	CO	D	1830-2200	GOES-4 on station at 135°W
	18	na	49	4	135	CO	D	1506-1647	checkout of S/DB
	24	na	55	4	135	CO	D	1220-2111	checkout of S/DB
	25	na	56	4	135	CO	D	1220-0009	checkout of S/DB
	26	na	57	4	135	CO	D	1230-1708	checkout of S/DB
	27	na	58	4	135	CO	D	1225-2208	checkout of S/DB
	16 Mar	na	75	4	135	CO	I	1215-1400	begin interrupt operation
	17	na	76	4	135	CO	I	1237-1405	
	18	na	77	4	135	CO	I	1216-1431	
	24	na	83	4	135	CO	I	1245-1401	checkout of S/DB
	25	na	84	4	135	CO	I	1205-1241	checkout of S/DB
	26	na	85	4	135	CO	I	1205-1401	checkout of S/DB
	27	na	86	4	135	CO	I	1242-	checkout of S/DB
	30	na	89	4	135	CO	I	1239-1359	checkout of S/DB
	1 Apr	na	91	4	135	CO	I	1215-1403	checkout of S/DB
	3	na	93	4	135	CO	I	1215-1355	checkout of S/DB
	6	na	96	4	135	CO	I	1229-1356	checkout of S/DB
	7	na	97	4	135	CO	I	1215-1353	checkout of S/DB

(1) Tarnished leads, O&A

Table 7-7 (Continued)

	Day	Sounding Coverage	Day	Sat	Loc (°W)	Type of Support	Mode of Op.	Archived	Comments
1981	8 Apr	na	98	4	98	CO	I	1215-1356	checkout of S/DB
	9	na	99	4	135	CO	I	1215-1356	checkout of S/DB
	10	na	100	4	135	CO	I	1216-1355	checkout of S/DB
	13	25-55°N	103	4	135	S	I	1215-1356	soundings archived
	14	25-55°N	104	4	135	S	I	1215-1354	soundings archived
	15	25-55°N	105	4	135	S	I	1215-1354	soundings archived
	16	25-55°N	106	4	135	S	I	1215-1354	soundings archived
	17	na	107	4	135	CO	I	1215-1355	checkout of S/C, S/DB
	6 May	na	126	4	135	CO	I	1432-1523	checkout of S/C, S/DB
	11	na	131	4	135	CO	I	1824-2001	checkout of S/C, S/DB
	8 Jun	na	159	5	85	CO	D	1200-	VAS-E checkout
	9	na	160	5	85	CO	D	1200-	VAS-E checkout
	22	na	173	5	85	CO	D	1503-	VAS-E checkout
	23	25-55°N	174	5	85	S	D	1742-2028	first VAS-E soundings
	24	na	175	5	85	CO	D	1401-	test patterns
	25	na	176	5	85	CO	D	1206-	test patterns
	29	na	180	5	85	CO	D	1502-2130	
	30	na	181	5	85	CO	D		S/DB problems
	1 Jul	25-55°N	182	5	85	S	D		soundings archived
	2	na	183	5	85	CO	D	1332-1447	
	8	na	189	5	85	CO	D	1130-1645	
	10	na	191	5	85	CO	D	1631-2153	
	13	20-55°N	194	5	85	SSD	D	1130-2352	begin summer 81 VAS Demo. GSFC paper
	14	20-55°N	195	5	85	CCOPE	D	1130-0037	CCOPE support
	15	20-55°N	196	5	85	ND	D	1130-2153	normal day
	16	20-55°N	197	5	85	SSD	D	1130-2353	severe storm day
	17	20-55°N	198	5	85	ND	D	1130-2200	
	20	20-55°N	201	5	85	SSD	D	1130-2352	Nowcasting paper
	21	20-55°N	202	5	85	ND	D	1130-2153	soundings archived
	22	20-55°N	203	5	85	ND	D	1130-2153	
	23	20-55°N	204	5	85	CCOPE	D	1130-0037	
	24	20-55°N	205	5	85	CCOPE	D	1130-0037	
	27	20-55°N	208	5	85	ND	D	1130-2153	soundings archived
	28	20-55°N	209	5	85	SSD	D	1130-0018	
	29	20-55°N	210	5	85	ND	D	1140-2153	
	30	20-55°N	211	5	85	CCOPE	D	1130-0047	
	31	20-55°N	212	5	85	ND	D	1130-2200	
	3 Aug	20-55°N	215	5	85	ND	D	1130-2153	SMS-II died, GOES-5 drifting to 75°W
	4	20-55°N	216	5	84	CO	D	1130-2150	soundings archived
	2 Sep	23-40°N	245	5	75	H	I	1130, 1430, 1730, 2030, 2330	begin GOES-5 interrupt operations
	3	23-40°N	246	5	75	H	I	0230, 0530, 0830, 1130	
	4	23-40°N	247	5	75	H	I	1430	
	9	23-40°N	252	5	75	H	I	1130, 1430	

Table 7-7 (Continued)

	Day	Sounding Coverage	Day	Sat	Loc (°W)	Type of Support	Mode of Op	Archived	Comments
1981	11 Sep	23-40°N	254	5	75	H	I	1130, 1430, 1730, 2030, 2330	
	12	23-40°N	255	5	75	H	I	0230, 0830, 1130, 1430, 1730, 2030, 2330	
	13	23-40°N	256	5	75	H	I	0230, 0830, 1130, 1430, 1730, 2030, 2330	Hurricane Harvey
	14	23-40°N	257	5	75	H	I	0230, 0830, 1130, 1430, 1730, 2030, 2330	Hurricane Harvey
	15	23-40°N	258	5	75	H	I	0230, 0830, 1130, 1430, 1730, 2030, 2330	Hurricane Harvey
	16	23-40°N	259	5	75	H	I	0230, 0830	Hurricane Harvey
	18	23-40°N	261	5	75	H	I	0830, 1730, 2030	
	21	23-40°N	264	5	75	H	I	1730, 2030, 2330	
	22	23-40°N	265	5	75	H	I	1730, 2030, 2330	
	23	23-40°N	266	5	75	H	I	0230, 1130, 1430, 1730, 2030, 2330	soundings archived
	24	23-40°N	267	5	75	H	I	0230, 0830, 1130, 1430, 1730, 2030, 2330	soundings archived
	25	23-40°N	268	5	75	H	I	0230, 0830	
	26	23-40°N	269	5	75	H	I	1130, 1430, 1730, 2030, 2330	
	27	23-40°N	270	5	75	H	I	0230, 0830, 1730, 2030, 2330	
	28	23-40°N	271	5	75	H	I	0230, 0830, 1130, 1430, 1730, 2030, 2330	
	29	23-40°N	272	5	75	H	I	0230, 0830, 1130, 1430, 1730, 2030, 2330	

Table 7-7 (Continued)

	Day	Sounding Coverage	Day	Sat	Loc (°W)	Type of Support	Mode of Op	Archived	Comments
1981	30 Sep	23-40°N	273	5	75	H	I	0230, 0530, 0830, 1130, 1430, 1730, 2030, 2330	
	1 Oct	23-40°N	274	5	75	H	I	0230, 0830, 1130, 1430, 1730, 2030, 2330	
	2	23-40°N	275	5	75	H	I	0230, 0830, 1430	
	10 Nov	28-52°N	314	4	135	LFM	I	1020	
	12	23-51°N	316	5	75	S	I	1430, 1730, 2030, 2330	
	19	23-51°N	323	5	75	S	I	1430, 1730, 2030, 2330	
	24	28-52°N	328	4	135	LFM	I	1020	
	26	23-51°N	330	5	75	S	I	1430, 1730, 2030, 2330	
	1 Dec	28-52°N	335	4	135	LFM	I	1020	problems with ΔF at S/DB
	3	23-51°N	337	5	75	S	I	1430, 1730, 2030, 2330	problems with ΔF at S/DB
	8	28-52°N	342	4	135	LFM	I	1020	problems with ΔF at S/DB
	10	23-51°N	344	5	75	S	I	1430, 1730, 2030, 2330	problems with ΔF at S/DB
	15	28-52°N	349	4	135	LFM	I	1020	problems with ΔF at S/DB
	17	23-51°N	351	5	75	S	I	1430, 1730, 2030, 2330	problems with ΔF at S/DB
	22	28-52°N	356	4	135	LFM	I	1020	problems with ΔF at S/DB
	24	23-51°N	358	5	75	S	I	1430, 1730, 2030, 2330	problems with ΔF at S/DB
	29	28-52°N	363	4	135	LFM	I	1020	problems with ΔF at S/DB
	31	23-51°N	365	5	75	S	I	1430, 1730, 2030, 2330	problems with ΔF at S/DB
1982	5 Jan	28-52°N	5	4	135	LFM	I	1020	S/DB ΔF problems persist
	7	23-51°N	7	5	75	S	I	1430, 1730, 2030, 2330	S/DB ΔF problems persist
	12	28-52°N	12	4	135	LFM	I	1020	S/DB ΔF problems persist
	14	23-51°N	14	5	75	S	I	1430, 1730, 2030, 2330	S/DB ΔF problems persist
	19	28-52°N	19	4	135	LFM	I	1020	S/DB ΔF problems persist
	21	23-51°N	21	5	75	S	I	1430, 1730, 2030, 2330	S/DB ΔF problems persist
	28	23-51°N	28	5	75	S	I	1430, 1730, 2030, 2330	S/DB working!
	6 Feb	23-51°N	37	5	75	SN	I	1100, 1430, 1730, 2030, 2330	AVE/VAS test day

Table 7-7 (Continued)

	Day	Sounding Coverage	Day	Sat	Loc (°W)	Type of Support	Mode of Op	Archived	Comments	
1982	8 Feb	na	39	5	75	S	T	1400-2030	first day of TMSI op	
	9	na	40	5	75	S	T	1500-2200		
	10	na	41	5	75	S	T	1500-2030		
	11	na	42	5	75	S	T	1400-2030		
	12	na	43	5	75	S	T	1400-1730		
	15	na	46	5	75	S	T	1400-2030		
	16	na	47	5	75	S	T	1400-2030		
	17	na	48	5	75	S	T	1400-2030		
	18	na	49	5	75	S	T	1400-2030		
	19	na	50	5	75	S	T	1400-2030		
	22	na	53	5	75	S	T	1400-2030		
	23	na	54	5	75	S	T	1400-2030		
	24	na	55	5	75	S	T	1400-2030		
	25	na	56	5	75	S	T	1400-2030		
	26	na	57	5	75	S	T	1400-2030		
	1 Mar	na	60	5	75	S	T	1400-2030		
	2	na	61	5	75	S	T	1400-2030		
	3	na	62	5	75	S	T	1400-2030		
	4	na	63	5	75	S	T	1400-2030		
	5	na	64	5	75	S	T	1400-2030		
	6	24-42°N	65	5	75	SN	I	1100, 1430, 1730, 2030, 2330		first AVE/VAS
	7	24-42°N	66	5	75	SN	I	0230, 0830, 1100		Special Network Day
	8	na	67	5	75	S	T	1400-2030		TMSI
	9	na	68	5	75	S	T	1400-2030		
	10	na	69	5	75	S	T	1400-2030		
	11	na	70	5	75	S	T	1400-2030		
	12	na	71	5	75	S	T	1400-2030		
	22	na	81	5	75	S	T	1430-1500		
	23	26-49°N	82	5	75	SS	T	1400-2048		first day of TVAS op (7hr/day)
	24	26-49°N	83	5	75	SS	T	1400-2048		
	25	26-49°N	84	5	75	SS	T	1400-2048		
26	26-49°N	85	5	75	SS	T	1400-2048			
27	24-42°N	86	5	75	SSN	I	1430, 1730, 2030, 2330	2nd AVE/VAS day		
29	26-49°N	88	5	75	SS	T	1400-2048	TVAS (7hr/day)		
30	26-49°N	89	5	75	SS	T	1400-2048	TVAS (7hr/day)		
31	26-49°N	90	5	75	SS	T	1400-2048	TVAS (7hr/day)		
1 Apr	26-49°N	91	5	75	SS	T	1400-2048	TVAS (7hr/day)		
2	26-49°N	92	5	75	SS	T	1400-2048	TVAS (7hr/day)		
5	26-49°N	95	5	75	SS	T	1400-2048	TVAS (7hr/day)		
6	26-49°N	96	5	75	SS	T	1400-2048	TVAS (7hr/day)		
7	26-49°N	97	5	75	SS	T	1400-2048	TVAS (7hr/day)		
8	26-49°N	98	5	75	SS	T	1400-2048	TVAS (7hr/day)		
9	26-49°N	99	5	75	SS	T	1400-2048	TVAS (7hr/day)		

Table 7-7 (Continued)

	Day	Sounding coverage	Day	Sat	Loc (°W)	Type of Support	Mode of Op	Archived	Comments
1982	12 Apr	26-49°N	102	5	75	SS	T	1400-2048	TVAS (7hr/day)
	13	26-49°N	103	5	75	SS	T	1400-2048	TVAS (7hr/day)
	15	26-49°N	105	5	75	SS	T	1400-2048	TVAS (7hr/day)
	16	26-49°N	106	5	75	SS	T	1400-2048	TVAS (7hr/day)
	19	26-49°N	109	5	75	SS	T	1400-2048	TVAS (7hr/day)
	20	26-49°N	110	5	75	SS	T	1400-2048	TVAS (7hr/day)
	21	26-49°N	111	5	75	SS	T	1400-2048	TVAS (7hr/day)
	22	26-49°N	112	5	75	SS	T	1400-2048	TVAS (7hr/day)
	23	26-49°N	113	5	75	SS	T	1400-2048	TVAS (7hr/day)
	24	24-42°N	114	5	75	SN	I	1430, 1730, 2030	3rd AVE/VAS day
	25	24-42°N	115	5	75	SN	I	0230, 0530, 0830, 1100	
	26	26-49°N	116	5	75	SS	T	1400-2048	TVAS (7hr/day)
	27	26-49°N	117	5	75	SS	T	1400-2048	TVAS (7hr/day)
	28	26-49°N	118	5	75	SS	T	1400-2048	TVAS (7hr/day)
	29	26-49°N	119	5	75	SS	T	1400-2048	TVAS (7hr/day)
	1 May	24-42°N	121	5	75	SN	I	1100, 1430, 1730, 2030, 2330	4th AVE/VAS day
	2	24-42°N	122	5	75	SN	I	0230, 0530, 0830, 1100	
	3	26-49°N	123	5	75	SS	T	1400-2048	TVAS
	4	26-49°N	124	5	75	SS	T	1400-2048	TVAS
	5	26-49°N	125	5	75	SS	T	1400-1548	
	6	26-49°N	126	5	75	SS	T	1400-2048	TVAS
	7	26-49°N	127	5	75	SS	T	1400-2048	TVAS
	21	26-49°N	141	5	75	SS	T	1430-0230	TVAS (16 hr/day)
	22	26-49°N	142	5	75	SS	T	1030-0230	TVAS (16 hr/day)
	23	26-49°N	143	5	75	SS	T	1030-0230	TVAS (16 hr/day)
	24	26-49°N	144	5	75	SS	T	1030-0230	TVAS (16 hr/day)
	25	26-49°N	145	5	75	SS	T	1030-0230	TVAS (16 hr/day)
	26	26-49°N	146	5	75	SS	T	1030-1830	TVAS (16 hr/day)
	27	26-49°N	147	5	75	SS	T	1030-1730	TVAS (16 hr/day)
	28	26-49°N	148	5	75	SS	T	1200-2020	TVAS (16 hr/day)
	29	26-49°N	149	5	75	SS	T	1200-1748	TVAS (16 hr/day)
	30	26-49°N	150	5	75	SS	T	1030-1648	TVAS (16 hr/day)
	31	26-49°N	151	5	75	SS	T	1030-1800	TVAS (16 hr/day)
	1 Jun	26-49°N	152	5	75	SS	T	1030-0230	TVAS (16 hr/day)
	2	26-49°N	153	5	75	SS	T	1730-1800	TVAS (16 hr/day)
	3	26-49°N	154	5	75	SS	T	1030-2218	TVAS (16 hr/day)
	4	26-49°N	155	5	75	SS	T	1030-0230	TVAS (16 hr/day)
	5	26-49°N	156	5	75	SS	T	1030-1748	TVAS (16 hr/day)
	6	26-49°N	157	5	75	SS	T	1030-2218	TVAS (16 hr/day)
	7	26-49°N	158	5	75	SS	T	1030-2031	TVAS (16 hr/day)
	8	26-49°N	159	5	75	SS	T	1030-1718	TVAS (16 hr/day)
	10	26-49°N	161	5	75	SS	T	1300-2148	TVAS (16 hr/day)

Table 7-7 (Continued)

	Day	Sounding Coverage	Day	Sat	Loc (°W)	Type of Support	Mode of Op	Archived	Comments
1982	11 Jun	26-49°N	162	5	75	SS	T	1030-1730	TVAS (16 hr/day)
	12	26-49°N	163	5	75	SS	T	1030-2330	TVAS (16 hr/day)
	13	26-49°N	164	5	75	SS	T	1030-2248	TVAS (16 hr/day)
	14	26-49°N	165	5	75	SS	T	1030-1918	TVAS (16 hr/day)
	15	26-49°N	166	5	75	SS	T	1030-1648	TVAS (16 hr/day)
	16	26-49°N	167	5	75	SS	T	1330-2230	TVAS (16 hr/day)
	18	26-49°N	169	5	75	SS	T	1100-1630	TVAS (16 hr/day)
	19	26-49°N	170	5	75	SS	T	1030-0230	TVAS (16 hr/day)
	20	26-49°N	171	5	75	SS	T	1030-0230	TVAS (16 hr/day)
	22	26-49°N	173	5	75	SS	T	1030-1730	TVAS (16 hr/day)
	23	26-49°N	174	5	75	SS	T	1030-2130	TVAS (16 hr/day)
	24	26-49°N	175	5	75	SS	T	1030-1730	TVAS (16 hr/day)
	25	26-49°N	176	5	75	SS	T	1030-2330	TVAS (16 hr/day)
	26	26-49°N	177	5	75	SS	T	1030-0230	TVAS (16 hr/day)
	27	26-49°N	178	5	75	SS	T	1030-2330	TVAS (16 hr/day)
	28	26-49°N	179	5	75	SS	T	1030-2248	TVAS (16 hr/day)
	29	26-49°N	180	5	75	SS	T	1030-2331	TVAS (16 hr/day)
	30	26-49°N	181	5	75	SS	T	1030-1800	TVAS (16 hr/day)
	1 Jul	26-49°N	182	5	75	SS	T	1030-1700	TVAS (16 hr/day)
	2	26-49°N	183	5	75	SS	T	1030-0230	TVAS (16 hr/day)
	3	26-49°N	184	5	75	SS	T	1030-1548	TVAS (16 hr/day)
	4	26-49°N	185	5	75	SS	T	1030-2018	TVAS (16 hr/day)
	5	26-49°N	186	5	75	SS	T	1030-2248	TVAS (16 hr/day)
	9	26-49°N	190	5	75	SS	T	1030-1730	TVAS (16 hr/day)
	10	26-49°N	191	5	75	SS	T	1030-1830	TVAS (16 hr/day)
	12	26-49°N	193	5	75	SS	T	1030-0230	TVAS (16 hr/day)
	13	26-49°N	194	5	75	SS	T	1030-0230	TVAS (16 hr/day)
	14	26-49°N	195	5	75	SS	T	1030-0230	TVAS (16 hr/day)
	15	26-49°N	196	5	75	SS	T	1030-0230	TVAS (16 hr/day)
	16	26-49°N	197	5	75	SS	T	1030-1730	TVAS (16 hr/day)
	17	26-49°N	198	5	75	SS	T	1030-1730	TVAS (16 hr/day)
18	26-49°N	199	5	75	SS	T	1030-0230	TVAS (16 hr/day)	
19	26-49°N	200	5	75	SS	T	1030-0230	TVAS (16 hr/day)	
20	26-49°N	201	5	75	SS	T	1030-2018, 2030-0246	TVAS, VR	
21	26-49°N	202	5	75	SS	T	1030-0230	TVAS (16)	
22	26-49°N	203	5	75	SS	T	1030-1720, 1730-0230	TVAS, VR	
23	26-49°N	204	5	75	SS	T	1030-1730	TVAS (16)	
24	26-49°N	205	5	75	SS	T	1030-0230	TVAS (16)	
25	26-49°N	206	5	75	SS	T	1030-1730	TVAS (16)	
26	26-49°N	207	5	75	SS	T	1030-0230	TVAS (16)	
27	26-49°N	208	5	75	SS	T	1030-1730	TVAS (16)	
28	26-49°N	209	5	75	SS	T	1030-0230	TVAS (16)	
29	26-49°N	210	5	75	SS	T	1030-1730	TVAS (16)	
30	26-49°N	211	5	75	SS	T	1030-0230	TVAS (16)	
31	26-49°N	212	5	75	SS	T	1030-1730	TVAS (16)	

Table 7-7 (Continued)

	Day	Sounding Coverage	Day	Sat	Loc (°W)	Type of Support	Mode of Op	Archived	Comments
1982	1 Aug	26-49°N	213	5	75	SS	T	1030-0230	TVAS (16)
	2	26-49°N	214	5	75	SS	T	1030-0230	TVAS (16)
	3	26-49°N	215	5	75	SS	T	1030-1448	TVAS (16)
	4	26-49°N	216	5	75	SS	T	1030-2118, 2131-2346	TVAS, VR
	5	26-49°N	217	5	75	SS	T	1030-0230	TVAS (16)
	6	26-49°N	218	5	75	SS	T	1030-0230	TVAS (16)
	7	26-49°N	219	5	75	SS	T	1030-0230	TVAS (16)
	8	26-49°N	220	5	75	SS	T	1030-0230	TVAS (16)
	9	26-49°N	221	5	75	SS	T	1030-0230	TVAS (16)
	10	26-49°N	222	5	75	SS	T	1030-1748	TVAS (16)
	11	26-49°N	223	5	75	SS	T	1030-1730	TVAS (16)
	13	26-49°N	225	5	75	SS	T	1230-1430	TVAS (16)
	14	26-49°N	226	5	75	SS	T	1030-0230	TVAS (16)
	15	26-49°N	227	5	75	SS	T	1030-1730	TVAS (16)
	16	26-49°N	228	5	75	SS	T	1030-0230	TVAS (16)
	17	26-49°N	229	5	75	SS	T	1030-1800	TVAS (16)
	18	26-49°N	230	5	75	SS	T	1030-1731	TVAS (16)
	19	26-49°N	231	5	75	SS	T	1030-0230	TVAS (16)
	20	26-49°N	232	5	75	SS	T	1030-0230	TVAS (16)
	21	26-49°N	233	5	75	SS	T	1030-0230	TVAS (16)
	22	26-49°N	234	5	75	SS	T	1030-1730	TVAS (16)
	23	26-49°N	235	5	75	SS	T	1030-0230	TVAS (16)
	24	26-49°N	236	5	75	SS	T	1030-2348	TVAS (16)
	26	26-49°N	238	5	75	SS	T	1030-0230	TVAS (16)
	27	26-49°N	239	5	75	SS	T	1030-0230	TVAS (16)
	28	26-49°N	240	5	75	SS	T	1030-0230	TVAS (16)
	29	26-49°N	241	5	75	SS	T	1030-1730	TVAS (16)
	30	26-49°N	242	5	75	SS	T	1030-1530	TVAS (16)
	31	26-49°N	243	5	75	SS	T	1030-0	TVAS (16)
	1 Sep	01-37°N	244	5	75	H	T	1030-0248	HRD B (643)
	2	03-39°N	245	5	75	H	T	1030-0248	HRD B (610)
3	03-39°N	246	5	75	H	T	1030-0248	HRD B (615)	
5	05-41°N	248	5	75	H	T	1030-0248	HRD B (585)	
6	26-49°N	249	5	75	SS	T	1030-0231	TVAS (16)	
7	26-49°N	250	5	75	SS	T	1030-0230	TVAS (16)	
8	4°S-27°N	251	5	75	H	T	1030-1831	HRD B (718)	
10	07-44°N	253	5	75	H	T	1030-0248	HRD B (515)	
11	26-49°N	254	5	75	SS	T	1030-0231	TVAS (16)	
12	26-49°N	255	5	75	SS	T	1030-0231	TVAS (16)	
13	03-39°N	256	5	75	H	T	1031-2018 2031-0246	HRD B (611), VR	
14	05-41°N	257	5	75	H	T	1031-0248	HRD B (579)	
15	11-46°N	258	5	75	H	T	1031-0248	HRD B (473)	
16	15-50°N	259	5	75	H	T	1031-0248	HRD B (434)	
17	10-45°N	260	5	75	H	T	1031-0248	HRD B (489)	
18	03-39°N	261	5	75	H	T	1031-0248	HRD B (615)	

Table 7-7 (Continued)

	Day	Sounding Coverage	Day	Sat	Loc (°W)	Type of Support	Mode of Op	Archived	Comments
1982	19 Sep	03-39°N	262	5	75	H	T	1031-0248	HRD B (602)
	20	01-37°N	263	5	75	H	T	1031-0248	HRD B (643)
	22	26-49°N	265	5	75	SS	T	1031-0231	TVAS (16)
	23	04-40°N	266	5	75	H	T	1031-0248	HRD B (595)
	24	06-43°N	267	5	75	H	T	1031-0248	HRD B (525)
	25	06-43°N	268	5	75	H	T	1031-0248	HRD B (525)
	26	18-54°N	269	5	75	H	T	1031-0248	HRD B (389)
	27	26-49°N	270	5	75	H	T	1031-0231	TVAS (16)
	28	26-49°N	271	5	75	SS	T	1031-1648, 1701-0246	TVAS (16), VR
	30	05-42°N	273	5	75	H	T	1031-0248	HRD B (541)
	1 Oct	05-42°N	274	5	75	H	T	1031-0248	HRD B (534)
	2	12-47°N	275	5	75	H	T	1031-0248	HRD B (460)
	3	15-50°N	276	5	75	H	T	1031-0248	HRD B (433)
	4	26-49°N	277	5	75	SS	T	1031-0231	TVAS (16)
	5	00-36°N	278	5	75	H	T	1031-0248	HRD B (651)
	6	5°S-26°N	279	5	75	H	T	1031-0248	HRD B (721)
	7	05-41°N	280	5	75	H	T	1031-2048	HRD B (583)
	8	26-49°N	281	5	75	SS	T	1031-1418, 1431-0246	TVAS (16), VR
	9	26-49°N	282	5	75	SS	T	1031-0231	TVAS (16)
	10	26-49°N	283	5	75	SS	T	1031-0231	TVAS (16)
	11	26-49°N	284	5	75	SS	T	1031-0231	TVAS (16)
	12	26-49°N	285	5	75	SS	T	1031-0231	TVAS (16)
	13	17-52°N	286	5	75	H	T	1031-0248	HRD B (417)
	14	26-49°N	287	5	75	SS	T	1031-1348	TVAS (16)
	15	9°S-22°N	288	5	75	H	T	1031-0248	HRD B (763)
	16	8°S-23°N	289	5	75	H	T	1031-0248	HRD B (751)
	17	26-49°N	290	5	75	SS	T	1031-0231	TVAS (16)
	18	26-49°N	291	5	75	SS	T	1031-2331	TVAS (16)
	20	26-49°N	293	5	75	SS	T	1031-0231	TVAS (16)
	21	01-37°N	294	5	75	H	T	1031-0248	HRD B (623)
	22	26-49°N	295	5	75	SS	T	1031-1248	TVAS (16)
2 Nov	26-49°N	306	5	75	SS	T	1031-0231	TVAS (16)	
3	26-49°N	307	5	75	SS	T	1031-0231	TVAS (16)	
4	26-49°N	308	5	75	SS	T	1031-0231	TVAS (16)	
5	26-49°N	309	5	75	SS	T	1031-0231	TVAS (16)	
6	26-49°N	310	5	75	SS	T	1031-0231	TVAS (16)	
7	26-49°N	311	5	75	SS	T	1031-0231	TVAS (16)	
8	26-49°N	312	5	75	SS	T	1031-0231	TVAS (16)	
9	26-49°N	313	5	75	SS	T	1031-0231	TVAS (16)	
10	26-49°N	314	5	75	SS	T	1031-0231	TVAS (16)	
11	26-49°N	315	5	75	SS	T	1031-1648, 1701-0246	TVAS (16), VR	
12	26-49°N	316	5	75	SS	T	1031-0231	TVAS (16)	
13	26-49°N	317	5	75	SS	T	1031-0231	TVAS (16)	
14	26-49°N	318	5	75	SS	T	1031-0231	TVAS (16)	

Table 7-7 (Continued)

	Day	Sounding Coverage	Day	Sat	Loc (°W)	Type of Support	Mode of Op	Archived	Comments
1982	15 Nov	26-49°N	319	5	75	SS	T	1031-0231	TVAS (16)
	16	26-49°N	320	5	75	SS	T	1031-1801	TVAS (16)
	17	26-49°N	321	5	75	SS	T	1031-0231	TVAS (16)
	18	26-49°N	322	5	75	SS	T	1031-0231	TVAS (16)
	19	26-49°N	323	5	75	SS	T	1031-0231	TVAS (16)
	20	26-49°N	324	5	75	SS	T	1031-0231	TVAS (16)
	21	26-49°N	325	5	75	SS	T	1031-0231	TVAS (16)
	22	26-49°N	326	5	75	SS	T	1031-0231	TVAS (16)
	23	26-49°N	327	5	75	SS	T	1031-0231	TVAS (16)
	24	26-49°N	328	5	75	SS	T	1031-0231	TVAS (16)
	25	26-49°N	329	5	75	SS	T	1031-0231	TVAS (16)
	26	26-49°N	330	5	75	SS	T	1031-1201	TVAS (16)
	27								GOES-4 died

Table 7-7 (Continued)

	Day	Sounding Coverage	Day	Sat	Loc (°W)	Mode of Op	Times Archived	Comments
1983	15 Apr	25-48°N	105	5	75	I	1830, 2030,	
	18	25-48°N	108	5	75	I	1300, 1430, 1830, 2030	
	19	25-48°N	109	5	75	I	1300, 1430	
	20	25-48°N	110	5	75	I	1300, 1430, 1830, 2030,	
	21	25-48°N	111	5	75	I	1300, 1430, 1830, 2030	
	22	25-48°N	112	5	75	I	1300, 1430, 1830	
	25	25-48°N	115	5	75	I	1300, 1430, 1830, 2030	
	26	25-48°N	116	5	75	I	1300, 1430, 1830, 2030	
	27	25-48°N	117	5	75	I	1300, 1430	
	28	25-48°N	118	5	75	I	1300, 1430, 1830, 2030	
	3 May	25-48°N	123	5	75	I	1300, 1430	
	4	25-48°N	124	5	75	I	1300, 1430, 1830, 2030	
	5	25-48°N	125	5	75	I	1300, 1430, 1830, 2030	
	6	25-48°N	126	5	75	I	1300, 1430	
	9	25-48°N	129	5	75	I	1300, 1430, 1830, 2030	
	10	25-48°N	130	5	75	I	1300, 1430, 1830, 2030	
	11	25-48°N	131	5	75	I	1300, 1430	
	17	25-48°N	137	6	135	CO		VAS-F checkout
	18	25-48°N	138	6	135	CO	1847-2130	
	23	25-48°N	143	6	135	CO	1310-0230	
	24	25-48°N	144	6	135	CO	1400-1900	
	11 Jul	25-48°N	192	5	75	T	1030-0300	Schedule A
	12	25-48°N	193	5	75	T	1500-0300	Schedule A
	13	25-48°N	194	5	75	T	1030-0300	Schedule A
	14	25-48°N	195	5	75	T	1030-2130	Schedule A
	15	25-48°N	196	5	75	T	1030-0300	Schedule A
	20	25-48°N	201	5	75	T	1030-1600	HRD B
	21	25-48°N	202	5	75	T	1030-1400	Schedule A
	22	25-48°N	203	5	75	T	1030-1800	Schedule A
	23	25-48°N	204	5	75	T	1030-1200	Schedule A
24	25-48°N	205	5	75	T	1030-0300	Schedule A	
25	25-48°N	206	5	75	T	1030-0300	Schedule A	
26	25-48°N	207	5	75	T	1030-0300	Schedule A	
27	1°S-32°N	208	5	75	T	1030-0300	HRD B (689)	
28	1°S-32°N	209	5	75	T	1030-0300	HRD B (687)	
29	01-35°N	210	5	75	T	1030-0300	HRD B (641)	

Table 7-7 (Continued)

	Day	Sounding Coverage	Day	Sat	Loc (°W)	Mode of Op	Times Archived	Comments	
1983	30 Jul	25-48°N	211	5	75	T	1500-0300	Schedule A	
	31	25-48°N	212	5	75	T	1030-1800	Schedule A	
	1 Aug	25-48°N	213	5	75	T	1030-0300	Schedule A	
	2	25-48°N	214	5	75	T	1030-1545	Schedule A	
	3	06-43°N	215	5	75	T	1030-0300	HRD B (529)	
	4	25-48°N	216	5	75	T	1030-1545	Schedule A	
	5	25-48°N	217	5	75	T	1030-0300	Schedule A	
	6	25-48°N	218	5	75	T	1030-1830	Schedule A	
	7	25-48°N	219	5	75	T	1030-2100	Schedule A	
	8	25-48°N	220	5	75	T	1030-1800	Schedule A	
	9	25-48°N	221	5	75	T	1030-1530	Schedule A	
	10	04-40°N	222	5	75	T	1030-1830	HRD B (571)	
	11	25-48°N	223	5	75	T	1030-1330	Schedule A	
	12	25-48°N	224	5	75	T	1030-1545	Schedule A	
	13	01-35°N	225	5	75	T	1030-0300	HRD B (647)	
	14	25-48°N	226	5	75	T	1030-0300	Schedule A	
	15	25-48°N	227	5	75	T	1030-2230	Schedule A	
	16	10-45°N	228	5	75	T	1030-2300	HRD B (495) Alicia	
	17	14-49°N	229	5	75	T	1030-0300	HRD B (459) Alicia	
	18	14-49°N	230	5	75	T	1030-0200	HRD B (459) Alicia	
	19	25-48°N	231	5	75	T	1030-1700	Schedule A	
	20	25-48°N	232	5	75	T	1030-0300	Schedule A	
	21	25-48°N	233	5	75	T	1030-0300	Schedule A	
	22	25-48°N	234	5	75	T	1030-0300	Schedule A	
	23	25-48°N	235	5	75	T	1030-1600	Schedule A	
	24	25-48°N	236	5	75	T	1030-1500	Schedule A	
								1400-0300	HRD B (479)
	25	14-49°N	237	5	75	T	1030-1600	HRD B (453)	
	26	14-49°N	238	5	75	T	1030-0300	HRD B (451)	
	27	10-45°N	239	5	75	T	1030-0300	HRD B (493)	
	28	25-48°N	240	5	75	T	1030-1600	Schedule A	
31	25-48°N	243	5	75	T	1030-0300	Schedule A		
1 Sep	25-48°N	244	5	75	T	1030-0300	Schedule A		
2	25-48°N	245	5	75	T	1030-0300	Schedule A		
3	10-45°N	246	5	75	T	1030-0300	HRD B (487)		
4	25-48°N	247	5	75	T	1030-0300	Schedule A		
5	25-48°N	248	5	75	T	1700-2230	Schedule A		
7	25-48°N	250	5	75	T	1200-0300	Schedule A		
8	17-53°N	251	5	75	T	1030-1700	HRD B (407)		
9	06-43°N	252	5	75	T	1030-0300	HRD B (529)		
10	25-48°N	253	5	75	T	1030-1800	Schedule A		
11	14-49°N	254	5	75	T	1030-0300	HRD B (451)		
12	16-51°N	255	5	75	T	1030-0300	HRD B (419)		
13	17-53°N	256	5	75	T	1030-0300	HRD B (399) Brazil		
								1151, 1303, 1455 @ 1048, 1118, 1148	
								763, 915, 1067 @ 1548, 1618, 1648	
								763, 915, 1067 @ 2148, 2218, 2248	

Table 7-7 (Continued)

	Day	Sounding Coverage	Day	Sat	Loc (°W)	Mode of Op	Times Archived	Comments
1983	14 Sep	15-50°N	257	5	75	T	1030-0300	HRD B (465) Brazil 1157, 1291, 1425@1848, 1918, 1948
	15	15-50°N	258	5	75	T	1030-0300	HRD B (469)
	16	03-39°N	259	5	75	T	1030-0300	HRD B (607)
	17	03-39°N	260	5	75	T	1030-1830	HRD B (609)
	18	03-39°N	261	5	75	T	1030-0300	HRD B (607)
	19	03-39°N	262	5	75	T	1030-1900	HRD B (607)
	20	?	263	5	75	T	1030-1700	HRD B
	23	1°S-32°N	266	5	75	T	1030-0300	HRD B (685)
	24	5°S-26°N	267	5	75	T	1030-0300	HRD B (729)
	25	25-48°N	268	5	75	T	1030-0300	Schedule A
	26	25-48°N	269	5	75	T	1030-0300	Schedule A

TABLE 7-8
Modes of Operation and Types of Support

Mode of Operation	Type of Support	Description
D		VAS Dedicated-GOES satellite dedicated to use by VAS Project
	CO	Checkout-Instrument or Ground System checks
	CCOPE	Cooperative Convective Precipitation Experiment—Nominal schedule shown in Table 7-2
	H	Hurricane Day
	ND	Normal Day—Nominal schedule shown in Table 7-1
	SSD	Severe Storm Day—Nominal schedule shown in Table 7-1
I		Interrupt Mode—NOAA Operational schedule interrupted at various times throughout the day for VAS data acquisition
	CO	Checkout—Instrument or Ground System checkout
	HD	Hurricane Day—Nominal schedule shown in Table 7-4
	LFM	Limited Fine Mesh Model—A special PDL schedule for collecting data over the North Pacific
	SN	Special Network—Nominal schedule shown in Table 7-3
T		Transparent Mode—This mode allows simultaneous collection of VAS and NOAA operational VISSR data from the same GOES satellite
	SS	Kansas City Support for severe storm forecasts
	HRDA	Hurricane Day (A) — This schedule is identical to RO(16) schedule except for slight time changes
	HRDB (CL)	Hurricane Day (B) — This schedule is shown in Table 7-6. CL is the frame centerline value.

**TABLE 7-8
(Continued)**

Mode of Operation	Type of Support	Description
<p>T (continued)</p>	<p>RO(MSI)</p>	<p>Routine Operations – Regular NOAA schedule with MSI substituted for VISSR (no dwell sounding)</p>
	<p>RO(7), RO(16)</p>	<p>Routine Operational – The 7 or 16-hour nominal schedule is shown in Table 7-5</p>
	<p>VR</p>	<p>VAS RISOP (Rapid Interval Storm Operations Plan) – This schedule includes several short MSI frames but no dwell sounding</p>

7.4 GSFC VAS DATA ARCHIVE

7.4.1 Data Availability

Table 7-9 lists all the VAS data that are available at NASA/GSFC through September 1983. The mode of operation, type of support, satellite name, satellite location, and the approximate latitudinal extent of dwell soundings (where applicable) are also given in this table. Table 7-8 lists the various types of support corresponding to the abbreviations in Table 7-9. The data listed in Table 7-9 reside on special archival tapes which are non-standard, and therefore, incompatible with the user's data processing system. A subset of the data listed in Table 7-9 is processed and stored onto computer compatible tapes (CCT's). This subset, shown in Table 7-10, is now available to users.

In order to determine if VAS data are available for a particular user's need, the following procedure is recommended:

1. Check Figure 7-1 to determine if any data were archived in the period of interest.
2. Check Table 7-9 to determine if data were archived on the particular day(s) of interest.
3. Check geographic coverage defined in Table 7-9 to see if the available data is located in the area of interest.
4. Using the "mode of operation" and "type of support" listed in Table 7-9, and the corresponding schedules given in Tables 7-1 through 7-6, determine if the available data are compatible with the user's requirements.

If acceptable data has been located, the procedure given in the following section should be used to order it.

7.4.2 How to Order GSFC Data

The Goddard Space Flight Center does not acquire all VAS data, but can provide 1600 or 6250-bpi, 9-track computer compatible tapes (CCT's) of special data sets collected since 1980.

Although the VAS processing facility at GSFC was designed primarily for analysis and scientific investigation (not for data production and distribution), GSFC will provide CCT's for specific VAS data sets to the scientific community. The conditions (i.e., response time, possible replacement of tapes by the customer, ancillary data requirements) for each order will be determined case-by-case.

To order VAS CCT's, contact either:

Dr. D. Chesters
Code 613
NASA/Goddard Space Flight Center
Greenbelt, MD 20771
(301) 344-6772

or

Dr. L. W. Uccellini
Code 612
NASA/Goddard Space Flight Center
Greenbelt, MD 20771
(301) 344-5786

Table 7-9
VAS Data Availability at GSFC

Date	Day of Year	Dwell Sounding Coverage	Satellite		Type of Support	Mode of Operation
			Location (°W)	Name		
1980						
7 Nov	312	20-50°N	98	4	CO	D
10	315	NA	98	4	CO	D
11	316	15-40°N	98	4	H	D
12	317	15-40°N	98	4	H	D
13	318	15-40°N	98	4	H	D
14	319	15-40°N	98	4	H	D
18	323	25-55°N	98	4	CO	D
24	329	25-55°N	98	4	CO	D
1981						
13 May	133	NA	135	4	CO	I
21	141	NA	135	4	CO	I
8 Jun	159	NA	85	5	CO	D
9	160	NA	85	5	CO	D
10	161	NA	85	5	CO	D
22	173	NA	85	5	CO	D
23	174	NA	85	5	CO	D
25	176	NA	85	5	CO	D
29	180	NA	85	5	CO	D
1 Jul	182	25-55°N	85	5	CO	D
13	194	20-55°N	85	5	SSD	D
14	195	20-55°N	85	5	CCOPE	D
15	196	20-55°N	85	5	ND	D
16	197	20-55°N	85	5	SSD	D
17	198	20-55°N	85	5	ND	D
20	201	20-55°N	85	5	SSD	D
21	202	20-55°N	85	5	ND	D
22	203	20-55°N	85	5	ND	D
23	204	20-55°N	85	5	CCOPE	D
24	205	20-55°N	85	5	CCOPE	D
27	208	20-55°N	85	5	ND	D
28	209	20-55°N	85	5	SSD	D
29	210	20-55°N	85	5	ND	D
30	211	20-55°N	85	5	CCOPE	D
31	212	20-55°N	85	5	ND	D
3 Aug	215	20-55°N	85	5	ND	D
4	216	20-55°N	86	5	CO	D
2 Sep	245	23-40°N	75	5	HD	I
11	254	23-40°N	75	5	HD	I
12	255	23-40°N	75	5	HD	I
13	256	23-40°N	75	5	HD	I
14	257	23-40°N	75	5	HD	I
15	258	23-40°N	75	5	HD	I
23	266	23-40°N	75	5	HD	I
24	267	23-40°N	75	5	HD	I

Table 7-9 (Continued)

Date	Day of Year	Dwell Sounding Coverage	Satellite		Type of Support	Mode of Operation
			Location (°W)	Name		
25 Sep	268	23-40°N	75	5	HD	I
26	269	23-40°N	75	5	HD	I
27	270	23-40°N	75	5	HD	I
28	271	23-40°N	75	5	HD	I
29	272	23-40°N	75	5	HD	I
1982						
6 Feb	37	23-51°N	75	5	SN	I
7	38	23-51°N	75	5	SN	I
6 Mar	65	23-47°N	75	5	SN	I
7	66	23-47°N	75	5	SN	I
27	86	23-43°N	75	5	SN	I
28	87	23-43°N	75	5	SN	I
24 Apr	114	23-43°N	75	5	SN	I
25	115	23-43°N	75	5	SN	I
1 May	121	22-47°N	75	5	SN	I
2	122	22-47°N	75	5	SN	I
24 Aug	236	10-45°N	75	5	HRDB	T
31	243	10-45°N	75	5	HRDB	T
3 Sep	246	10-45°N	75	5	HRDB	T
5	248	10-45°N	75	5	HRDB	T
6	249	10-45°N	75	5	HRDB	T
8	251	10-45°N	75	5	HRDB	T
10	253	10-45°N	75	5	HRDB	T
11	254	10-45°N	75	5	HRDB	T
13	256	10-45°N	75	5	HRDB/VR	T
14	257	10-45°N	75	5	HRDB/VR	T
15	258	10-45°N	75	5	HRDB	T
16	259	10-45°N	75	5	HRDB	T
23	266	10-45°N	75	5	HRDB	T
24	267	10-45°N	75	5	HRDB	T
1983						
17 May	137	NA	135	6	CO	D
18	138	NA	135	6	CO	D
23	143	NA	135	6	CO	D
24	144	NA	135	6	CO	D
17 Aug	229	14-49°N	75	5	HDRB	T
18	230	14-49°N	75	5	HDRB	T
24	236	25-48°N	75	5	HDRA	T
25	237	14-49°N	75	5	HDRB	T
26	238	14-49°N	75	5	HDRB	T
27	239	10-45°N	75	5	HRDB	T
9 Sep	252	6-43°N	75	5	HRDB	T
28	271	10-45°N	75	5	HRDB	T
29	272	10-45°N	75	5	HRDB	T
30	273	10-45°N	75	5	HRDB	T

Table 7-10
VAS Data on CCT at GSFC

Activity	Time Period
Special Network Days	6-7 March 1982 24-25 April 1982 27-28 March 1982 1-2 May 1982
Case Studies	13 July 1981 20 July 1981 27-28 July 1981
Hurricanes	
Emily	2-3 September 1981
Beryl	31 August-11 September 1982
Chris	10-11 September 1982
Miscellaneous	
GOES-4 Assessment	7, 18, 20 November 1980
GOES-5 Assessment	10, 22, 26, 29 June and 4 August 1981
GSFC/UW Comparison	6 March and 1 May 1982
El Chichon Eruption	6-8 April 1982
Time Series	
Synoptic Dwells	July 1981
All Day	13-17, 20-24, 27-31 July 1981

REFERENCES

- "GSFC SVAS Ground Station Report." Westinghouse Electric Corporation, Defense and Electronic Systems Center, Command and Control Division, Baltimore, MD 21203. (Report FIS-78-4044 under contract NAS5-24306.), 1978, 170 pp.
- "VAS S/DB Calibration Parameter Definition. *ibid.*, (Contract NAS5-32582), 1978, 8 pp.
- "Wallops VAS S/DB Mode AA Output Format (Revision B)." *ibid.*, 1979, 58 pp.
- "GSFC VAS Preprocessor Data Formats (Revision D)." *ibid.*, 71 pp.
- "GSFC VAS Preprocessor Real Time Software (Revision A)." *ibid.*, 1979, 100 pp.
- "GSFC VAS Preprocessor Off Line and Test Simulator Software." *ibid.*, 1979, 22 pp.
- "Synchronizer Data Buffer System Design Report for the CDA Station." *ibid.*, 1979, 320 pp.
- "VAS Preprocessor Software Manual." *ibid.*, 1980, 240 pp.
- Anthony, R. W., and G. S. Wade, 1983: "VAS Operational Assessment Findings for Spring 1982/1983." *Fifth Conference on Severe Local Storms*, October 17-20, Tulsa, Oklahoma, AMS, Boston, MA.
- Barnes, S. L., 1964: "A Technique for Maximizing Detail in Numerical Map Analysis." *J. Appl. Meteor.*, **3**, pp. 396-409.
- Barton, I. J., 1983: "Dual Channel Measurements of Sea Surface Temperature." *Quart. J. Roy. Meteor. Soc.*, **109**, accepted for publication.
- Bates, J. J., 1983: "Use of VAS Multispectral Data for Sea Surface Temperature Determination." *Satellite Derived Sea Surface Temperature Workshop II*, June 22-24, Pasadena, California, JPL.
- Bruce, R. F., L. D. Duncan, and J. H. Pierluissi, 1977: "Experimental Study of the Relationship Between Rawinsonde Temperatures and Satellite Derived Temperatures." *Mon. Wea. Rev.*, **105**, pp. 493-496.
- Chan, J. C. L., and W. M. Gray, 1982: "Tropical Cyclone Movement and Surrounding Flow Relationships." *Mon. Wea. Rev.*, **110**, pp. 1354-1374.
- Chesters, D., 1980: "Statistically Conditioned Least-Squares Retrievals Planned for the VAS Demonstration Experiment." *VAS Demonstration Sounding Workshop*, 1980: D. L. Endres and L. W. Uccellini, eds. NASA CP-2157 (NTIS-81N19709), pp. 67-79.
- _____, L. W. Uccellini, H. E. Montgomery, A. Mostek, and W. D. Robinson, 1981: "Assessment of the First Radiances Received From the VISSR Atmospheric Sounder (VAS) Instrument." NASA TM 83827 (NTIS-82N19730), 124 pp.
- _____, L. W. Uccellini, and A. Mostek, 1982: "VISSR Atmospheric Sounder (VAS) Simulation Experiment for a Severe Storm Environment." *Mon. Wea. Rev.*, **110**, pp. 198-216.
- _____, L. W. Uccellini, and W. D. Robinson, 1983: "Low-level Water Vapor Fields From the VISSR Atmospheric Sounder (VAS) Split Window Channels." *J. Clim. Appl. Meteor.*, **22**, pp. 725-743.
- _____, and W. D. Robinson, 1983: "Performance Appraisal of VAS Radiometry for GOES-4, -5, and -6." NASA TM 85125, 55 pp.
- Endres, D. L. and L. W. Uccellini, 1980: *VAS Demonstration Sounding Workshop*. NASA CP-2157 (NTIS-81N19709), 81 pp.
- Fankhauser, J. C., 1969: "Convective Processes Resolved by a Mesoscale Rawinsonde Network." *J. Appl. Meteor.*, **8**, pp. 778-798.
- Fuelberg, H. E., and G. J. Jedlovec, 1982: "A Sub-Synoptic-Scale Kinetic Energy Analysis of the Red River Valley Tornado Outbreak (AVE-SESAME I)." *Mon. Wea. Rev.*, **110**, pp. 2005-2024.
- Gatlin, J. A., 1982: "Correlation of 3-Hour Radiosonde Data with Coincident NIMBUS-7 Total Ozone Measurements." *VISSR Atmospheric Sounder (VAS) Research Review*, 1983: J. R. Greaves, ed. NASA CP-2253 (NTIS-83N24028), pp. 31-33.
- Greaves, J. R., H. E. Montgomery, L. W. Uccellini, and D. L. Endres, 1982: "1982 AVE/VAS Ground Truth Field Experiment: Satellite Data Acquisition Summary

and Preliminary Meteorological Review. NASA/GSFC X-903-82-17, 27 pp.

_____, 1983: *VISSR Atmospheric Sounder (VAS) Research Review*. NASA CP-2253 (NTIS-83N24028), 52 pp.

Hayden, C. M., 1980: "Low-level Moisture from VAS." *VAS Demonstration Sounding Workshop*, 1980: D. L. Endres and L. W. Uccellini, eds. NASA CP-2157 (NTIS-81N19709), pp. 57-65.

_____, 1982: VAS Temperature Retrievals for NASA Special Network Observations of 6 March 1982." *VISSR Atmospheric Sounder (VAS) Research Review*, 1983: J. R. Greaves, ed. NASA CP-2253 (NTIS-83N24028), pp. 33-36.

Hildebrand, F. B., 1962: *Advanced Calculus for Applications*. Prentice-Hall, Inc., 646 pp.

Hill, C. K., and R. E. Turner, 1983: "NASA's AVE/VAS Program." *Bull. Amer. Meteor. Soc.*, **64**, pp. 796-797.

Keller, D. L., 1982: "A Statistical Severe Weather Forecasting Technique Using Satellite Soundings and Radiosonde Data." M. S. thesis, Department of Meteorology, University of Wisconsin, Madison, Wisconsin 53706, 54 pp.

_____, and W. L. Smith, 1983: "A Statistical Technique for Forecasting Severe Weather From Vertical Soundings by Satellite and Radiosonde." NOAA Technical Memorandum NESDIS 5, 41 pp.

Koch, S. E., M. desJardins, and P. J. Kocin, 1983: "An Interactive Barnes Objective Analysis Scheme for Use with Satellite and Conventional Data." *J. Clim. Appl. Meteor.*, **22**, pp. 1487-1503.

Lee, T. H., D. Chesters, and A. Mostek, 1983: "The Impact of Conventional Surface Data Upon VAS Regression Retrievals in the Lower Troposphere." *J. Clim. Appl. Meteor.*, **22**, pp. 1853-1874.

Lewis, J. M., C. M. Hayden, and A. J. Schreiner, 1983: "Adjustment of VAS and RAOB Geopotential Analysis Using Quasi-Geostrophic Constraints." Accepted by *Mon. Wea. Rev.*

Lord, R. J., W. P. Menzel, and L. E. Pecht, 1984:

"ACARS Wind Measurements: An Intercomparison with Radiosondes, Cloud Motion and VAS Thermally Derived Winds." Accepted for publication by *J. Atmos. Oceanic Tech.*

Malinowski, F. R. and R. D. Ruiz, 1980: *VAS-D GOES Data Book* (2 volumes). Santa Barbara Research Center, Hughes Aircraft Co., 75 Coromar Drive, Goleta, CA 93017. (Contract NAS5-20769.) 650 pp.

Menzel, W. P., 1980: "Prelaunch Study Report of VAS-D Performance." University of Wisconsin, Space Science and Engineering Center, 1225 West Dayton Street, Madison, WI 53706. (Contract NAS5-21965.) 65 pp.

_____, 1981: "Postlaunch Study Report of VAS-D Performance." *ibid.*, 25 pp.

_____, 1981: "Prelaunch Study Report of VAS-E Performance." *ibid.*, 9 pp.

_____, 1981: "Postlaunch Study Report of VAS-E Performance." *ibid.*, 11 pp.

_____, 1983: "Prelaunch Study Report of VAS-F Performance." *ibid.*, 7 pp.

_____, 1983: "Postlaunch Study Report of VAS-F Performance." *ibid.*, 12 pp.

_____, W. L. Smith, and L. D. Herman, 1981: "Visible Infrared Spin-scan Radiometer Atmospheric Sounder Radiometric Calibration: An Inflight Evaluation From Intercomparisons with HIRS and Radiosonde Measurements." *Applied Optics*, **20**, pp. 3641-3644.

_____, W. L. Smith, and T. R. Stewart, 1983: "Improved Cloud Motion Wind Vector and Altitude Assignment Using VAS." *J. Clim. Appl. Meteor.*, **22**, pp. 377-384.

_____, W. L. Smith, G. S. Wade, L. D. Herman, and C. M. Hayden, 1983: "Atmospheric Soundings from a Geostationary Satellite." *Applied Optics*, **22**, pp. 2686-2689.

Montgomery, H. E. and D. L. Endres, 1977: "Survey of Dwell Sounding for VISSR Atmospheric Sounder (VAS)." NASA/GSFC X-942-77-157, 50 pp.

_____, 1980: *Execution Phase Project Plan for*

Operational Satellite Improvement Program Plan – VISSR Atmospheric Sounder (VAS) Demonstration (Revision 2). NASA/GSFC Management Copy. 101 pp.

Mosher, F. R., 1979: "Cloud Drift Winds from Geostationary Satellites." *Atmospheric Technology*, **10**, pp. 53-60.

_____, and T. R. Stewart, 1981: "Characteristics of Water Vapor Tracked Winds." *NAVENVPREDRSCHFAC Contractor Report, CR 81-06*, 55 pp.

Mostek, A., L. W. Uccellini, R. A. Petersen, and D. Chesters, 1984: "Case Study of a Pre-convective Environment Using VAS Sounding Profiles." Submitted to *Mon. Wea. Rev.*

Neumann, C. J., and J. M. Pelissier, 1981: "Models for the Prediction of Tropical Cyclone Motion over the North Atlantic: An Operational Evaluation." *Mon. Wea. Rev.*, **109**, pp. 522-538.

O'Lenic, E. A., 1982: "Evaluation of the Effect of VAS Data on Some NMC Analyses and Forecasts." NOAA NWS NMC Office Note 253.

Petersen, R. A., L. W. Uccellini, D. Chesters, and A. Mostek, 1983: "The Use of VAS Satellite Data in Weather Analysis, Prediction and Diagnosis." *Nat. Wea. Digest*, **8**, pp. 12-23.

_____, L. W. Uccellini, A. Mostek, and D. A. Keyser, 1983: "The Use of VAS Moisture Channels in Delineating Regions With A Potential for Convective Instability." Accepted by *Mon. Wea. Rev.*

Petterssen, S., 1956: *Weather Analysis and Forecasting, Volume I. Motion and Motion Systems*. McGraw Hill, 428 pp.

Prabhakara, C., G. Dahu, and V. G. Kunde, 1974: "Estimation of Sea Surface Temperature From Remote Sensing in the 11 to 13 μm Window Region." *J. Geophys. Res.*, **79**, pp. 5039-5044.

Reynolds, R. W., 1982: "A Monthly Averaged Climatology of Sea Surface Temperatures. NOAA Technical Report NWS-31, 35 pp.

Sanders, F., A. C. Pike, and J. P. Gaertner, 1975: "A Barotropic Model for Operational Prediction of Tracks

of Tropical Storms." *J. Appl. Meteor.*, **14**, pp. 265-280.

Sienkiewicz, M. E., 1982: "AVE/VAS II – 25 mb Sounding Data." Texas A&M University, College Station, TX 77843. Interim contractor report prepared for Marshall Space Flight Center, Alabama 35812. (Contract NAS8-34133). NASA CR-170691 (NTIS-83N17013), 303 pp.

_____, 1982: "AVE/VAS III – 25 mb Sounding Data." *ibid.*, NASA CR-170692 (NTIS-83N15997), 305 pp.

_____, 1983: "AVE/VAS I – 25 mb Sounding Data." *ibid.*, NASA CR-170735 (NTIS-83N24047), 36 pp.

_____, 1983: "AVE/VAS IV – 25 mb Sounding Data." *ibid.*, NASA CR-170739 (NTIS-83N25266), 330 pp.

_____, 1983: "AVE/VAS V – 25 mb Sounding Data." *ibid.*, NASA CR-170740 (NTIS-83N25267), 322 pp.

Smith, W. L., 1970: "Iterative Solution of the Radiative Transfer Equation for Temperature and Absorbing Gas Profiles of an Atmosphere." *Applied Optics*, **9**, pp. 1993-1999.

_____, V. E. Suomi, W. P. Menzel, H. M. Woolf, L. A. Sromovsky, H. E. Revercomb, C. M. Hayden, D. N. Dickson, and F. R. Mosher, 1981: "First Sounding Results from VAS-D." *Bull. Amer. Meteor. Soc.*, **62**, pp. 232-236.

_____, and H. M. Woolf, 1981: "Algorithms Used to Retrieve Surface Skin Temperature and Vertical Temperature and Moisture Profiles from VISSR Atmospheric Sounder (VAS) Radiance Observations." Reprint volume: *Fourth Conference on Atmospheric Radiation*, June 16-18, Toronto, Canada, AMS, Boston, MA, 1982.

_____, and F. X. Zhou, 1982: "Rapid Extraction of Layer Relative Humidity, Geopotential Thickness, and Atmospheric Stability from Satellite Sounding Radiometer Data." *Applied Optics*, **21**, pp. 924-928.

_____, V. E. Suomi, F. X. Zhou, and W. P. Menzel, 1982: "Nowcasting Applications of Geostationary Satellite Atmospheric Sounding Data." *Nowcasting*, K.

A. Browning ed., Academic Press, New York, NY, pp. 123-135.

_____, 1983: "The Retrieval of Atmospheric Profiles and VAS Geostationary Radiance Observations." *J. Atmos. Sci.*, **40**, pp. 2025-2035.

Sparkman, J. K., and J. Giraytys, 1981: "ASDAR: A FGGE Real Time Data Collection System." *Bull. Amer. Meteor. Soc.*, **62**, pp. 394-400.

Suomi, E. W., 1982: "The Videocassette GOES Archive System – 21 Billion Bits on a Videocassette." *IEEE Transactions on Geoscience and Remote Sensing, GE-20*, pp. 119-121.

Suomi, V. E., R. Fox, S. S. Limaye, and W. L. Smith, 1983: "McIDAS III: A Modern Interactive Data Access and Analysis System. *J. Clim. Appl. Meteor.*, **22**, pp. 766-778.

Szejwach, G., 1982: "Analysis of Multispectral Data Using An Unsupervised Classification Technique – Application to VAS." *VISSR Atmospheric Sounder (VAS) Research Review*, 1983: J. R. Greaves, ed. NASA CP-2253 (NTIS-83N24028), pp. 11-12.

Tabata, S., 1978: "Comparison of Observations of Sea Surface Temperature at Ocean Station P and NOAA Buoy Stations and Those Made By Merchant Ships Traveling in Their Vicinities in the Northeast Pacific Ocean." *J. Appl. Meteor.*, **17**, 374-385.

Uccellini, L. W., and D. R. Johnson, 1979: "The Coupling of Upper and Lower Tropospheric Jet Streaks and Implications for the Development of Severe Convective Storms." *Mon. Wea. Rev.*, **107**, pp. 682-703.

_____, D. Chesters, and A. Mostek, 1982: "The Application of the VISSR Atmospheric Sounder (VAS) to the Study of Severe Convective Storms." *Preprints, Twelfth Conf. on Severe Local Storms*, San Antonio, AMS, Boston, MA, pp. 471-474.

Velden, C. S., W. L. Smith, and M. Mayfield, 1984: "Applications of VAS and TOVS to Tropical Cyclones. Accepted for Publication in *Bull. Amer. Meteor. Soc.*

APPENDIX

Publications and Reports Supported by the VAS Demonstration

BOOK AND JOURNAL ARTICLES

Chesters, D., L. W. Uccellini and A. Mostek, 1982: "VISSR Atmospheric Sounder (VAS) Simulation Experiment for a Severe Storm Environment." *Monthly Weather Review*, **110**, pp. 198-216.

Chesters, D., L. W. Uccellini and W. D. Robinson, 1983: "Low-level Water Vapor Fields from the VISSR Atmospheric Sounder (VAS) Split Window Channels. *Journal of Climate and Applied Meteorology*, **22**, pp. 725-743.

Koch, S. E., M. desJardins and P. J. Kocin, 1983: "An Interactive Barnes Objective Analysis Scheme for Use with Satellite and Conventional Data. Accepted by *Journal of Climate and Applied Meteorology*.

Lee, T. H., D. Chesters and A. Mostek, 1983: "The Impact of Conventional Surface Data Upon VAS Regression Retrievals in the Lower Troposphere. Accepted by *Journal of Climate and Applied Meteorology*.

Lewis, J. M., C. M. Hayden and A. J. Schreiner, 1983: "Adjustment of VAS and RAOB Geopotential Analysis Using Quasi-Geostrophic Constraints. Accepted by *Monthly Weather Review*.

Menzel, W. P., W. L. Smith and L. D. Herman, 1981: "Visible Infrared Spin-scan Radiometer Atmospheric Sounder Radiometric Calibration: An Inflight Evaluation from Intercomparisons with HIRS and Radiosonde Measurements." *Applied Optics*, **20**, pp. 3641-3644.

Menzel, W. P., W. L. Smith and T. R. Stewart, 1983: "Improved Cloud Motion Wind Vector and Altitude Assignment Using VAS." *Journal of Climate and Applied Meteorology*, **22**, pp. 377-384.

Menzel, W. P., W. L. Smith, G. S. Wade, L. D. Herman and C. M. Hayden, 1983: "Atmospheric Soundings from a Geostationary Satellite." *Applied Optics*, **22**, pp. 2686-2689.

Mostek, A., L. W. Uccellini, R. A. Petersen, D. Chesters and T. H. Lee, 1983: "A Case Study of the Impact of VAS Soundings in the Analysis of a Pre-convective

Environment." In preparation for *Monthly Weather Review*.

Petersen, R. A., L. W. Uccellini, D. Chesters and A. Mostek, 1983: "The Use of VAS Satellite Data in Weather Analysis, Prediction and Diagnosis." *National Weather Digest*, 8, pp. 12-23.

Petersen, R. A., L. W. Uccellini, A. Mostek and D. A. Keyser, 1983: "The Use of VAS Moisture Channels in Delineating Regions With A Potential for Convective Instability." Accepted by *Monthly Weather Review*.

Smith, W. L., V. E. Soumi, W. P. Menzel, H. M. Woolf, L. A. Sromovsky, H. E. Revercomb, C. M. Hayden, D. N. Dickson and F. R. Mosher, 1981: "First Sounding Results from VAS-D." *Bulletin of the AMS*, 62, pp. 232-236.

Smith, W. L., V. E. Suomi, F. X. Zhou and W. P. Menzel, 1982: "Nowcasting Applications of Geostationary Satellite Atmospheric Sounding Data." *Nowcasting*, ed. K. A. Browning, Academic Press, New York, NY, pp. 123-135.

Smith, W. L., 1983: "The Retrieval of Atmospheric Profiles from VAS Geostationary Radiance Observations." *Journal of Atmospheric Sciences*, 40, pp. 2025-2035.

Suomi, V. E., R. Fox, S. S. Limaye and W. L. Smith, 1983: "McIDAS III: A Modern Interactive Data Access and Analysis System." *Journal of Climate and Applied Meteorology*, 22, pp. 766-778.

REVIEWS OF THE VAS DEMONSTRATION

GSFC VAS Demonstration Review, 1977: H. E. Montgomery, ed. VAS Working Group Meeting, held January 27, 1977. 95 pp.

Execution Phase Project Plan for Operational Satellite Improvement Program Plan - VISSR Atmospheric Sounder (VAS) Demonstration (Revision 2), 1980: H. E. Montgomery, Project Manager. NASA/GSFC Management Copy. 101 pp.

VAS Demonstration Briefing Book, 1980: R. J. Pinnamonti and H. E. Montgomery, ed. Graphic Materials Based Upon Presentations to A. J. Calio on September 2, 1980. NASA/GSFC VAS Demonstration Management Copy. 70 pp.

VAS Demonstration Sounding Workshop, 1980: D. L. Endres and L. W. Uccellini, ed. NASA CP-2157 (NTIS-81N19709). 81 pp.

VISSR Atmospheric Sounder (VAS) Research Review, 1983: J. R. Greaves, ed. NASA CP-2253 (NTIS-83N24028). 52 pp.

Final Report of the VAS Demonstration, 1984: H. E. Montgomery and L. W. Uccellini, ed. (In preparation).

PRESENTATIONS AT CONFERENCES AND WORKSHOPS

Anderson, R. K., 1982: "Use of VAS Water Vapor Imagery to Analyze Upper-Level Flow Patterns." *VISSR Atmospheric Sounder (VAS) Research Review*, 1983: J. R. Greaves, ed. NASA CP-2253 (NTIS-83N24028), pp. 29-30.

Anthony, R. W. and G. S. Wade, 1983: "VAS Operational Assessment Findings for Spring 1982/83." Preprints, *Thirteenth Conference on Severe Local Storms*, Tulsa: AMS, Boston, MA, pp. J23-J28.

Chesters, D., L. W. Uccellini and W. D. Robinson, 1982: "Low-level Water Vapor Fields from the VAS "Split Window" Channels at 11 and 12 Microns." *VISSR Atmospheric Sounder (VAS) Research Review*, 1983: J. R. Greaves, ed. NASA CP-2253 (NTIS-83N24028). pp. 5-6.

desJardins, M. And R. A. Petersen, 1983: "GEMPAK - An Interactive Meteorological Display and Analysis System." Preprints, *Ninth Conference on Aerospace and Aeronautical Meteorology*, Omaha: AMS, Boston, MA, pp. 55-59.

Gatlin, J. A., 1982: "Correlation of 3-Hour Radiosonde Data with Coincident NIMBUS-7 Total Ozone Measurements." *VISSR Atmospheric Sounder (VAS) Research Review*, 1983: J. R. Greaves, ed. NASA CP-2253 (NTIS-83N24028), pp. 31-33.

Hayden, C. M., 1980: "Low-Level Moisture from VAS." *VAS Demonstration Sounding Workshop*, D. L. Endres and L. W. Uccellini, ed. NASA CP-2157 (NTIS-81N19709), pp. 57-65.

Hayden, C. M., 1982: "VAS Temperature Retrievals for NASA Special Network Observations of 6 March 1982." *VISSR Atmospheric Sounder (VAS) Research*

- Review, 1983, J. R. Greaves, ed. NASA CP-2253 (NTIS-83N24028), pp. 33-36.
- Hayden, C. M., H. B. Howell, E. R. Westwater and G. S. Wade, 1983: "Results of Combining the Profiler and VAS for Determining Temperature and Moisture in the Atmosphere." Preprints, *Ninth Conference on Aerospace and Aeronautical Meteorology*, Omaha: AMS, Boston MA, pp. 188-190.
- Heckman, B., W. Carle and R. Anthony, 1982: "VAS Operational Procedures and Results at the Kansas City Satellite Field Services Station." *VISSR Atmospheric Sounder (VAS) Research Review*, 1983, J. R. Greaves, ed. NASA CP-2253 (NTIS-83N24028). pp. 21-24.
- Koch, S. E., P. J. Kocin and M. desJardins, 1983: "The GEMPAK Barnes Objective Map Analysis Scheme." Preprints, *Ninth Conference on Aerospace and Aeronautical Meteorology*, Omaha: AMS, Boston, MA, pp. 34-39.
- Jedlovec, G. J., 1982: "AVE/VAS Experiment: Synoptic Summary and Preliminary Results." *VISSR Atmospheric Sounder (VAS) Research Review*, 1983: J. R. Greaves, ed. NASA CP-2253 (NTIS-83N24028), pp. 39-44.
- Kruidenier, M., 1982: "VAS Applications at Colorado State University." *VISSR Atmospheric Sounder (VAS) Research Review*, 1983, J. R. Greaves, ed. NASA CP-2253 (NTIS-83N24028), pp. 45-48.
- Lewis, J. M., 1982: "Adjustment of VAS Geopotential Analyses by Using Precedent RAOB Analyses and Quasi-Geostrophic Constraints." Proceedings of *Fourteenth Stanstead Conference*, at Bishop's University, Lennoxville, Quebec, July 12-16, 1982; pp. 115-125.
- Menzel, W. P., T. R. Stewart and W. L. Smith, 1982: "Specifying Heights and Velocities of Cloud Motion from Geostationary Sounding Data." *VISSR Atmospheric Sounder (VAS) Research Review*, 1983, J. R. Greaves, ed. NASA CP-2253 (NTIS-83N24028), pp. 25-26.
- Montgomery, H. E., 1982: "VAS System Description." *VISSR Atmospheric Sounder (VAS) Research Review*, 1983, J. R. Greaves, ed. NASA CP-2253 (NTIS-83N24028), pp. 1-4.
- O'Lenic, E. A. and N. Phillips, 1982: "Evaluation of the Effect of VAS Data on Some NMC Analyses and Forecasts." *VISSR Atmospheric Sounder (VAS) Research Review*, 1983, J. R. Greaves, ed. NASA CP-2253 (NTIS-83N24028), pp. 27-29.
- Petersen, R. A., L. W. Uccellini, D. Chesters, A. Mostek and D. Keyser, 1982: "Diagnosing Convective Instability Using VAS Data." *VISSR Atmospheric Sounder (VAS) Research Review*, 1983, J. R. Greaves, ed. NASA CP-2253 (NTIS-83N24028), pp. 7-8.
- Petersen, R. A. and A. Mostek, 1982: "The Use of VAS Moisture Channels in Delineating Regions of Potential Convective Instability." Preprints, *Twelfth Conference on Severe Local Storms*, San Antonio: AMS, Boston, MA, pp. 168-171.
- Petersen, R. A., L. W. Uccellini, D. Chesters, A. Mostek and D. Keyser, 1982: "The Use of VAS Satellite Data in Weather Analysis, Prediction and Diagnosis." Preprints, *Ninth Conference for Weather Forecasting and Analysis*, Seattle: AMS, Boston, MA, pp. 219-226.
- Petersen, R. A., D. A. Keyser, A. Mostek and L. W. Uccellini, 1983: "Techniques for Diagnosing Mesoscale Phenomena Affecting Aviation Using VAS Satellite Data." Preprints, *Ninth Conference on Aerospace and Aeronautical Meteorology*, Omaha: AMS, Boston, MA, pp. 12-17.
- Petersen, R. A., D. A. Keyser, A. Mostek and L. W. Uccellini, 1983: "Severe Storms Analysis and Forecasting Techniques Using VAS Satellite Data." Preprints, *Thirteenth Conference on Severe Local Storms*, Tulsa: AMS, Boston, MA, pp. J29-J32.
- Robinson, W. D., D. Chesters and L. W. Uccellini, 1983: "Low-level Water Vapor Fields from the VISSR Atmospheric Sounder (VAS) Split Window Channels." Preprints, *Ninth Conference on Aerospace and Aeronautical Meteorology*, Omaha: AMS, Boston, MA, pp. 165-170.
- Rodgers, E. B. and J. Stout, 1982: "The Inference of Tropical Cyclone Dynamics Using GOES VISSR/VAS Data." *VISSR Atmospheric Sounder (VAS) Research Review*, 1983, J. R. Greaves, ed. NASA CP-2253 (NTIS-83N24028), pp. 13-16.
- Scoggins, J. R., 1982: "AVE/VAS Experiment: Ground Truth Network." *VISSR Atmospheric Sounder (VAS) Research Review*, 1983, J. R. Greaves, ed. NASA CP-2253 (NTIS-83N24028), pp. 37-38.

Shenk, W. E., 1982: "Future Research Contributions of the VAS." *VISSR Atmospheric Sounder (VAS) Research Review*, 1983, J. R. Greaves, ed. NASA CP-2253 (NTIS-83N24028), pp. 49-50.

Smith, W. L. and H. M. Woolf, 1982: "Algorithms Used to Retrieve Surface-Skin Temperature and Vertical Temperature and Moisture Profiles from VISSR Atmospheric Sounder (VAS) Radiance Observations." Preprints, *Fourth Conference on Atmospheric Radiation*, Toronto: AMS, Boston, MA, pp. 13-17.

Smith, W. L., 1982: "VAS Assessment Status and Preliminary Results. *VISSR Atmospheric Sounder (VAS) Research Review*, 1983: J. R. Greaves, ed. NASA CP-2253 (NTIS-83N24028), pp. 17-19.

Suomi, E. W., 1982: "The Videocassette GOES Archive System – 21 Billion Bits on a Videocassette." *IEEE Transactions on Geoscience and Remote Sensing, GE-20*, pp. 119-121.

Szejwach, G., 1982: "Analysis of Multispectral Data Using an Unsupervised Classification Technique – Application to VAS." *VISSR Atmospheric Sounder (VAS) Research Review*, 1983, J. R. Greaves, ed. NASA CP-2253 (NTIS-83N24028), pp. 11-12.

Uccellini, L. W., R. A. Petersen, D. Chesters, A. Mostek and T. H. Lee, 1982: "Use of VAS for Analysis in a Prethunderstorm Environment." *VISSR Atmospheric Sounder (VAS) Research Review*, 1983, J. R. Greaves, ed. NASA CP-2253 (NTIS-83N24028), pp. 9-10.

Uccellini, L. W., D. Chesters and A. Mostek, 1982: "The Application of the VISSR Atmospheric Sounder (VAS) to the Study of Severe Convective Storms." Preprints, *Twelfth Conference on Severe Local Storms*, San Antonio: AMS, Boston, MA, pp. 471-474.

Wilson, G. S., 1982: "Some Potential Research Applications of GOES/VAS Data in Meteorology." *VISSR Atmospheric Sounder (VAS) Research Review*, 1983, J. R. Greaves, ed. NASA CP-2253 (NTIS-83N24028), pp. 51-53.

TECHNICAL REPORTS FROM NASA/GSFC

Chesters, D., 1980: "Approach to Sounding on the VAS Processor." NASA TM-80713 (NTIS-80N28056). 18 pp.

Chesters, D., L. W. Uccellini, H. E. Montgomery, A. Mostek and W. D. Robinson, 1981: "Assessment of the First Radiances Received from the VISSR Atmospheric Sounder (VAS) Instrument." NASA TM 83827 (NTIS-82N19730). 124 pp.

Chesters, D., L. W. Uccellini and A. Mostek, 1982: "VISSR Atmospheric Sounder (VAS) Simulation Experiment for a Severe Storm Environment. NASA TM 83822 (NTIS-82N19774). 32 pp.

Chesters, D., 1982: "Effects of El Chichon Eruptions on Satellite Observations – VAS on GOES." *Radiative Effects of the El Chichon Volcanic Eruption: Preliminary Results Concerning Remote Sensing*, W. R. Bandeen and R. S. Fraser, ed. NASA TM 84959 (NTIS-83N19372). pp 4-25 to 4-29.

Chesters, D., L. W. Uccellini and W. D. Robinson, 1983: "Low-level Water Vapor Fields from the VISSR Atmospheric Sounder (VAS) Split Window Channels. NASA TM 83951 (NTIS-82N32914). 33 pp.

Chesters, D. and W. D. Robinson, 1983: "Performance Appraisal of VAS Radiometry for GOES-4, -5 and -6. NASA TM 85125, 55 pp.

Greaves, J. R., H. E. Montgomery, L. W. Uccellini and D. L. Endres, 1982: "1982 AVE/VAS Ground Truth Field Experiment: Satellite Data Acquisition Summary and Preliminary Meteorological Review. NASA/GSFC X-903-82-17. 27 pp.

Koch, S. E., M. desJardins and P. J. Kocin, 1981: "The GEMPAK Barnes Objective Analysis Scheme." NASA TM 83851 (NTIS-82N21921). 56 pp.

Lee, T. H., D. Chesters and A. Mostek, 1983: "The Impact of Conventional Surface Data upon VAS Regression Retrievals in the Lower Troposphere." NASA TM 83987 (NTIS-83N27522). 76 pp.

Montgomery, H. E. and D. K. Endres, 1977: "Survey of Dwell Sounding for VISSR Atmospheric Sounder (VAS)." NASA/GSFC X-942-77-157. 50 pp.

TECHNICAL REPORTS FROM SBRC

Phase II Design Review of VAS (2 volumes), 1974. Santa Barbara Research Center, Hughes Aircraft Co., 75 Coromar Drive, Goleta, CA 93017. (Contract NAS5-20769). 410 pp.

Malinowski, F. R. and R. D. Ruiz, 1980: *VAS-D GOES Data Book* (2 volumes). *ibid.*, 650 pp.

TECHNICAL REPORTS FROM NOAA/UW/SSEC

Keller, D. L. and W. L. Smith, 1983: "A Statistical Technique for Forecasting Severe Weather from Vertical Soundings by Satellite and Radiosonde." Available from the NOAA/NESDIS Development Laboratory, 1225 West Dayton Street, Madison, Wisconsin 53706. 41 pp.

Lord, R. J., W. P. Menzel and L. E. Pecht, 1983: "Acars Wind Measurements: "An Intercomparison with Radiosonde, Cloud Motion, and VAS Thermally Derived Winds." A report from the Space Science and Engineering Center, 1225 West Dayton Street, Madison, Wisconsin 53706. 6 pp.

Menzel, W. P., 1980: "Prelaunch Study Report of VAS-D Performance." University of Wisconsin, Space Science and Engineering Center, 1225 West Dayton Street, Madison, Wisconsin 53706 (Contract NAS 5-21965). 65 pp.

_____, 1981: "Postlaunch Study Report of VAS-D Performance." *ibid.*, 25 pp.

_____, 1981: "Prelaunch Study Report of VAS-E Performance." *ibid.*, 9 pp.

_____, 1981: "Postlaunch Study Report of VAS-E Performance." *ibid.*, 11 pp.

_____, 1983: "Prelaunch Study Report of VAS-F Performance." *ibid.*, 7 pp.

_____, 1983: "Postlaunch Study Report of VAS-F Performance." *ibid.*, 12 pp.

Menzel, W. P., 1981: "An Overview of the UW VAS Program." A Report From the Space Science and Engineering Center, 1225 West Dayton Street, Madison, Wisconsin 53706. 29 pp.

Menzel, W. P., W. L. Smith, G. S. Wade and C. M. Hayden, 1983: "An Evaluation of Atmospheric Soundings from a Geostationary Satellite. A report from the Space Science and Engineering Center, 1225 West Dayton Street, Madison, Wisconsin 53706. 13 pp.

Smith, W. L., 1983: "VAS – Characteristics and Appli-

cations." Presented at the *International Direct Broadcast Services Users Conference*, 7-10 June, Washington, D.C.. Available from the NOAA/NESDIS Development Laboratory, 1225 West Dayton Street, Madison, Wisconsin 53706. 11 pp.

Togstad, W. E., J. M. Lewis and H. M. Woolf, 1982: "A Method for Improving the Estimation of Conditional Instability from Satellite Retrievals. NOAA TR NESS-93 (NTIS-83N31260). 31 pp.

Wade, G. S., W. P. Menzel and W. L. Smith, 1982: "Applications of VAS Toward Monitoring Severe Weather." University of Wisconsin, Space Science and Engineering Center, 1225 West Dayton Street, Madison, Wisconsin 53706 (Contract NAS 5-21965). 9 pp.

TECHNICAL REPORTS FROM WESTINGHOUSE CORP.

Anon., 1978: "GSFC SVAS Ground Station Report." Westinghouse Electric Corporation, Defense and Electronic Systems Center, Command and Control Division, Baltimore, MD 21203. (Report FIS-78-4044 under contract NAS 5-24306). 170 pp.

_____, 1978: "VAS S/DB Calibration Parameter Definition. *ibid.*, (Contract NAS 5-23582). 8 pp.

_____, 1979: "Wallops VAS S/DB Mode AA Output Format (Revision B). *ibid.*, 58 pp.

_____, 1979. "GSFC VAS Preprocessor Data Formats (Revision D)." *ibid.*, 71 pp.

_____, 1979: "GSFC VAS Preprocessor Real Time Software (Revision A)." *ibid.*, 100 pp.

_____, 1979: "GSFC VAS Preprocessor Off Line and Test Simulator Software." *ibid.*, 22 pp.

_____, 1979: "Synchronizer Data Buffer System Design Report for the CDA Station." *ibid.*, 320 pp.

_____, 1980: "VAS Preprocessor Software Manual." *ibid.*, 240 pp.

TECHNICAL REPORTS FROM CSC

Allen, M. S., D. P. Helfer, S. R. Carter, F. D. Eastham, W. P. Gross, R. K. Jamros, W. J. Koster, M. A. Kostka,

- T. H. Lee, C. A. Raab, W. D. Robinson, N. E. Sarstedt and H. M. Sielski, 1980: "VAS Processing System User's Guide (version 2)." CSC TR-80-6001, Computer Sciences Corporation, Silver Spring, MD. (Contract NAS 5-24350). 276 pp.
- Allen, M. S., 1981: "Options for Exchange of Sounding Data Between the VAS and AOIPS Processors, Design Study. CSC TM-81-6072, *ibid.*, 56 pp.
- Carter, S. R., 1979: "Programming Techniques for the PDP-11/70 VAS Processor (interim report 2)." CSC TM-79-6094, *ibid.*, 111 pp.
- Carter, S. R., D. Chesters, F. Y. Yap and T. H. Lee, 1979: "VAS Science Software (interim report 3)." CSC TM-79-6092, *ibid.*, 101 pp.
- Carter, S. R. and M. S. Allen, 1980: "Datasets Resident on the VAS Processor (interim report 5)." CSC TM-80-6317, *ibid.*, 53 pp.
- Grace, L. L., D. P. Helfer, J. R. Karahisar and L. A. Rollin, 1979: "VISSR Atmospheric Sounder (VAS) Processing System – System Description." CSC SD-79-6007, *ibid.*, 460 pp.
- Gross, W., S. R. Carter and D. Chesters, 1978: "Collection and Preparation of Datasets for the VASP (interim report 2)." CSC TM-78-6290, *ibid.*, 39 pp.
- Gross, W., 1979: "Mesoscale Case Studies (interim report 3)." CSC TM-79-6095, *ibid.*, 60 pp.
- Helfer, D. P., L. L. Grace and J. R. Karahisar, 1979: "VISSR Atmospheric Sounder (VAS) Processing System Programmer's Guide (version 2)." CSC SD-79-6132, *ibid.*, 283 pp.
- Helfer, D. P., M. S. Allen, L. L. Grace, J. R. Karahisar and L. A. Rollin, 1979: "System Description for the VISSR Atmospheric Sounder (VAS) Processing System (version 2)." CSC SD-79-6136, *ibid.*, 690 pp.
- Koster, W. J., 1981: "VISS Atmospheric Sounder (VAS) Applications Programmer's Guide." CSC SD-81-6004, *ibid.*, 322 pp.
- Koster, W. J., 1982: "VISSR Atmospheric Sounder (VAS) Software System Operator's Guide." CSC TM-82-6054, *ibid.*, 45 pp.
- Koster, W. J., F. D. Eastham and N. S. Cyprych, 1982: "Systems Programmer's Guide for the VISSR Atmospheric Sounder (VAS) Processing System (2 volumes)." CSC SD-81-6003, *ibid.*, 1120 pp.
- Lee, T. H. and F. Y. Yap, 1980: "Prelaunch Study of VAS Linear Regression Retrievals." CSC TM-80-6302, *ibid.*, 25 pp.
- Lynch D. M., 1980: "DUP11/ADCCP Handler User's Guide." CSC TM-80-6090, *ibid.*, 23 pp.
- Milman, A. S., 1978: "Retrieving Water Vapor from VAS Data." CSC Subcontract to SASC. Report R-SAD-12/78-08, *ibid.*, 52 pp.
- Mostek, A., 1980: "Simulated Mesoscale Gradient Retrievals on the VAS Processor – Catalog of Product Datasets." CSC TM-80-6312, *ibid.*, 38 pp.
- Mottershead, T., 1978: "VAS Radiance Image Simulation and Processing for Cloud Pattern Analysis (interim report 1)." CSC TM-78-6294, *ibid.*, 14 pp.
- Pitter, R. L., 1979: "Survey of Potential VAS Products." CSC TM-79-6188, *ibid.*, 57 pp.
- Robinson, W. D. and F. Y. Yap, 1979: "VAS Radiance Simulation and Processing for Cloud and Radiance Information." CSC TM-79-6093, *ibid.*, 35 pp.
- Robinson, W. D., 1981: "Survey of VAS Observations of Hurricane Jeanne, November 11-14, 1980." CSC TM-81-6071, *ibid.*, 15 pp.
- Sielski, H. M. and J. B. Dunham, 1980: "Visible and Infrared Spin-Scan Radiometer (VISSR) Atmospheric Sounder (VAS) Navigation Operational Support Plan." CSC TM-80-6216, *ibid.*, 53 pp.
- Wnuk, R. S., 1979: "Shared Disk Support Documentation for the VAS Processor-to-Preprocessor Configuration." CSC SD-79-6137, *ibid.*, 129 pp.
- Yap, F. Y., D. Chesters, M. Nack, T. Mottershead, R. Pitter, S. R. Carter and W. Gross, 1978: "VAS Science Applications Support Plan and Progress Report (interim report 2)." CSC TM-78-6293, *ibid.*, 59 pp.

TECHNICAL REPORTS FROM MSFC/TAMU

Sienkiewicz, M. E., 1982: "AVE/VAS II – 25 mb

Sounding Data." Texas A&M University, College Station, Texas 77843. Interim Contractor Report Prepared for Marshall Space Flight Center, Alabama 35812. (Contract NAS 8-34133). NASA CR-170691 (NTIS-83N17013), 303 pp.

_____, 1982: "AVE/VAS III - 25 mb Sounding Data." *ibid.*, NASA CR-17092 (NTIS-83N15997), 305 pp.

_____, 1983: "AVE/VAS I - 25 mb Sounding Data." *ibid.*, NASA CR-170735 (NTIS-83N24047), 36 pp.

_____, 1983: "AVE/VAS IV - 25 mb Sounding Data." *ibid.*, NASA CR-170739 (NTIS-83N25266), 330 pp.

_____, 1983: "AVE/VAS V - 25 mb Sounding Data." *ibid.*, NASA CR-170740 (NTIS-83N25267), 322 pp.

BIBLIOGRAPHIC DATA SHEET

1. Report No. NASA RP-1151	2. Government Accession No.	3. Recipient's Catalog No.	
4. Title and Subtitle VAS Demonstration: (VISSR Atmospheric Sounder) Description and Final Report		5. Report Date October 1985	
		6. Performing Organization Code 625 and 610	
7. Author(s) H. E. Montgomery and L. W. Uccellini, Editors		8. Performing Organization Report No. 85F0274	
9. Performing Organization Name and Address Goddard Space Flight Center Greenbelt, Maryland 20771		10. Work Unit No.	
		11. Contract or Grant No.	
		13. Type of Report and Period Covered	
12. Sponsoring Agency Name and Address National Aeronautics and Space Administration Washington, DC 20546		Reference Publication	
		14. Sponsoring Agency Code	
15. Supplementary Notes			
16. Abstract The VAS Demonstration (VISSR Atmospheric Sounder) was a project designed to evaluate the VAS instrument as a remote sensor of the earth's atmosphere and surface. This report describes the instrument and ground processing system, the instrument performance, the validation as a temperature and moisture profiler compared with ground truth and other satellites, and assesses its performance as a valuable meteorological tool. The report also addresses the availability of data for scientific research.			
17. Key Words (Selected by Author(s)) Meteorology, Synchronize Data buffer, Sensor design, sensor performance, Remote sensing		18. Distribution Statement Unclassified - Unlimited Subject Category 47	
19. Security Classif. (of this report) Unclassified	20. Security Classif. (of this page) Unclassified	21. No. of Pages 198	22. Price* A09

**National Aeronautics and
Space Administration
Code NIT-3**

**Washington, D.C.
20546-0001**

**Official Business
Penalty for Private Use, \$300**

**SPECIAL FOURTH CLASS MAIL
BOOK**

**Postage and Fees Paid
National Aeronautics and
Space Administration
NASA-451**



NASA

**POSTMASTER: If Undeliverable (Section 158
Postal Manual) Do Not Return**
